Light Water Reactor Safety Research Program Semiannual Report, October 1982 – March 1983

Marshall Berman

Prepared for
U. S. NUCLEAR REGULATORY COMMISSION

LIGHT WATER REACTOR SAFETY RESEARCH PROGRAM
SEMIANNUAL REPORT, OCTOBER 1982 - MARCH 1983

Marshall Berman
May   1984

Approved: _____

Manager, Reactor Safety Research Department

_____

Director, Nuclear Fuel Cycle Programs

Sandia National Laboratories
Albuquerque, NM 87185
Operated by
Sandia Corporation
for the
U.S. Department of Energy

Previous documents in series:

Light Water Reactor Safety Research Program Semiannual Report, April-September 1981, NUREG/CR-2481 (SAND82-0006).

Light Water Reactor Safety Research Program Semiannual Report, October 1981-March 1982, NUREG/CR-2841 (SAND82-1572).

Lignt Water Reactor Safety Research Program Semiannual Report, April-September 1982, NUREG/CR-3407 (SAND83-1576).

ABSTRACT

This report describes the investigations and analyses conducted at Sandia National Laboratories, Albuquerque, in support of the Light Water Reactor Safety Research Program from October 1982 through March 1983. The Molten Fuel/Concrete Interactions (MFCI) Study investigates the mechanism of concrete erosion by molten core materials, the nature and rate of generation of evolved gases, and the effects on fission-product release. The Core Melt/Coolant Interactions (CMCI) Study investigates the characteristics of explosive and non-explosive interactions between molten core materials and concrete, and the probabilities and consequences of such interactions. In the Hydrogen Program, the HECTR code for modelling hydrogen deflagration is being developed, experiments (including those in the FITS facility) are being conducted, and the Grand Gulf Hydrogen Igniter System II is being reviewed. All activities are continuing.

CONTENTS

CONTENTS (cont.)

CONTENTS (cont.)

CONTENTS (cont.)

CONTENTS (cont.)

CONTENTS (cont.)

LIST OF ILLUSTRATIONS

ILLUSTRATIONS (Cont.)

ILLUSTRATIONS (Cont.)

ILLUSTRATIONS (Cont.)

LIST OF TABLES

LIGHT WATER REACTOR SAFETY RESEARCH PROGRAM
SEMIANNUAL REPORT, OCTOBER 1982-MARCH 1983

1. MOLTEN FUEL/CONCRETE INTERACTIONS STUDY

(R. K. Cole, Jr., D. P. Kelly, M. A. Ellis)

1.1 Summary

The Molten Fuel/Concrete Interactions (MFCIs) study currently consists of analytical investigations of the chemical and physical phenomena associated with interactions between molten core materials and concrete. Such interactions are possible during hypothetical fuel melt accidents in light water reactors (LWRs). Our main purpose is to identify and understand the dominant phenomena in order to evaluate the following:

(1) The generation rate and nature of evolved gases.

(2) The effects of gas generation on fission product release.

(3) The mechanism, rate, and directional nature of concrete erosion by the melt.

The program is directed toward the development of the CORCON computer code, a state-of-the-art computer model of molten core material/concrete interactions capable of providing quantitative estimates of reactor fuel-melt accident situations. We are now well along in the development of a MOD2 version of CORCON, with greater applicability than the released MOD1. The major extensions will be the inclusion of a crust-formation/freezing model and a model for (nonexplosive) interactions with coolant in the reactor cavity. In addition, other model improvements will be made, based on the results of our assessment of the MOD1 code.

A heat-transfer model that accounts for the effects of crust formation and freezing was installed into CORCON during the previous reporting period.[1] The model uses two one-dimensional (axial and radial) quasi-steady heat-transfer solutions to represent the average two-dimensional heat transfer. A number of "bugs" that remained at the end of September have been eliminated during this reporting period. This involved some modification of numerical methods and inclusion of a routine to project pool-side heat transfer relations from crust to no-crust conditions or vice versa. This projection is used by the routine SURFEB which performs an energy balance at the pool/concrete interface. Inclusion of the crust

model eliminates the need for the two-phase viscosity multi-
pliers, evaluated at interface temperatures, which were pre-
viously used to reduce (convective) heat-transfer coeffi-
cients and reduce heat losses when the surface of a layer
fell below the solidification temperature. As this model
has been implicated in a number of cases of peculiar code
behavior, it has been eliminated. The resulting version of
CORCON, designated Version 1.02.00, contains the crust-
formation/freezing model, the Shaw model for viscosity of
oxidic mixtures, and the various other improvements described
in previous reports. It represents a major milestone in
development of MOD2.

The crust/freezing model is iterative, while the previous
heat-transfer models were not. A simple timing study was
done to determine if this will have a significant impact on
run times. The results showed that the new model is not a
significant contributor to execution time, consuming perhaps
10% of the total. This should be compared with approximately
50% spent on heat transfer at the pool-concrete interface and
30% spent on chemistry. The present version runs at very
nearly the same speed as MOD1, typically calculating several
hours of problem time per minute of computer time on a
CDC7000-class or CRAY1 machine.

The new model has less effect on results than might have
been expected, demonstrating yet again the extent to which
the entire process is dominated by conservation of energy.

Some further work is needed involving the manner in which
the crust-formation/freezing model is coupled to other
models in CORCON. A decision must be made concerning the
ability of a solid crust to block penetration of gases.
This affects both the heat-transfer regime within the pool
and the thermal characteristics of the pool/concrete inter-
face region (the gas film). Within-pool effects are already
allowed for by the natural-convection limit of heat trans-
fer, which will automatically come into play if bubbles are
blocked. For the interface with concrete, we will require
an alternate model for film thickness, perhaps from lubrica-
tion theory. Finally, changes in the ablation/recession
model would be necessary to treat correctly the penetration
of material sufficiently frozen to be structurally rigid.

The largest remaining task is activation of the coolant
layer, to allow consideration of (nonexplosive) interactions
between melt and coolant in the reactor cavity. The coolant
layer already existed in MOD1, in the sense that it was
included in the data structure and a large fraction of the
program logic, but it was not made active there because we
believed that it would produce meaningless answers in the
absence of a crust model. It was primarily the absence of

constitutive relations (thermophysical and transport proper-
ties, and heat-transfer correlations) that made the model
inoperable. After these have been added to CORCON, we will
be able to determine what other modifications are required.
Some problems should be expected in the energy equation
because of boiling of the coolant and the need to track the
saturation line.

The second correction set and informational memo for CORCON-
MOD1, was sent to all known users on February 22, 1983. It
includes corrections for a number of additional "bugs" dis-
covered in CORCON-MOD1 since the C1 correction set was dis-
tributed in November 1981. Most are minor and should have
no effect on calculated results. One correction involves a
minor model change, something which we had hoped to avoid,
but no other solution is possible. An interior corner (a
point projecting into the pool) will lag behind for the
shape-change procedure used in MOD1, which can lead to patho-
logical cavity shapes as the corner sharpens. We have found
that increasing the recession rate of such points by just
the amount necessary to prevent corner-sharpening is suffi-
cient to eliminate the problem. The change should not be
significant for any calculation not showing geometry problems
with the old version.

A CORCON user at Westinghouse has reported unusual behavior
in the production of carbon monoxide in one of his calcula-
tions. Production fell by an order of magnitude shortly
before depletion of zirconium from the metal layer and
increased to an order of magnitude greater than its initial
value for a short period afterwards, despite an almost con-
stant ablation rate. We traced this to the phenomenon of
"coking", the reduction of carbon monoxide to elemental car-
bon in the presence of a metal with a greater affinity for
oxygen. This carbon was being "held up" in the metal for a
short period and then rapidly burned out when the zirconium
was gone. The effects on containment response would probably
be minor.

We verified that the chemical equilibrium routines were
indeed finding a minimum of the Gibbs function for CORCON's
values of the chemical potentials. This does not mean that
the prediction of coking is correct, merely that the calcu-
lation is consistent. Whether coking will occur in the real
world is unknown (to us), and we would be interested in any
information on the subject. The memo accompanying correc-
tion set C2 included a discussion of this phenomenon.

1.2 CORCON Model Development

CORCON is a user-oriented computer program written in a modu-
lar structure. It is intended to serve as a state-of-the-art
research tool while retaining utility for more routine appli-
cations. With the completion and release of CORCON-MOD1,

model development has concentrated on the long-term aspects of molten fuel/concrete interactions, although several old models (such as cavity recession and oxidic-phase viscosity) have been revised or replaced as a result of our assessment of MOD1. Inclusion of a crust-formation/freezing model, as described in Reference 1, has required several further modifications to existing models, two of which we will describe below.

1.2.1 Extrapolation of Pool-Side Heat Transfer

The subroutine SURFEB is used in CORCON to perform a surface energy balance at the pool/concrete interface. It evaluates the local temperature of the interface between the melt and the gas film using the requirement that the heat flux from the interior of the pool to this interface must equal the heat flux from the interface to the ablating concrete surface (through the gas film). The nonlinear equation

$$q_p = q_w = \sigma_B F(T_A^4 - T_w^4) + h_F(T_A - T_w) \tag{1-1}$$

where

q_p = the pool-to-interface heat flux

q_w = the interface-to-concrete heat flux

σ_B = the Stefan-Boltzmann constant

F = the radiation form factor

h_F = the film heat-transfer coefficient

T_A = the interface temperature

T_w = the concrete ablation temperature

is solved for T_A using a Newton iteration.

In CORCON-MOD1 [2], the pool-side heat flux is represented in terms of a heat-transfer coefficient

$$q_p = h_p(T_B - T_A) \tag{1-2}$$

where T_B is the (bulk) pool temperature. The dependence of h_p on T_A (if any) is ignored in the iteration, and the value for the last previous evaluation of within-pool heat transfer used. This approximation was quickly found to be inadequate when a crust model was included, because of the discontinuity in dq_p/dT_A when T_A passes through the solidification temperature, T_S. When T_A is slightly greater than T_S, this derivative is given by a convective heat-transfer coefficient which is typically large. When T_A is slightly less than T_S, a small change in surface temperature merely changes the (steady) crust thickness with very little change in the heat flux. The qualitative dependence of q_p on T_A is shown in

1-4

Figure 1.1; the problem is with extrapolation across $T_A = T_S$, which led sometimes to unphysical results and sometimes to failure of the iteration.

A complete solution, including the full evaluation of pool-side heat transfer within the iteration loop, could be extremely expensive in computer time because the energy balance is typically performed at hundreds of points along the pool/concrete interface. A simpler alternative is currently being used in Version 1.02.00, where the linear relation of Eq. 1-2 is replaced by a piecewise-linear relation with two pieces. If T_A is on the same side of T_S as it was when within-pool heat transfer was last evaluated, q_p is linearly projected along the tangent to the curve of q_p vs T_A evaluated at that time. If T_A is less than T_S but there was no crust previously, q_p is taken as the projected value for $T_A = T_S$. If T_A is greater than T_S but there was a crust previously, q_p is interpolated linearly between the projected value at $T_A = T_S$ and zero at $T_A = T_M$. The resulting approximation for q_p as a function of T_A is shown in Figure 1.2. We are currently taking T_M as the average temperature of the layer. This is correct only for a layer without significant crusts on any surfaces, so that T_M is essentially equal to the liquid temperature. Although no problems have been observed yet, we are attempting to generalize the definition of T_M.

1.2.2 Liquid-Phase Heat Transfer

In CORCON-MOD1 [2], heat transfer within a liquid pool layer (the only regime considered) was calculated from correlations for bubble-enhanced convection. A rather arbitrary natural-convection limit is included, primarily to prevent calculational problems in the absence of gas flow. No consideration is given to the conduction limit, and heat-transfer coefficients can be calculated which are smaller than conduction values. These limits become more important at late times because of both the reduction in gas generation and the possibility that partial solidification of the pool will block gas penetration. The current evolutionary version, designated Version 1.02.00, contains improved models for these limits which will be described here. Unless unexpected difficulties are encountered, we expect to include them unchanged in MOD2.

1.2.2.1 Natural Convection Limit

Correlations have been developed by Kulacki with various coworkers [3] for heat transfer to the top and bottom surfaces of internally heated pools (without bubbling) in the form
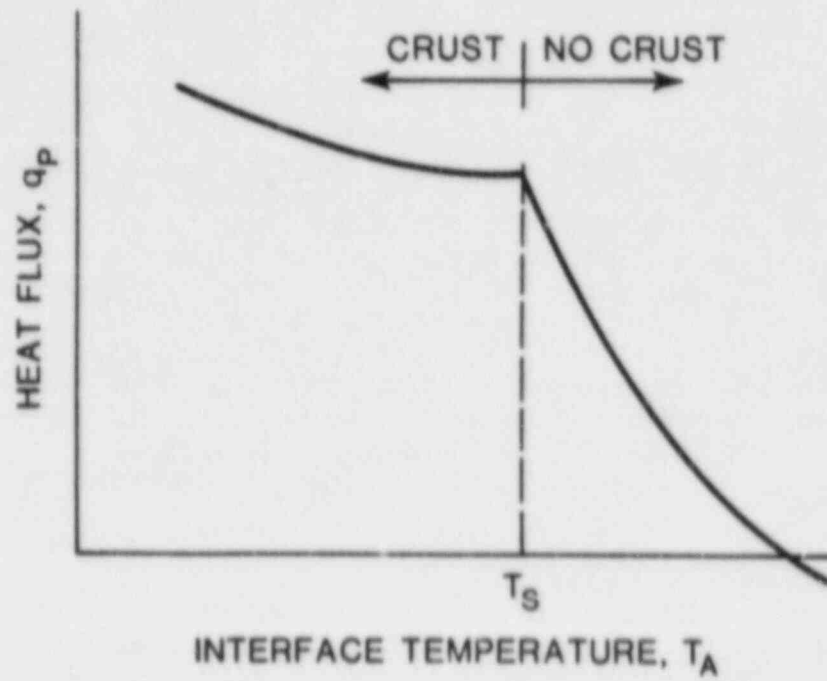
Figure 1.1. Dependence of Heat Flux on Surface Temperature
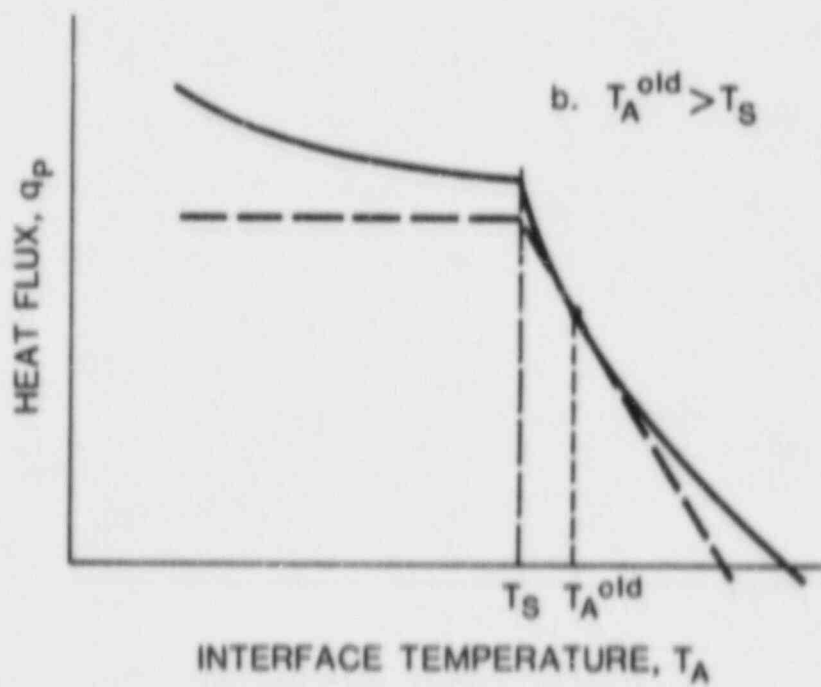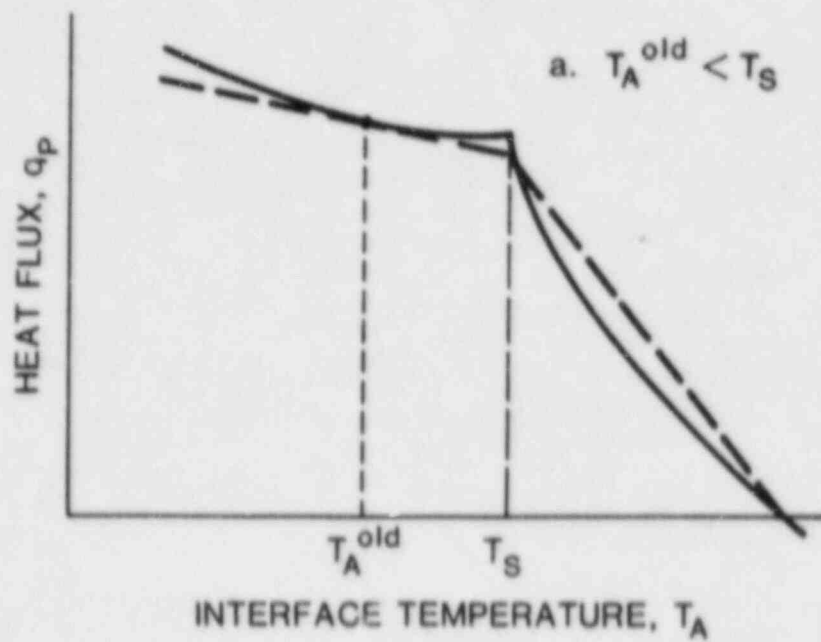
Figure 1.2. Approximation for Heat Flux as a Function of Interface Temperature

$$Nu = ARa'^m \qquad (1-3)$$

where

$$Nu = hL/k \qquad (1-4)$$

is the Nusselt number and

$$Ra' = g\beta HL^5/2\nu\kappa k \qquad (1-5)$$

is the internal Rayleigh number. Here

h = heat transfer coefficient
L = thickness of the layer
k = thermal conductivity
g = acceleration of gravity
β = thermal expansivity
H = volumetric heating
υ = kinematic viscosity
κ = thermal diffusivity

Such correlations are available for the case where the top
and bottom boundary temperatures are equal, and the case
where the bottom surface is adiabatic.

We have previously shown [4] that the conventional Nusselt-
Rayleigh correlations for heat transfer by natural convec-
tion, as given in Reference 5,

$$Nu = 0.54 \ Ra^{1/4} \qquad Ra < 2 \times 10^7 \qquad (1-6)$$

$$Nu = 0.14 \ Ra^{1/3} \qquad 2 \times 10^7 < Ra \qquad (1-7)$$

combined with conservation of energy, could be used to
reproduce the various internal-Rayleigh-number correlations
with a maximum error of 30% and an average error closer to
10%. In Eqs. 1-6 and 1-7,

$$Ra = g\beta\Delta T \ L^3/\nu\kappa \qquad (1-8)$$

is the external Rayleigh number, where ΔT is the tempera-
ture difference. The analysis in Reference 4 showed that
the upward Nusselt number, Nu_T, may be calculated directly
from Eqs. 1-6 and 1-7, and the downward Nusselt number, Nu_B,
taken as

$$Nu_B = 1 + [1 + 2 \ Nu_T \ \Delta T_T/\Delta T_B]^{1/2} \qquad (1-9)$$

in the case where the pool is cooled (or at least not heated)
from below. If the pool (or layer) were heated from below
as well, Eqs. 1-6 and 1-7 would also be used for the bottom
surface. Here, of course, the ΔT's are measured between
the surfaces of the pool and its interior.

The internal Rayleigh number is derived from the external Rayleigh number by eliminating the temperature difference in favor of the internal heating. In the experiments, which were one dimensional and steady-state, the two are uniquely related; in the case of a two-dimensional pool this is not the case because of radial heat flows. The temperature difference, which is characteristic of temperature gradients, seems the more fundamental variable. Eq. 1-9 may be viewed as describing the effect of convective flows driven by an unstable temperature gradient at the top of a layer on steepening the stable temperature profile at the bottom, thereby increasing the heat flow for a given temperature difference. Because these results are based on temperature differences, and agree well with the results of the one-dimensional experiments, we believe that they are more appropriate for application to a two-dimensional pool than the correlations based on internal Rayleigh numbers.

It seems reasonable to assume that the same results would apply (with "top" and "bottom" reversed) if the layer were being heated from both above and below. The natural-convection limits applied to bubble-enhanced convective heat transfer in Version 1.02.00 use these results; in fact, it is assumed that Eq. 1-9 may be applied even when Nu_T is evaluated for bubble-enhanced convection.

For radial heat transfer, a Nusselt-Rayleigh correlation from Reference 5 is again used,

$$Nu_R = hL/k = 0.59 \ Ra^{1/4} \tag{1-10}$$

$$Nu_R = hL/k = 0.10 \ Ra^{1/3} \tag{1-11}$$

Note that the characteristic length is the layer thickness (height).

1.2.2.2 Conduction Limit

For very thin or very viscous layers, the natural-convection correlations above can yield smaller heat fluxes than would result from simple conduction. Therefore, an approximate conduction limit is imposed on heat transfer in Version 1.02.00, in the form of a lower limit on the Nusselt number. The formulation is based on the average temperature of the layer, consistent with CORCON usage and normal practice for convective heat transfer. For convection, there is an assumption (usually unstated) that boundary layers are thin and that the local temperature is essentially equal to the average temperature almost everywhere. This is not the case at or near the conduction limit, where the temperature profile (for a uniform volumetric source) is quadratic. Therefore, we have chosen an "approximate" limit rather than an "exact" one.

In the radial direction, the exact conduction result for a quadratic temperature profile is

$$q_R = 4k(\bar{T} - T_R)/R \tag{1-12}$$

and the Nusselt number based on layer thickness is

$$Nu = 4L/R \tag{1-13}$$

This provides the desired lower bound on radial heat transfer.

The axial conduction result is

$$q_T = 2k[\bar{T} - T_T + (-T_B + 2\bar{T} - T_T)]/L \tag{1-14}$$

$$q_B = -2k[\bar{T} - T_B + (-T_B + 2\bar{T} - T_T)]/L \tag{1-15}$$

where the fluxes are positive up, and "B" and "T" refer to the bottom and top surfaces, respectively. In most cases, heat transfer will be near steady state, for which the internal heating, the fluxes, and the temperatures are related through

$$HL = q_T - q_B = 6k(-T_B + 2\bar{T} - T_T)/L \tag{1-16}$$

so that

$$\bar{T}_{ss} = (T_B + T_T)/2 + HL^2/12k \tag{1-17}$$

Then, at steady state, the fluxes are

$$q_{Tss} = k(T_B - T_T)/L + HL/2 \tag{1-18}$$

$$q_{Bss} = k(T_B - T_T)/L - HL/2 \tag{1-19}$$

(which follows simply from the linearity of the conduction problem).

Note that q_T in Eq. 1-14 does not necessarily have the same sign as $\bar{T} - T_T$ (and similarly for q_B and $T_B - \bar{T}$), which would greatly complicate an attempt to impose the "exact" limit. In order to avoid this complication, we have considered the expressions

$$q_T = 2k\{\bar{T} - T_T + 2[\max((\bar{T} - T_T)(\bar{T} - T_B), 0)]^{1/2}\}/L \tag{1-20}$$

$$q_B = -2k\{\bar{T} - T_B + 2[\max((\bar{T} - T_T)(\bar{T} - T_B), 0)]^{1/2}\}/L \tag{1-21}$$

These have the desired sign properties, and the same values as Eqs. 1-14 and 1-15 for the limiting cases of no internal heating ($\bar{T} = (T_B + T_T)/2$) and of large internal heating ($\bar{T} - T_T \approx \bar{T} - T_B$). It is easily shown that they satisfy Eqs. 1-17 and 1-18 at steady state, so that they also give the correct partition of heat between upward and downward fluxes. In fact, given the boundary temperatures and the volumetric heating, the approximation errs only in the temperature at which steady state is achieved, given by

$$\bar{T}_{ss} = \begin{cases} (T_T + T_B)/2 + HL^2/4k, & (\bar{T}_{ss} - T_T)(\bar{T}_{ss} - T_B) < 0 \\ (T_T + T_B)/2 + \{2[1 + 12(k(T_1 - T_0)/ \\ SL^2)^2]^{1/2} - 1\} HL^2/12k, & \text{otherwise.} \end{cases} \quad (1-22)$$

This steady-state temperature, which will be approached using the approximate heat-transfer relations of Eqs. 1-20 and 1-21, is plotted against volumetric heating in Figure 1.3 and compared with the exact result of Eq. 1-17. The maximum error is one-third the temperature difference across the layer and occurs at the point where the heat flux at one boundary is zero. This error is unavoidable if we wish the heat fluxes to have the same sign as the temperature differences. In any case, if the conduction limit in a liquid is reached, the layer must be relatively thin and the temperature difference relatively small so that the error in $\bar{T}_{ss}$ represents only a only a minor error in the sensible heat content of the layer and has no other consequences. Eqs. 1-20 and 1-21, rewritten in the form of Nusselt numbers based on layer thickness, are employed in Version 1.02.00 as a lower bound on the possible Nusselt numbers in a liquid layer.

1.2.3 Results for Sample Problem Using Crust Model

We performed calculations with Version 1.02.00 of CORCON for the sample problem included in the CORCON manual.[2] This problem involves deposition of the entire molten core of a large (3411 MWt) PWR, together with 140 metric tonnes of molten steel into a 3.125-m-radius cavity in limestone/ common sand concrete, 13000 s after reactor SCRAM. The calculation was carried out for 10 hours of interaction time, which required 77 s of CRAY-1 computer time. After about 4.7 hours of interaction, the calculated temperatures of the bottom and radial surfaces of the metal layer fell below the freezing temperature, and a solid crust began to form. Figures 1.4 through 1.6 show the crust thicknesses, while Figure 1.7 shows the resulting cavity profiles at one-hour intervals. For comparison, Figure 1.8 shows the results of a calculation in which the crust/freezing model was disabled (but no other changes made) and heat-transfer was calculated from convective correlations alone. Note that this is not

1-11
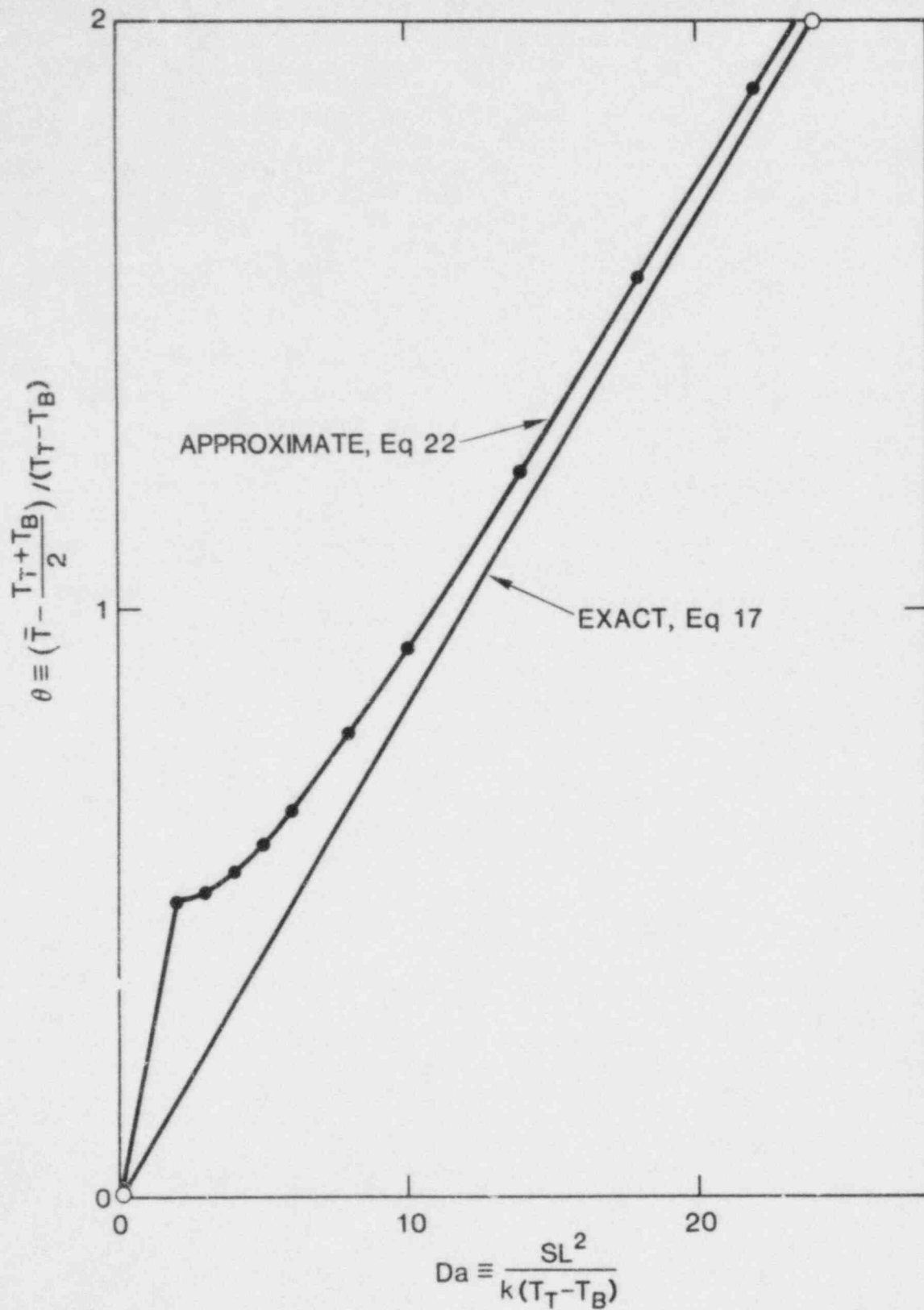
Figure 1.3. Dimensionless Steady-State Temperature as a Function of Dimensionless Volumetric Heating
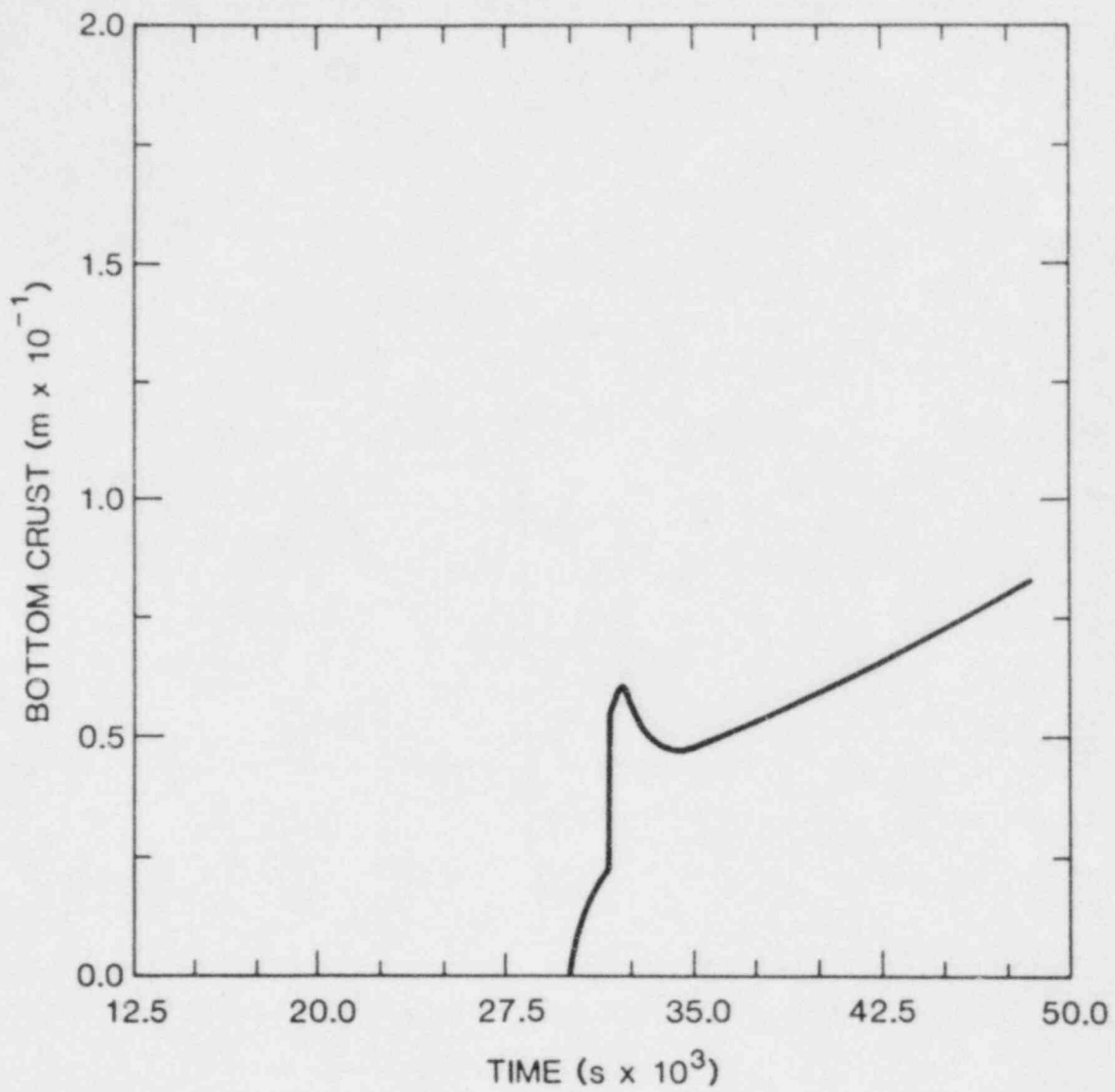
Figure 1.4.   Crust Thickness on Bottom of Metal Layer
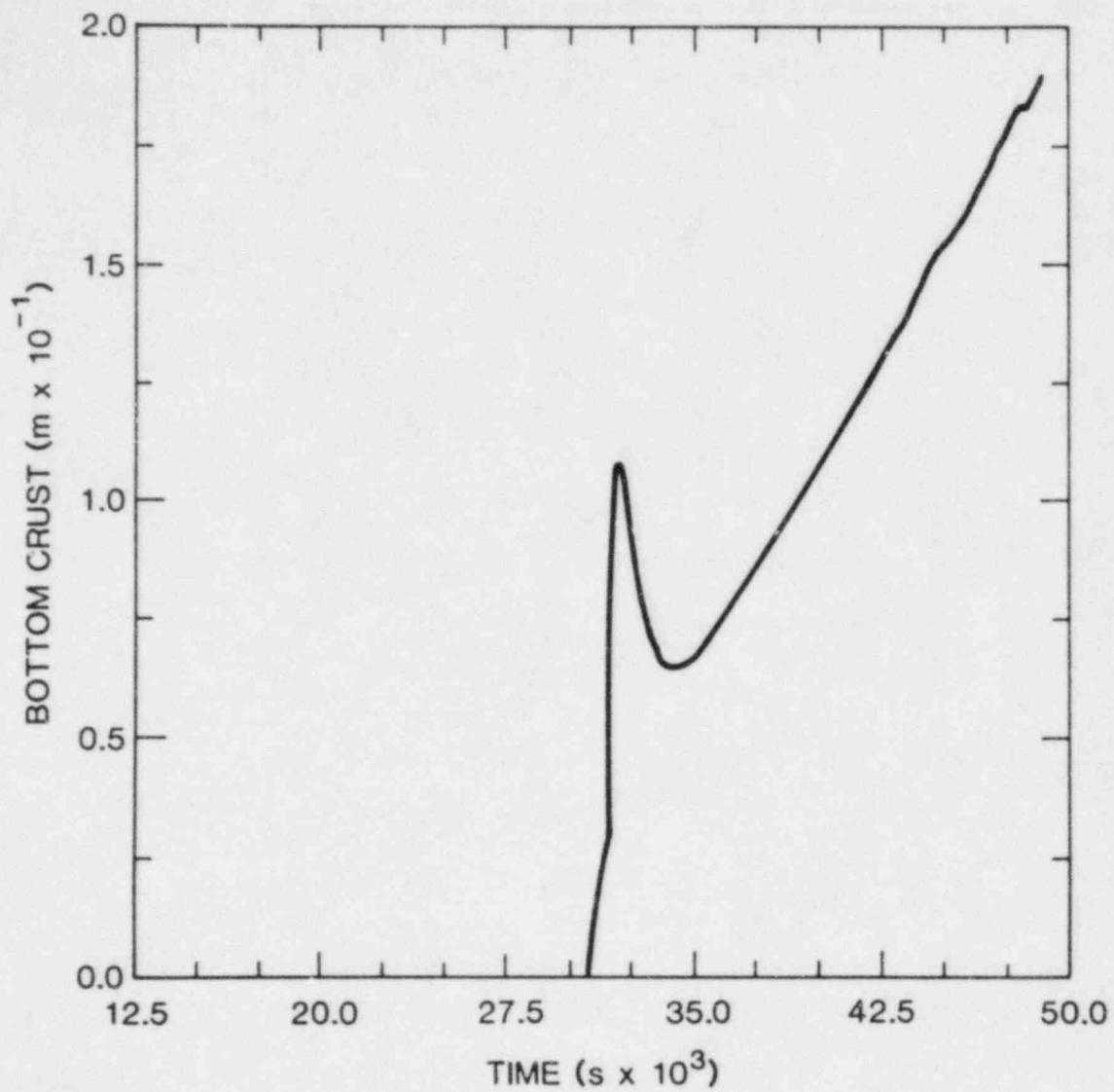
Figure 1.5.   Crust Thickness on Side of Metal Layer
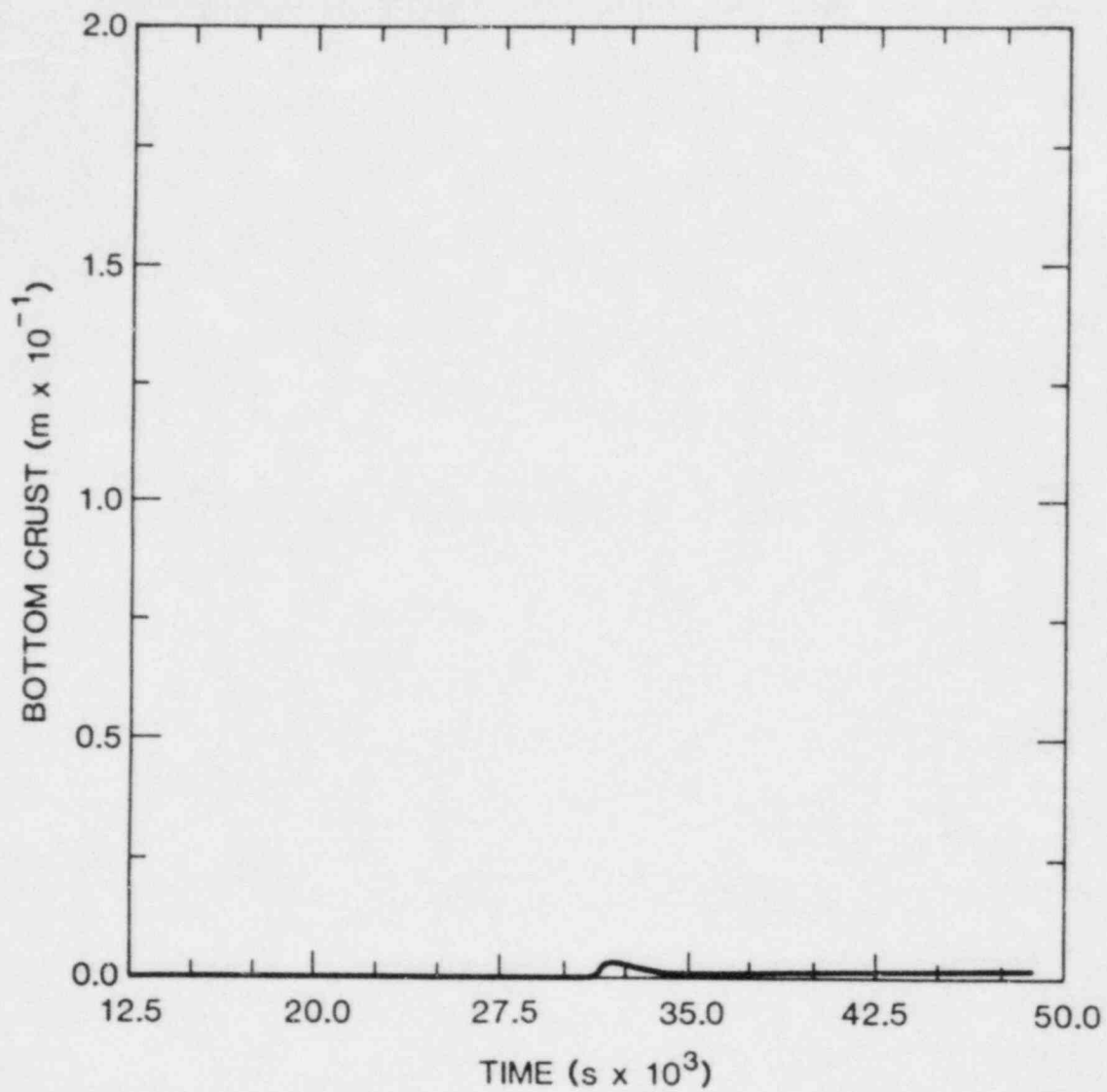
Figure 1.6.   Crust Thickness on Top of Pool
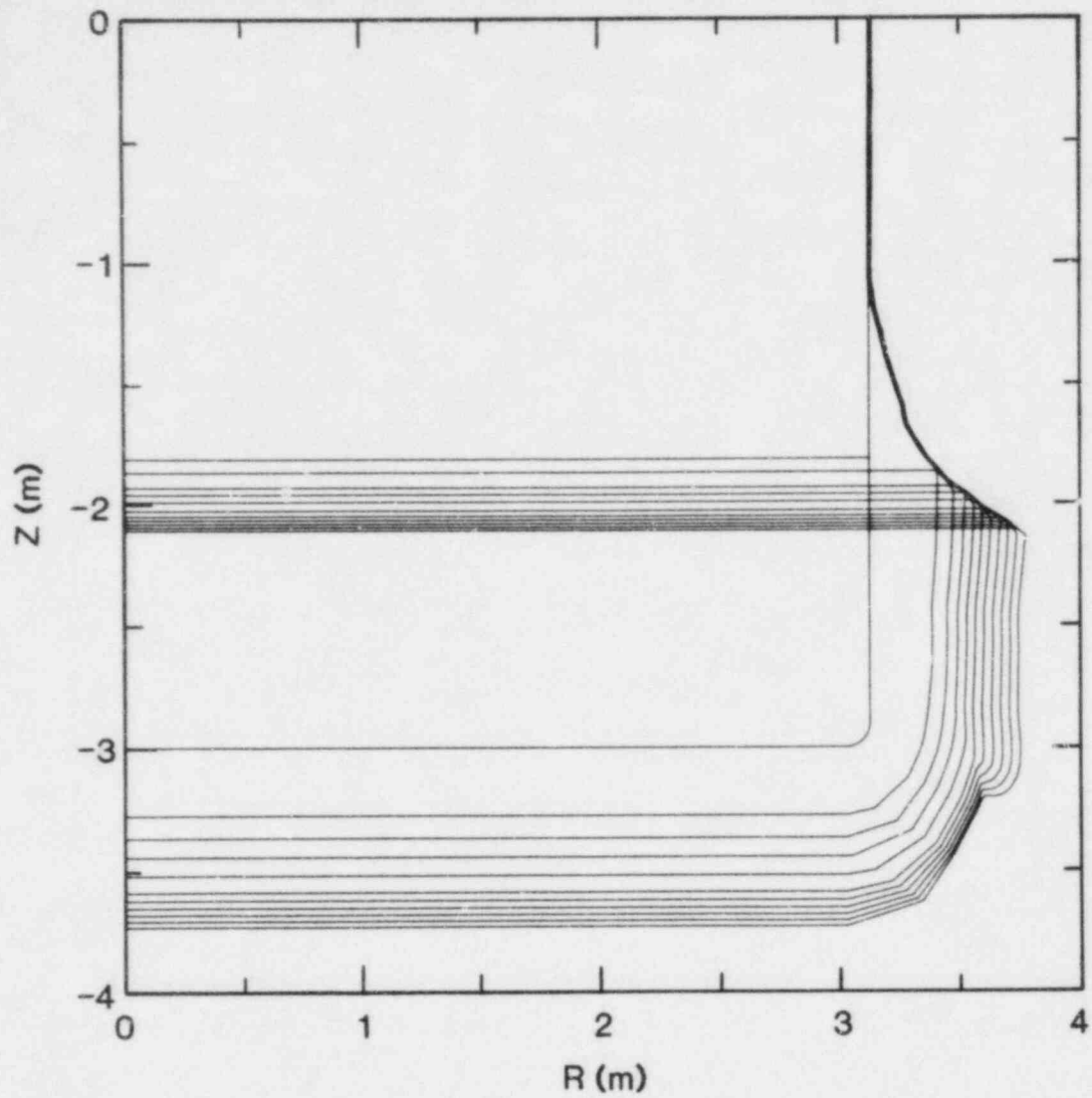
Figure 1.7. Cavity Profiles at 1-h Intervals
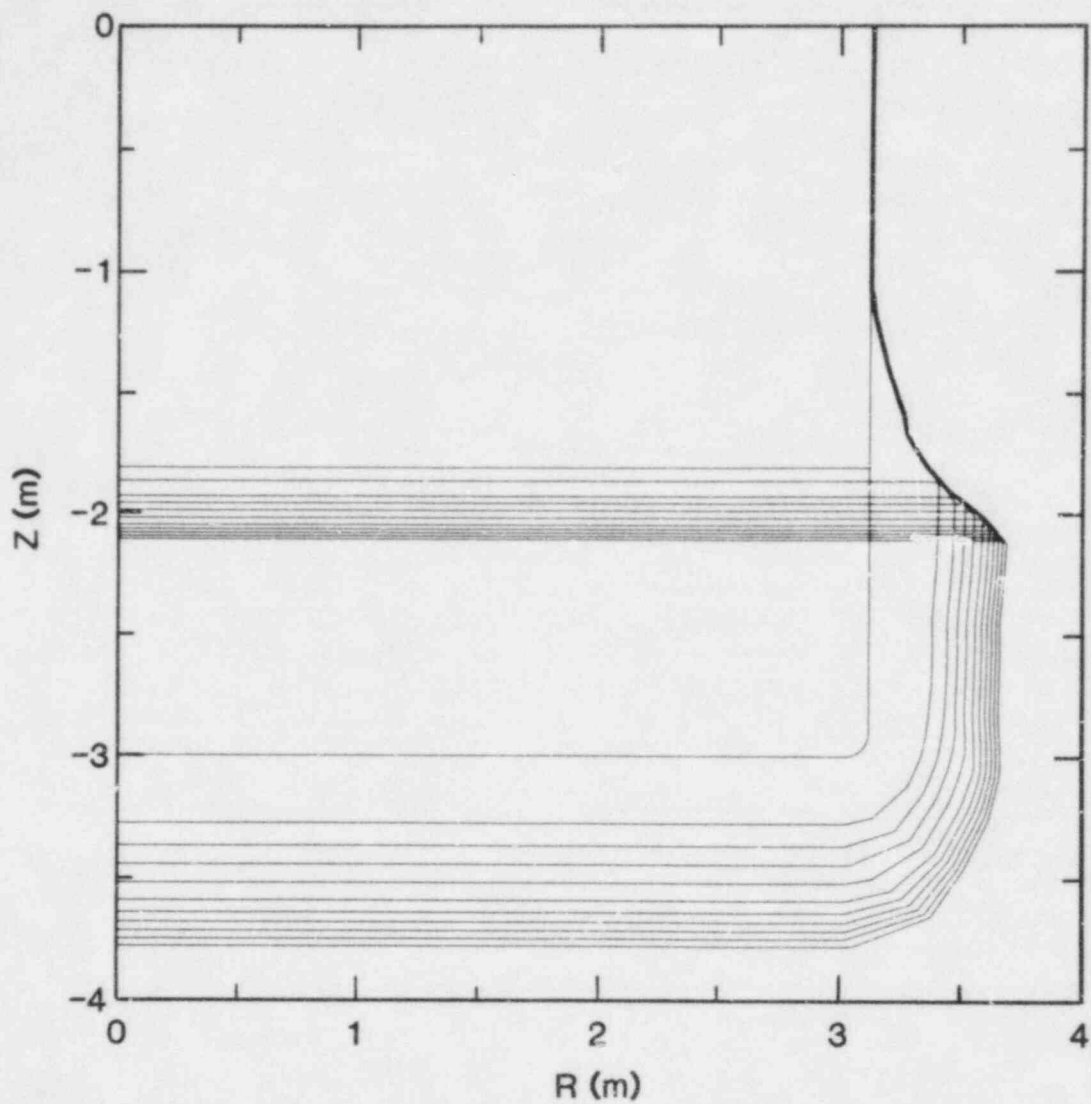
Figure 1.8. Cavity Profiles at 1-h Intervals, Crust Model Disabled

equivalent to MOD1, with the largest difference being in the viscosity modelling.

The principal effect of the crust model in this calculation is a reduction in the radial ablation by the metal layer, caused by a 10 to 20 cm solid crust on its radial surface. A 5 to 10 cm crust on the bottom surface has a much lesser effect on downward penetration. The increased thermal resistance between the metal and the concrete was largely compensated for by the formation of a thin (few millimeter) crust on the pool surface which tended to reduce the surface temperature and the radiative losses. Because the situation is almost steady, heat loss to concrete and heat loss from the surface must balance internal (decay) heating so that any reduction in one must be accompanied by an increase in the other. In this case, the total concrete erosions predicted by the calculations with and without the crust model were equal within 0.1%.

1.3 Oxidic-Phase Viscosity Model

The extended Shaw viscosity model was described in detail in the previous semi-annual report. During this reporting period, the model has been placed in the code and undergone final testing. The viscosity results from the new and old models are compared in Figure 1.9 for the DWR sample problem given in the CORCON-MOD1 user's guide. As opposed to the old model (an extrapolation of the Bottinga-Weill correlation), the new model yields more reasonable viscosity estimates that are continuous functions of both temperature and composition. The old model exhibits an abrupt change in viscosity of the light oxide (probably as a result of temperature extrapolation) and a sharp rise in the viscosity of the oxidic mixture when the model is changed to account for 15% silica content. Of course, both models predict an abrupt change in viscosity at layer flip when the heavy oxides (primarily OO2 and ZRO2) mix with the light oxides (concrete decomposition products). This is indicated in the figure by a vertical dashed line at approximately four hours after SCRAM. The continuous nature of the new model is reflected in the plots of layer variables (e.g., layer temperature) where the curves are smoothed considerably compared to the old results. This improvement has been incorporated in MOD2.

1.4 Code Assessment

Assessment work during this period has concentrated on the three major heat transfer modelling areas in CORCON; (1) melt/concrete heat transfer, (2) pool layer heat transfer, and (3) pool surface heat transfer. A summary of the salient results is presented here with detailed descriptions of these tests included in the assessment report.[6]
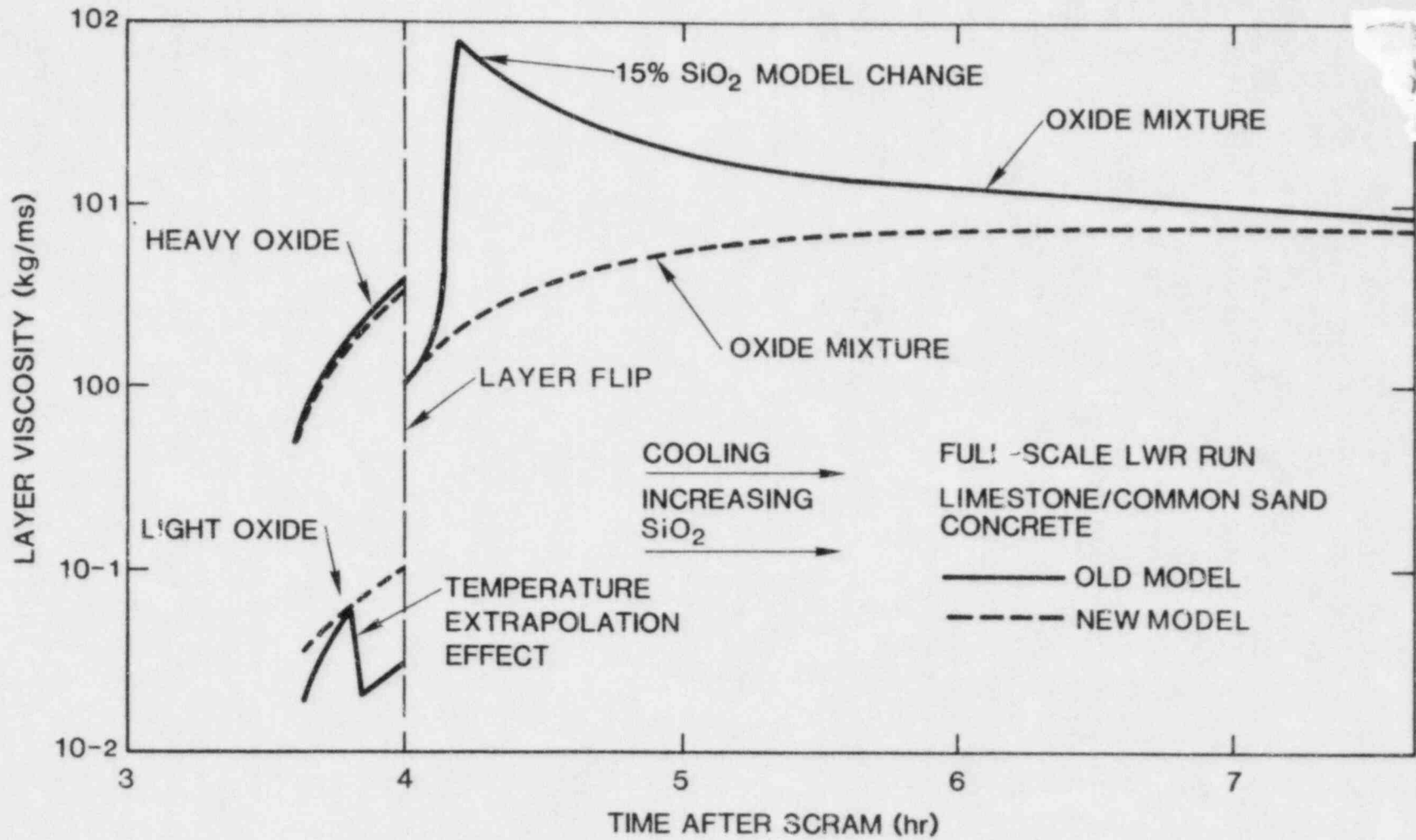
Figure 1.9. Viscosity Model Comparison

1.4.1 Melt/Concrete Heat Transfer

The interface between the melt and the concrete is assumed
to consist of a gas film sustained by concrete-decomposition
gases. Conduction and convection through, and radiation
across, the film are considered as the heat-transfer mecha-
nisms. The radiative contribution is evaluated from the
equation for parallel gray plates separated by an optically
transparent medium. For horizontal or near-horizontal
films, conductive heat transfer is assumed, with a Taylor-
instability bubbling model used to evaluate the film thick-
ness. For inclinations greater than 15°, a flowing film is
assumed, with a thickness determined by the requirement that
pressure losses in the film match the change in gravitational
head in the pool. At small flow Reynolds numbers, conduction
is assumed; above Re=100, the Reynolds analogy for turbulent
flow is used. The results are cast in the form of Nusselt-
Reynolds correlations. Transitions are introduced at model
changes, resulting in the five regions shown in Figure 1.10.

Testing in this area indicated that changes in the values of
the gas film heat transfer coefficients for all three
regimes (bubbling film, laminar flowing film, and turbulent
flowing film) are compensated by radiative heat transfer due
to the effect of the gas-film/melt-interface temperature.
Therefore, as long as a gas film is assumed to be present,
the convective modelling of heat transport across the film
has limited influence on the results.

1.4.2 Pool-Layer Heat Transfer

Convective transfer from the interior of the pool to its
periphery and across layer interfaces is strongly affected
by the flow into the pool from the decomposing concrete.
Due to vigorous circulation of the melt by the gases passing
through it, one bulk temperature for each melt layer is
assumed except near the layer boundaries where the tempera-
ture varies to its boundary value across a relatively thin
thermal boundary layer, δ_t. A schematic of the core-melt-
pool/concrete configuration showing the heat transfer regimes
of interest is given in Figure 1.11. Enhanced heat transfer
as a result of the gas-driven circulation may be divided into
two categories: (1) indirect or "bubble agitation" - for sur-
faces across which there is no gas flow (Region II), and
(2) direct or "gas injection" - for surfaces through which
there is a gas flow (Regions I and III). The latter includes
heat transfer across liquid/liquid interfaces in the pool.

The code results are very sensitive to this area of heat
transfer modelling. Particularly, increases in layer-to-
layer interfacial heat transfer resulted in high melt surface
temperatures, which resulted in large increases in radiative
heat transfer from the melt surface to the surroundings and
a consequent reduction in cavity recession. The partition
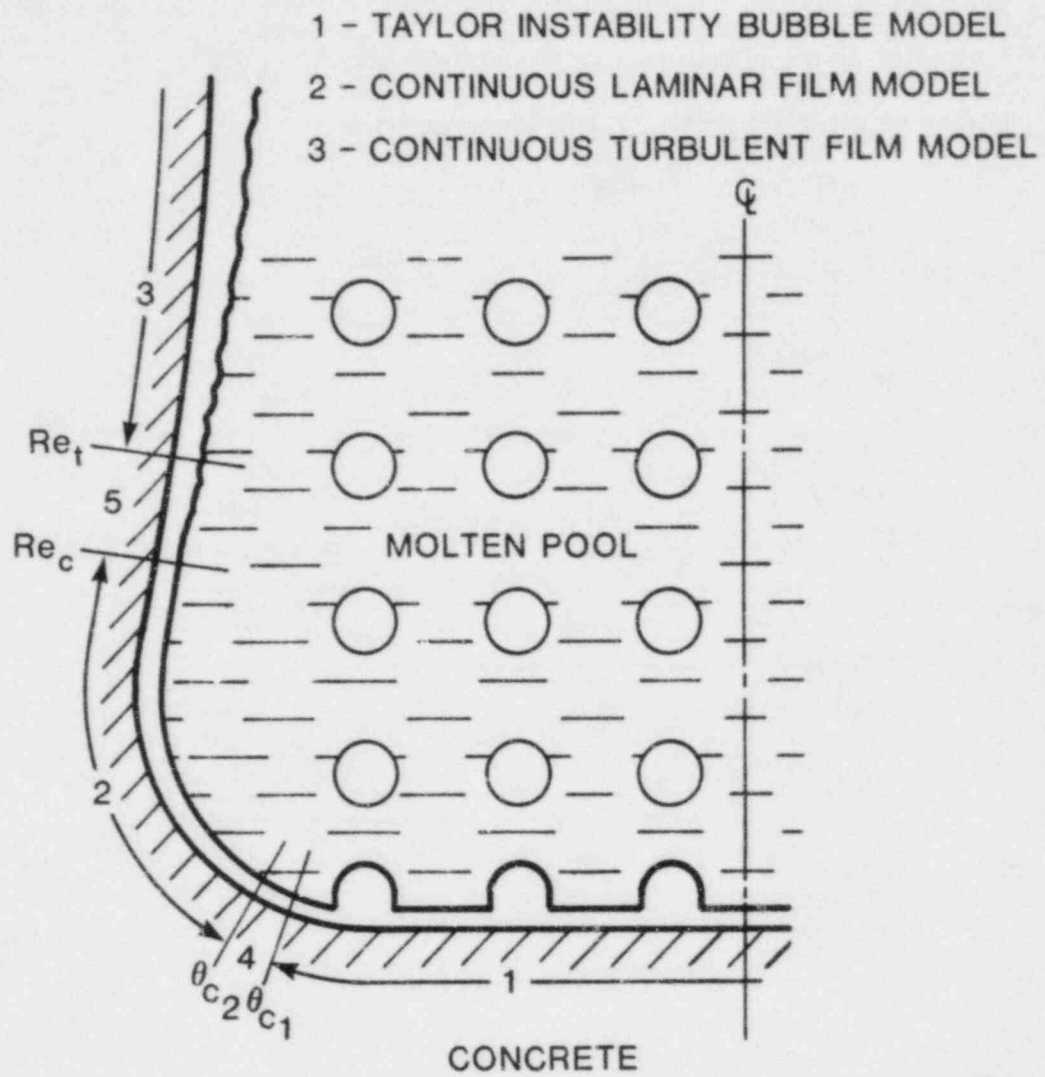
Figure 1.10. Melt/Concrete Interface Heat Transfer
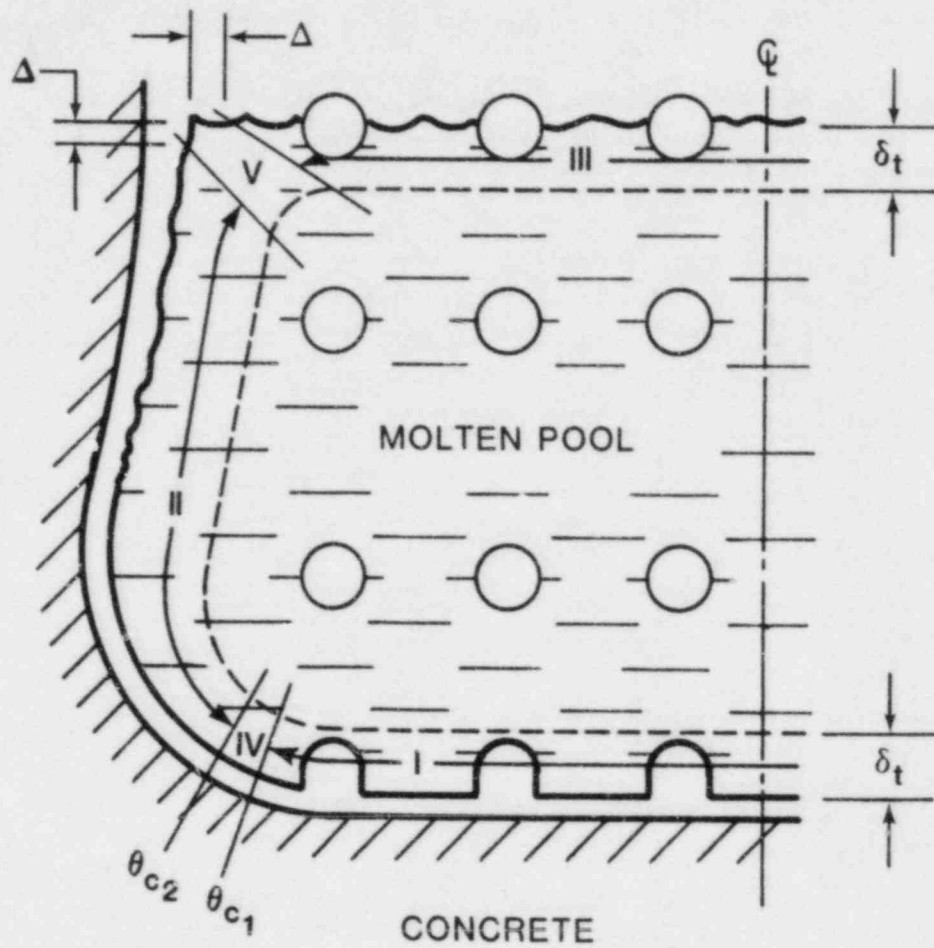
REGION	CONDITION
I, III	SURFACE WITH GAS INJECTION
II	SURFACE WITH BUBBLE AGITATION
IV, V	TRANSITION REGIONS

Figure 1.11. Pool Internal Heat Transfer

of the decay heat generated in the melt appears to be significantly influenced by this model.

1.4.3 Pool Surface Heat Transfer

Heat transfer from the pool surface includes both convection to the atmosphere and radiation to the atmosphere surroundings. Thermal radiation is considered to be the dominant heat loss mechanism. The atmosphere is assumed to be optically transparent and the pool surface and surroundings to be gray bodies with known emissivities.

Results of the sensitivity tests indicated that the principal results are only moderately sensitive to changes in the effective convective and radiative heat transfer coefficients for heat transfer from the pool surface to the surroundings.

1.5 References for Section 1

1. M. Berman, Light Water Reactor Safety Research Semiannual Report, April–September 1982, NUREG/CR-3407 (SAND83-1576), Sandia National Laboratories, Albuquerque, NM, 1983.

2. J. F. Muir, et al, CORCON-MOD1: An Improved Model for Molten-Core/Concrete Interactions, SAND80-2415, Sandia National Laboratories, Albuquerque, NM, July 1981.

3. F. A. Kulacki and R. J. Goldstein, J. Fluid Mech., Volume 55, p. 271, 1975.

   F. A. Kulacki and M. E. Nagle, J. Heat Transfer, Volume 97, p. 204, 1975.

   F. A. Kulacki and A. A. Emara, Trans ANS, Volume 22, p. 447, 1975.

4. M. Berman, Light Water Reactor Safety Research Quarterly Report, January–March 1981, SAND81-1261/1 of 4, Sandia National Laboratories, Albuquerque, NM, 1981.

5. W. H. McAdams, Heat Transmission, McGraw-Hill Book Co., New York, NY, 1954.

6. D. P. Kelly, Assessment of CORCON-MOD1: A Core/Concrete Interaction Code, SAND83-1777, Sandia National Laboratories, Albuquerque, NM.

2. CORE MELT-COOLANT INTERACTIONS (CMCI)

(M. Berman, N. A. Evans, D. E. Mitchell, J. M. McGlaun,
M. S. Krein, M. L. Corradini)

The three main purposes of the core melt-coolant interaction
program are: (1) to identify experimentally the magnitudes
and time characteristics of pressure pulses and other initial
conditions which are necessary to trigger and propagate
explosive interactions between water and molten LWR mate-
rials; (2) to determine the conditions for, and the nature
of, nonexplosive interactions which produce significant
pressurization by steam and noncondensable gas generation;
and (3) to assess the probability and consequences of such
interactions during postulated melt-down accidents in LWRs.
The program is being conducted in four areas: (1) small
scale, single droplet experiments; (2) intermediate-scale
experiments, both ex- and in-chamber (FITS); (3) modelling
and analysis of experimental observations; and (4) structural
consequences of the pressurization processes and effects on
the overall accident progression.

2.1 Summary

2.1.1 Small-Scale Experiments

The triggered steam explosion experiments with single drops
of melt were brought to a conclusion at the end of FY 82,
and we currently do not expect any resumption in the near
future.

2.1.2 Intermediate-Scale Experiments

Intermediate-scale testing was in abeyance during this
reporting until late in March, 1983 when the first of a new
series of tests (EXO-FITS-CM) was performed to specifically
investigate coarse mixing phenomena. In this first test,
19 kg of molten iron-alumina was dropped into a pool with a
1-ft by 1-ft cross section and 4-ft deep. The water was
subcooled approximately 10°C. When the molten metal con-
tacted the water surface an unexpected expulsive event
occurred.

2.1.3 The Effects of CMCIs on Severe Accident Risk in Light Water Reactors

By using generalized accident sequences developed from Prob-
abilistic Risk Assessments (PRA) for 7 PWRs and 5 BWRs, it
is shown that core melt-coolant interactions can occur over
the whole ambient pressure-time plane, and can involve all
the principal types of initiating events (all sizes of loss-
of-coolant accidents (LOCAs), transients, isolation failure,
and major vessel rupture). It is also shown that, although

in-vessel steam explosions produce a low containment failure probability (P_α), the effect on the early death risk can be significant: for a particular PWR, a value $P_\alpha = 0.01$ increased the estimate of early death from other failure modes risk by 59%.

The generalized accident sequence has been continued in detail beyond the core melt condition to show that CMCIs are possible (as a result of accident progression, system response, or operator action) in the core barrel, the lower plenum, and the cavity. Using the currently available data base, it was very approximately estimated that the greatest risk stemmed from a CMCI, occurring explosively or nonexplosively, in the cavity, and leading to indirect containment failure. A steam explosion in the lower plenum might lead to indirect containment failure, direct containment failure, or only primary system failure. The high levels of uncertainty were reflected by the wide ranges in the estimated risk for each consequence.

2.1.4 Models for the Various Phases of a CMCI

We outline research work that is underway in every phase of modelling and analysis of CMCI. In particular, we are developing models to be used in probabilistic risk assessment (PRA) applications as well as to analyze and scale CMCI experiments in regard to fuel-coolant mixing, triggering, explosion propagation, and expansion. All of this work will be used to establish boundary and initial conditions for modelling of CMCI experiments using more detailed analysis tools, such as the CSQ code, and to provide simple models for PRA parametric calculations.

2.1.5 Wave Code Analysis of a Steam Explosion

The explosion and expansion phases of the FITS-9B intermediate scale steam explosion experiment were analyzed with the two-dimensional Eulerian wave code, CSQII. Excellent comparison between experimental and calculated early time (1 to 2.5 ms) data indicate that CSQII is well suited for the application. The early time agreement substantially improves confidence in the later time calculated kinetic energy of the water slug.

2.1.6 Monte Carlo Analysis of In-Vessel Steam Explosions

The earlier Monte Carlo analysis of in-vessel steam explosions is currently being refined using revised input distributions, with more emphasis on evaluating the uncertainties involved.

2.2 Intermediate-Scale Explosions
(N.A. Evans)

The first test in the EXO-FITS-CM series has been conducted with the following initial conditions: iron-alumina melt mass delivered -18.7 kg; water vessel dimensions (cross-section x depth, ft) -1 x 1 x 4; coolant subcooling -9°C; drop height of melt -1.0 ft. The objective of this test series is to investigate the coarse mixing process, using relatively deep water with low subcooling to obtain longer observation time with less likelihood of triggering a steam explosion. However, the first test produced an expulsive event which was triggered at the surface after the melt had penetrated a few inches into the water. The submerged melt was then driven to the bottom of the vessel with no further explosions occurring, while the majority of the melt (still above the water surface) was scattered to distances up to 100 ft from the interaction site. This test will be repeated to determine whether the unexpected surface trigger persists. In this first experiment, the surface interaction significantly reduced the mass of melt that entered the water. The subsequent mixing of the melt that did enter was probably forced and, therefore, different from that in earlier tests in which an explosion was triggered after the melt contacted the base of the water vessel.

2.3 Analysis and Modelling of CMCI

2.3.1 The Effects of CMCIs on Severe Accident Risk in Light Water Reactors
(N. A. Evans)

2.3.1.1 Introduction

The ultimate safety objective in the operation of nuclear power reactors is the prevention of significant radioactive releases to the environment. In LWR design, there are three barriers to radioactive release: the fuel rod cladding, the reactor vessel system, and the containment building. A severe accident is defined as one that results in severe fuel damage which, in the extreme, could involve core melt-down. With a severe accident, the first barrier is automatically breached, and serious threats are placed against the second and third barriers, depending on the subsequent course of the accident. Hence, a better understanding of the nature of severe reactor accidents is required in order to improve risk assessments of existing plants, and to determine licensing requirements for existing and new plants.

An accident can occur in response to a particular initiating event if certain engineered safety features (ESFs) for reactor core protection are rendered inoperative, or fail to operate, and cause unacceptable temperature excursions in the core. If the accident progresses to severe core damage,

a special question arises as to the outcome of interactions between core melt and coolant. If an accident disturbs the normal coolant circulation, emergency coolant systems are brought into play with the intention of preventing core damage, and permitting a safe shutdown. This constitutes the design basis accident (DBA), but failures of the emergency coolant systems, singly and in combinations (again dependent on the specific accident scenario), go beyond the DBA, through degraded core accidents, and into the severe accident regime involving core melt. In this last situation, there is significant potential or a CMCI due to progression of the accident, system response to the accident, or faulty operator intervention.

Through the evolving methodology of PRA, a severe accident evaluation for a specific plant is divided into three parts:

(1) An estimate of the frequency (occurrences per reactor-year) of an accident sequence, which consists of an initiating event followed by the failure of certain ESFs (an individual ESF failure frequency is estimated from fault tree analysis);

(2) A determination of the response of the containment building to particular phenomenon resulting from the accident sequence;

(3) A calculation of the radioactivity released as a result of 1 and 2 above (when this is combined with the local population and property distributions, and the prevailing meteorology, the risk can be expressed in terms of health effects on that population, and economic losses).

In the following sections, a summary of related work will be given, together with the currently available data base on CMCI, and interpretations by different investigators. This will be followed by statements of the conditions now recognized as influencing CMCI behavior, and the outcomes to be expected.

For risk assessment purposes, in order to quantify the appropriate prototypic conditions for the various CMCI outcomes, a representative LWR accident sequence will be extended beyond the point of core melt, and a determination made of the currently uncertain or unknown CMCI factors that could significantly affect the result.

Finally, taking into account all the significant uncertain and unknown factors, a program plan of analysis and experiment will be proposed to resolve the phenomenological uncertainties that will allow a proper evaluation of CMCI during accidents in LWRs.

2.3.1.2 Related Work, Available Data Base, and Interpretations

2.3.1.2.1 Results from the Reactor Safety Study (WASH-1400)

Although investigations of the behavior of hot liquid-cold liquid interactions (typically referred to as vapor explosions) have been in progress for many years in such areas as the metal foundry and paper-making industries, and in liquid natural gas transport, its potential importance for LWR safety came into prominence with publication of the Reactor Safety Study (RSS) in 1975.[1] This document introduced, and described in detail, the PRA method for use in reactor safety work. By augmenting the data base then available with certain assumptions, it was concluded in the RSS from a relatively simple analysis that, if a core melt occurred, the relative direct failure probability of containment due to an in-vessel steam explosion was $P_\alpha = 10^{-2(+1, -2)}$. Compared with other containment response probabilities of significance (P_β - failure to isolate containment, P_γ - failure due to hydrogen burning, P_δ - failure by overpressure), P_α is considered to be rather small, but, as indicated, was judged to have substantial uncertainty. When combined with the accident sequences considered dominant in leading to core melt, containment failure due to a steam explosion was not overall dominant in estimated frequency. However, the particular nature of containment failure by a steam explosion has the most serious consequences with respect to fission product release so that it was placed in the first (i.e., the most serious) of the total of seven release categories for core melt accidents. This resulted in a risk of radioactive release that was approximately one order of magnitude less than the average of the other three most serious containment failure modes (β, δ, and γ).

2.3.1.2.2 Available Data Base

Since the RSS was published, a considerable amount of work has been done at various locations around the world to better quantify, and reduce the uncertainties of reactor-related CMCI phenomena. Sandia's contributions started with gram-scale flooding tests in an arc melter. Field-type tests in which molten iron-alumina and corium thermites were dropped into open tanks of water followed. These experiments have progressed to carefully controlled, detailed studies of single melt droplet (~50 mg) behavior, and experiments at intermediate scale with 20 kg of melt (FITS).[2] This has been accompanied by the development of a fairly comprehensive, inter-connected set of models to explain the behavior observed during the experiments, with a level of empiricism that we consider relatively modest, but acceptable, for predicting the principal outcomes of a CMCI at reduced scale. Much of the work to date at Sandia has been concerned with in-vessel steam explosions, and the direct containment threat

by a large mass missile resulting from vessel failure. From this work, it is clear that a typical steam explosion consists of four phases: coarse mixing of melt and coolant, triggering, propagation, and expansion work. These are shown in Figure 2.1, with the horizontal axis representing experiments with increasing scale to the right, and the vertical axis representing analysis and model development, which terminates with a containment failure probability estimate, P_α, obtained by a Monte Carlo technique. The value of this quantity, using the most recent experimental information is $P_\alpha = 5 \times 10^{-4}$, with a large associated uncertainty. It should be noted that this result, while suggesting that direct containment failure by a steam explosion may be relatively unimportant compared with other failure modes, has considerable uncertainty for several reasons, the most important being the lack of information on CMCI behavior at reactor scale. Currently available experimental data using 20 kg melts represents a mass scale approximately two to three orders of magnitude below what might be expected at reactor scale.

To establish a CMCI data base, Table 2.1 shows the ranges of the various conditions used in the small-scale and intermediate scale experiments. To date, the program has concentrated on a determination of the occurrence probability of a steam explosion, and the consequences of such an event. The results show that molten corium A+R will explode as readily as a molten iron-alumina simulant. Such explosions occur spontaneously when an apparent threshold in melt volume (~0.5 ℓ for both materials) is exceeded. Theory and experiment both indicate that triggering becomes more difficult (but still possible), with both increase in ambient pressure and decrease in coolant subcooling.

At ambient pressure, $P_\infty \sim 1$ bar, the kinetic energy conversion ratio from intermediate-scale tests is $\eta_{KE} \sim 2\%$ within a factor of 3 either way, for both corium and iron-alumina. A set of small scale tests has shown that the conversion ratio determined from the steam bubble work increased by a factor of 4 to 5 when the ambient pressure increased by an order of magnitude. Only one intermediate-scale experiment at elevated pressure ($P_\infty \sim 11$ bars) (with an explosion by applied trigger) has been conducted, and no significant change was observed in η_{KE}. Bird at AEA Winfrith, using ~500 g of molten UO_2 in water, has shown that the conversion ratio also increases with decrease in subcooling.[3] To this point, the trend in results may be summarized as follows: at reduced scale (compared with prototypic) a steam explosion becomes more difficult to trigger with increased ambient pressure and decreased subcooling, but simultaneously the conversion ratio increases; this resistance to triggering may also decrease with increase in melt volume due to the threshold effect, but this is currently only speculation. Other results have shown that: (1) explosions are possible with
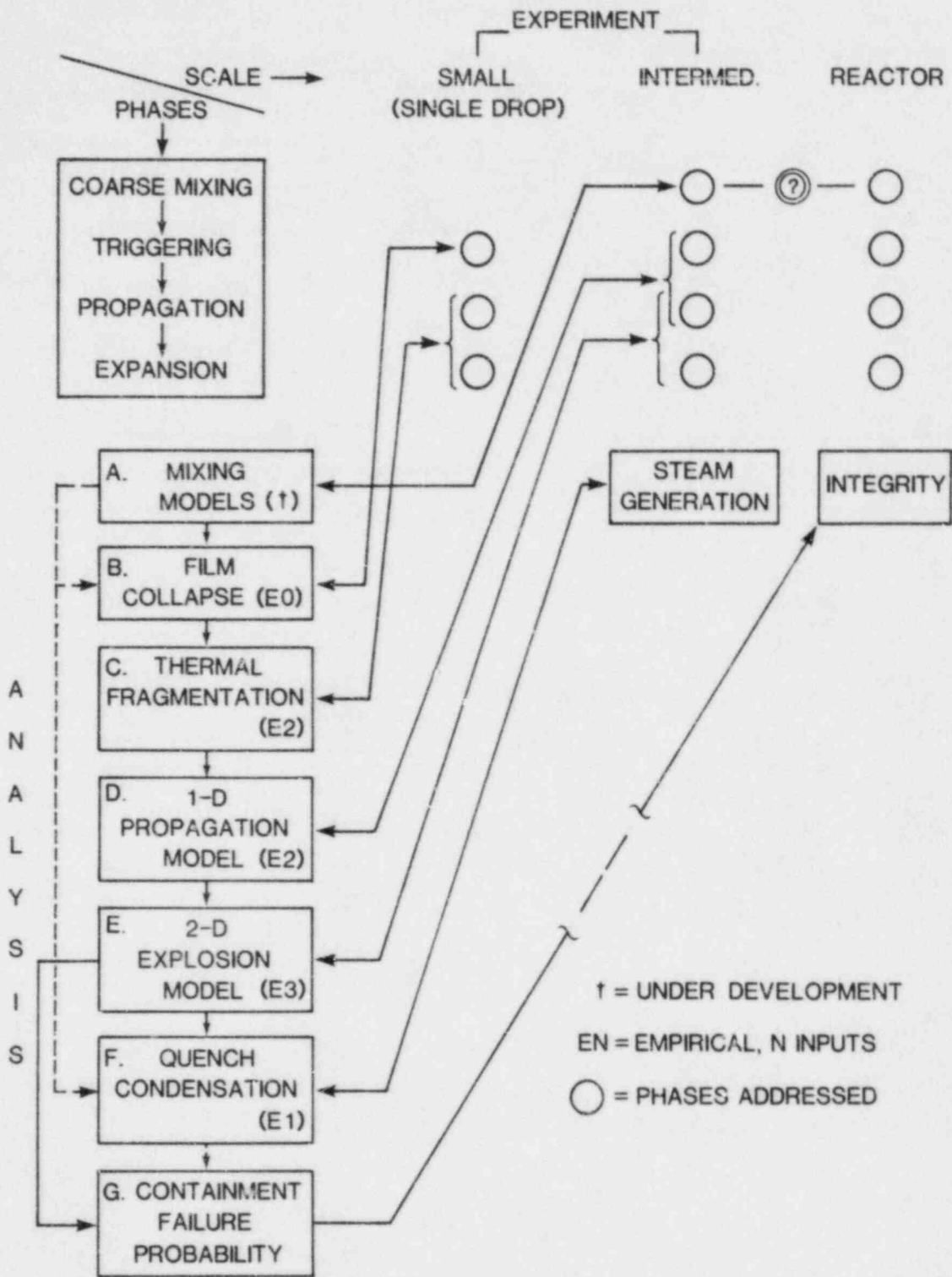
Figure 2.1. CMCI Program Integration

Table 2.1

Ranges of Experimental Variables Studied

	Small Scale	Intermediate Scale	Reactor-Scale
Molten fuel mass	0.015-15 g	0.6-20 kg	200-200,000 kg
Fuel composition	Fe, FeO_x, coriums UO_x, ZrO_x, $U-Zr_x-O_y > Al_2O_3$, silica alumina	$Fe-Al_2O_3$, FeO_x, corium A+R	Oxidic and metallic coriums
Fuel temperature	1800-3500 K	~2700-3000 K	1800-3200 K
Water/fuel mass ratio	∞	1.5:1 to 50:1	~0.21:1 to ∞
Water subcooling	0-160 K	0-80 K	0-300 K
Contact mode	Pour, flood	Pour	Pour, flood, spray
Water depth	∞	0.1-0.8 m	0-5 m
Tank area	∞	0.1-0.5 m^2	~20 m^2 and larger
Coolant Composition	Water, salt solutions, hydrocarbons	Water	Water
Structure	---	Some in open geometry	Complex
Ambient pressure	0.83-12 b*	0.83 b, 11 b	1-100 b
Fall height	8-50 mm	~1-2 m	~0-5 m
Entry velocity	0.4-1 m/s	~1-7 m/s	Low to very high
Trigger pressure	sp†, 1-16 b, 40 b, 100 b	sp, ~100-500 b	Unknown

†sp = spontaneous
*b = bar

melt temperatures at the melting point (including the presence of partial solidification): (2) explosion triggering of single melt droplets is easier with _initial_ increase in ambient pressure (1 bar $\leq P_\infty \leq$ 7.5 bars); and (3) in several intermediate-scale tests, spontaneous double explosions occurred in which the first explosion appeared to enhance fragmentation and mixing ahead of the second explosion, with total conversion ratios (composed of slug kinetic energy produced and energy stored in the chamber air) being generally greater than for single explosion tests. In addition, hydrogen generation rate measurements have shown that approximately 20-30% of the metal content of both, the iron-alumina and corium A+R melts can be rapidly reacted in a steam explosion, but only 4% to 10% (and more slowly) in the nonexplosive case. Small-scale tests have also shown that the presence of noncondensable gas in the film around a molten drop, by either entrainment or generation, will increase resistance to triggering due to a cushioning effect. In other words, oxidic melts undergoing small drop heights (lower entrainment) into coolant will be more easily triggerable since the hydrogen generation is lower.

When the experimental circumstances permitted (such as after in-chamber FITS experiments), the CMCI debris was collected and analyzed for particle number, mass, and surface area characteristics. It has been generally observed that there is a strong correlation between the fineness of particle fragmentation produced in a steam explosion and the total energy conversion ratio. This debris bed information is also used as input data for studies of debris coolability.

Further details of these, and other results can be found in the series of quarterly reports[3] and in several topical reports.[4-7]

2.3.1.2.3 Data Interpretations and Questions

Although it appears at this stage that the probability of direct containment failure by a steam explosion may not be particularly high, the possibility of a steam explosion may be important because of the contribution it may make to containment failure modes by hydrogen burning (γ mode) or by overpressure (δ mode), as well as debris bed coolability. Furthermore, a steam explosion may be sufficiently energetic to damage (by missile production) accident management systems such as sprays and fans, and indirectly cause, or contribute to, containment failure. The basic energy for these damage processes resides, of course, in the degraded core, and a steam explosion can be regarded simply as a mechanism that increases the rate at which a portion of the energy exchange occurs, so that the mitigating systems (such as deliberate ignition) are overloaded.

There has been much controversy over whether a very large steam explosion is even possible under prototypic conditions. One side has maintained that such steam explosions are impossible for several reasons:

(1) Sufficient coarse mixing of large masses of melt and coolant cannot be achieved because of space and time constraints in the full-scale pressure vessel or reactor cavity;

(2) If, by some means, the coarse mixing process could be started, then there would be so much steam generation that the melt and coolant would be driven apart;

(3) Even if a satisfactory coarse mixing state were reached there would be triggering difficulties, especially at elevated ambient pressure.

High speed photographic data from Sandia FITS experiments have been analyzed to develop models for the coarse mixing process (see Section 2.3.1.9.2 for additional details), and it appears that steam generation may be assisting the process in several different ways: vapor generation (as coolant penetrates the melt) helps to break up the melt especially by dispersion in the horizontal direction; vapor generation causes coolant swell, thereby increasing the effective contact time between materials, especially with low coolant-to-melt mass ratio; increased vertical differential pressure across a melt particle due to high-temperature vapor generation in the stagnation region might be decreasing the vertical particle speed, and increasing the effective mixing time.

Questions have been raised as to whether the current data base is properly applicable to prototypic conditions.[8] For example, the experimental values of coolant-to-melt mass ratio were considered too large, and the range of ambient pressure insufficient. As shown in the following section, the large number of variables governing CMCI leads to an enormous test matrix, which for obvious economic reasons, must be sampled with utmost care, using the results of each test to guide the next. We hope that further improvement on this issue of the effectiveness of limited test results for prototypic application will be achieved by identifying more clearly those conditions under which significant CMCIs would occur in particular accident sequences.

2.3.1.3 Conditions Affecting CMCI Behavior

The conditions affecting a CMCI can be divided into three types: initial, boundary, and external conditions. Initial conditions concern the states of the melt and the coolant at the start of an interaction, and the thermodynamic state prevailing at that instant. Boundary conditions relate to the

geometric state of the system, while external (more arbi-
trary) conditions are those that may be imposed by operator
intervention (involving possible coolant injection and pres-
sure venting), and can be regarded as a subset of the ini-
tial conditions.

Assuming that a particular accident sequence has reached core
melt, the detailed conditions requiring quantification are
the following:

(1) Core melt state:
   a. Melt quantity
      i. Amount available
      ii. Amount involved in CMCI
   b. Melt temperature and heat content
   c. Melt composition
   d. Melt configuration (e.g., contact mode potential)

(2) Coolant state:
   a. Coolant quantity
      i. Amount available
      ii. Amount involved in CMCI
   b. Coolant temperature (i.e., subcooling)
   c. Coolant configuration

(3) Thermodynamic state:
   a. System pressure (effect on CMCI, material failure)
   b. System temperature (local effect on material
      strength, heat transfer effects)

(4) Geometric State
   a. Configuration at CMCI site (potential effect on
      mixing, triggering, propagation, expansion)
   b. Configuration elsewhere (potential effect on energy
      dissipation, energy escape paths (e.g., downcomers)

2.3.1.4 Potentially Significant Outcomes of CMCIs

Even if the threat of direct containment failure by an in-
vessel steam explosion were of relatively low significance,
the processes occurring in a CMCI (especially when explosive)
could still seriously influence the following considerations.

(1) The probability of pressure vessel failure; such a fail-
    ure would represent a lost opportunity for confining the
    accident within the primary system and could result in
    a major impact on further accident management, e.g., it
    might necessitate a major evacuation of the surrounding
    population; furthermore, even if the accident could be
    arrested at this stage, there would still be a substan-
    tial post-accident clean-up task, with associated risks
    of exposure to workers and the nearby inhabitants, as
    well as severe financial penalties

(2) The generation rate and amount of hydrogen, and contribute to the P_γ mode of containment failure if a burn were to occur; rapidly generated hydrogen could lead to flame acceleration or detonation

(3) The generation rate and amount of steam and hydrogen (with no combustion) contributing to overpressure failure of containment (δ mode)

(4) The source term by early and extensive fission-product release from the fuel, and by affecting the timing of primary system failure and containment failure

(5) Core debris coolability through the degree of fragmentation coupled with the degree of material dispersal (e.g., a deep [i.e., nondispersed] bed of fine particles is less coolable)

(6) The course of a particular accident, and perhaps change the sequence

2.3.1.5 Determination of LWR Dominant Accident Sequences

If an accident disturbs the normal reactor coolant circulation, and if emergency coolant systems initially fail to operate so that core melt occurs, then, depending on the availability of coolant, there is a possibility for the occurrence of an explosive or nonexplosive, CMCI. The availability of coolant will depend on accident sequence progression, system response to the accident, or operator intervention.

In order to better quantify the conditions under which potentially significant CMCIs could occur, we have selected important accident sequences from available PRAs. The Accident Sequence Evaluation Program (ASEP) is studying PRAs and other safety-related program results in order to produce generic accident sequences that might lead to the determination of "accident likelihoods." The MELPROG program has incorporated the first phase of the ASEP work by combining the sequences from seven pressurized water reactors (PWRs) and five boiling water reactors (BWRs).[9]

The resulting generalized PWR sequences are shown in Figure 2.2, with the BWR sequences in Figure 2.3. The figures show the relative time for each sequence from the initiating event to fuel cladding failure (first radioactivity release) and the relative ambient pressure at that time. Early, intermediate, and late times are defined, respectively, as <6, 6 to 20, >20 h. Low, medium, and high pressure are defined, respectively, as <100, 100 to 1000, >1000 psia. A certain time interval, of the order of 0.5 to 2 h (depending on the sequence), must be added to the above fuel cladding failure times to reach the core melt state. These results
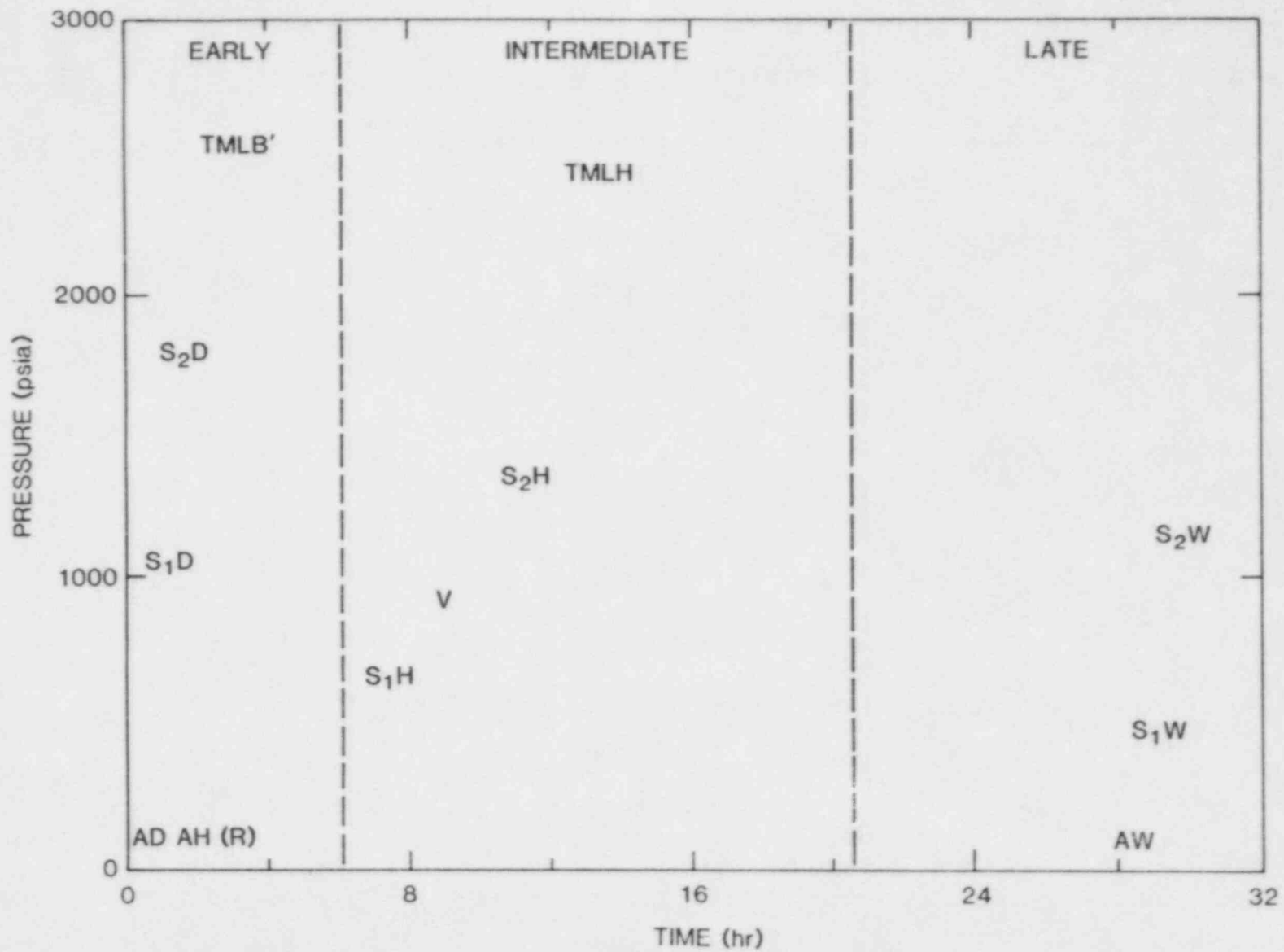
Figure 2.2. PWR Sequence Fission Product Release Time and System Pressure
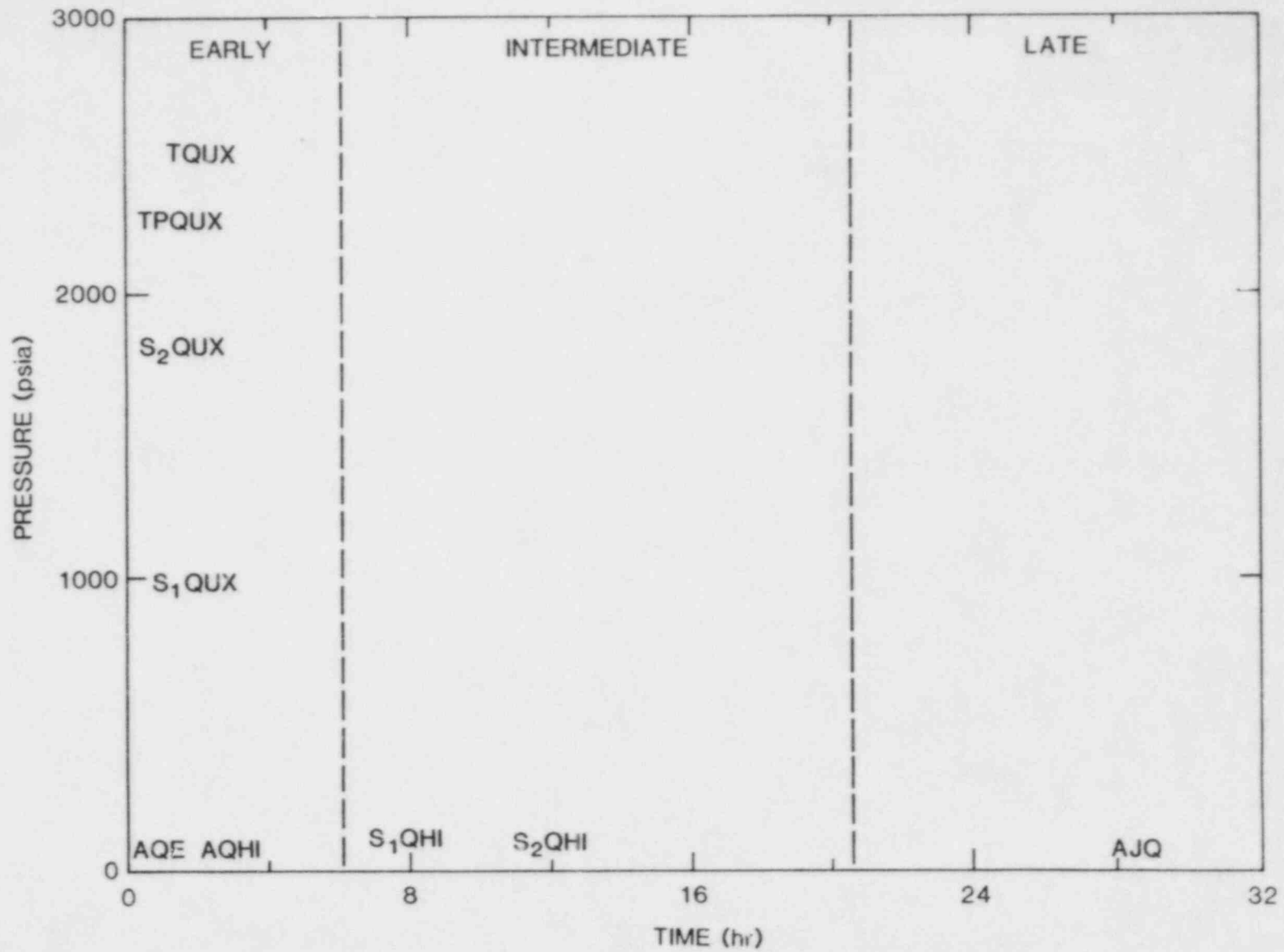
Figure 2.3. BWR Sequence Fission Product Release Time and System Pressure

will then provide a first estimate, for a particular generalized sequence, of the earliest time for a possible CMCI (which will strongly influence the fission product source term), together with the ambient pressure under which the CMCI might occur (potentially strong influence on steam explosion triggering).

Taking together the generalized accident sequences for PWRs and BWRs, the results in Figures 2.2 and 2.3 show that core melt could occur over essentially the entire pressure-time plane, and that all types of accidents (transient, all sizes of LOCAs, isolation failure, and vessel rupture) are involved.

2.3.1.6 The Effect of Steam Explosion Containment Failure Probability on Risk

S. W. Hatch at Sandia has calculated the effect on risk due to probability of direct containment failure by an in-vessel steam explosion, in relation to the combination of all other containment failure modes (see Subsection 2.3.1.2.1 for further details). Using a typical, northern U.S. river valley nuclear power plant as a base model, risk factors were calculated and normalized to relate release category placement to consequences. Use of this normalized risk factor does not allow calculation of absolute risk for a specific plant, but changes in risk can be determined, assuming that the relative consequences between release categories are not site-specific.

Sensitivity calculations were based on specific plant PRA results, which depend on the particular accident sequence involved, and MARCH code calculations. It should be noted that this code has no phenomenological models for CMCI, and makes many simplifying assumptions for the phenomena. Results are presented in Tables 2.2, 2.3, 2.4, and 2.5, respectively, for Sequoyah (ice condenser PWR), Calvert Cliffs (large, dry PWR), Peach Bottom (Mark I BWR), and Grand Gulf (Mark III BWR), in terms of change in the early death risk, and contribution to the early death risk, with changes in the probability, P_{α}, of containment failure due to an in-vessel steam explosion.

The first line in each table ("original") corresponds to the plant PRA results, which used mixed values of $P_{\alpha} = 10^{-2}$ and 10^{-4}, corresponding to low and high ambient pressures, respectively. The other lines in each table use the indicated values of P_{α} as uniform.

The results show that significant differences exist between plants, due to the different dominant accident sequences involved. As the original mixed values case (using $P_{\alpha} = 10^{-2}$ and 10^{-4}) is changed to a uniform $P_{\alpha} = 10^{-4}$, there is a

Table 2.2

Effect of In-Vessel Steam Explosion Probability on Total Risk at Calvert Cliffs (Large, Dry PWR)

Probability of In-Vessel Steam Explosion	Percent Increase in Risk			Percent Contribution to Risk	
	Early	Latent	Combined	Early	Latent
Original Results	–	–	–	2	0.1
0.0001	-1	0	0	1	0.1
0.005	68	2	7	42	3
0.01	140	6	16	59	6
0.05	700	25	73	88	24
0.1	1400	49	150	94	40
0.2	2800	100	290	97	60
0.5	7000	250	730	99	86
0.9	13000	440	1300	100	98

Table 2.3

Effect of In-Vessel Steam Explosion Probability on Total
Risk at Sequoyah (Ice Condenser PWR)

Probability of In-Vessel Steam Explosion	Percent Increase in Risk			Percent Contribution to Risk	
	Early	Latent	Combined	Early	Latent
Original Results	–	–	–	17	2
0.0001	-16	-2	-8	1	0.1
0.005	6	0.2	3	22	2
0.01	30	2	15	36	5
0.05	220	18	110	75	21
0.1	450	37	230	86	36
0.2	910	76	460	93	55
0.5	2300	190	1200	98	83
0.9	4100	350	2100	100	98

Table 2.4

Effect of In-Vessel Steam Explosion Probability on Total Risk at Peach Bottom (Mark I BWR)

Probability of In-Vessel Steam Explosion	Percent Increase in Risk			Percent Contribution to Risk	
	Early	Latent	Combined	Early	Latent
Original Results	–	–	–	9	1
0.0001	-9	-1	-3	0.4	0
0.005	7	0.1	2	15	1
0.01	23	1	7	27	2
0.05	150	7	44	66	12
0.1	310	14	90	80	22
0.2	630	29	180	90	38
0.5	1600	74	470	97	71
0.9	2900	130	840	100	96

Table 2.5

Effect of In-Vessel Steam Explosion Probability on Total Risk at Grand Gulf (MARK III BWR)

Probability of In-Vessel Steam Explosion	Percent Increase in Risk			Percent Contribution to Risk	
	Early	Latent	Combined	Early	Latent
Original Results	-	-	-	2	1
0.0001	-3	-1	-1	0.1	0
0.005	1	-0.2	0	4	1
0.01	4	0.1	1	7	2
0.05	31	3	8	29	8
0.1	64	6	16	47	15
0.2	130	12	32	66	29
0.5	330	31	81	89	62
0.9	600	57	150	99	94

decrease in total risk, and as expected, a decrease in the contribution to that total from steam explosion effects. As P_α is increased by small increments, there are significant increases in total risk and in the steam explosion contribution to that total. For $P_\alpha = 0.01$ (meaning that the combined containment failure probability from all other causes would be 0.99), the increase in total risk for early deaths would be 140% at Calvert Cliffs, with steam explosion effects contributing 59% to that total. This is a good example of how a low-probability event ($P_\alpha = 0.01$) of serious consequence (e.g., in release category 1) can have a significant outcome. By contrast, for $P_\alpha = 0.01$ at Grand Gulf, the corresponding values would be 4% and 7%, emphasizing the wide range of values that are possible between plant types.

These results indicate the importance of steam explosions for containment failure in relation to other containment failure modes. In Section 2.3.1.8, estimates of risks for CMCIs in general were made for both vessel and containment failure, without referring directly to other containment failure modes.

2.3.1.7   Detailed Dominant Accident Sequence Extension
          Involving CMCI

Once the core melt state is reached, the potential for a CMCI will depend on the availability of coolant. The accident is continued from core melt in detail on Figure 2.4 to show by location (in-core, lower plenum, and cavity) the possibilities for coolant availability as a result of sequence progression (SP), system response (SR) to the accident, or operator action (OA). A path segment of Figure 2.4 finishes either with a CMCI in a particular location (with continuation, as indicated, on a subsequent figure), or with a potential containment failure.

2.3.1.7.1   CMCI in the Core Barrel

The first possibility for a CMCI will be in the core barrel (Figure 2.4, with continuation on Figure 2.5).

At high ambient pressure (e.g. with a transient, or small break LOCA accident initiation), the coolant level will be relatively high (possibly still immersing the lower part of the core barrel), since there would be limited capacity for steam flashing, and a small break LOCA would produce a relatively low coolant loss rate. Additional coolant for a CMCI could occur by injection.

Available data from reduced scale experiments suggests that, under these conditions of high pressure, the triggering of a steam explosion will be more difficult, but the energy conversion ratio may be high (compared with conditions of low pressure). The effects of scale and the molten core-coolant
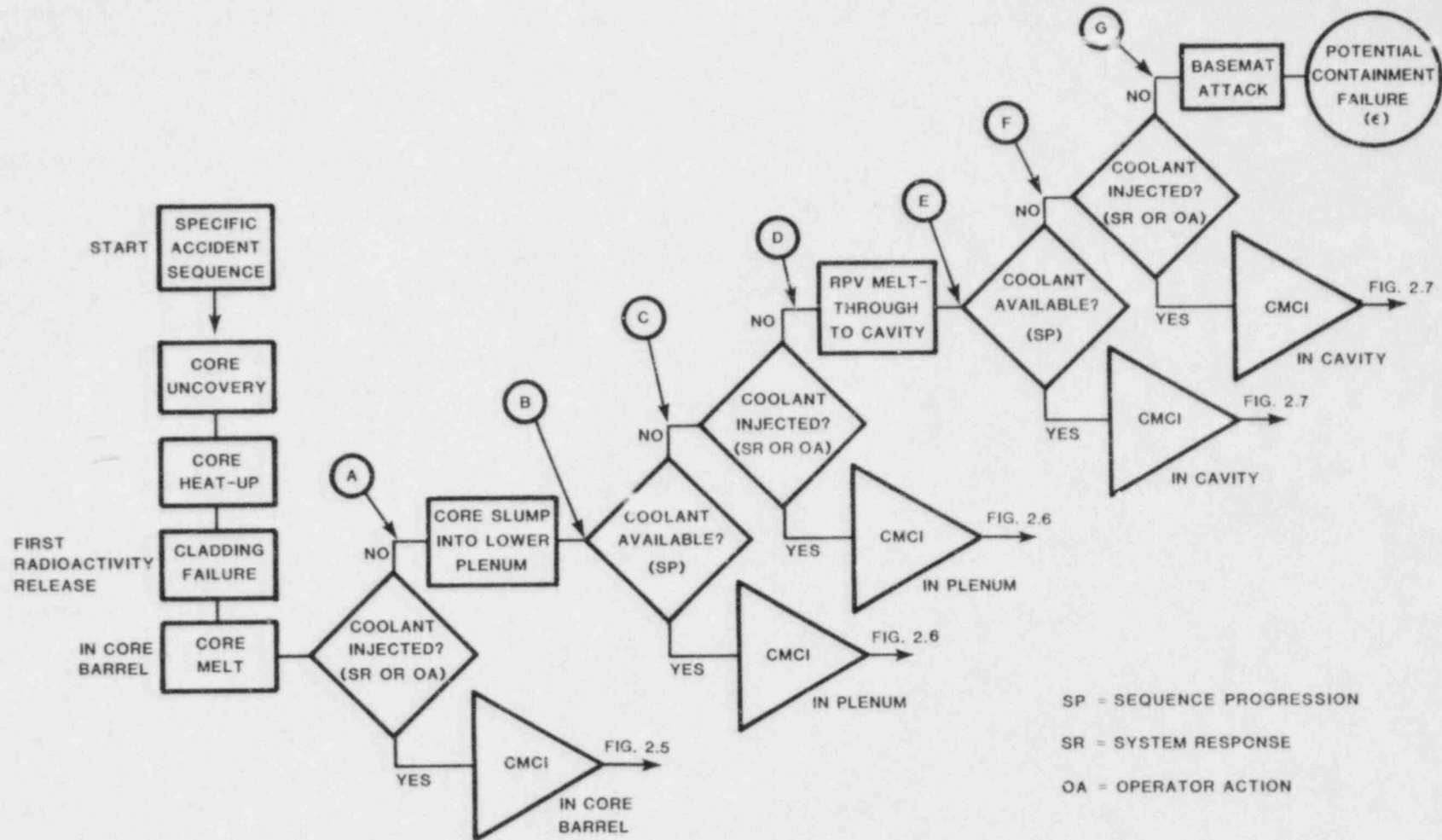
Figure 2.4. Possible Locations for CMCIs
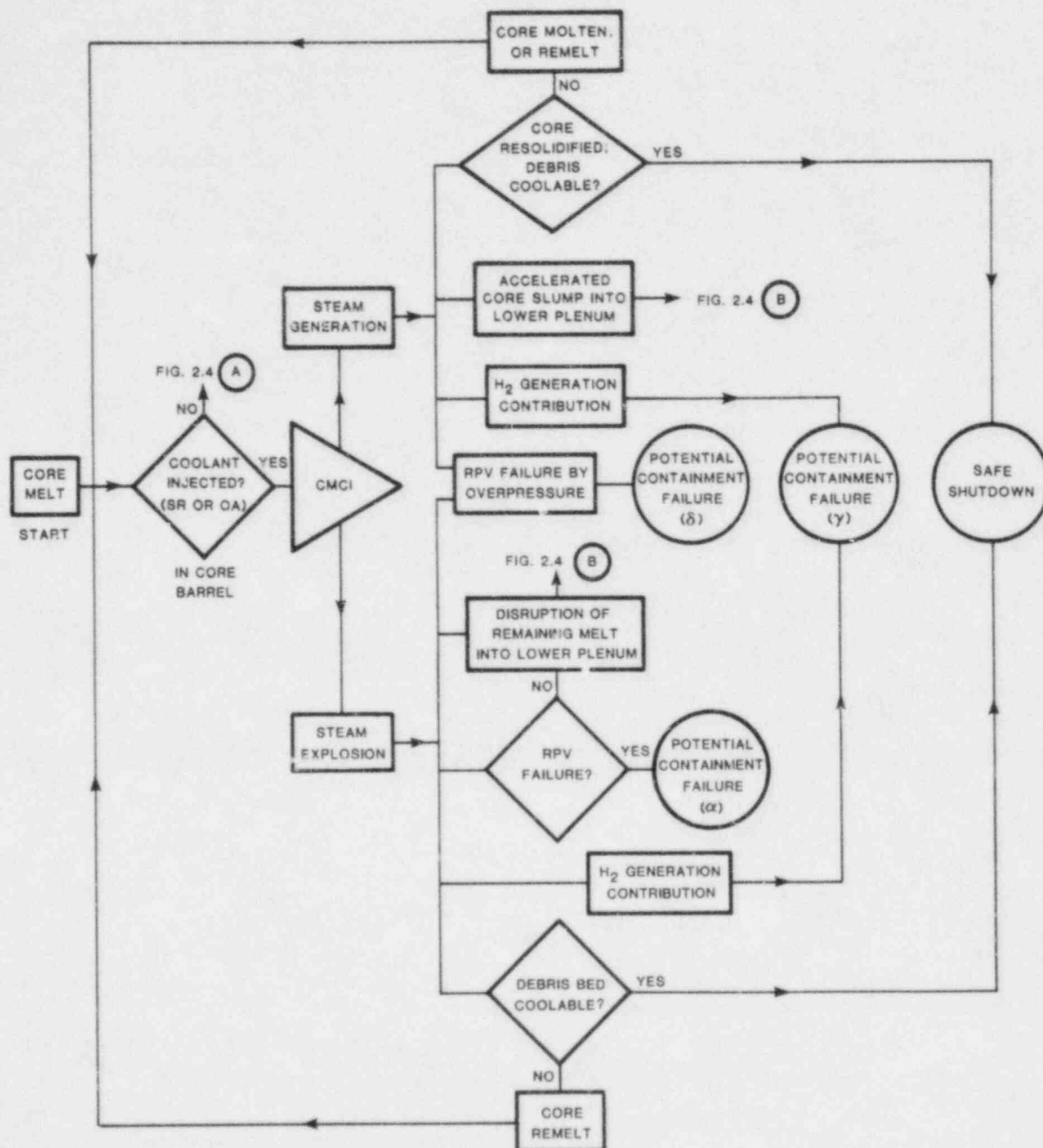
Figure 2.5. CMCI Occurring in the Core Barrel

contact mode on coarse mixing in the core barrel (of a reflooding type), and the availability of a sufficiently energetic trigger are unknown factors. In addition, in a BWR, coolant can be injected through the core spray system, representing another, uninvestigated, contact mode.

With a steam explosion, there is a possibility for vessel failure, and with a sufficiently vigorous explosion (as might occur if large enough quantities of molten core and coolant could be satisfactorily mixed), there is a possibility of direct containment failure by large mass missile from failure of the upper head of the vessel. Additional uncertainties here involve the generation of an appropriate, energetic slug (composed of liquid and vapor coolant, with core and structure debris), and how it might breach the vessel and produce a large-mass missile. In the core barrel with coolant injection at a slow rate in the reflood mode from below, an early, low-energy steam explosion could occur before a significant mass of water could mix with melt. The production of a less energetic missile from vessel failure due to a steam explosion could cause damage to accident management systems (sprays and fans) and lead to an indirect containment failure.

For both types of CMCI, there will by hydrogen generated as the metallic content of the molten corium is oxidized by the steam. Although preliminary information on hydrogen generation rates is available for both explosive and nonexplosive situations involving corium, the effect of pressure above a few bars is not known. With a steam explosion, the hydrogen generation rate could be high, with the amount governed by the interaction among the quantity of melt participating, its (large) surface area of contact (due to the degree of fine fragmentation), and its temperature decrease rate. This process could produce a rapid burst of hydrogen that could defeat a deliberate mitigating scheme, such as deliberate ignition. With nonexplosive steam generation, the hydrogen generation rate will be lower due to smaller contact area, but the entire melt mass can participate (as can the part of the melt that does not participate directly in a steam explosion). The end result may or may not be the generation of a larger quantity of hydrogen than for a steam explosion: the interplay among the various factors (given above) is not understood.

At high pressure, the associated relatively low coolant injection rate may simply result in an increased steam generation rate, which could produce increased oxidation of the zirconium cladding. This is a highly exothermic reaction that could overcome the steam cooling effect. Hence, coolant injection under these conditions could exacerbate the accident by accelerating core slump into the lower plenum.

With coolant made available by injection, pressure venting (by operator action, or by vessel failure [perhaps by thermal shock]) will increase the possibility of a steam explosion through easier triggering. The actual pressure lowering rate could also be a trigger source, especially if the decompression were explosive. However, the situation will be complicated, since a higher pressure venting rate will cause faster flashing, and the complex fluid motions in the vessel will affect the core melt-coolant contact mode and the nature of the CMCI.

A low pressure accident (caused, for example, by a large break LOCA initiator) would be accompanied by significant steam flashing that could essentially empty the vessel at original coolant. As the pressure falls below a value of the order of 700 psi, the accumulators would automatically discharge (typically 10 s after accident initiation), and, after allowing for flow bypass to the break and boil-off in the hot vessel, the lower plenum could be partially filled with coolant having moderate to high subcooling. Failure of the low pressure injection or circulation systems would result in core melt in about 0.5 h. If the failed system could be restored to inject additional cold coolant at a sufficient rate, it is possible that the molten core could be resolidified for a safe shutdown. If this were not achievable, there would be a possibility, of some significance, for a steam explosion due to easier triggering at low pressure and moderate subcooling. However, as with high pressure, the effects of scale and the reflooding type of contact mode on the coarse mixing of core melt and coolant are not well understood. If the failed system could not be restored, then core slump into the lower plenum would occur with, possibly a subsequent CMCI in that location (Figure 2.4 (point A) Figure 2.6, and Section 2.3.1.7.2).

If a CMCI in this region leads to a failure of the primary system, the course of the accident can change. Finally, the coolability of the core debris bed, and whether or not it will remelt, will depend on the nature of the CMCI. Generally, a more vigorous steam explosion is associated with finer particle fragmentation, and this would result in debris that is more difficult to cool. Furthermore, a steam explosion will tend to disrupt material into the lower plenum, and the coolant there could be deep enough to stratify the fragmented core debris, increasing further the difficulty of cooling and preventing remelting. If coolant injection did not result in a steam explosion, and the core could be resolidified, it appears possible that it could be maintained in that condition and a safe shutdown achieved. If remelting were to occur in the core barrel, then the possibility of further CMCI would have to be considered by returning to the starting point on Figure 2.6.
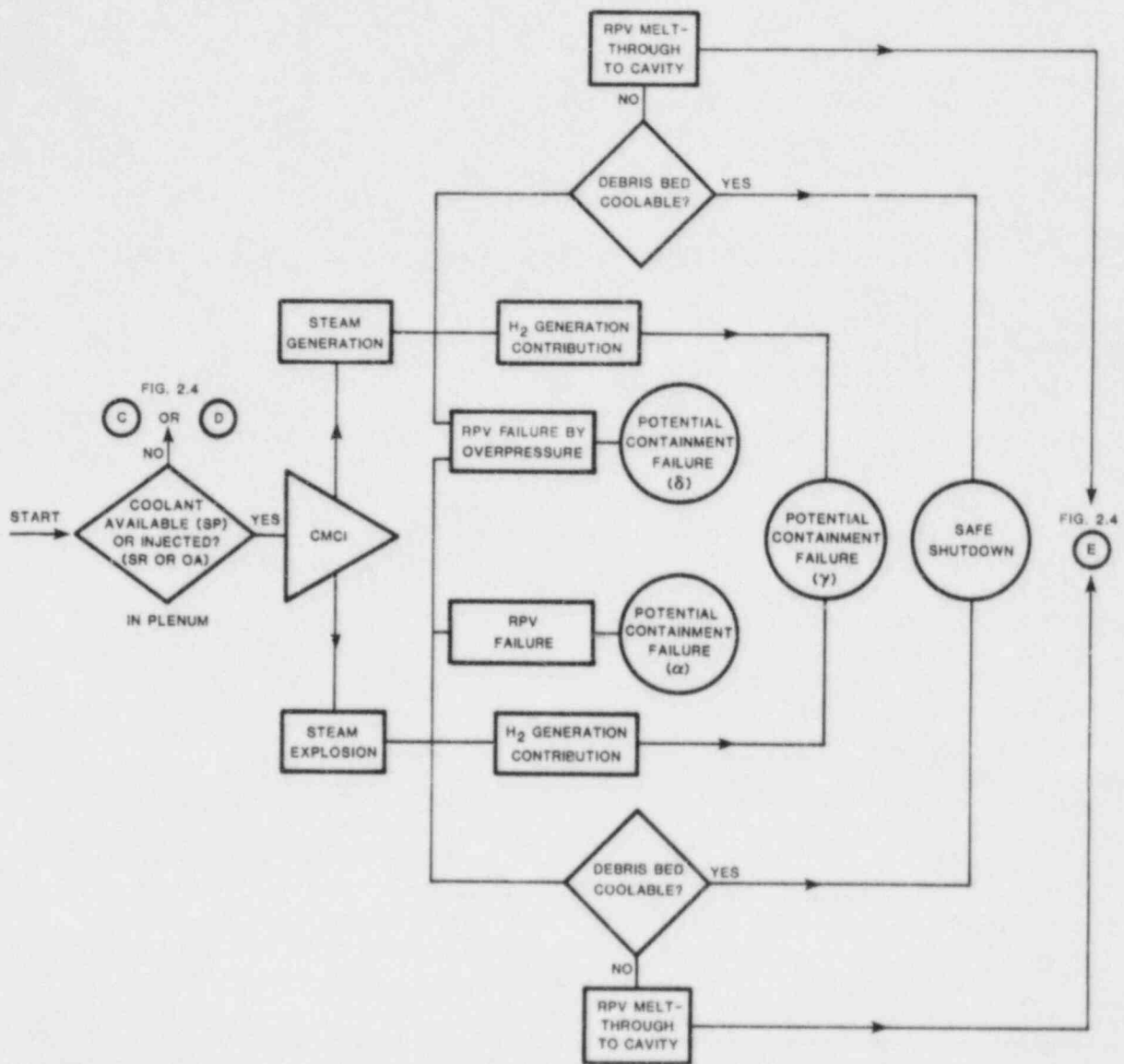
Figure 2.6. CMCI Occurring in the Lower Plenum

2.3.1.7.2 CMCI in the Lower Plenum

The second possibility for a CMCI will be in the lower plenum
(Figure 2.4, with continuation on Figure 2.6). There are
many similarities to the situation described in the previous
section for a CMCI in the core barrel, and except for differ-
ences and their possible effects, which will be emphasized
here for CMCI in the lower plenum, the phenomenological
information Section 2.3.1.7.1 will be considered to apply
here.

We can generally expect coolant to be available in the lower
plenum as a result of accident sequence progression and/or
system response to the accident (accumulator discharge for
an ambient pressure less than approximately 700 psi). There
will be a tendency for less coolant subcooling with accidents
at higher pressure, especially above 700 psi when there will
have been no accumulator cold water injection. After core
slump in the core barrel, it is not clear how much of the
core will be molten at a particular instant, what configura-
tion it will take, and how it might relocate into the lower
plenum. Two general relocation possibilities have been con-
sidered: (1) radial spread of the molten pool until it
breaks out as a side pour down the annulus at the core barrel
baffle (this will probably result in an incomplete pour of
the pool), and, (2) if bottom-of-core cooling were limited
(as, for instance, if the plenum water level were low), a
bottom pour could occur with discharge of essentially the
entire molten pool. Both types of pour under gravity would
produce a molten core-coolant contact mode that would be
different from the case where operator action might cause
flooding of the melt from above. For both types of pour, it
seems reasonable to expect that a large proportion of the
core would have to be molten in order for it to break out.
The various combination possibilities of ambient pressure,
subcooling, and contact mode will affect the probability and
vigor of a steam explosion. The effect of structure in the
lower plenum will be an additional, unknown factor. Only
rather fragmented information (at reduced scale) is cur-
rently available on these issues. If the CMCI does not
result in a steam explosion, then there will be steam gen-
eration. There is the possibility of vessel failure in
either case (Figure 2.6), which could lead to direct con-
tainment failure.

For a given type of CMCI, the possibility of, and problems
resulting from, hydrogen generation and difficulties with
debris bed coolability in the lower plenum, are similar in
nature to those in the core barrel, except that, with the
longer elapsed time, larger quantities of molten core (and
structure) could be involved.

With melt in the lower plenum, either in the absence of coolant, or forming a continuous pool underneath the coolant with steam generation, melt-through to the reactor cavity would be expected in a matter of minutes.

It is possible that a mild steam explosion in the lower plenum (rather than slow steam generation) could delay melt-through of the vessel, or even prevent it if the final debris were coolable.

In summary, the principal differences between CMCI behavior in the lower plenum (as opposed to the core barrel) involve possible differences in contact mode (flooding from above in the lower plenum, versus flooding from below in the core barrel), and the possibility of larger melt masses being available in the lower plenum. These events will also determine if and how the vessel fails.

2.3.1.7.3 CMCI in the Reactor Cavity

Compared with the previous cases in the core barrel and the lower plenum, there are two main differences for a CMCI in the reactor cavity (Figures 2.4 and 2.7): (1) the ambient pressure will always be low due to the connection with the containment building (via the suppression pool for a BWR, and via the keyway for a PWR), and (2) molten core delivery by melt-through of the lower plenum could occur under high vessel pressure. A jet would then form with different contact mode characteristics from a gravity pour, and in addition, the jet could break apart before entry into the coolant due to the expansion of entrapped vapor.

Lower pressure would enhance the triggering of a steam explosion, and this would tend to disperse debris and fission products to the containment floor.

Questions concerning hydrogen generation and debris bed coolability due to a CMCI in the cavity are similar to those for the lower plenum and core barrel locations, with emphasis on the low pressure situation that will influence the type of CMCI occurring.

With no coolant in the cavity, or with core melt in a pool beneath coolant, basemat attack will occur.

2.3.1.8 Potentially Significant CMCIs and Associated Prototypic Conditions

With the various CMCI possibilities described in Section 2.3.1.7, it is now necessary to rank the CMCI in order of significance, and to determine the prototypic initial and boundary conditions for each case. This will be followed, in subsequent sections, by identification of the conditions affecting CMCI behavior and the pertinent unknown or
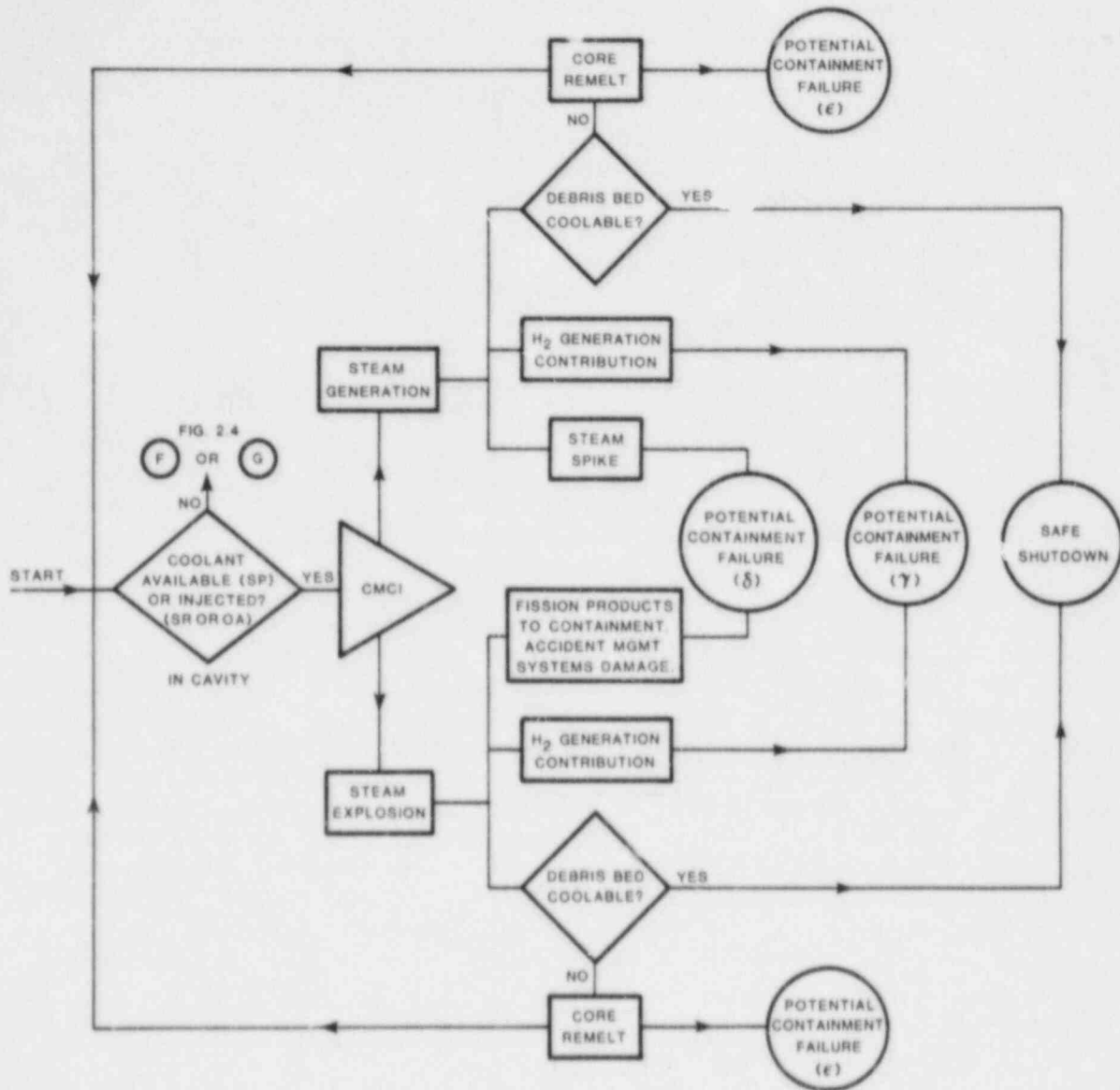
Figure 2.7. CMCI Occurring in the Reactor Cavity

uncertain factors, together with a listing of the issues, the research questions, and the program elements required to resolve the issues.

The detailed continuation of the accident sequence (Figures 2.4 through 2.7) show that CMCIs are possible in the core barrel, in the lower plenum, and in the cavity.

The overall risk, R, from a potential CMCI involves considerations of a probability factor, P, and a consequence factor, C. If our scale for C also includes a factor relating to time (for the strength of the fission product term), then, for purposes of comparison to establish priority among different CMCI situations, the risk will be defined as $R = P \times C$. If scales of 0 to 3 are assigned to P and to C, then the resulting values of R will indicate the relative importance among the various situations. In view of the absence of certain items of information (which the research program will attempt to obtain), this procedure is highly speculative and subjective. In particular, factors contributing to uncertainties in P include: effect of scale (typically two to three orders in mass above current experimental conditions); coarse mixing for a steam explosion (core melt mass that can mix, and the smallness of melt particle size that can be achieved); the strength of trigger required to initiate an explosion, especially at elevated pressure and reduced subcooling; the availability of the required trigger; the effect of structural geometry, both on the triggering and propagation phases of an explosion, and on the energy dissipation of a slug projectile; and the production, behavior, and damage potential of such a slug, especially with respect to its vapor content. The resulting numbers for R are intended to represent trends and should be considered as providing only the crudest qualitative estimates of relative importance. However, making the best use of available knowledge, and asking appropriate questions about deficiencies, should give reasonable answers for the most effective course of research to be followed.

Starting with a particular location, the progression of a CMCI will involve the following phases:

(1) Possible Immediate Results
    a. Steam explosion or steam generation (distinguished by rate of increase of pressure)
    b. Hydrogen generation
    c. Degree of core fragmentation
    d. Possible reactant (melt, coolant) dispersal and relocation

(2) Possible Implications
    a. Missile generation
    b. Debris bed coolability
    c. Contribution to overpressure

d. Contribution to high temperature excursion
    e. Damage to accident management systems
    f. Pressure vessel motions
    g. Effect on fission product term (aerosol production,
       etc.)
    h. Effect on accident sequence (modification or change)

(3) Possible Consequences
    a. Accident termination (safe shutdown but with fuel
       damage)
    b. Primary system failure
    c. Indirect containment failure
    d. Direct containment failure

Estimates of R will now be made for a CMCI in each of the
locations shown in Figures 2.4 through 2.7.

2.3.1.8.1 In the Core Barrel Region

If coolant were available early enough, and in sufficient
quantity, then it appears possible that the accident could
be terminated with the core resolidified.

For nonexplosive situations:

    Immediate results: Steam generation (1a),
                          hydrogen generation (1b),
                          minor core fragmentation (1c)

    Implications: None of importance

    Consequence: Accident termination, C = 0

    Probability: P = 0 to 3, depending on ESF restor-
                          ability, pressure level, and opera-
                          tor action

    Risk: R = P x C = 0

The possibility of an in-core steam explosion will depend on
the ambient pressure and the availability of sufficient trig-
ger. The strength of the explosion will depend on the
amounts of melt available (involves time into accident), and
degree of mixing achievable with coolant.

For steam explosions:

    Additional results: All

    Implications: All

    Consequences: 3a. Accident termination:
                              C = 0, P = 0-3, R = 0

2-30

3b. Primary system failure:
                            C = 1, P = 0-2, R = 0-2

                       3c. Indirect containment failure:
                            C = 2, P = 0-1, R = 0-2

                       3d. Direct containment failure:
                            C = 3, P = 0, R = 0

2.3.1.8.2 In the Lower Plenum

Further time into the accident will have elapsed, and it is
possible that up to 80% of the core has melted and been held
up in the core region before relocation occurred into the
lower plenum. With a rapid bottom pour from the core barrel
into the lower plenum (as opposed to a side pour, with only
a limited amount of pouring possible), the question of effec-
tive melt-coolant mixing arises due to obvious space and time
constraints. This, together with possible triggering diffi-
culties at high pressure, affects the likelihood of the
occurrence, and the strength of a steam explosion.

For nonexplosive steam generation:

     Additional results: All but 1d.

     Implications: 2b, 2c, and 2d.

     Consequences: 3a. Accident termination:
                               C = 0, P = 0-3, R = 0

                          3b. Primary system failure:
                               C = 1, P = 0-1, R = 0-1

                          3c. Indirect containment failure:
                               C = 2, P = 0-1, R = 0-2

                          3d. Direct containment failure:
                               C = 3, P = 0, R = 0

For a steam explosion:

     Additional results: All

     Implications: All

     Consequences: 3a. Accident termination:
                               C = 0, P = 0-3, R = 0

                          3b. Primary system failure:
                               C = 1, P = 0-2, R = 0-2

2-31

3c. Indirect containment failure:
C = 2, P = 0-2, R = 0-4

3d. Direct containment failure:
C = 3, P = 0-1, R = 0-3

The ranges given for P reflect uncertainty due to effects of scale (mixing), pressure, subcooling, and structure.

2.3.1.8.3 In the Cavity

A CMCI occurring in the cavity will be at lower pressure, and this will tend to increase the possibility of a steam explosion with:

Additional results: All

Implications: All but 2a and 2f

Consequences: 3a. Accident termination:
C = 0, P = 0-2, R = 0

3c. Indirect containment failure:
C = 2, P = 0-3, R = 0-6

3d. Direct containment failure:
C = 3, P = 0, R = 0

In the absence of a steam explosion, steam generation would involve:

Additional results: 1b and 1c

Implications: 2b and 2c

Consequences: 3a. Accident termination:
C = 0, P = 0-2, R = 0

3c. Indirect containment failure:
C = 2, P = 0-3, R = 0-6

3d. Direct containment failure:
C = 3, P = 0, R = 0

2.3.1.9 Summary of Important Consequences and Identification of Significant Unknown or Uncertain Factors Affecting CMCI Behavior

2.3.1.9.1 Important Consequences

From Subsection 2.3.1.8, on a scale of 0 to 9, the risks R $\geq$ 2 from CMCI are listed in Table 2.6.

Table 2.6

Relative Estimated Risks from CMCI

Consequence	Cause	Location	Risk, R
Indirect containment failure	Steam explosion	In-core lower plenum cavity	0-2 0-4 0-6
	Steam generation	Lower plenum cavity	0-2 0-6
Direct containment failure	Steam explosion	Lower plenum	0-3
Failure of primary system	Steam explosion	In-core lower plenum	0-2 0-2

The greatest potential risk (R = 0-6) from a CMCI, occurring explosively or nonexplosively in the cavity, is the possibility of indirect containment failure. An additional possibility with significant risk (R = 0-4) for the same consequence could occur as a result of a steam explosion in the lower plenum.

The next most serious risk (R = 0-3) is the possibility of direct containment failure due to a steam explosion in the lower plenum, followed by the risk (R = 0-2) of primary system failure due to a steam explosion, either in-core, or in the lower plenum.

Note that the numbers given are our crude and approximate estimates of relative risk, R, and not simply the probability, P. For example, direct containment failure (R = 0-3, with P = 0-1) depends explicitly on the occurrence of primary system failure, but the risk from this latter consequence is judged as only R = 0-2, with P = 0-2. This higher value of P = 0-2 very roughly indicates that by no means do all primary system failures result in direct containment failure (P = 0-1).

The extent of the ranges of the given risk values is a measure of the uncertainty by which they should be judged.

2.3.1.9.2 Unknown or Uncertain Factors Affecting CMCI

When making the above estimates for R, use was made of the available data base (Section 2.3.1.2.2). Although sufficient progress has been made to enable us to make the subjective judgments on _relative_ risk shown in Table 2.6, the uncertainties are still large. The most important research questions that need to be addressed are shown in Table 2.7, along with the program elements suggested for the resolution of those questions. The obvious goal of the research is to develop models that will predict the dependence of the CMCIs on the initial and boundary conditions created by the accident scenarios and the nature of the CMCIs themselves (explosive or nonexplosive, hydrogen generation rates, resultant debris bed characteristics). The program elements are designed to be cost-effective in terms of providing the necessary information. For example, we believe that small scale experiments may be sufficient to resolve questions on the triggerability of steam explosions at high ambient pressure.

Obviously, not all of the research questions listed in Table 2.7 are of equal priority. In the summary, we indicated our thoughts as to the relative importance of the questions. We currently believe that the most important research question deals with scale effects. An experimental facility capable of delivering approximately 1000 kg of melt will probably be needed if models are to extrapolated with reasonable confidence to prototypic conditions (involving perhaps 1,000 to 200,000 kg of melt).

As an example of the connection between the safety issues, the research questions and the program elements, consider the current state of knowledge concerning the amount of molten core that could conceivably mix with water to produce a CMCI. Based on FITS experimental data, Corradini has produced an expression for the initial diameter of a spherical mass of melt that can mix in a given depth of water.[10] The melt particle size after mixing was assumed to be limited by fluidization from the steam generated during the process: with increase in melt to be mixed, the steam generation rate is higher, and the melt particle diameter after mixing is larger. An upper bound on the amount that could mix at reactor scale can be calculated by extrapolating these results and assuming that the above (spherical) diameter is used as the diameter of a cylindrical volume of melt, with a length equal to the water depth into which the pour occurs. These results for the corium melt mass that can mix for a typical PWR (total core mass of 130,000 kg) and the resulting particle size are shown in Figure 2.8. For a typical PWR, with the lower plenum filled with coolant to a depth of 3 m or for the cavity filled to a depth of 5 m, Corradini's expressions predict that approximately 10% and 30%, respectively, of the original core (if molten) could mix. An important

Table 2.7

Program to Resolve Issues

Issue	Research Questions	Program Elements
1. **Steam explosion phenomena**		
a. Melt-coolant mixing	Effect of scale, melt/coolant geometry and contact mode, melt temperatures, structural geometry. Melt particle size achievable from mixing.	FITS and EXO-FITS (~100 kg) plus larger tests.
b. Triggering and propagation	Effect of ambient pressure, coolant subcooling and mass (threshold and scale), coarse mixing particle size.	Small scale (single droplet), High pressure (~170 b).
c. Energy conversion ratio	Effect of scale, coolant-to-melt-mass ratio, pressure, subcooling, structural geometry, inertial confinement (tamping and directional constraint), melt temperature. Correlation with debris size.	EXO-FITS (with special slug impact measuring plate); larger scale tests.
d. Water slug	Slug production, kinetic energy achievable and dissipation mechanisms. Effects of scale and void fraction on damage potential.	FITS and EXO-FITS
2. **Steam explosion modelling**	Develop models to extrapolate experimental results to reactor accidents; refine estimates of vessel and containment failure probabilities.	Analysis and modelling at Univ. of Wisconsin and computer code development and application at SNLA.
3. **Steam generation**	Dependence of generation rate on melt-coolant mixing, as for 1a above. Effect of mitigating boundary losses (wall condensation, relief valve operation). Steam "spike" rates.	FITS (~100 kg), larger scale tests.
4. **Hydrogen generation**	Generation rate and amount. Dependence on melt particle size (explosive and nonexplosive interactions), and melt temperatures.	FITS (~100 kg), using inerted (nitrogen) atmosphere.
5. **Debris Bed**	Particle size and distribution; bed porosity.	FITS (~100 kg).
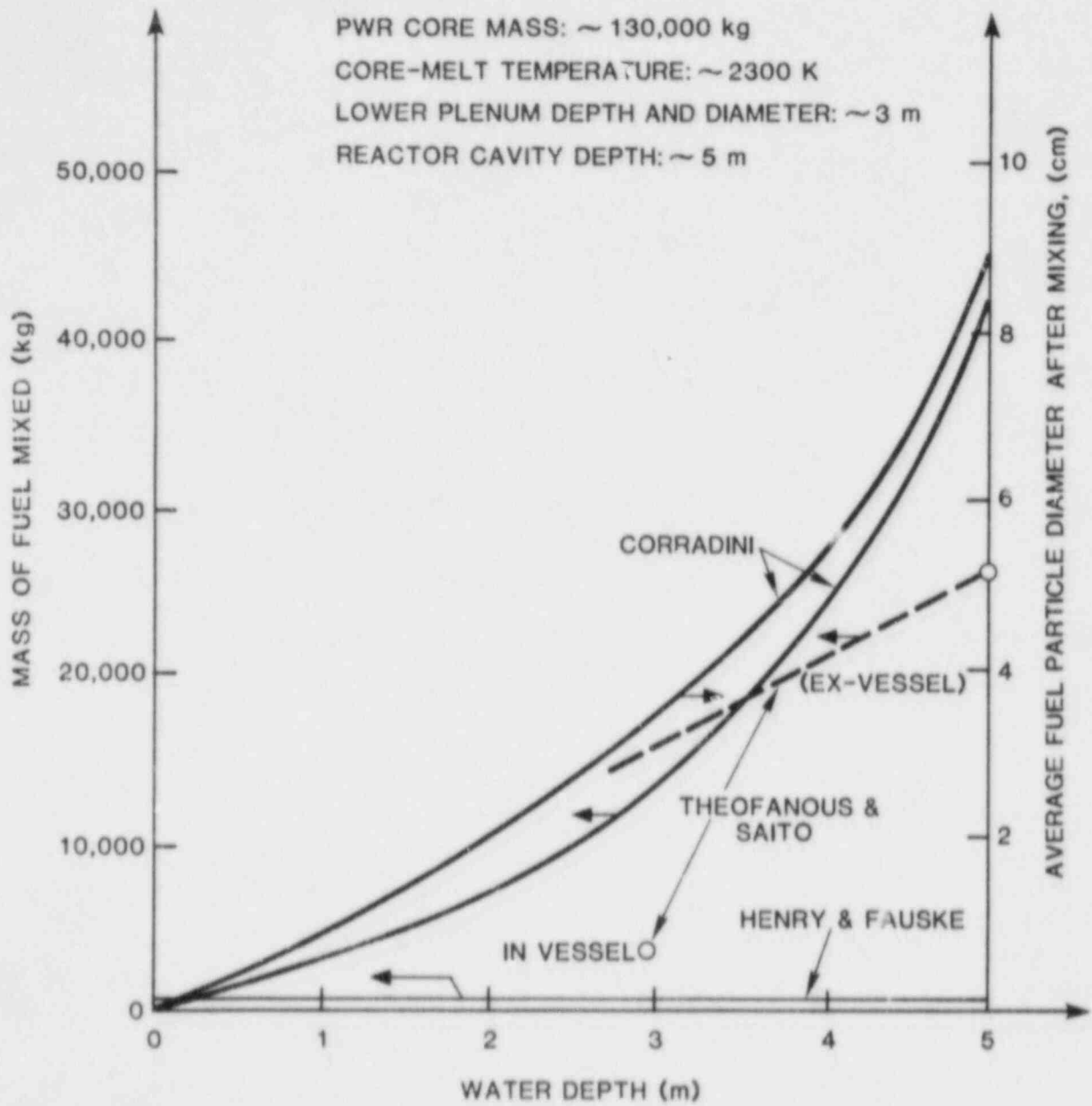
Figure 2.8. Predicted Limits on Core Melt-Coolant Mixing in a Typical PWR

question remains as to whether the average melt particle sizes after mixing ex-vessel (in the diameter range 3 to 8 cm) can result in an explosible mixture under these conditions. Henry and Fauske's result for the mass of fuel that can mix (Figure 2.8) is a few hundred kilograms, and is independent of depth (a strong parameter in Corradini's results).[11] Theofanous and Saito's results give a point value of approximately 4,000 kg for the in-vessel case, and up to 13,000 kg to 26,000 kg for the ex-vessel case, depending on the water depth in the reactor cavity.[12]

Current FITS data are limited to melt masses of approximately 20 kg, with the possibility of increasing this value to 50 to 150 kg. In order to distinguish between the various mixing models, and possibly validate any one of them, we expect that it will be necessary to conduct large-scale tests with melt masses to 1,000 kg, and possibly to 2,000 kg.

2.3.1.10 Conclusions

By using generalized dominant accident sequences based on actual PRAs for both BWR and PWR nuclear power plants, it was shown that CMCIs could occur throughout the pressure-time plane (0-150 bars pressure and up to 30 h from accident initiation) and could involve all dominant accident initiators (transients, all sizes of LOCAs, isolation failure, and massive vessel rupture).

The accident sequence was continued in detail from core melt to show that CMCIs of potential significance could occur in the core barrel, in the lower plenum, and in the reactor cavity if coolant were available as a result of the accident sequence progression, system response to the accident, or operator action.

By means of very simple scales for estimating the probability and consequence for each CMCI possibility, it was crudely determined that the most serious risk was the possibility of indirect failure of containment due to an explosive or non-explosive CMCI in the reactor cavity. In descending order of risk, a steam explosion in the lower plenum could also lead to indirect containment failure, as well as direct containment failure, and primary system failure. Finally, a steam explosion in the core barrel could produce (with equal risk) indirect containment failure and primary system failure. The risks were estimated using the currently available data base, and the high levels of uncertainty are reflected by the wide ranges in the estimated risk for each consequence.

It was also shown for a particular plant that, when considering all other dominant containment failure modes (such as failure due to hydrogen burning or overpressure), direct containment failure by an in-vessel steam explosion at low

relative probability $P_\alpha = 0.01$ could contribute almost 60% to the total risk. To reduce the uncertainties in the current risk analysis and allow the development of models to extrapolate reduced scale results with reasonable confidence to reactor scale, the following issues were identified for resolution by an appropriate research program: steam explosion phenomena (involving melt-coolant mixing, triggering, energy conversion ratio, and water slug production); steam explosion modelling; steam generation; hydrogen generation; and debris bed coolability. Research questions related to these CMCI issues include determination of the effects due to scale, melt and coolant configurations (contact mode), melt temperature, coolant subcooling, ambient pressure, hydrogen and steam generation rates, and core debris particle size distributions. To resolve the important issue of scale effects, we feel that it will be necessary to perform tests with melt masses of the order of 1,000 kg to determine which, if any, of the current melt-coolant mixing models is valid. The first order indications of the effect of high pressure (~170 bars) on triggering could be most cost-effectively obtained in small scale, single melt droplet apparatus, with first answers to the remaining questions obtained in the FITS facility.

2.3.2 Modelling the Various Phases of a Steam Explosion
       (M. L. Corradini)

CMCI is a physical event that can be conceptually divided into four phases of energy transfer:

(1) Hot molten material (core melt) mixes with colder more volatile liquid (water coolant); this process involves melt breakup into smaller sizes as it disperses in the coolant and as the melt undergoes heat transfer while in film boiling.

(2) Large energy transfer rates are triggered between the melt and the coolant by film boiling collapse and subsequent liquid-liquid contact at melt temperatures substantially above the coolant boiling point.

(3) Once 'triggered,' rapid melt fragmentation occurs and increases the exposed melt surface area and the energy transfer rate even further. This transfer of energy by heat transport goes into the nearby coolant and vaporizes it to high pressures. If the melt-coolant mixture is large enough, it produces its own inertial constraint, and this explosive energy transfer can spatially 'propagate' through the mixture much like a chemical explosion.

(4) The high pressure coolant vapor then expands against the surrounding liquid (possibly both melt and coolant), and transforms its internal energy to kinetic energy of the explosion zone and surrounding liquid. Continued energy transfer can occur during this expansion.

The CMCIs are important phenomena for a number of reasons:

(1) The CMCI mixing and explosion can cause the melt to break into smaller sizes and be quenched as solid particles. The relative size distribution of this debris is important for subsequent debris bed heat transfer considerations and possible dryout and remelting.

(2) The CMCI also produces steam, and possibly hydrogen if the melt is partially metallic. These gas sources are important because they may contribute to early containment overpressurization.

(3) Finally, if the CMCI is explosive, one is also concerned about the kinetic energy imparted to the liquid/solid surrounding materials, in regard to missile generation and early containment failure.

The modelling and analyses that we are performing have two purposes. First, we are analyzing current small-scale and intermediate-scale (FITS) experiments, with the objective of getting a better understanding of the CMCI phenomenon and how it would scale to reactor accident conditions. Second, we are trying to establish the reactor initial conditions and consequences of the CMCI process with simple phenomenological models to better characterize processes during a severe accident for PRA purposes.

We now present our recent progress in the various phases of the CMCI. Our emphasis will be both on the physics of the CMCI and the possible implications to severe reactor accidents.

2.3.2.1 Mixing Phenomena

2.3.2.1.1 A Dynamic Model for Melt-Coolant Mixing

Containment integrity may be threatened by physical processes that involve contact between the overheated and possibly molten core materials (Corium fuel) and other materials present in the containment, such as water, steel, or concrete. In this short progress report, consideration is given to CMCIs both in-vessel and ex-vessel, given a scenario of melt-coolant contact.[13-17] Specifically, we present a dynamic model for melt-coolant mixing when corium pours into a water pool and breaks apart producing steam and hydrogen (if the melt is metallic), prior to or in the absence of a steam explosion.

Past research into melt-coolant mixing (sometimes called 'premixing') has been directed at predicting the physical limits for which mixing could or could not occur. Fauske originally proposed that the melt-coolant interface temperature upon liquid-liquid contact must exceed the spontaneous nucleation temperature to allow premixing for an energetic FCI.[18,19] The physical picture was that stable film boiling is established above this limit for a liquid-liquid system, and this allows the melt time to penetrate and mix with the coolant. For the LWR system, the melt and coolant easily satisfy this first criterion. Cho et al. considered the energy used in melt-coolant mixing that creates more surface area and overcomes frictional effects.[20] They concluded that frictional effects dominate the energy mixing requirements. Fauske and Henry subsequently proposed the physical concept that the melt can break up and premix with the water to a uniform size no smaller than that which would prevent liquid from entering the mixture zone.[21,22] The minimum diameter was given by

$$D_{MIN} = \frac{6m_m q_{DROP}''}{\rho_m A_c q_{CHF}''} \qquad (2-1)$$

where m_m, ρ_m are the melt mass and density, respectively, A_c is the coolant chamber area, q_{CHF}'' is the critical heat flux, used as the limit for steam outflow and water inflow, and q_{DROP}'' is heat flux from the melt (primarily radiation).

More recently Corradini suggested that the limit to melt-coolant mixing was determined by melt or coolant liquid fluidization; e.g.,

$$D_{MIN} = \left[\left(\frac{3}{4}\right)\left(\frac{\alpha_m}{\alpha_v}\right)^2 \left(\frac{6q_{DROP}''}{\rho_v i_{fg}}\right)^2 \left(\frac{C_D H_C}{g}\right)^2 \left(\frac{\rho_v}{\rho_m}\right) \right]^{1/3} \qquad (2-2)$$

where α_m and α_v are the melt and vapor volume fraction at any time as the mixing evolves, H_C is the coolant depth, C_D is the drag coefficient, and i_{fg} is the latent heat vaporization.[23]

This last criterion implies that the dynamic evolution of the mixture be known. In this regard, we are developing a transient melt-coolant mixing model for a pouring mode of contact. The melt is considered to fall or be injected into a coolant pool (e.g., Figure 2.9), mix with the coolant, and, in the absence of a steam explosion, settle on the base of the vessel as either a molten pool, a debris bed, or both. This is modelled numerically by subdividing the fuel pour stream (or mass) into a finite number of Lagrangian 'parcels.' A new molten parcel can enter the calculation each
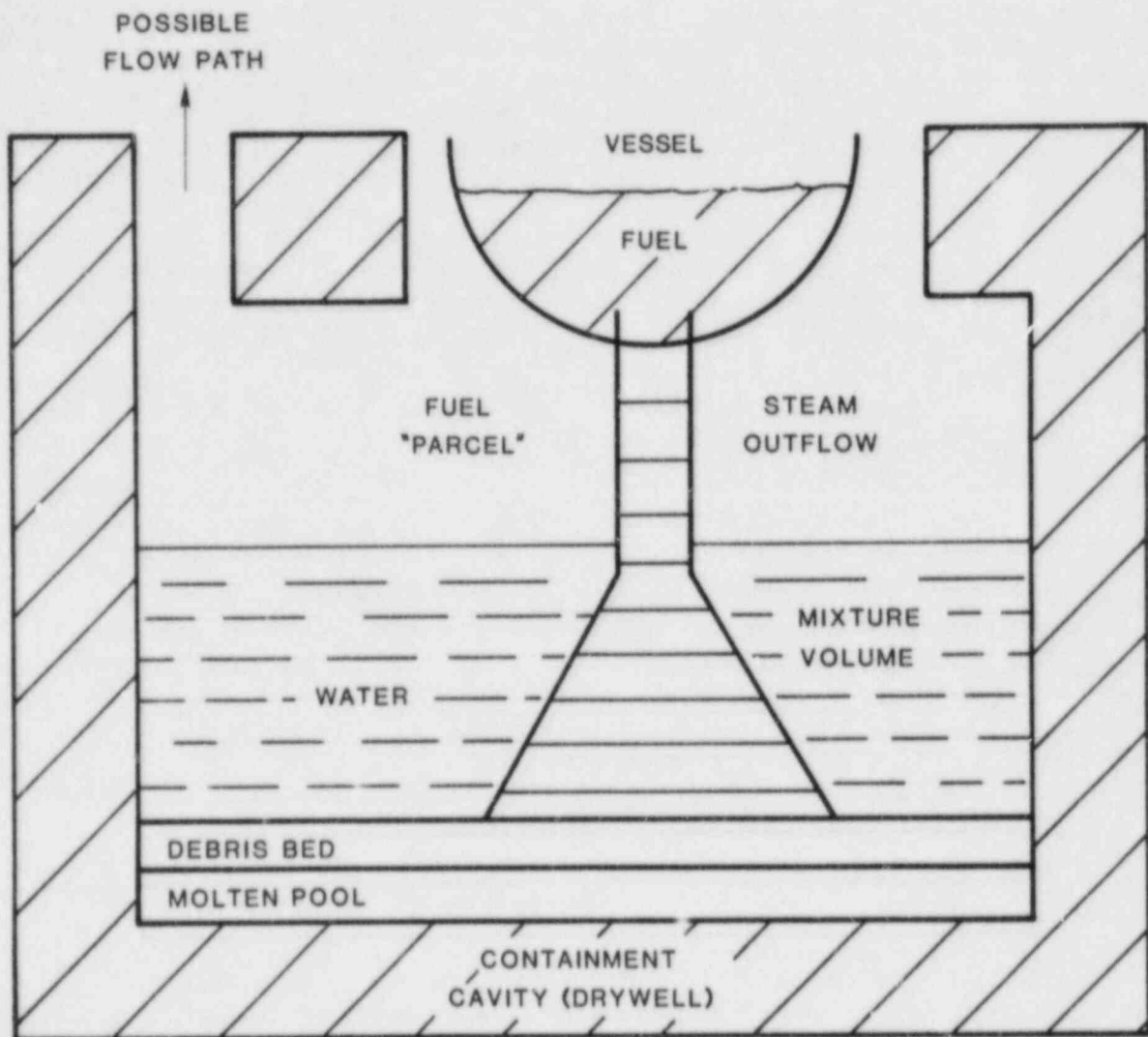
Figure 2.9. Computer Model of Fuel-Coolant Mixing

time step, and each of the other parcels falls at its characteristic velocity. The parcel reaching the base (or debris/pool interface) is accumulated in the molten pool or debris bed, depending on temperature. As the parcels fall through the coolant pool they break up into smaller masses due to relative velocity differences, and transfer energy to the surrounding coolant liquid while in film boiling. This energy transfer heats the coolant pool and generates steam that then flows upward into the gas atmosphere as water flows into the fuel-coolant mixture from the sides and below. If the melt is partially metallic, then the generated steam can diffuse to the metal surface and oxidize it as hydrogen diffuses away; the rate of chemical reaction increases as the melt surface area increases due to further mixing.

In this model, each parcel is considered to be fragmented due to hydrodynamic forces initiated by melt-coolant relative velocities. The characteristic diameter, D_m, is given below as mixing develops

$$D_m = D_{mi} \exp \left[-\frac{v_m t}{D_{mi}} \left(\frac{\rho_c}{\rho_m} \right)^{1/2} \right] \qquad (2-3)$$

where v_m and D_{mi} are the initial melt velocity and diameter, respectively, and the overall dimensionless time is easily derived from a one-dimensional momentum balance on the melt mass. The steam production rate is given by an energy balance at the coolant vapor-liquid interface, and hydrogen generated is assumed to be controlled by the rate of steam diffusion to the metallic surface.[4]

$$\dot{N}_{H_2} = \frac{2D_o \Delta P_g}{R_o T_v} \qquad (2-4)$$

where D_o is the mass-transfer coefficient for a stagnant gas $(2D_{H_2}/\Delta)$.[24] As the steam and hydrogen are produced they are added to the gas atmosphere, increasing its temperature and pressure.

A sample calculation was performed using this transient model. The Sandia FITS-1G experiment was chosen because it involved a simulant melt pour (iron-alumina ~ 20 kg) into water in the absence of a steam explosion.[25] The water (44 kg) was initially saturated at the ambient pressure. Because the water mass was small, the water depth was shallow and mixing occurred in the first 100 msec. Figures 2.10 and 2.11 show pressure and water level as a function of time and the amount of steam and hydrogen generated. Notice that the pressure and water level rise as the melt pour continues; after the melt has settled on the interaction chamber base,
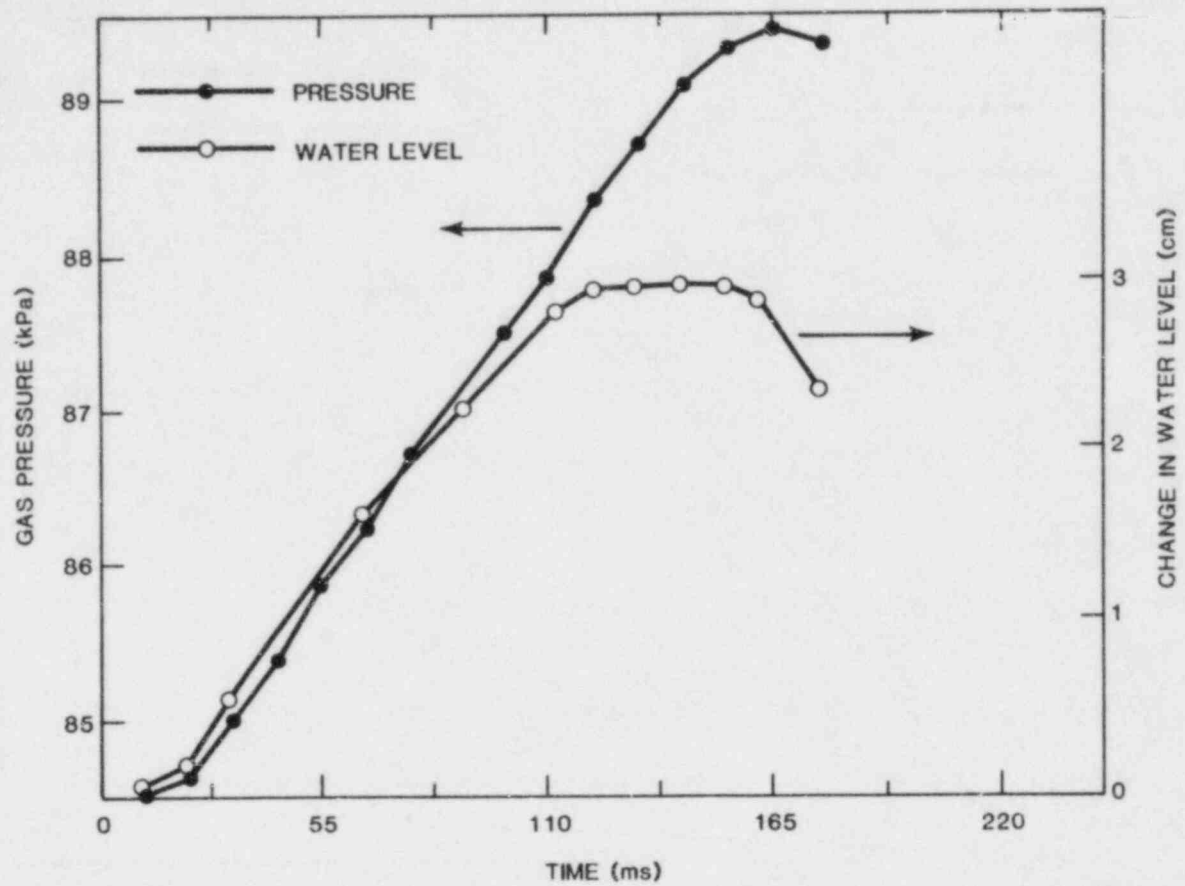
Figure 2.10. Simulation of FITS-1G Test During Fuel Pour
Phase for Gas Pressure and Change in Water
Level vs Time
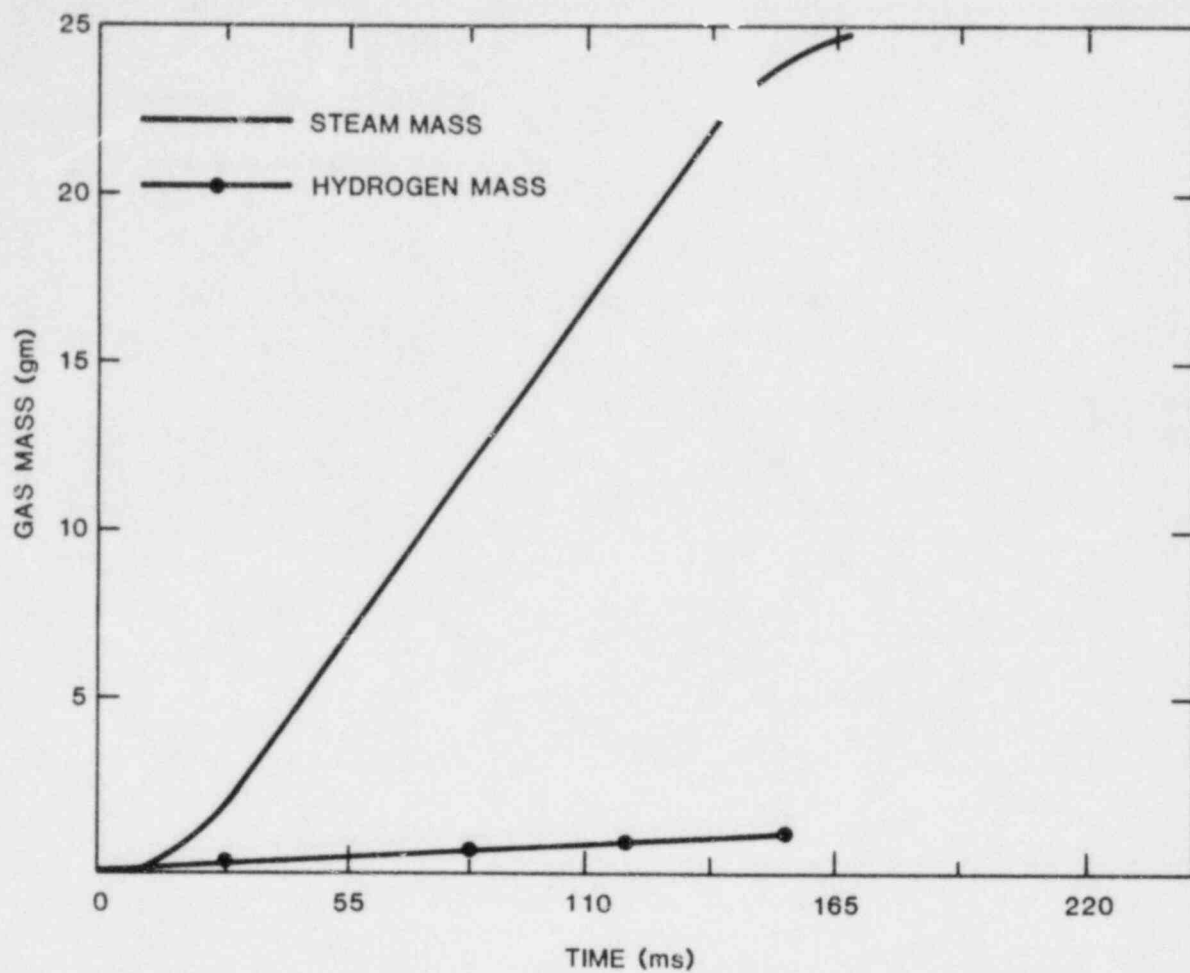
Figure 2.11. Simulation of FITS-1G Test During the Fuel Pour Phase for Gas Mass Produced Due to the FCI vs Time

the water swell height decreases. The amount of steam pro-
duced during the melt fall through the water is much larger
than the hydrogen mass. In fact, for this case, the hydrogen
produced corresponds to less than 1% of the metallic fuel
mass reacted.

This dynamic model for melt-coolant mixing is being developed
to describe the transient process when melt pours into a
coolant pool and breaks apart producing steam and possibly
hydrogen. Sample calculations of the FITS-1G test at Sandia
indicate that in the absence of an explosion, very small
amounts of hydrogen are generated (less than a few percent
of metallic fuel reacted).

2.3.2.1.2 Possible Mechanisms for Melt-Coolant Mixing

Mixing of a melt and coolant in a pouring contact mode can
be divided into isothermal and nonisothermal processes. In
an isothermal process with no heat flow between fluids, the
relative velocity of the fluids is the main factor which,
under certain conditions (e.g., exceeding a critical Weber
number), can cause dispersion of one fluid into another.
The relative velocity leads to instabilities causing dis-
persal of the fluid. Deformation of the fluid is resisted
by surface tension and viscous forces. These hydrodynamic
instabilities can be classified as a Rayleigh-Taylor, or a
Kelvin-Helmholtz instability, or some combination of them.
If the perpendicular component of the relative velocity is
directed from the low to high density fluid, we would ini-
tially induce Taylor instabilities. If a component of the
relative velocity is parallel to the fluid interface, then
Helmholtz instabilities could develop.

In nonisothermal processes in which there is heat transferred
between two fluids, vapor film boiling will be the likely
process at the interface. This vapor film will oscillate
due to local pressure fluctuations as the fuel melt mixes
with the water and cools due to heat transfer. Eventually,
the melt will cool sufficiently so that film collapse will
occur and an energetic interaction may be triggered. These
pressure fluctuations brought on by steam generation may
also contribute to melt-coolant mixing above and beyond what
hydrodynamic instabilities may cause. For example, Fauske
has suggested that the pressurization rate in the mixture
may be quite high due to steam production.[26] This steam
production may aid in breaking up the melt and dispersing it
in the liquid coolant.

Let us first consider hydrodynamic instabilities for the
isothermal situation; heat transfer will be included later.

2.3.2.1.2.1 The Time Constant for the Early Stage of Growth
            of Taylor and Helmholtz Instabilities

From Pennington's analysis [27], the amplitude, η, of the
Taylor instability is related to the time, t, by:

$$\eta \sim \cosh(nt) \tag{2-5}$$

provided that:

(1) Two fluids are of infinite depth and the geometry is
    planar (a reasonable simplification for a large radius
    of curvature)

(2) The initial perturbation is of the form $\cos(kx)$, with
    the amplitude small compared to the wavelength

(3) The fluids are incompressible, and only the linear terms
    in the equations of hydrodynamics are used for the early
    growth phase ($\eta < \lambda$).

In Eq. 2-5, t is the time and n is given by

$$n^2 = \frac{a(\rho_2 - \rho_1)k}{\rho_2 + \rho_1} - \frac{\sigma}{\rho_1 + \rho_2} k^3 \tag{2-6}$$

where a is acceleration, ρ is the density, k is the wave
number, σ is the surface tension, and the subscripts 1 and
2 indicate the low and high density fluids, respectively.

The amplitude of the initial disturbance grows only when
$n^2 > 0$; then

$$\lambda_{crit} = \frac{2\pi}{k_{crit}} \geq 2\pi \left(\frac{\sigma}{a(\rho_2 - \rho_1)} \right)^{1/2} \tag{2-7}$$

where λ_{crit} is the critical wavelength for growth. Thus for
$\lambda > \lambda_{crit}$, there is instability growth. The fastest growing
wavelength is given by

$$\lambda_{max} = \frac{2\pi}{k_{max}} = 2\pi \left(\frac{3\sigma}{a(\rho_2 - \rho_1)} \right)^{1/2} = \sqrt{3} \ \lambda_{crit} \tag{2-8}$$

Substituting this value into Eq. 2-6, we get

$$n^2_{max} = \frac{2}{\sqrt{27}} \frac{[a(\rho_2 - \rho_1)]^{3/2}}{\sigma \ (\rho_2 - \rho_1)} \tag{2-9}$$

The time constant for growth is given by

$$\tau_T \equiv \frac{1}{n_{max}} = \left[\frac{3\sqrt{3}\sigma\,(\rho_2 + \rho_1)}{[a(\rho_2 - \rho_1)]^{3/2}}\right]^{1/2} \tag{2-10}$$

For the Kelvin-Helmholtz instability, the instability will not develop unless the initial wavelength is above a certain threshold given by

$$\lambda_{crit} \geq \frac{2\pi\sigma}{(v_2 - v_1)^2}\left(\frac{\rho_2 + \rho_1}{\rho_2\rho_1}\right) \tag{2-11}$$

where v is the velocity of the fluid parallel to the interface and the subscripts 1 and 2 represent the low- and high-density fluids, respectively.[28] The growth rate parameter is given by

$$n_H \equiv \left|\left(\frac{2\pi^3}{\lambda}\right)\frac{\sigma}{2(\rho_1 + \rho_2)}\right|^{1/2} \tag{2-12}$$

or

$$\tau_H \equiv \frac{1}{n_H} = \left|\left(\frac{\lambda}{2\pi}\right)^3\frac{2(\rho_1 + \rho_2)}{\sigma}\right|^{1/2} \tag{2-13}$$

The actual imposed wavelength on the melt is unknown, but is probably some fraction of the melt mass diameter.

With a spherical shape for the melt falling into the water, the balance of forces gives us

$$\left(\rho_2\frac{\pi D_2^3}{6}\right)a = \frac{\pi}{4}D_2^2 C_D\frac{\rho_1(v_2 - v_1)^2}{2} - \left(\rho_2\frac{\pi D_2^3}{6}\right)g \tag{2-14}$$

where a is the melt mass acceleration (dv_2/dt), D_2 is the melt diameter, and C_D is the drag coefficient. If we take representative values for melt and water from the FITS data:

$$D_2 = 0.13 \text{ m}$$
$$\rho_2 = 3830 \text{ kg/m}^3$$
$$v_2 = 5 \text{ m/s}$$
$$\sigma = 0.5 \text{ N/m}$$
$$\rho_1 = 1000 \text{ kg/m}^3$$
$$v_1 \sim 0$$
$$C_D \sim 1$$

2-47

then, the linear time constant for the growth of Taylor instabilities is approximately 20 ms ($\tau_T = 20$). If one assumes that the initial wavelength is some fraction of the melt diameter (e.g., $\lambda \sim 0.1\ D_2$), then $\lambda \gg \lambda_{crit}$, and it will grow with a time constant of about 15 ms ($\tau_H = 20$). This suggests that both instabilities have approximately the same growth rate for the linear growth phase when $\eta < \lambda$.

2.3.2.1.2.2 The Time Constant for the Long Time Growth of Hydrodynamic Instabilities

The time constants derived in the previous section are only valid when the instability amplitude is less than the initial wavelength, $\eta < \lambda$. When η becomes equal to or greater than λ, then the rate of melt breakup and mixing will decrease (time constant increases). Let us first try to estimate the time constant for breakup based on first principles, regardless of the hydrodynamic mechanism.

We estimate the time needed for the melt to deform and break-up through a distance equal to the melt diameter, D_2. For this deformation we may write, approximately,

$$\rho_2 \frac{dv_D}{dt} \cong \nabla P \tag{2-15}$$

where ρ_2 is the density of melt (high density), ∇P is the pressure gradient causing the acceleration, and v_D is the velocity of deformation. If τ_D is the time taken for the deformation and D_2 is the distance of deformation, then a representative velocity of deformation, v_D, would be given by $v_D \sim D_2/\tau D$. The pressure gradient may be approximated by the peak pressure difference across the melt mass caused by a dynamic pressure divided by the distance of deformation ($\nabla P \sim \Delta P/D_2$). The dynamic pressure difference across the melt droplet is

$$\Delta P \sim \left(\frac{C_D \rho_1 v_2}{2} \right)^2 \tag{2-16}$$

where C_D is the drag coefficient.

When we combine Eqs. 2-16 and 2-15 and our approximation for v_D and ΔP, we get

$$\tau_D \sim \frac{D_2}{v_2} \left(\frac{\rho_2}{\rho_1} \right)^{1/2} \left(\frac{2}{C_D} \right)^{1/2} \tag{2-17}$$

If we use the previous experimental values for the FITS tests, we find that $\tau_D \sim 71$ ms. This characteristic time can be used to nondimensionalize the time of melt-coolant mixing giving

$$T^+ \equiv \frac{tv_2}{D_2} \left(\frac{\rho_1}{\rho_2}\right)^{1/2} \tag{2-18}$$

Notice that this dimensionless time is that used in hydrodynamic droplet breakup experimental correlations for the boundary layer stripping mechanism where it is believed that Helmholtz instabilities dominate (complete droplet breakup occurs between $3 \leq T^+ \leq 6$).[29]

If the melt breakup and mixing are caused by Taylor instabilities, then the characteristic time for deformation, τ_{DT}, is caused by the nonlinear phase of the instability growth when $\eta > \lambda$ and is given by

$$\tau_{DT} \sim D_2/v_T \tag{2-19}$$

where v_T is the Taylor instability nonlinear growth velocity [30] given by

$$v_T \sim 4(a\lambda_{max})^{1/2} \tag{2-20}$$

where a is the acceleration of the melt derived from Eq. 2-14

$$a \sim \frac{3}{4} \frac{C_D}{D_2}\left(\frac{\rho_1}{\rho_2}\right) v_2^2 \tag{2-21}$$

and λ_{max} is the fastest growing Taylor wavelength given by

$$\lambda_{max} \sim 2\pi \left(\frac{3\sigma}{a(\rho_2 - \rho_1)}\right)^{1/2}. \tag{2-22}$$

Substituting the values of Eqs. 2-20 through 2-22 in Eq. 2-19 we get

$$\tau_{D_T} = \frac{D_2}{4(a\lambda_{max})^{1/2}} \tag{2-23a}$$

or

$$\tau_{D_T} = \left(\frac{D_2}{10}\right)\left(\frac{3\sigma v_2^2}{D_2(\rho_2 - \rho_1)}\right)^{-1/4}\left(\frac{\rho_1}{\rho_2}\right)^{-1/4} \tag{2-23b}$$

Again, if we use the previous experimental values for the FITS tests, we find that $\tau_{D_T} \sim 30$ ms. If we rearrange the

expression for this Taylor instability time constant, τ_{D_T}. we get a dimensionless time of

$$t^* \equiv \frac{t}{\tau_{D_T}} \sim \frac{v_2 t}{D_2} \; We^{-1/4} \; \epsilon^{1/2} \left(\frac{\rho_2 - \rho_1}{\rho_2} \right)^{1/4} \qquad (2\text{-}24)$$

where We is the Weber number

$$We \equiv \frac{\rho_1 v_2^2 D_2}{\sigma} \qquad (2\text{-}25)$$

and ϵ is the melt-to-coolant density ratio

$$\epsilon \equiv \frac{\rho_2}{\rho_1}. \qquad (2\text{-}26)$$

Once again, notice that this is a similar dimensionless breakup time to that used for high-Weber-number hydrodynamic fragmentation, where Taylor instabilities are believed to be the dominant breakup mechanism.[29]

Based on these calculations, it appears that for representative FITᶜ experimental conditions, the Taylor instability may grow more rapidly and may be the important mechanism for mixing. This tentative conclusion would be further supported if it is found that FITS mixing data exhibited a better correlation using t* as the dimensionless time rather than T⁺.

2.3.2.2. Triggering Studies

2.3.2.2.1 Analysis of Film Collapse Experiments

When the core melt and liquid coolant become intermixed, the melt temperature is high enough that a stable film boiling is established between the liquid melt and coolant. This allows the melt to break up due to hydrodynamic and boiling forces before triggering and rapid heat transfer begins. It is believed that triggering of the steam explosion is associated with film boiling destabilization and collapse. Recently, "separate effects" experiments have been conducted to investigate the effect of velocity and sphere diameter on the minimum film boiling point during film collapse.[31] In Rezakhany's experiments, a small solid sphere (3 to 8 mm in diameter) at an elevated temperature was moved vertically downward at a predetermined velocity (0 to 200 mm/s) into a quiescent liquid. The temperature history of the solid sphere was measured as it cooled down in film boiling, proceeded through film collapse, and was finally quenched while in transition and nucleate boiling. This temperature record

was translated into a heat flux versus sphere surface temperature (or surface temperature minus fluid saturation temperature) boiling curve; from this, one can identify the minimum film boiling heat flux and corresponding temperature. The independent variables in these experiments were sphere velocity, diameter, coolant composition, and subcooling. These experiments are unique in two ways, compared with past film boiling experiments with spheres, e.g., References 32 and 33. First, they investigate film boiling collapse at Reynolds numbers (0 to 3000), which are characteristic of the terminal velocity of the hot body in the coolant (a situation that is quite likely to occur in steam explosion triggering). Second, the sphere diameter is one of the major variables; in fact, the diameters used are small (3 to 8 mm below the critical Taylor wavelength for gravitational acceleration) and quite characteristic of what may be expected during melt-coolant mixing before triggering occurs.

We are currently reviewing the results of the experiments and trying to apply the data to melt-coolant triggering phenomena. Some results are quite intriguing. First, as the sphere diameter decreases, the minimum film boiling temperature increases. Second, as the characteristic Reynolds number of the falling sphere decreases below some critical value, the minimum film boiling temperature increases. These results in combination suggest that spontaneous film collapse may occur at a temperature higher than previously thought, perhaps partially explaining the spontaneous triggering of steam explosions at high melt temperatures.

2.3.2.2.2 Hydrodynamic Instabilities during Spherical Expansions

During film boiling the pressure in the vapor coolant film can be above the ambient pressure in the liquid coolant. This may occur due to oscillations of the film as the melt droplet cools or during the film collapse when the vapor-liquid interface is decelerated. In either case, the acceleration vector is directed outward from the vapor to the liquid coolant, i.e., from the less dense fluid to the more dense fluid. This condition is hydrodynamically unstable and the Rayleigh-Taylor instabilities will develop. Our current analysis is unique because we consider the spherical Rayleigh-Taylor instability growth in contrast to previous planar instability models.

The model considered here is that of two fluids accelerated radially outward in spherical symmetry. The inner fluid is at a lower density than the outer fluid, causing an unstable situation.[34]

In the first subsection, we consider the simplest case in which the interface between the inner and outer fluid is assumed to be fixed in space and is in the general shape of

a spherical harmonic wave. The acceleration of the fluids is represented by an apparent body force, in a similar manner to planar analyses.[35-38] The second subsection presents a model derivation based on a moving fluid interface. In both of these two subsections, our major assumption is that the amplitude of the instability wave, η, is small compared to the instability wavelength, λ, and the radius of the inter- face; therefore, only the linear terms of the perturbation function in the hydrodynamic equations are used. Also, we initially neglect the effect of viscosity and surface ten- sion; subsequently, the effect of surface tension on the instability is included in the analysis.

2.3.2.2.2.1 Instability on a Stationary Interface

2.3.2.2.2.1.1 No Surface Tension

The interface (neglecting perturbations) is the spherical surface, $r = a$, a is the bubble radius and the r axis is in the radial direction. The initial perturbation will be of the form $Y_\ell^m(\Theta,\phi)$, with amplitude, $\eta_o(a,\Theta,\phi)$, small compared to radius a; $Y_\ell^m(\Theta,\phi)$ is the spherical harmonic function for angles Θ and ϕ. The problem is then three-dimensional and time depen- dent, and the true equation of the interface at any time is $R = a + \eta(r,\Theta,\phi,t)$ where R is the actual interface position and η is to be determined from subsequent analyses.

The density of the fluids may vary in the radial direction, i.e., a function of r, $\rho_0(r)$. Also the acceleration of the fluids may be a function of r, $g(r)$. Let the actual density at any point (r, Θ, ϕ) as a result of a disturbance be $\rho_0 + \delta\rho$, and let δP denote the corresponding perturbation in the pres- sure, P, so that $P = P_0 + \delta P$.

The linearized hydrodynamic equations after small perturbation theory has been applied become

$$\nabla \cdot U' = 0 \tag{2-27}$$

and

$$\rho_o \frac{\partial U_r'}{\partial r} = - \frac{\partial \delta P}{\partial r} + \delta\rho \, g_1(r) \tag{2-28}$$

where $U_r' = - \frac{\partial \phi'}{\partial r}$ is the perturbation velocity of the fluid in the r-direction and g_1 is the acceleration from fluid 1 into fluid 2. The continuity equation is based on the assumption that the density change of a fluid element follow- ing a streamline is zero;[34] i.e.,

$$\frac{d\rho}{dt} = 0 \tag{2-29}$$

or

$$\frac{\partial \delta\rho}{\partial t} = -U_r' \frac{\partial \rho_o}{\partial r} \tag{2-30}$$

$$\delta\rho = -\int U_r' \frac{\partial \rho_o}{\partial r} dt \tag{2-31}$$

Now let us insert Eq. 2-31 into Eq. 2-28 and integrate Eq. 2-28 from the origin of the bubble, for which $r = 0$, $U_r = 0$, and $\delta\rho = 0$. Also let us assume that the radial density gradient is given by

$$\frac{\partial \rho_o}{\partial r} = r^2 \delta(r - a)(\rho_2 - \rho_1) \tag{2-32}$$

where $\delta(r - a)$ is the Dirac delta function $= \begin{cases} \infty & r = a \\ 0 & r \neq a \end{cases}$

and ρ_1, ρ_2 are the fluid densities of the inner and outer fluid, respectively. This mathematically corresponds to a sharp density gradient at the interface. The resulting radial momentum equation becomes

$$\int_0^\infty - \rho_o \frac{\partial \phi'}{\partial t} dr = \int_0^\infty - \frac{\partial \delta P}{\partial r} dr +$$

$$\int_0^\infty \int g_1(r) U_r' \delta(r - a) r^2 (\rho_2 - \rho_1) dt \, dr \tag{2-33}$$

or

$$\rho_2 \frac{\partial \phi_2'}{\partial t} - \rho_1 \frac{\partial \varphi_1'}{\partial t} \Bigg|_a = g_1(a) (\rho_2 - \rho_1) \int_0^+ U_r'(a) \, dt \tag{2-34}$$

and

$$\phi_2' = -C \frac{a^{\ell+2}}{(\ell + 1) r^{\ell+1}} Y_\ell^m(\theta,\phi) f(t) \tag{2-35}$$

$$\phi_1' = C \frac{r^\ell}{\rho a^{\ell-1}} Y_\ell^m(\theta,\phi) f(t) \tag{2-36}$$

where ϕ_1', ϕ_2' are the velocity potentials of the inner and outer fluid, respectively, and $Y_\ell^m(\theta,\phi)$ is the spherical harmonic function. Note that because we have neglected surface tension in this treatment, $\delta P = 0$ at the interface, and substituting for the velocity potential in Eq. 2-34 yields

$$a \frac{\rho_2}{\ell + 1} + \frac{\rho_1}{\ell} \frac{d^2 f(t)}{dt^2} - (\rho_2 - \rho_1) g_1(a) f(t) = 0 \qquad (2\text{-}37)$$

A solution to this differential equation is $f(t) = \cosh(nt)$, which satisfies the initial condition that $U_r' = 1$ at $t = 0$. The value for n^2 is given by

$$n^2 = \frac{(\rho_2 - \rho_1) g_1(a)}{a \left(\dfrac{\rho_2}{\ell + 1} + \dfrac{\rho_1}{\ell} \right)} \qquad (2\text{-}38)$$

The free boundary condition at $R = a + \eta$ is

$$-\left(\frac{\partial \phi'}{\partial r} \right)_a = U_r'(a) \approx \frac{dR}{dt} = \frac{d\eta}{dt} \approx \frac{\partial \eta}{\partial t} \qquad (2\text{-}39)$$

so that

$$\eta(r,\theta,\phi,t) = \frac{C}{n} \cosh(nt) Y_\ell^m(\theta,\phi) \qquad (2\text{-}40)$$

where C is a constant that can be determined by the initial amplitude of the disturbance.

2.3.2.2.2.1.2 Effect of Surface Tension

We now introduce the effect of surface tension into the equations of the previous section. It is to be expected that the presence of surface tension will remove the instability for sufficiently small wavelengths as in the planar case.[36]

To introduce surface tension into the previous equations, we need merely to replace the condition $\delta p|_a = 0$ by

$$(P_o + P)_{a+} - (P_o + P)_{a-} = \sigma \left(\frac{1}{R_1} + \frac{1}{R_2} \right) \qquad (2\text{-}41)$$

where R_1 and R_2 are the principal radii of curvature of the surface,

$$R = a + \eta(r,\theta,\phi,t) \qquad (2\text{-}42)$$

and σ is the surface tension. It has been shown by Lamb [37] that

$$[(\delta P)_{a+} - (\delta P)_{a-}] = \sigma\left(\frac{C(\ell - 1)(\ell + 2)}{a^2} Y_\ell^m(\theta,\phi) \int f(t)dt\right) \quad (2-43)$$

With these corrections for surface tension, the differential equation for f(t) (Eq. 2-37) becomes

$$\left(a \frac{\rho_2}{\ell + 1} + \frac{\rho_1}{\ell}\right) \frac{d^2 f(t)}{dt^2} - $$

$$\left[(\rho_2 - \rho_1) g_1(a) - \frac{\sigma(\ell - 1)(\ell + 2)}{a^2} f(t)\right] = 0 \quad (2-44)$$

so that

$$n = \left[-\frac{(\rho_2 - \rho_1)g_1(a) - \frac{\sigma(\ell - 1)(\ell + 2)}{a^2}}{a\left(\frac{\rho_2}{\ell + 1} + \frac{\rho_1}{\ell}\right)}\right]^{1/2} \quad (2-45)$$

We see from Eq. 2-45 that the amplitude of the initial disturbance grows only when

$$(\rho_2 - \rho_1) g_1(a) - \frac{\sigma(\ell - 1)(\ell + 2)}{a^2} > 0 \quad (2-46)$$

or remember that ℓ is the eigenvalue in the spherical harmonic

$$\frac{2\pi}{\theta_c} = \ell = \left|a^2 \frac{g_1(a)(\rho_2 - \rho_1)}{\sigma} + \frac{9}{4}\right|^{1/2} - \frac{1}{2} \quad (2-47)$$

Therefore, the critical wavelength, λ_{crit}, below which no instability will grow is approximately given by

$$\lambda_{crit} = a \, \theta_c \approx 2\pi / \left(\frac{1}{a^2} + \frac{1}{L^2}\right)^{1/2} \quad (2-48)$$

and L is the Laplace constant given by

$$L^2 \equiv \left|\frac{g_1(a)(\rho_2 - \rho_1)}{\sigma}\right|^{-1} = [length]^2 \quad (2-49)$$

The reader should note that, in the limit as the radius of curvature goes to infinity (a planar geometry), we retrieve the planar expression for the critical Taylor wavelength. Also, as the radius of curvature approaches the Laplace constant, the critical Taylor wavelength decreases, allowing smaller wavelengths to become unstable and grow where they would not grow in a planar geometry. Finally, one finds that the fastest growing wavelength is not a unique constant times λ_{crit} as in planar analyses.

2.3.2.2.2.2 Instability on a Moving Interface (a $\neq$ constant)

Now this analysis considers the case where the interface of the bubble is not fixed. In this case, the acceleration of the bubble will not appear as a body force in Section 2.3.2.2.2.1. We continue to use the assumption as stated in Eq. 2-29. Therefore, the unperturbed equations governing the motion of these inviscid fluids (neglecting surface tension) are

$$\nabla \bullet \bar{U}_r = 0 \tag{2-50}$$

$$\frac{\partial \bar{U}_r}{\partial t} + \frac{1}{2} \frac{\partial U_r^2}{\partial r} = - \frac{1}{\rho_0} \frac{\partial \rho_0}{\partial r} \tag{2-51}$$

where $\bar{U}_r$ is fluid velocity (unperturbed).

Integrating from the surface of the bubble, for which $r = a(t)$, $\bar{U}_a = da/dt$, $P_0 = P_b$, to an infinite distance where $P_0 = P_\infty$ the ambient pressure and $\bar{U}_r = 0$, also $\rho_0 = $ const, gives the Rayleigh Eq. 2-34

$$\frac{d^2 a}{dt^2} = \frac{1}{a(t)} \left(P_b - P_\infty \right) - \frac{3}{2} \left(\frac{da}{dt} \right) \tag{2-52}$$

The shape of the bubble interface in a fluid considering instabilities is again treated using small perturbation theory. The equations of motion can be written as:

$$(\rho_0 + \delta\rho) \frac{\partial(U_r' + \bar{U}_r)}{\partial t} + \frac{1}{2} \frac{\partial(U_r' + \bar{U}_r)^2}{\partial r} + \frac{\partial(P_0 + \delta P)}{\partial r} = 0 \tag{2-53}$$

and

$$\nabla \bullet (\bar{U}_r + U_r') = 0 \tag{2-54}$$

where $\rho_0 + \delta\rho$, $P_0 + \delta P$, and $\bar{U}_r + U_r'$ are the actual density, pressure, and velocity as a result of the disturbance.

Neglecting the squares of disturbance properties and combining with the unperturbed equation (Eq. 2-51), Eq. 2-53 can be simplified to give

$$\rho_o \left(\frac{\partial U_r'}{\partial t} + \frac{\partial U_r' \bar{U}_r}{\partial r} \right) + \delta\rho \left(\frac{\partial \bar{U}_r}{\partial t} + \frac{1}{2} \frac{\partial \bar{U}_r^2}{\partial r} \right) + \frac{\partial \delta\rho}{\partial r} = 0 \qquad (2\text{-}55)$$

or

$$\rho_o \left(\frac{\partial U_r'}{\partial t} + \frac{\partial U_r' \bar{U}_r}{\partial r} \right) = \frac{\delta\rho}{\rho_o} \quad \frac{\partial \rho_o}{\partial r} - \frac{\partial \delta\rho}{\partial r} \qquad (2\text{-}56)$$

And, by Eq. 2-54, we know that

$$\frac{D(\rho_o + \delta\rho)}{Dt} = 0 \qquad (2\text{-}57)$$

or

$$\frac{\partial(\rho_o + \delta\rho)}{\partial t} + (\bar{U}_r + U_r') \frac{\partial(\rho_o + \delta\rho)}{\partial r} = 0 \qquad (2\text{-}58)$$

After simplifying, we obtain,

$$\frac{\partial \delta\rho}{\partial t} + \bar{U}_r \frac{\partial \delta\rho}{\partial r} + U_r' \frac{\partial \rho_o}{\partial r} = 0 \qquad (2\text{-}59)$$

From Eqs. 2-55 and 2-59, we conclude that when $\delta\rho$ is negative and a change in $\delta\rho$ with r is also negative, the perturbations will be unstable, i.e., the instability will grow with time. Since Eq. 2-59 is a partial differential equation, it is unclear if we can solve analytically for the instability growth without some simplifications. Let us assume that the density change ($\delta\rho$) with r due to the perturbation is small, and the mean density of the inner and outer fluid is constant with time. The first assumption appears reasonable if the major density gradient is due to the mean density change across the bubble interface from ρ_1 to ρ_2 where the mean density change with time is not large (only the early expansion phase).

Eq. 2-59 can now be simplified to:

$$\delta\rho \approx - \int U_r' \frac{\rho_o}{r} \, dt \qquad (2\text{-}60)$$

and substituted into Eq. 2-55, and then integrated from r = 0 to r = ∞. After this integration, Eq. 2-55 becomes

$$
- \rho_2 \frac{\partial \phi_2'}{\partial t}\bigg|_a + \rho_1 \frac{\partial \phi_1'}{\partial t}\bigg|_a + \rho_2 U_{r_1}' \bar{U}_{r_1}\bigg|_a - \rho_1 U_{r_2}' \bar{U}_{r_2}\bigg|_a
$$

$$
+ \int_0^\infty \left[-\int U_r' \frac{\partial \rho_o}{\partial r} dt \right] \left[\frac{\partial \bar{U}_r}{\partial t} + \frac{1}{2} \frac{\partial \bar{U}_r^2}{\partial r} \right] dr = 0 \tag{2-61}
$$

where ϕ_2', ϕ_1' are the velocity potentials of perturbation motion outside and inside the bubble, respectively.

$$
\phi_2' = \frac{c \, a(t)^{\ell+2}}{(\ell + 1) \, r^{\ell + 1}} Y_\ell^m(\theta, \phi) f(t) \tag{2-62a}
$$

$$
\phi_1' = - \frac{c r^\ell}{\ell a(t)^{\ell-1}} Y_\ell^m(\theta, \phi) f(t) \tag{2-62b}
$$

and

$$
\phi_2 = \frac{a^2 \frac{da}{dt}}{r} \tag{2-63a}
$$

$$
\phi_1 = \frac{-r^2}{2r} \frac{da}{dt} \tag{2-63b}
$$

If we use the continuity equation (Eqs. 2-54 and 2-60) in conjunction with the simplified momentum equation (Eq. 2-61) and an assumed density function (Eq. 2-32) we get

$$
\left[A \frac{da(t)}{dt} f(t) + B a(t) \frac{df(t)}{dt} \right] +
$$

$$
(\rho_2 - \rho_1) \left[\int \frac{d^2 a(t)}{dt^2} f(t) dt - f(t) \frac{da}{dt} \right] = 0 \tag{2-64}
$$

or

$$
A \frac{d^2 a}{dt^2} f(t) + (A + B - \rho_2 + \rho_1) \frac{da(t)}{dt} \frac{df(t)}{dt} + B a(t) \frac{d^2 f(t)}{dt^2} = 0 \tag{2-65}
$$

where

$$
A \equiv \left(\rho_2 \frac{\ell + 2}{\ell + 1} - \rho_1 \frac{\ell - 1}{\ell} \right) \tag{2-66}
$$

2-58

$$B \equiv \frac{\rho_2}{\ell + 1} + \frac{\rho_1}{\ell} \qquad (2\text{-}67)$$

Now Eq. 2-65 is a second-order nonlinear ordinary differential equation for f(t) (the growth function of the instability), with time-varying coefficients (radius, velocity, acceleration). Therefore, we must numerically integrate this equation simultaneously with Eq. 2-52, which is the Rayleigh growth equation for the bubble to determine the actual growth of the instability. This, along with the effect of surface tension and viscosity, will be considered in terms of film collapse and triggering in the next reporting period.

2.3.2.3 Explosion Propagation and Expansion Analysis

2.3.2.3.1 Criteria for Melt Fragmentation and Possible Mechanisms

A steam explosion is due to a very rapid increase in heat-transfer surface area and results in high-pressure coolant vaporization, shock waves, fine-scale melt debris, and steam and hydrogen generation. The increase in surface area is directly caused by melt fragmentation mechanisms.

We consider three criteria to be of primary importance to aid us in determining the dominant mechanism. They are (1) energy required for fragmentation, (2) the fragmentation time, and (3) the fragmentation area.

2.3.2.3.1.1 Fragmentation Criteria

With respect to melt fragmentation and intermixing, Cho et al. suggested that such processes are governed by the frictional energy dissipation; his model considered a geometric progression of breakup and a constant mixing velocity during each stage of fragmentation. Based on these assumptions, the minimum mixing energy is found to be

$$E_{mix,min} = 1.81 \, \rho_c V_m \left(\frac{V_m^{2/3}}{t_{mix}^2} \right) \left(1 - \frac{R^2}{V_m^{2/3}} \right) \ell n \left(\frac{V_m^{1/3}}{R} \right) \qquad (2\text{-}68)$$

where

ρ_c = coolant density
V_m = initial volume
t_{mix} = total mixing time
R = fragmented particle size (D/2)

If this mixing energy is less than some fraction of the thermal energy of the melt, it can be said that the energy requirement for rapid fine-scale fragmentation is satisfied.

2-59

For the case of progressive mixing with minimum required fragmentation energy, the surface area is seen to increase exponentially.[39] The surface area following the ith stage, A_i, is

$$A_i = A_n \frac{R}{R_o} e^{1.74i} \tag{2-69}$$

where

A_n = final melt surface area
R_o = initial melt size

As the progressive mixing was defined, it implies some sort of coarse premixing preceding the final fine-scale mixing. The key issue is to be able to predict the fuel melt fragmentation size, R.

The corresponding time from the onset of fragmentation until the end of the ith stage, t_i, is

$$t_i = t_{mix} \frac{1 - e^{-1.74i}}{1 - (R/R_o)} \tag{2-70}$$

Comparing the proposed area increase to the time scale, it can be seen that the rapid heat transfer leading to a violent coolant vaporization would occur in the final few fragmentation steps.

Area increase in the observed time span would be formulated according to the postulated fragmentation mechanism.

2.3.2.3.1.2 Possible Fragmentation Mechanisms

We reviewed all the mechanisms proposed in past publications (e.g., Reference 40) and selected four that we believe may be important, though each of them is not complete enough to explain the observed fragmentation process by itself. They are hydrodynamic fragmentation by relative velocities, vapor bubble collapse, fragmentation by internal pressurization, and fragmentation by solidification. A very brief summary of each is given below.

If a molten droplet is subjected to relative velocity-induced surface forces sufficient to overcome the cohesive effects of surface tension, fragmentation of the droplet may occur. The potential to cause breakup can be expressed in terms of the Weber number,

$$We = \frac{\rho_c D V^2}{\sigma} \tag{2-71}$$

where

ρ_c = coolant density
D = droplet diameter
V = relative velocity of droplet
σ = surface tension of droplet

Experimental results show that a fragmentation threshold occurs at a critical value between 10 and 20.

Rayleigh-Taylor instability and Kelvin-Helmholtz instability are believed to be involved in this process. Theofanous suggested that the fastest rate of fragmentation would be by Taylor instabilities and that the breakup time would be proportional to the Weber number.[41]

When a vapor bubble is produced and expands as a result of film destabilization, it will eventually collapse due to condensation, and a high-velocity jet of liquid coolant, directed toward the melt, is formed. The jet of coolant penetrates the melt and rapidly increases the contact area. Subsequent vaporization of liquid coolant beneath the melt surface leads to a high-pressure shock wave and disperses the surrounding melt into the coolant, causing another vapor bubble growth-and-collapse process.[42]

The work potential for fragmentation can be related to some fraction of the bubble energy

$$E_b = \frac{4}{3} R_b^3 [\Delta P] \tag{2-72}$$

where

R_b = the maximum bubble radius
ΔP = pressure difference between the bubble
and the ambient.

It is believed that the surface area of contact between the melt and the jet increases exponentially:

$$A = A_o e^{t/\tau} \tag{2-73}$$

$$\tau = \frac{11}{4} \left(\frac{\rho_f}{\rho_c}\right)^{1/2} \frac{D_o}{V_o} \tag{2-74}$$

where

A_o = the initial surface area of the jet
V_o = jet velocity.

This may give a rapid area increase in a short time scale.

Internal acoustic cavitation within the molten material may be induced by fluctuating pressure waves generated in the melt as a result of oscillatory surface film boiling and attendant film collapse.[43] Two conditions necessary for melt fracture by cavitation are cavitation bubble inception and continued growth. The minimum threshold pressure for melt bubble cavitation is

$$P^{th} = \left[\frac{9.06 \ \sigma^3 / KT}{\left(\frac{1.45 \ N^2 \sigma}{P^{th} M^{3/2} R_O T} \right) - \left(\frac{2}{KT} \right)} \right]^{1/2}$$

(2-75)

where

K = Boltzmann's constant
N = Avogadro's number
M = molecular weight
L = latent heat of vaporization
R_O = gas constant
ρ = liquid density.

In the melt-coolant interaction, rapid quenching of melt leads to surface solidification that may result in a thermal stress-initiated fragmentation process.[44] To determine the fragmentation size, the criterion for the breakup and for the generation of new solid surface area must be known. Although the phenomenon of fracture can be described, the reasons for its occurrence are not adequately understood, and the fracture theories are capable of predicting only crack initiation and not when complete failure occurs. However, at the times of maximum strain-energy density, the thermally induced strain work in the outer shell is approximately the same order of magnitude as the estimated maximum bubble energy. In order to predict the fragmentation size from such energy deposition, a knowledge of the work required to create new solid surface must be assessed in terms of mechanical fracture properties.

Present knowledge of the above mechanisms is not complete enough to predict the relative importance of each mechanism in light of the three proposed criteria. Some of them may need more consideration before a choice is made or if further modelling is deemed necessary.

2.3.2.3.2 Thermodynamic Model for Explosion Work

The melt-coolant mixture can produce high-pressure steam when undergoing a steam explosion, and this can do work against its surroundings and may cause structural damage or

generate missiles. Our ultimate objectives for the propagation and expansion of steam explosions are to provide information about the damage potential to the nuclear reactor, debris size, and gas generation rates. Initially we are investigating the explosion work potential.

There are three basic models from which the expansion work potential from a steam explosion can be estimated: (1) the thermodynamic explosion model, (2) the one-dimensional model, and (3) the two-dimensional model.

The thermodynamic approach does not take into account any of the rate processes involved. This explosion model estimates the maximum work potential available from a CMCI, and this corresponds to the upper bound of the work potential from a steam explosion.

We can consider two kinds of thermodynamic work potential models: one in which high-pressure coolant expands to a specified ambient pressure and another in which high-pressure coolant expands to a specified volume. Past work has considered this latter case in terms of explosion work potential.[45] We, therefore, concentrate on the former with auxiliary calculations done for the latter.

2.3.2.3.2.1 Fixed Ambient Pressure Model

Suppose the melt-coolant interaction occurs in an idealized process, where we assume the following for convenient analysis.

(1) All the heat lost by the melt during the process is transferred to the coolant.

(2) Liquids are incompressible.

(3) The specific volume of liquid is negligible compared with that of the vapor.

(4) The vapor behaves as a perfect gas.

(5) The specific heat and latent heat are constant.

(6) The volume of melt does not change during the process.

Consider a two-stage process where subprocess I is thermal transfer from melt to coolant at constant volume. Suppose that the mass of coolant, m_c, at the absolute temperature, T_c, mixes intimately with the mass of melt, m_m, at the absolute temperature, T_m, and thermal equilibrium is established instantaneously.

Choose as the system the mixture of melt and coolant. By the first law of thermodynamics for the system during the adiabatic and constant volume subprocess and neglecting potential and kinetic energy changes, we obtain

$$\Delta U = \delta Q - \delta W = 0 \qquad (2-76a)$$

where ΔU is the change in internal energy, δQ is the heat transport, and δW is work output.

$$\left(m_c C_{v_c} + m_m C_{v_m} \right) T_e - \left(m_c C_{v_c} T_c + m_m C_{v_m} T_m \right) = 0 \qquad (2-76b)$$

or, rearranging,

$$T_e = \frac{m_c C_{v_c} T_c + m_m C_{v_m} T_m}{m_c C_{v_m} + m_m C_{v_m}} \qquad (2-77)$$

where

m_c = coolant mass

C_{v_c} = coolant liquid specific heat

m_m = melt mass

C_{v_m} = melt specific heat

T_e = the equilibrium temperature

From the thermodynamic state equation, we obtain the entropy of equilibrium state, S_e:

$$dS = \frac{C_v}{T} dT + \left(\frac{\partial p}{\partial T} \right)_v dV \qquad (2-78)$$

$$S_e = S_1 + C_v \ln \frac{T_e}{T_1} \qquad (2-79)$$

Now we can obtain the quality and the pressure of the equilibrium state from the steam tables, using the specific volume and the entropy of the equilibrium state.

Subprocess II: Isentropic expansion of melt-coolant mixture in thermal equilibrium (adiabatic, reversible process). Suppose the melt-coolant mixture expands in a reversible and

adiabatic manner to get the maximum work potential (Figure 2.12) where P_0 is the ambient pressure and ΔV_{sys} is the change change in system volume.

The total energy of the system and the environment is conserved during the whole process:

$$\Delta E^* = 0$$

where

$E^* \quad$ = total energy

$\Delta E^* \quad = \Delta E_{sys} + \Delta E_{env} = 0$ (2-80)

$\Delta E_{sys} = \Delta U + \Delta KE + \Delta PE$ (2-81)

$\Delta E_{env} = P_0 \, \Delta V_{sys}$ (2-82)

and subscript env stands for the environment.

By substituting we get

$$0 = \Delta U + \Delta KE + \Delta PE + \Delta P_0 \Delta V_{sys} \tag{2-83}$$

Suppose the time-variation of each energy term involved during the process is as qualitatively depicted in Figure 2.13.

From the thermodynamic analysis, we have defined

$$\Delta W_{sys} = -\Delta U = \Delta KE + \Delta PE + P_0 \, \Delta V_{sys} \tag{2-84}$$

The actual work, which can damage the surrounding structure at any time, is the kinetic energy; however, we cannot calculate this from this thermodynamic analysis. Therefore, the ΔW_{sys} calculated should be viewed as an upper bound of the actual work potential.

First consider the case where the whole expansion process is within the saturation region.

$$\Delta W_{sys} = m_m \, \Delta U = -\Delta(m_c U_c + m_m U_m) \tag{2-85}$$

From the thermodynamic state principle for the mixture

$$T_{mix} d S_{mix} = d h_{mix} - v_{mix} d P_{mix} \tag{2-86}$$

where we define the mixture enthalpy to be

$$h_{mix} = \frac{m_c C_{p_c} T + m_c x h_{f_{g_c}} + m_m C_{p_m} T}{m_c + m_m} \tag{2-87}$$
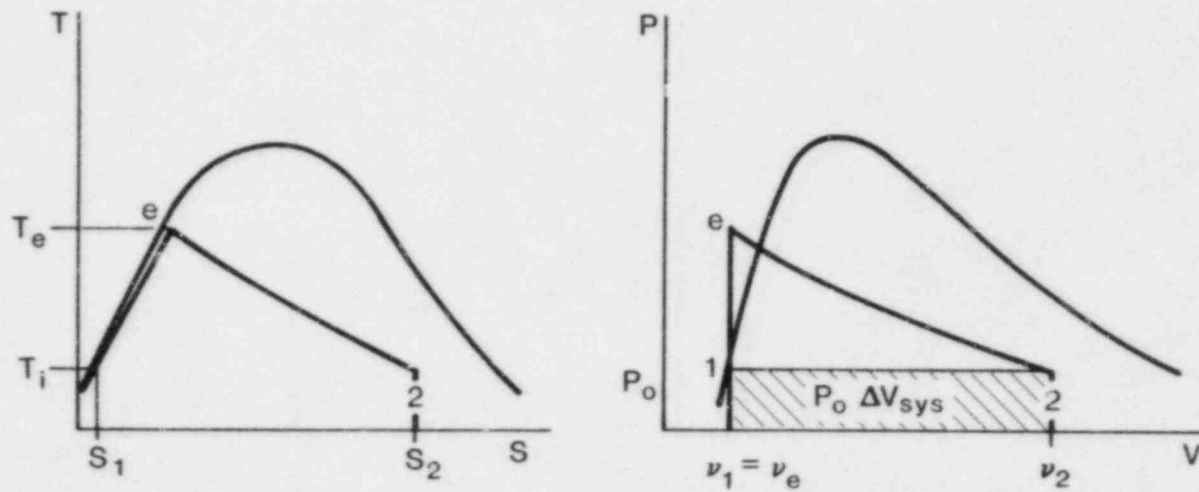
SUB-PROCESS 1 - e: CONSTANT VOLUME PROCESS

SUB-PROCESS e - 2:   EXPANSION PROCESS

Figure 2.12.   T-S Diagram and P-V Diagram for Coolant
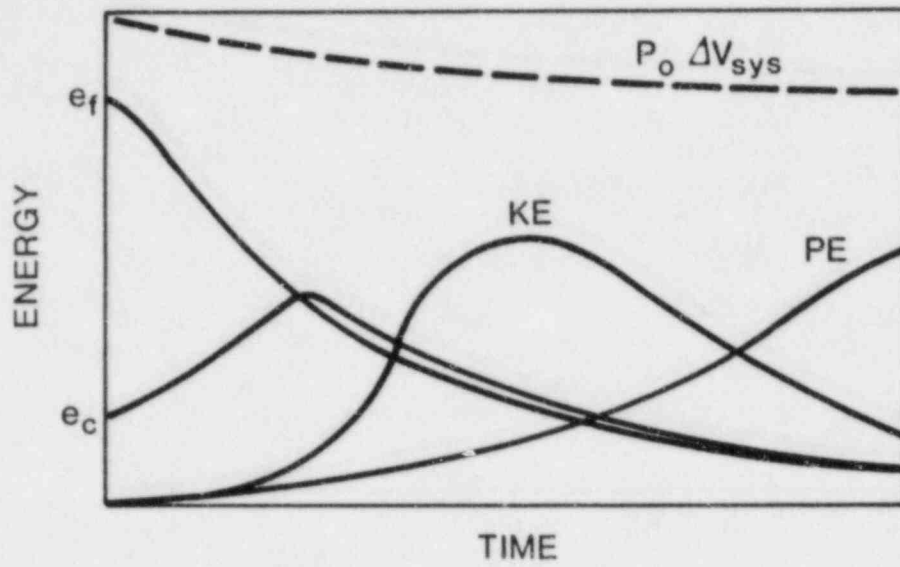
Figure 2.13. Energy Partition during the Steam Explosion

where C_p is the constant pressure specific heat, x is the steam quality, and $h_{f_{g_c}}$ is the enthalpy required to convert saturated liquid coolant to saturate vapor. By differentiating

$$dh_{mix} = \frac{\left(m_c C_{p_c} + m_m C_{p_m} \right) dT + m_c h_{f_{g_c}} dx}{m_c + m_m} \quad \ldots \quad (2\text{-}88)$$

Using the simplification for the mixture volume, one obtains

$$v_{mix} = \frac{x\, m_c v_{g_c}}{m_c + m_m} = \left(\frac{xRT}{p} \right)\left(\frac{m_c}{m_c + m_m} \right) \quad (2\text{-}89)$$

Using the Clausius-Clapeyron equation,

$$dp_{mix} = \left(\frac{dp}{dt} \right)_{\substack{sat \\ coolant}} \qquad dT = \frac{p h_{f_{g_c}}\, dT}{R_c T^2} \quad (2\text{-}90)$$

Substituting Eqs. 2-88 through 2-90 into Eq. 2-87, one obtains

$$\left(m_c C_{p_c} + m_m C_{p_m} \right) \frac{dT}{T} + m_c h_{f_{g_c}}\, d\left(\frac{x}{T} \right) = 0 \quad (2\text{-}91)$$

Integrating this result between the equilibrium and the final states:

$$\left(m_c C_{p_c} + m_m C_{p_m} \right) \ell n\, \frac{T_2}{T_e} + m_c h_{f_{g_c}} \left(\frac{x_2}{T_2} \right) - m_c h_{f_{g_c}} \left(\frac{x_e}{T_o} \right) = 0 \quad (2\text{-}92)$$

or

$$x_2 = T_2 \left[\frac{x_e}{T_e} + \left(\frac{m_c C_{p_c} + m_f C_{pf}}{m_c h_{f_{g_c}}} \right) \ell n\, \frac{T_e}{T_2} \right] \quad (2\text{-}93)$$

Next, consider only the portion of the expansion process in which the coolant state is a superheated state.

From Eq. 2-88, one obtains

$$dh_{mix} = \frac{\left(m_c C_{p_{vc}} + m_m C_{p_m}\right) dT}{m_c + m_m} \tag{2-94}$$

where $C_{p_{vc}}$ is the specific heat of the coolant vapor, and from Eq. 2-89,

$$v_{mix} = \left(\frac{RT}{P}\right)\left(\frac{m_c}{m_c + m_m}\right) \tag{2-95}$$

and from Eq. 2-90, obtain

$$dp_{mix} = dp_{coolant} \tag{2-96}$$

Substituting Eqs. 2-94 through 2-96 into Eq. 2-87, one obtains

$$\left[\frac{m_c C_{p_{vc}} + m_f C_{p_f}}{m_c R_c}\right] \frac{dT}{T} = \frac{dp}{p} \tag{2-97}$$

Integrating this result from the saturated vapor (when x = 1) or the superheated state to the known final superheated state, one gets

$$T_2 = T\left(\frac{p_2}{p}\right)^{1/n} \tag{2-98}$$

where

$$n = \frac{m_c C_{p_{vc}} + m_m C_{p_m}}{m_c R_c} \tag{2-99}$$

Now consider the four types of path that can occur during the process. For the coolant, draw the T-s diagram (Figure 2.14).

From Figure 2.13, we have:

      path 1:   equilibrium state e :   saturation region
                    final   state 2 :   saturation region

      path 2:   equilibrium state e :   saturation region
                    final   state 2 :   superheated region
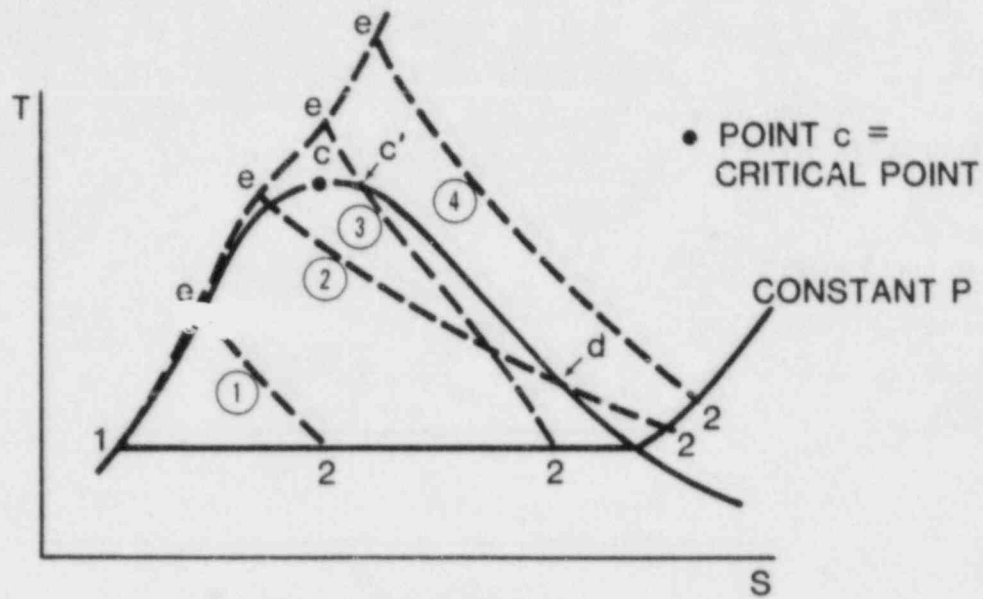
Figure 2.14. Coolant Process Paths

path 3:   equilibrium state e :   superheated region
           final   state 2 :   saturation region

path 4:   equilibrium state e :   superheated region
           final   state 2 :   superheated region

In the cases of paths 1, 2, and 4, the explosion work poten-
tial can be obtained from the previous analysis. In the
case of path 3, we must determine the point c' during the
process. When the point c' is located at the left side of
the critical point, we can think of this path as a combina-
tion of path 4 and path 1. When the point c' is located at
the right side of the critical point, we search for point c'
to satisfy Eq. 2-98 and the saturation vapor point condi-
dition. Again, we think of this path as a combination of
path 4 and path 1 ($x = 1$), and then we can get the system
work, ΔW_{sys}. For example, consider the path 2

$$\Delta W_{sys} = - \Delta U = - \Delta(m_c U_c + m_m U_m) =$$

$$m_c [C_{vc}(T_e - T_d) + x_e (h_{fg} - pv_{fg})_e - (h_{fg} - pv_{f_g})_2] +$$

$$m_m C_{vm}(T_e - T_d) + (m_c C_{vvc} + m_m C_{vm})(T_d - T_2) \qquad (2\text{-}100)$$

where T_d is the temperature corresponding to $X_d = 1$.

Conversion ratio is usually defined as the ratio of the work
measured experimentally to the melt internal energy. In
that case, work was considered as the kinetic energy of
water-debris slug (for FITS tests) and calculated by using
the impulse delivered to the chamber.

$$W = m \frac{V^2}{2} = \frac{I^2}{2m} \qquad (2\text{-}101)$$

where

$$m = m_c + m_m$$

so the conversion ratio was expressed by

$$CR = \frac{I^2}{2(m_c + m_m)} \; / \; m_m c_m (T_m - T_{ref}) \qquad (2\text{-}102)$$

In our thermodynamic model we calculate the conversion ratio
by using the work damage potential at the end of the expan-
sion

$$CR = \frac{\Delta W_{sys}}{m_f c_f (T_f - T_{ref})} = \frac{\Delta KE + \Delta PE + p_o \Delta V_{sys}}{m_f c_f (T_f - T_{ref})} \qquad (2\text{-}103)$$

Because we do not know the partition of each term in ΔW_{sys}, this is the maximum work output.

2.3.2.3.2.2 Fixed Volume Model

Suppose the melt-coolant interaction occurs through the fixed volume process. Melt and coolant mix nd expand instantaneously within the reactor vessel with a fixed volume.

In this case, we are interested in the final pressure of the system, which might damage the structure by overpressure when the explosion occurs. The same assumptions are considered as those of the previous case. The system has no heat transfer with the environment, and no work is done against the environment.

From the first law one gets

$$m_m c_m (T_m - T_{ref}) + m_c (U_{ci} - U_{ref}) =$$

$$m_m c_m (T_e - T_{ref}) + m_c (U_{ce} - U_{ref}) \ldots \qquad (2\text{-}104)$$

where

T_m = fuel temperature of initial state

T_e = system temperature of final state

U_{ci} = coolant internal energy of initial state

U_{ce} = coolant internal energy of final state

When the final state is in the saturation region, one obtains

$$m_m c_m (T_f - T_e) = m_c [C_{p_c}(T_e - T_i) + x_e U_{f_{g_e}} - x_i U_{f_{g_i}}]) \qquad (2\text{-}105)$$

When the final state is in the superheated region,

$$m_m c_m (T_f - T_e) = m_c [C_{p_{vc}} T_e - C_{p_c} T_i - x_i U_{f_{g_i}}] \qquad (2\text{-}106)$$

The temperature and the pressure of the final state are obtained from the above equations by a trial and error iteration method using a computer subroutine package of the steam tables. One can define the specific volume of the system as

$$V = \frac{V_R - V_m}{m_{c_{liq}} + m_{c_{vap}}} \qquad (2\text{-}107)$$

where

V_R = reactor vessel free volume

V_m = fuel volume

$m_{c_{liq}}$ = initial mass of coolant

$m_{c_{vap}}$ = initial mass of steam in the system

$m_{c_{vap}}$ is negligibly small compared to $m_{c_{liq}}$ at the initial state. Then

$$v \doteq \frac{V_R - V_m}{m_{c_{liq}}} \qquad (2-108)$$

For our calculation, we can select the initial conditions. At the initial state, the system is composed of melt, water, and steam; steam in the mixture is assumed to be 50% by volume and

m_m = 15000 kg

P_i = 5 MPa

V_R = 50 ~ 150 m^3

Figures 2.15 and 2.16 illustrate the thermodynamic model results for a constant ambient pressure expansion under the specific conditions of an isentropic mixture and coolant expansion. Notice that, because the isentropic mixture expansion allows thermal equilibrium between the core melt and coolant during expansion, the work output is larger. Also, notice the large contribution from the $p_o \Delta V$ work term. Figure 2.17 illustrates the maximum quasi-static pressure generated from the explosion for a constant final volume. In this case, as the mass of coolant increases, the maximum quasi-static pressure goes through a maximum and decreases substantially as m_c/m_m becomes large.

2.3.2.3.3 Material Properties for Melt-Coolant Interaction Analysis

We are currently performing modelling and analysis of CMCIs. It includes calculation of the work output during steam explosion, condition for triggering, mixing phenomena, etc. In order to carry out the above calculations, we need thermophysical and transport properties of melt, coolant, and structural materials at high temperature. These values are not readily available, especially for the molten state. So we are trying to collect this data from various references. If they do not experimentally exist, we plan to estimate
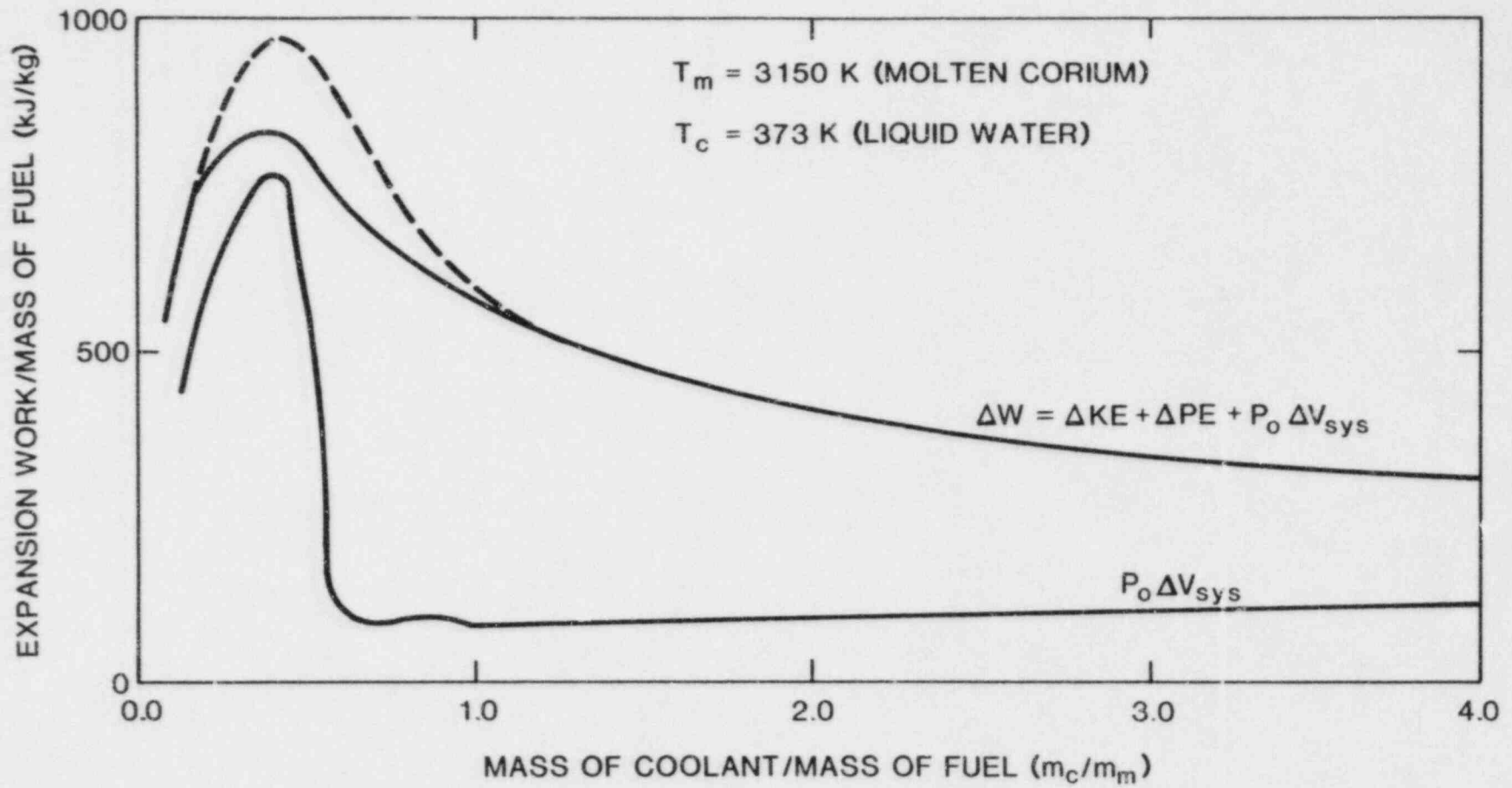
Figure 2.15. Isentropic Mixture Expansion to Atmospheric Pressure
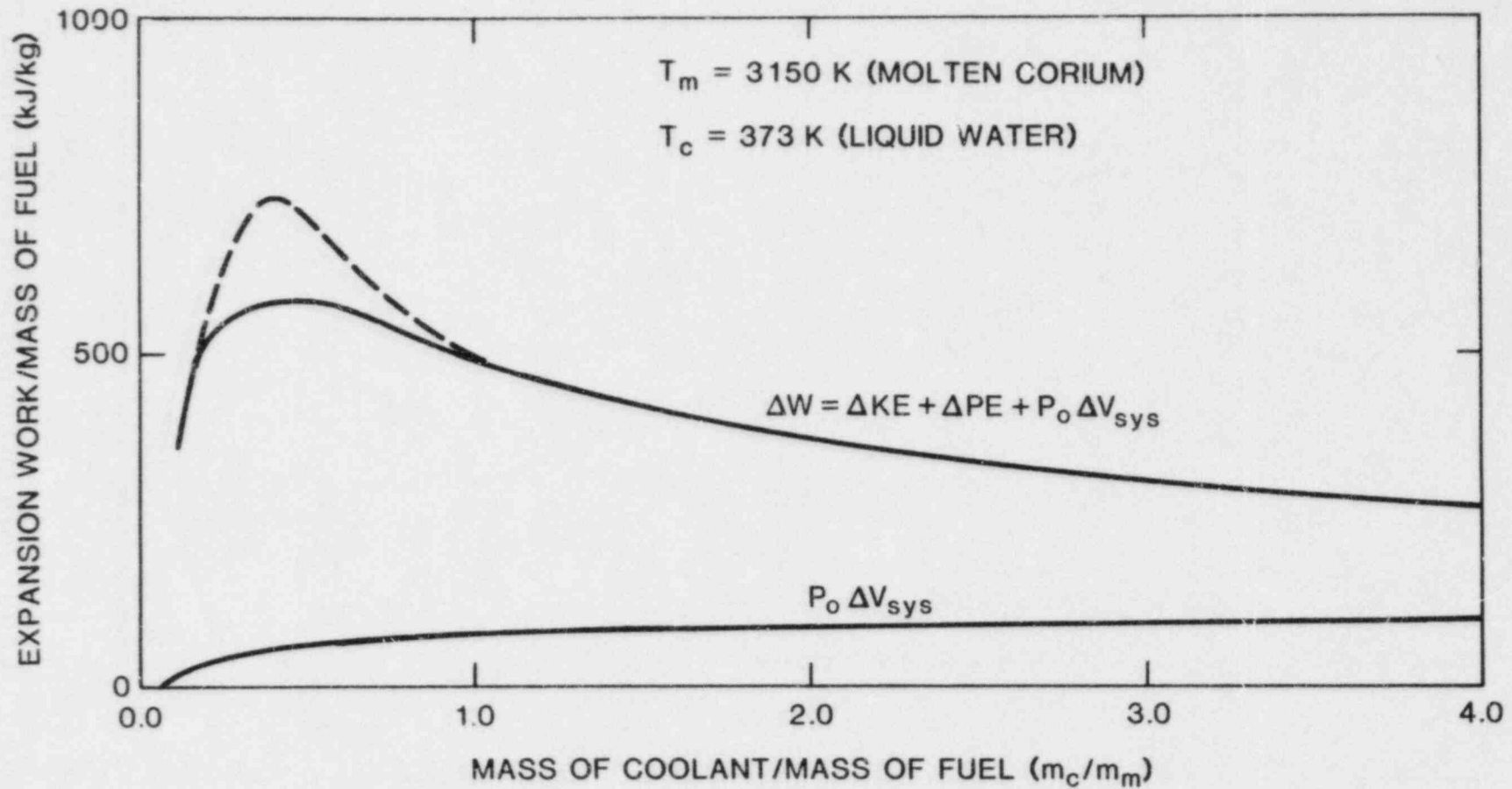
Figure 2.16.   Isentropic Coolant Expansion to Atmospheric Pressure
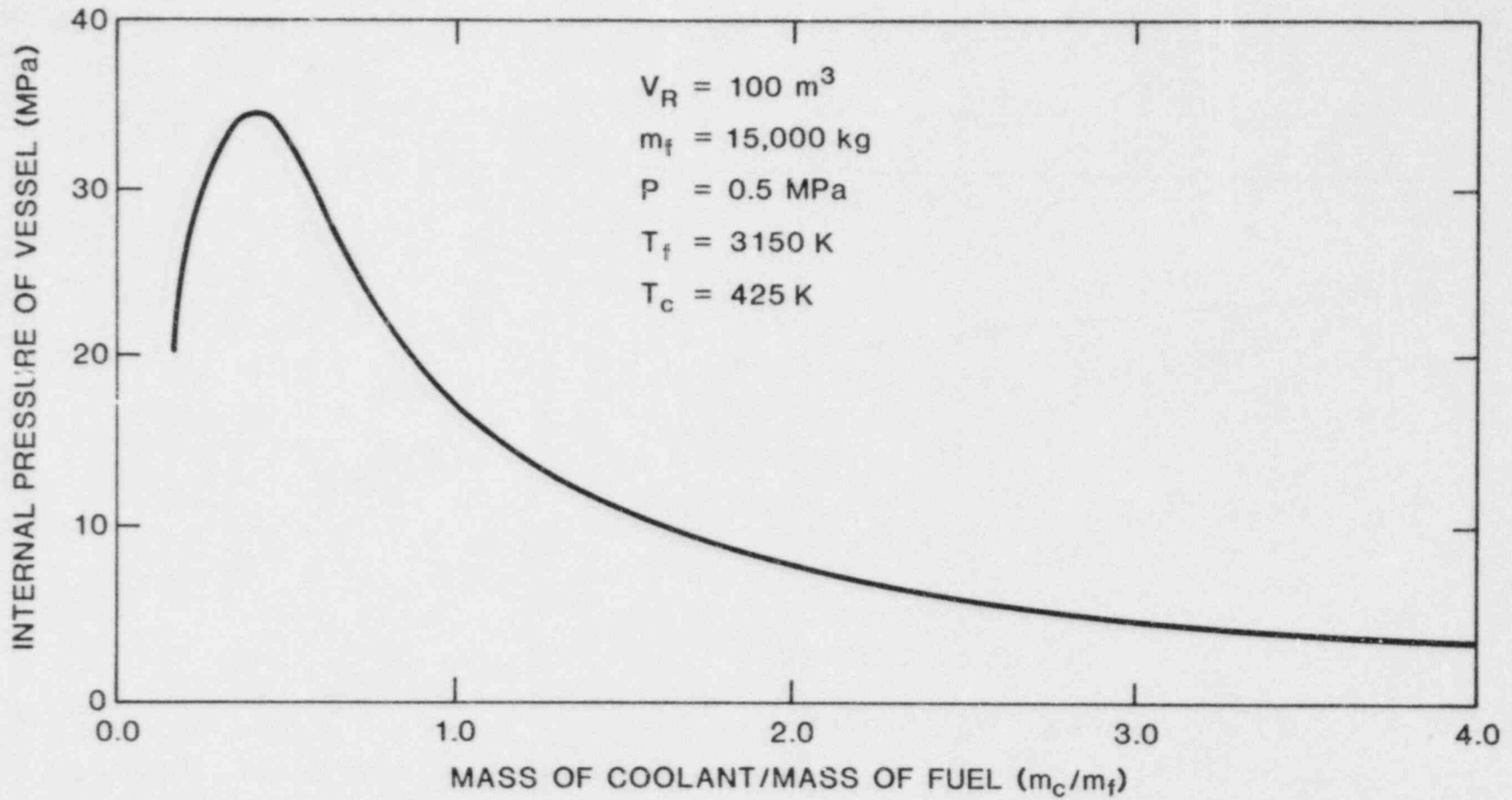
Figure 2.17. Pressure Generated for a Constant Final Volume

Chart annotations:

INTERNAL PRESSURE OF VESSEL (MPa) — y-axis (0 to 40)

MASS OF COOLANT/MASS OF FUEL (m_c/m_f) — x-axis (0.0 to 4.0)

$V_R = 100 \text{ m}^3$

$m_f = 15,000 \text{ kg}$

$P = 0.5 \text{ MPa}$

$T_f = 3150 \text{ K}$

$T_c = 425 \text{ K}$

them. This work will also be useful for preparing experiments regarding CMCIs.

Table 2.8 shows the properties that have been collected so far. Values near and above the melting point are tabulated as far as temperature dependent properties are concerned.

2.3.3 Wavecode Analysis of a Steam Explosion
(J. M. McGlaun and N. A. Evans)

2.3.3.1 Introduction

The wavecode CSQII has been used to analyze an intermediate-scale experiment, FITS 9B, which involved dropping 18.7 kg of molten iron-alumina into water with a coolant-to-melt-mass ratio of 9. The water was in a clear lucite vessel (0.61 m square with an initial water depth of 0.46 m), positioned on a stand inside the FITS chamber. This arrangement allowed high-speed photographic observation (through side ports) of the melt-coolant interaction, control of the ambient pressure and cover gas material, and the collection of all explosive debris for analysis. Three fast-response pressure transducers were installed on the coolant vessel base at radii of 0.178 m from the center and at successive angles of 120°. Two similar transducers were mounted on two sides of the lucite vessel, 0.229 m above the base. Another pressure transducer was mounted in the upper head of the FITS chamber.

The photographs showed the melt entering and mixing with the water, with the explosion triggered at the point where the melt-coolant mixture contacted the base of the water vessel. Time-of-flight measurements, using a fragment of the ruptured coolant vessel as a tracer, indicated a water speed of approximately 95 m/s occurred within approximately 5 ms of triggering the explosion.

2.3.3.2 Numerical Simulation of Early Time Phenomena

The initial geometry was determined from the photographs at the time of explosive initiation. The measured water level swell and melt volume allowed determination of the average coolant density in the mixing region. The geometry is not unique because the three-dimensional configuration had to be approximated with a two-dimensional axisymmetric configuration. This mixing region was assumed to consist only of two-phase water. The low-strength lucite vessel was not included in the calculation. The vessel's supporting stand was modeled as rigid. The boundary of the computational mesh approximated the boundary of the FITS chamber. Approximately 0.01-m-square zones were used in the neighborhood of the water. The zone lengths and heights increased at larger radial and axial distances.

Table 2.8

Properties of Melt Components

	Melting Temp K	Boiling Temp K (0.1 MPa)	Heat of Fusion cal/g	Heat of Vaporiz cal/g (0.1 MPa)	C_p cal/g·K	Linear Expansion Coefficient x 10^5/K	Surface Tension dyne/cm	Thermal Conduct W/m·K	Emissivity E	Viscosity cp	Density g/cm^3
Fe	1810	3023	65	1862	0.19* / 0.197*	1.19	1628	42.5	0.6 / 0.346	6.56	7.1 / 6.8
Cr	2123	2945	62.1	1813	0.26 / 0.18	1.33	1515	63	0.4		6.46 / 7.78
Ni	1728	3005	71.5	1500	0.145 / 0.175	1.84	1650	75.6	0.2 / 0.34	4.1	5.6
Zr	2141	4650	60	1655	0.08 / 0.088	0.93	1457	31.5	0.3	5.45	
ZrO$_2$	2963	4573	168.8	1240	0.23 / 0.17	2.0		2.3	0.5		
SS-304	1700	3080	63.9	1770	0.16 / 0.19	2.25 / 3.313		340 / 178		6.416	0.2 / 6.9
SS-316	1700	3090	65.2	1800	0.16 / 0.19	2.256 / 3.076	450	344 / 180		6.416	7.3 / 7.0
UO$_2$	3138	3760	66.2	405	0.167 / 0.12	1.48 / 3.12	584	3.66 / 3.11	0.87 / 0.84	4.3 / 4.01	9.7 / 8.8
FeO	1641	2700	107.2	790	0.212 / 0.226	1.52					
Fe$_3$O$_4$	1811		142.5		0.21						
Fe$_2$O$_3$	1835				0.22 / 0.21						
Cr$_2$O$_3$	2573	3273	27.6		0.21 / 0.247				0.7		
NiO	2230		12	111	0.23						

When two values are listed, the first is quoted at the melting temperature for the liquid; the second, above the melting temperature by a couple hundred degrees Kelvin if known.

The rapid energy transfer driving the steam explosion was simulated with the high-explosive model in CSQII. This model requires the propagation speed of the detonation front, width of the front and energy deposited across the front. The photographs did not clearly show the propagation of the explosion in this experiment. A 300-m/s propagation speed had been measured in previous similar experiments and was used in the calculation. The other two parameters for the high-explosive model were inferred from the experimental records and refined in a series of calculations. A front width of 0.4 m and an energy deposition rate of 85 kJ/kg were used. The maximum coolant velocity of 100 m/s agreed well with the experimental value of 95 m/s. The somewhat poorer agreement between code and experimental pressure values at transducers 4 and 5 located on the sides of the lucite vessel was partially attributed to the influence of the lucite wall and the lack of adequate zoning.

2.3.3.3 Numerical Simulation of Late Time Phenomena

The calculation with the refined initial conditions was continued to 30 ms to determine the energy distribution among the FITS chamber contents. The maximum calculated kinetic energy of the water was approximately 1 MJ and of the air was 0.16 MJ. Much of the kinetic energy of the water was directed radially rather than axially. If it is assumed that:

(1) the liquid water remains a liquid,

(2) none of the two-phase water used to approximate the mixture condenses,

(3) the steam and air are at the same temperature and pressure,

then the pressure measured at the top of the FITS chamber indicates only 10.1 to 14.1 MJ of energy remain in the steam and air in the 30 to 500-ms time range. The rest of the energy has transferred to the liquid water and experimental apparatus.

2.3.3.4 Summary

The two-dimensional wavecode CSQII was used to successfully simulate the FITS-9B steam explosion experiment. This analysis concluded that 17 MJ of the 52-MJ melt energy participated in the explosion process. The remainder of the melt energy is transferred to the surroundings over a longer time scale. Good agreement was observed between measured and calculated pressure profiles and water velocities. The maximum calculated kinetic energy of the water was approximately 1 MJ. Analysis of late time data indicates that less than

one-third of the melt energy is transferred to the steam and air prior to 0.5 s. This energy controls the late time pressure in the chamber.

2.3.4 Monte Carlo Analysis of In-Vessel Steam Explosions
(D. V. Swenson and A. J. Wickett)

An in-vessel steam explosion occurring during a core-melt accident could generate missiles which could fail containment, releasing radioactivity.

In October 1981, a SAND report entitled "Monte Carlo Analysis of LWR Steam Explosions" was issued. The report described a probabilistic assessment of steam explosions and concluded that the probability of containment failure was small. This report has initiated considerable discussion, both with regard to uncertainties associated with the stated probability and the philosophy of how to approach this very ill-defined problem. Because the report is impacting decisions with respect to steam explosions, we decided to redo the analysis using the same approach but updatin⁻ the input distributions, making some changes to the model, nd performing a more consistent uncertainty evaluation. Work on this reanalysis is now in progress.

2.4 References for Section 2

1. N. C. Rasmussen, Reactor Safety Study; An Assessment of Accident Risks in U. S. Commercial Nuclear Power Plants, WASH-1400, NUREG 75/014, October 1975.

2. M. Berman, Light Water Reactor Safety Research Program Quarterly Reports, Sandia National Laboratories, Albuquerque, NM, NUREG/CR2163, January-March 1981; NUREG/CR-2481, April-September 1981.

3. M. J. Bird, "Thermal Interactions Between Molten Uranium Dioxide and Water: An Experimental Study Using Thermite Generated Uranium Dioxide," HTD - Vol. 19, ASME Winter Meeting, Washington, DC, November 1981.

4. M. L. Corradini, "Phenomenological Modelling of the Triggering Phase of Small-Scale Steam Explosion Experiments" Nuclear Science and Engineering Vol. 78, pp. 154-170, (1981).

5. L. S. Nelson and P. M. Duda, Steam Explosion Experiments with Single Drops of Iron-Oxide Melted in a CO_2 Laser, Sandia National Laboratories, Albuquerque, NM, NUREG/CR-2295, 1981.

6. M. L. Corradini, D. E. Mitchell, and L. S. Nelson, "Recent Experiments and Analysis Regarding Steam Explosions with Simulant Molten Reactor Fuels," HTD - Vol. 19, ASME Winter Meeting, Washington, DC, November 1981.

7. D. E. Mitchell and N. A. Evans, The Effect of Water to Fuel Mass Ratio and Geometry on the Behavior of Molten Core-Coolant Interactions at Intermediate Scale, International Meeting on Thermal Nuclear Safety, ANS/ENS, Chicago, IL, August 1982.

8. Memorandum from L. S. Tong to R. B. Minogue, Technical Review Meeting on Steam Explosion, May 24, 1982.

9. J. B. Rivard, "Modeling of LWR Coolant Systems During Severe Accidents: MELPROG Perspectives," Sandia National Laboratories, Albuquerque, NM, unpublished data.

10. M. Berman, "Light Water Reactor Safety Research Semi-annual Report," Sandia National Laboratories, Albuquerque, NM, April-September 1982, NUREG/CR-3407 (SAND83-1576).

11. R. E. Henry and H. K. Fauske, "Required Initial Conditions for Energetic Steam Explosions," HTD - Vol. 19, ASME Winter Meeting, Washington, DC, November 1981.

12. T. G. Theofanous, M. Saito, and R. Viskanta, LWR and HTGR Coolant-Dynamics: The Containment of Severe Accidents, NUREG/CR-2318, October 1981.

13. L. D. Buxton, Molten Core-Water Contact Analysis, Sandia National Laboratories, SAND77-1842, 1979.

14. W. B. Murfin, Editor, Report of the Zion/Indian Point Study: Vol. 1, Sandia National Laboratories SAND80-0617/1; NUREG/CR-1410, (1980).

15. J. F. Meyer et al, Preliminary Assessment of Core Melt Accidents at the Zion and Indian Point Nuclear Power Plants and Strategies for Mitigating Their Effects, NUREG-0850, Vol. 1, USNRC Report 1981.

16. G. Klopp et al, Zion Probabilistic Safety Study, Commonwealth Edison Co., 1981.

17. R. E. Henry et al, "Establishment of a Permanently Coolable State," Trans. Am. Nucl. Soc, 39, 368 (1981).

18. H. K. Fauske, "Some Aspects of Liquid-Liquid Heat Transfer and Explosive Boiling," Proc. Fast Reac. Safety Mtg., Beverly Hills, CA (1974).

19. R. E. Henry and H. K. Fauske, "Nucleation Characteristics in Physical Explosions," Proc. of Third Spec. Mtg. on Sod. Fuel Int. in Fast Reac., Tokyo, Japan (1976).

20. D. H. Cho et al, "Mixing Considerations for Large-Mass, Energetic Fuel-Coolant Interactions," Proc. ANS/ENS Fast Reac. Safety Mtg., Chicago, IL, (1976) CONF-761001.

21. R. E. Henry and H. K. Fauske, "Core Melt Progression and the Attainment of a Permanently Coolable State," Proc. of Ther. Reac. Fuels Mtg., Sun Valley, ID (1981).

22. R. E. Henry and H. K. Fauske, "Required Initial Conditions for Energetic Steam Explosions," Fuel-Coolant Interactions, HTD - Vol. 19, ASME, Wash., DC, 1981.

23. M. L. Corradini, "Proposed Model for Fuel-Coolant Mixing During a Core Melt Accident," Proc. Int'l Mtg. on Thermal Reactor Safety, NUREG/CP-0027 (August 1982).

24. L. Baker and L. C. Just, Studies of Metal-Water Reactions at High Temperatures, III Experimental and Theoretical Studies of Zr-H_2O Reactions, ANL-6548, Argonne (May 1982).

25. M. Berman, <u>Light Water Reactor Safety Quarterly</u>, Sandia National Laboratories, SAND80-1304; January-March, 1 of 4 (1980), April-June, 2 of 4 (1980) July-Sept., 3 of 4 (1981), Oct.-Dec., 4 of 4 (1981).

26. H. K. Fauske, <u>Assessment to Steam Explosion Potential in Hypothetical LWR Core Melt Down Accident</u>, Vol. 1 - main report for Nuclear Safety Analysis Center, Electric Power Research Institute.

27. R. Bellman and R. H. Pennington, "Effects of Surface Tension and Viscosity on Taylor Instability," <u>Quar. Applied Math.</u>, <u>Vol. 12</u>, pp. 151-162, (1954).

28. S. Chandrasekhar, <u>Hydrodynamic and Hydromagnetic Stability</u>, 2nd Edition, Oxford, England (1968).

29. M. Pilch, "Hydrodynamic Droplet Fragmentation," Ph.D. Thesis, University of Virginia (1980).

30. M. L. Corradini, "Heat Transfer and Fluid Flow Aspects of Fuel-Coolant Interactions," Ph.D. Thesis, MIT, Cambridge (1978).

31. S. Rezakhany, "Experimental Investigation of the Minimum Film Boiling Point for Spheres in Forced Convection," Preliminary Research Proposal, University of Wisconsin (November 1981).

32. V. K. Dhir and G. P. Purohit, "Subcooled Film Boiling Heat Transfer from Spheres," ASME Heat Transfer Conf., 77-HT-78, Salt Lake City, 1977.

33. C. Shih, "Film Boiling and Vapor Explosions from Small Spheres," Ph.D. Thesis, University of Wisconsin (May 1979).

34. Robert H. Cole, <u>Underwater Explosions</u>. Princeton, NJ (1948).

35. Sir G. I. Taylor, "The Instability of Liquid Surfaces When Accelerated in a Direction Perpendicular to Their Plane I," <u>Proc. Roy. Soc. London A</u>, <u>201</u>, p. 192, (1950).

36. R. Bellman and R. H. Pennington, "Effects of Surface Tension and Viscosity on Taylor Instability," <u>Quart. J. Appl. Math</u> Vol. 12, p. 151, (1954).

37. H. Lamb, <u>Hydrodynamics</u>, Cambridge, England, p. 475 (1932).

38. S. Chandrasekhar, <u>Hydrodynamic and Hydromagnetic Stability</u>, Chapter X, 2nd Ed., Oxford, England (1968).

39. D. Cho et al, <u>Mixing Consideration for Large Mass,</u> <u>Energetic Fuel-Coolant Interactions</u>, Argonne National Laboratory, ANL/RAS 76-35, November 1976.

40. A. W. Cronenberg and M. A. Grolmes, "A Review of Fragmentation Models Relative to Molten UO_2 Breakup When Quenched in Sodium," ASME Tech. Pub., 74 WA/HT-42, New York, 1974.

41. T. G. Theofanous et al, "Fuel-Coolant Interactions and Hydrodynamic Fragmentation," <u>Proc. of Fast Reac. Safety</u> <u>Mtg.</u>, Seattle, WA (1979).

42. D. J. Buchanan and T. A. Dullforce, "Mechanism for Vapor Explosions," <u>Nature</u>, <u>245</u> (5419), p. 32 (September 1973).

43. M. S. Kazimi, "Theoretical Studies on Some Aspects of Molten-Fuel-Coolant Interactions," Ph.D. Thesis, MIT, Cambridge (1973).

44. M. L. Corradini and N. E. Todreas, "Prediction of the Minimum UO_2 Particle Size Based on Thermal Stress Initiated Fracture," <u>Nucl. Eng. Design</u>, <u>53</u> (1), p. 105 (June 1979).

45. M. L. Corradini and D. V. Swenson, <u>Probability of Con-</u> <u>tainment Failure Due to a Steam Explosion Followed by a</u> <u>postulated Core Melt Accident</u>, Sandia Laboratories, SAND80-2131, March 1981.

46. G. Samsonov, <u>The Oxide Handbook</u>, IFI/PLENUM (1973).

47. <u>Thermophysical Properties of High Temperature Solid</u> <u>Materials</u>, TPRC (1967).

48. Properties for LMFBR Safety Analysis, ANL-CEN-RSD-76-1, Argonne National Laboratories (1976).

49. <u>Core Melt Down Experimental Review</u>, SAND 74-0382, Sandia Laboratory (1974).

50. <u>Handbook of Chemistry and Physics</u>, CRC (1981-82).

51. <u>Thermodynamic Properties of Minerals</u>, U.S. Government Printing Office (1978).

52. <u>JANAF Thermochemical Tables</u> (1980).

53. G. Samsonov, <u>Handbook of Physical-Chemical Properties</u> <u>of the Elements</u> (1968).

54. D. Fling, "Surface Tension of Liquid Metals," <u>Journal</u> <u>of Nuclear Materials</u> <u>Vol. 16</u>, (1965).

3. HYDROGEN PROGRAM

3.1 Analysis and Code Development

3.1.1 HECTR Analysis and Code Development
(A. L. Camp, S. E. Dingman, M. J. Wester,
D. J. Rzepecki, R. A. Watson)

HECTR is a multicompartment hydrogen deflagration code that models the containment pressure-temperature response to hydrogen-generating accidents. During the past six months we have made significant improvements and additions to HECTR. We have also performed calculations using HECTR to evaluate HECTR's transport modelling capability. In addition, we have presented papers at several conferences and have provided support for other Reactor Safety programs at Sandia. This recent work and our future plans are discussed below.

3.1.1.1 Code Development

We added several new models and improved existing models in HECTR. The preliminary ice condenser model, the convective heat transfer model, and the radiative heat transfer model were all upgraded. We also added sump and source terms directly from a tape generated by MARCH. To upgrade the thermodynamic modelling of steam, we added a compressibility factor to the steam equation of state and forced the steam to follow the saturation curve rather than allowing the steam to subcool. These developments are discussed in the following sections.

3.1.1.1.1 Ice Condenser Model

The preliminary ice condenser model for HECTR was described previously.[1] Since then, we have made several improvements to the model, which are described below. The compartmentalization used in the model is described first, then the equations used to calculate the ice condenser phenomena are discussed.

To model an ice condenser in HECTR, we subdivide the ice region into four compartments and use two more compartments for the lower and upper plenums. This relatively large number of compartments is necessary because the steam concentration can vary significantly across the ice condenser. There is no limit on the number of surfaces in the lower and upper plenums, but only two surfaces are used for each compartment in the ice region. One of the two surfaces in each ice region compartment models the ice and the other surface models the ice condenser walls and the metal baskets. Each ice surface is maintained at a constant temperature. The metal surfaces are treated as lumped masses.

Since conditions in the ice region are significantly different from conditions elsewhere in the containment, we added a convective heat transfer correlation to the code that is more appropriate for the ice region. The heat-mass transfer analogy is still used, but the sensible heat transfer is calculated from the following forced convection correlation:

$$h = 0.023 \ C \ Re^{0.8} \ Pr^{0.3} \tag{3-1}$$

where

h = heat transfer coefficient
Re = Reynolds number
Pr = Prandtl number
C = Heat-transfer augmentation due to basket roughness and presence of water film (currently set to 5)

The ice melting rate is calculated by the following expression:

$$W_{ice} = (q*A_{ice})/(h_{liq} - u_{ice}) \tag{3-2}$$

where

W_{ice} = ice melting rate
q = sensible heat flux to ice
A_{ice} = ice heat transfer area
h_{liq} = enthalpy of water at 273 K
u_{ice} = internal energy of ice at ice temperature

The ice is assumed to melt from the bottom up in each compartment. The mass of unmelted ice is calculated by integrating the ice melting rate during the transient. The corresponding surface area of the ice for heat transfer is calculated using:

$$A_{ice} = (M_{ice}/M_{ice,o})*A_{ice,o} \tag{3-3}$$

where

$A_{ice,o}$ = initial ice heat transfer area
M_{ice} = unmelted ice mass
$M_{ice,o}$ = initial ice mass

As the ice melts, the metal baskets containing the ice will be exposed and subsequently will be heated by the steam. To account for this heat sink, we increase the mass of the metal surface in each ice region as the ice melts and adjust the surface temperature using the following equations:

$$M_{met} = M_{met,old} + M_{bask}*(M_{ice} - M_{ice,old})/M_{ice,o} \tag{3-4}$$

$$T_{met} = \frac{(M_{met,old} {}^* T_{met,old}) + (M_{met} - M_{met,old}) {}^* T_{ice}}{M_{met}} \qquad (3\text{-}5)$$

where

M_{bask} = mass of baskets

M_{met} = mass of metal heat transfer surface

$M_{met,old}$ = M_{met} from previous time step

$M_{ice,old}$ = M_{ice} from previous time step

T_{met} = temperature of metal surface

$T_{met,old}$ = T_{met} from previous time step

The water formed in the ice region by melting ice and steam condensation falls down through the ice condenser to a sump on the floor of the lower plenum. Although this process is too poorly characterized at present to allow analytical modelling, the heat and mass transfer from the steam to the water is significant. Therefore, we have included a simple model for the process in HECTR that can be varied parametrically to bound the phenomena. For this model, we assume that the water does not heat up significantly in the ice region. Thus, all of the heat and mass transfer occurs while the water falls through the lower plenum. We also assume that the latent heat transfer from steam condensation on the water is much larger than the sensible heat transfer. Using these assumptions and a user-specified final water temperature, the condensation rate of the lower plenum steam on the water drops is calculated from the following equation:

$$W_{c,LP} = [(W_{ice} + W_{c,ice}) {}^* (h_{l,f} - h_{liq}) +$$
$$W_{c,met}(h_{l,f} - h_{l,m})]/(h_{stm} - h_{l,f}) \qquad (3\text{-}6)$$

where

$W_{c,LP}$ = steam condensation rate in lower plenum

$W_{c,ice}$ = steam condensation rate on ice

$W_{c,met}$ = steam condensation rate on metal surfaces

$h_{l,f}$ = enthalpy of liquid at drain temperature

$h_{l,m}$ = enthalpy of liquid at metal temperature

h_{stm} = enthalpy of steam in lower plenum

We have also upgraded the ice condenser door model. The preliminary door model allowed flow to occur through a door in only one direction. The door was assumed to open and close instantaneously, and it was not allowed to be partially open. To more realistically model the doors, we now allow the user to specify a minimum differential pressure that

must be exceeded before the door will be allowed to open. We also specify the flow area as a function of the differential pressure across the door, rather than assuming it to be fully open. The flow area is calculated from the following equations, which have been used extensively by others.[2]:

$$\frac{\theta}{\theta} = \frac{\Delta P \cos \theta}{\Delta P_o \cos \theta_o} \qquad (3-7)$$

$$\frac{A}{A_o} = \frac{1 - \cos \theta}{1 - \cos \theta_o} \qquad (3-8)$$

where

    A = flow area
    ΔP = differential pressure across door
    θ = door angle
    o = fully open condition

3.1.1.1.2 Sump Model

A sump model was also added to HECTR. It collects water from the following sources: the portion of the break flow that does not flash to steam, condensation on the containment walls, spray droplets that reach the bottom of a compartment, and water draining from the ice condenser. Water can be drawn from the sump to supply emergency core coolant and spray injection at a user-specified rate. Condensation on the sump surface and evaporation of the sump are also modelled. Assuming the sump is at a spatially uniform temperature, the transient sump temperature and volume are calculated from mass and energy balances.

3.1.1.1.3 Heat Exchanger Model

A heat exchanger model was added to HECTR to calculate the spray injection temperature during the recirculation mode of spray injection. In this mode, water for spray injection is removed from the sump, then cooled by the heat exchanger rather than injected directly from storage tanks.

This heat exchanger model was taken from MARCH.[3]

3.1.1.1.4 Heat Transfer Upgrades

The liquid layer was removed from the convective heat transfer calculations. The heat transfer resistance from this layer is negligible for many cases, so removing it does not significantly affect the convective heat transfer rate. However, removing the layer significantly reduces the calculation time because it eliminates the iteration on the liquid-gas interface temperature. The correlations currently used to determine the heat transfer rates are as follows:

Forced Convection

$$Nu = .037 \, Re^{.8} Pr^{.333} \qquad\qquad (3-9)$$

Free Convection

Vertical Surface

$$Nu = .13 \, (Gr \, Pr)^{.333} \qquad\qquad (3-10)$$

Pool Surface

$$Nu = .27 \, (Gr \, Pr)^{.25} \qquad\qquad (3-11)$$

where

    Nu = Nusselt number used to calculate sensible heat
         transfer
    Gr = Grashof number
    Re = Reynolds number

A simplistic, noniterative liquid layer model may be added
in the future.

The radiative heat-transfer calculations were also modified
to reduce the computer calculation time. The seven-band
model previously used to calculate the emissivity of steam
was replaced with the Cess-Lian model. Calculating the
emissivity with this model is much faster than with the
Edward's model and gives comparable results. The new equa-
tion for emissivity is

$$e_{H_2O} = a_0 \, [1 - \exp(-a_1 \, x^{0.5})] \qquad\qquad (3-12)$$

where

e_{H_2O} = steam emittance

x = $P_{H_2O} L_e \, (300 \, P/T) \, (1 + x_{H_2O} \, (b - 1))$

b = $5(300/T)^{0.5} + .5$

P_{H_2O} = steam partial pressure

L_e = characteristic path length

P = total gas pressure

T = gas temperature

x_{H_2O} = steam mole fraction

a_0, a_1 determined from:

3-5

T(K)	a_0	a_1
300	.683	1.17
600	.674	1.32
900	.700	1.27
1200	.673	1.21
1500	.624	1.15

3.1.1.1.5 Treatment of Gases

A compressibility factor was added to the steam equation of state. The new equation is:

$$PV = ZNRT \tag{3-13}$$

where

P   = pressure
V   = volume
Z   = compressibility factor
N   = moles
R   = universal gas constant
T   = absolute temperature

The compressibility factor, Z, is interpolated from tables that are functions of both temperature and pressure. Thus, an iterative procedure is now required to calculate the steam partial pressure. Convergence is usually achieved after one or two iterations.

Under some conditions, such as in the ice condenser upper plenum, HECTR previously allowed steam to exist as a sub-cooled gas. We have modified the steam property calculations such that the steam will be forced to follow saturation for conditions that would previously have resulted in subcooling. For these conditions, the liquid portion of the saturated mixture is immediately transferred to the sump. This is necessary because HECTR does not model suspended droplets.

3.1.1.1.6 MARCH Interface

We developed an interface that allows HECTR to read source terms directly from a MARCH-generated tape. This eliminates the tedious task of manually inputting transient steam and hydrogen flow rates and energies.

3.1.1.2 Publications

Papers entitled "HECTR: A Computer Program for Modelling the Response to Hydrogen Burns in Containments" and "Applications of HECTR to Reactor Containments" were presented at the Second International Workshop on the Impact of Hydrogen on Water Reactor Safety. "Development and Applications of a Program for Modelling the Response to Hydrogen Burns in Containments" was presented at the CUBE Symposium. "Development

and Applications of a Computer Program for Modelling the
Response to Hydrogen Burns in Containment" was presented at
the Second International Topical Meeting on Nuclear Reactor
Thermal-Hydraulics.

3.1.1.3 Sequoyah Calculations

The containment pressure-temperature response has been exa-
mined for an ice condenser containment using HECTR. Calcu-
lations were performed for several accident scenarios and
the input parameters were varied to determine their influence
on the calculations. The results of this analysis are dis-
cussed in this section.

The containment model used for the calculations is shown in
Figure 3.1. The containment was divided into nine compart-
ments: the upper compartment, the upper and lower plenums,
the lower compartment (which includes a single volume sump),
a dead-end region, and four ice condenser regions. Flow
junctions are also indicated in Figure 3.1. Of particular
importance are junctions 2, 4, 9, and 10. Junction 2 repre-
sents floor drains connecting the upper and lower compart-
ments. Gas flow through this junction ceases when the sprays
are initiated or when the sump level rises above the drain
exit. Junction 4 represents bypass flow around the ice con-
denser intermediate deck doors, and junctions 9 and 10 repre-
sent the intermediate deck doors and the lower plenum inlet
doors, respectively. Fans that transfer gas from the upper
compartment (and a smaller amount from the lower compartment)
to the dead-ended region are modeled.

No igniters are included in the ice region or the ice con-
denser lower plenum. Thus, the only burns that occur in
those compartments are those that start in other compart-
ments and propagate into the ice condenser. Twenty-nine
heat transfer surfaces were modelled in this analysis.

Steam and hydrogen sources are introduced into the lower
compartment. Containment sprays come initially from a con-
stant temperature reservoir and later from the sump via a
heat exchanger. The sprays are assumed to fall only into
the upper compartment, and any water carry-over is trans-
ferred to the sump. Both the sprays and the fans are acti-
vated when pressure setpoints are exceeded.

The 41 different cases that will be examined for the ice
condenser containment are described in Table 3.1. These
cases were chosen to include scenarios that are the highest
contributors to risk and to examine the major uncertainties
that affect the results.

Twenty-seven of the cases listed in Table 3.1 have been com-
pleted. These cases are all degraded core accident scenarios
and are designated in Table 3.1 by the letters B, C, F, H,
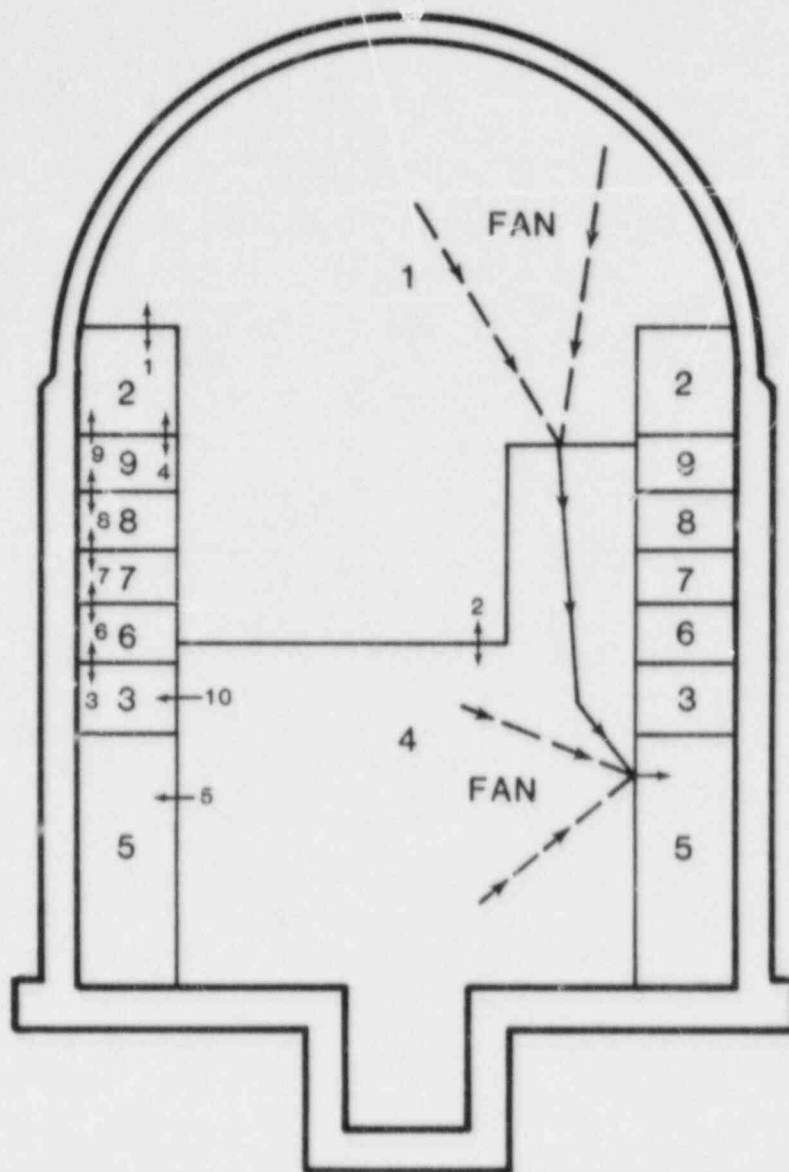
KEY

1 – COMPARTMENT NUMBER

1 – FLOW JUNCTION NUMBER

→ – ONE-WAY FLOW JUNCTION

←→ – TWO-WAY FLOW JUNCTION

Figure 3.1. Compartmentalization Used for the Seqouyah Cal-
culations. The arrows indicate flow functions
with positive flow in the direction of the
arrow.

Table 3.1

Case Description

First table

Case No.	Accid. Seq.	Restore ECC	Extent Oxid.	Spray Trains	Recirc. Fans	Cont. Vent	Ignit. Limits	Ice Condenser Drain Temp.	Mixer Coeff.	Extent Corr.	Flame Speed	Comments
B.00	S2D.2"	yes	75%	2	2	no	8%	310	0	0	d	
C.00	b2D.2"	yes	CLASIX	2	2	no	8%	310	0	0	d	
D.00	b2D.2"	no	100%	2	2	no	8%	310	0	0	d	
E.00	b2D.2"	no	min	2	2	no	8%	310	0	0	d	
F.00	b1D.6"	yes	75%	2	2	no	8%	310	0	0	d	
G.00	AL	no	100%	2	2	no	8%	310	0	0	d	
H.00	b1M.6"	yes	75%	2inj	2	no	8%	310	0	0	d	
I.00	b1M.6"	yes	75%	2inj	2	no	8%	310	0	0	d	
J.00	b1M.6"	no	100%	2inj	2	no	8%	310	0	0	d	
K.00	b1m.6"	no	min	2	2	no	8%	310	0	0	d	
K.00	TbuU	yes	75%	2rcvr	2rcvr	no	14int	310	0	0	d	12% before power recovered
M.00	TbuU	yes	100%	0	0	no	12%	310	0	0	d	
N.00	TbuU	no	min	0	0	no	12%	310	0	0	d	

Second table

Case No.	Accid. Seq.	Restore ECC	Extent Oxid.	Spray Trains	Recirc. Fans	Cont. Vent	Ignit. Limits	Ice Condenser Drain Temp.	Mixer Coeff.	Extent Corr.	Flame Speed	Comments
B.01	b2D.2"	yes	75%	2	0	no	8%	310	0	0	d	
B.02	b2D.2"	yes	75%	1	1	no	8%	310	0	0	d	
B.03	b2D.2"	yes	75%	2	2	no	8%	310	0	0	d	
B.04	b2D.2"	yes	75%	0	2	no	8%	310	0	0	d	Surface heat xfer coeff. × 5.
B.05	b2D.2"	yes	75%	2	2	no	8%	310	0	0	d	
B.06	b2D.2"	yes	75%	2	2	no	8%	310	0	0	d	
B.07	b2D.2"	yes	75%	2	2	no	7%	310	0	0	d	
B.08	b2D.2"	yes	75%	2	2	no	8%	310	0	0	d	
B.09	b2D.2"	yes	75%	2	2	no	10%	310	0/5	.75×3	d	
B.10	b2D.2"	yes	75%	2	2	no	8%	310	4×5	0	3×d	
B.11	b2D.2"	yes	75%	2	2	no	8%	310	0	0	d/3	
B.12	b2D.2"	yes	75%	2	2	no	8%	310	0	0	d	Suppress upper plenum ignition.
B.13	b2D.2"	yes	75%	2	2	no	8%	310	0	0	d	Partially pre-inerted.
B.14	b2D.2"	yes	75%	2	2	no	8%	348	0	85%	6 fps	Comparison to CLASIX base case.
C.01	S2D.2"	yes	CLASIX	2	2	no	?	?	?	?	?	Comparison to CLASIX base case.
C.02	b2D.2"	yes	CLASIX	2	2	no	?	?	?	?	?	Comparison to COMPARE.
E.01	b2D.2"	no	100%	2	2	yes	8%	310	0	0	d	
E.01	b2D.2"	no	min	2	2	yes	8%	290	0	0	d	
I.01	b1M.6"	yes	75%	2inj	2	no	8%	310	0	0	d	
I.02	b1M.6"	yes	75%	2inj	2	no	8%	310	0	0	d	
I.03	b1M.6"	yes	75%	2inj	2	no	8%	310	0	0	d	
I.04	b1M.6"	yes	75%	2inj	2	no	8%	310	0	0	d	
I.05	b1M.6"	TCS	75%	2inj	2	no	8%	310	0	0	d	Surface heat xfer coeff. × 5.
J.01	b1M.6"	no	100%	2inj	2	yes	8%	310	0	0	d	
J.02	b1M.6"	no	min	2inj	2	yes	8%	310	0	0	d	
N.01	TbuU	no	100%	0	0	no	8%	310	0	0	d	
O.01	TbuU	no	min	0	0	no	8%	310	0	0	d	

Keys: d = default
      inj = injection
      min = minimum
      rcvr = recover

I, L, and M. The core is recovered with approximately 75% cladding reaction occurring for each case. Results for these cases are summarized in Table 3.2. The number of burns each compartment is presented, along with the peak pressure and the compartment(s) that the peak pressure occurred in (or compartments with pressures within a few kPa of the peak pressure).

Cases B.01 to B.04 examined the importance of the ESFs (fans and sprays) for an S_2D scenario. Reducing the fan flow rate results in higher baseline pressures before the burns, due to reduced ice condenser effectiveness. Correspondingly, the pressure after each burn is higher than with fans operating fully. Reduced fan flow rates also allow more hydrogen to accumulate in the upper plenum, with less being transferred to the upper compartment. Thus, there are more upper plenum burns, and fewer concentrations are observed in the ice condenser. By the time 8% hydrogen is reached in the upper plenum, the hydrogen concentration in the top compartment of the ice region is above 30%. Because HECTR cannot treat detonations or accelerated flames, this hydrogen was burned in a relatively benign manner.

The first part of the S_2D calculation is not affected by the failure of containment sprays. During the this time, the ice condenser is removing most of the steam and providing containment cooling. However, as the ice melts, the containment pressure begins increasing due to steam buildup. Eventually, all of the ice melts, so that the only containment heat removal mechanism left is heat transfer to the containment structure. Thereafter, the pressure will continue to increase until the failure pressure is reached.

Cases B.06 through B.12 examine the sensitivity of the results to various combustion parameters. In general, higher ignition limits produce fewer burns that are faster, more complete, and give higher pressure rises. Assuming that burns are only 75% as complete as in the base case results in more burns with lower pressure rises because less hydrogen is consumed in each burn. The peak pressure is larger when the flame speed is increased since there is less time for heat transfer to occur.

Case B.13 assumes that the upper plenum igniters do not function properly. This might occur if a fog formed in the upper plenum or if a limited electrical failure occurred. Without the upper plenum igniters, the hydrogen is distributed throughout the containment rather than burning in the upper plenum. Therefore, there are fewer burns, but more hydrogen is consumed in each, yielding higher pressure rises.

Case B.14 examines the effects of partially depleting the containment atmosphere of oxygen before the accident. Although HECTR does not predict substantial differences

Table 3.2

HECTR Sequoyah Results
(Degraded-Core Scenarios)

CASE	NUMBER OF BURNS BY COMPARTMENT 1	2	3	4	5	6	7	8	9	Maximum Pressure (kPa) and Comp. #
B.00	5	6	0	0	0	0	0	0	0	342.5 (1,2)
C.00	5	19	1	1	0	1	2	5	8	233.0 (1,2)
F.00	2	7	6	10	0	6	3	3	3	399.1 (1,2)
H.00	2	6	6	10	0	6	2	2	3	360.5 (1,2)
I.00	2	5	5	6	0	5	3	3	3	475.1 (ALL)
L.00	5	12	1	2	0	3	0	0	0	357.3 (1,2)
M.00	4	10	1	1	0	0	1	7	10	354.1 (1,2)
B.01	2	24	0	0	2	0	0	2	6	521.3 (1,2)
B.02	6	22	0	0	0	0	0	2	11	380.3 (1,2)
B.03	4	7	0	0	0	0	0	0	0	440.2 (ALL)
B.04	1	25	0	0	2	0	4	4	7	631.0 (1,2)
B.05	5	10	0	0	0	0	0	0	0	361.1 (ALL)
B.06	6	43	1	1	0	1	0	0	0	217.8 (1,2)
B.07	7	16	0	0	0	0	0	0	0	278.6 (1,2)
B.08	4	3	0	0	0	0	0	0	0	383.9 (1,2)
B.09	3	2	0	0	0	0	0	0	2	419.4 (1,2)
B.10	6	9	0	0	0	0	0	0	0	286.1 (1,2)
B.11	5	5	0	0	0	0	0	0	0	404.7 (1,2)
B.12	5	7	0	0	0	0	0	0	0	240.7 (1,2,3,6,7,8,9)
B.13	3	2	2	2	2	2	2	2	2	414.7 (1,2)
B.14	5	5	0	0	0	0	0	0	0	331.5 (1,2)
C.01	0	30	0	10	0	0	0	0	0	167.6 (ALL)
I.01	1	5	5	6	0	4	3	3	3	493.5 (ALL)
I.02	1	5	5	9	0	5	3	3	4	451.4 (ALL)
I.03	1	4	3	5	0	3	2	2	2	495.7 (1,2,3,6,7,8,9)
I.04	2	6	6	10	0	6	3	3	5	501.6 (ALL)
I.05	1	5	5	6	1	5	3	3	4	420.4 (ALL)

between this case and case B.00, some benefit from partial oxygen depletion would actually be expected. Oxygen depletion is expected to decrease the flame speed and combustion completeness, but these decreases are not modelled in HECTR.

Previous analyses of the Sequoyah plant have been performed by TVA using the CLASIX code[4], and by Los Alamos National Laboratory, using the COMPARE code.[5] These analyses were also made for an S_2D scenario, but an older version of MARCH was used to generate the source terms. Thus, the source terms used in the analyses are different from those used in the B cases discussed above. The total amount of hydrogen injected is about the same for the two source terms, but the hydrogen is released more quickly in the CLASIX source. Much more steam is released in the source term used for case B.00 than in the CLASIX source. Thus, the steam: hydrogen injection ratio is much higher for the source used in case B.00 than in the CLASIX source. Case C.00 was run to examine the sensitivity of the results to these source terms differences. Case C.00 uses the source terms used in the CLASIX and COMPARE analyses, but uses the input assumptions used in case B.00 rather than those used in the CLASIX and COMPARE analyses. The greater amounts of steam present in case B.00 tend to impede combustion in the lower compartments and also allow more hydrogen to be transported into the upper compartment before combustion begins in the upper plenum. These results illustrate the sensitivity of the calculations to different MARCH modelling assumptions.

Case C.01 was run as a direct comparison to the CLASIX base case from Reference 4. Results of this comparison are shown in Table 3.3. The burn sequences are similar, with HECTR predicting three more burns in the lower compartment than CLASIX. Since HECTR decreases the lower compartment volume as the sump fills up, the hydrogen concentration can rise more rapidly, which may account for the larger number of lower compartment burns in HECTR. The peak gas temperatures predicted by the two codes are comparable, with differences due to surface areas and different heat-transfer models. The pressure responses calculated by HECTR and CLASIX for the preburn phase of the accident agree very well. The CLASIX peak pressures following burns are slightly higher than HECTR's, but CLASIX predicts much larger pressure differences between the compartments. HECTR and COMPARE both predict small pressure differences between compartments, which we feel is more realistic since the flow areas between compartments are large. Volume averaging the pressures from CLASIX gives good agreement with HECTR peak pressures. In general, the agreement between HECTR and CLASIX is good for this case.

Table 3.3

Code Comparison

	Compartment	Case C.01	
		CLASIX	HECTR
No. of burns	LC	7	10
	UP	30	30
	UC	0	0
Peak Temperature	LC	947	896
(K)	UP	933	1006
	UC	346	355
Peak Pressure	LC	230.3	187.6
(kPa)	UP	191.6	166.1
	UC	173.0	185.9
Ice Remaining		36 %	24 %

Key: LC = Lower Compartment
       UP = Upper Plenum
       UC = Upper Compartment
       Note: no burns occurred in any other
             compartments for these cases.

3-13

Cases I.01 to I.04 examine the effects of ice condenser modelling parameters for a S_1HF accident. The ice condenser drain temperature was decreased and increased by 20 K in cases I.01 and I.02, respectively. A higher pressure rise is calculated with a lower drain temperature because less heat is transferred to the water falling through the lower plenum. The ice condenser heat transfer coefficient was decreased and increased by a factor of 5 in cases I.03 and I.04, respectively. Case I.03 initially predicts higher pressures than case I.04 because less steam is removed in case I.03. These higher baseline pressures produce substantially higher burn pressures. However, at late times the pressure is lower in case I.03 because some ice is still remaining, while in case I.04 the ice has all melted.

The base calculations for the F, H, I, L, and M cases examined different accident scenarios (Table 3.1). Since the hydrogen and steam sources are different for each scenario, the burn sequences are also different. The highest pressure is calculated for case I.00, which is an S_1HF accident with sprays failing in the recirculation mode.

Cases B.05 and I.05 examine the effects of increasing the surface heat-transfer coefficients by a factor of 5. Some pressure reductions from the base cases are predicted, due to increased steam condensation rates. However, the basic sequence of events is unchanged.

3.1.1.4 Transport Analysis

We are currently evaluating the ability of HECTR to calculate gas transport and mixing by comparing HECTR calculations with both experimental data and other analytical models. In particular, HECTR calculations are being compared with results from hydrogen distribution experiments performed at the Battelle Institute-Frankfurt (BF) and with the standard problems on hydrogen mixing and distribution that were performed at the Hanford Engineering Development Laboratory (HEDL) and sponsored by the EPRI. HECTR is also being compared directly with the RALOC code for some of the calculations performed for an analysis of Grand Gulf.[6] Finally, results from an earlier version of HECTR are being compared to results from the current version to determine the effect of modelling changes we have made. We have completed two of the experimental comparisons and most of the analytical comparisons. These are described below. We expect to complete this work and prepare a draft report during the next reporting period.

BF tests 2 and 6 were performed in a pair of cylindrically symmetric rooms with a total volume of about 74 m^3. The goal of these experiments was to examine the hydrogen transport between two compartments connected vertically by a relatively small (1-m^2) orifice. Figure 3.2 shows the compartmentalization we used to model these tests with HECTR.
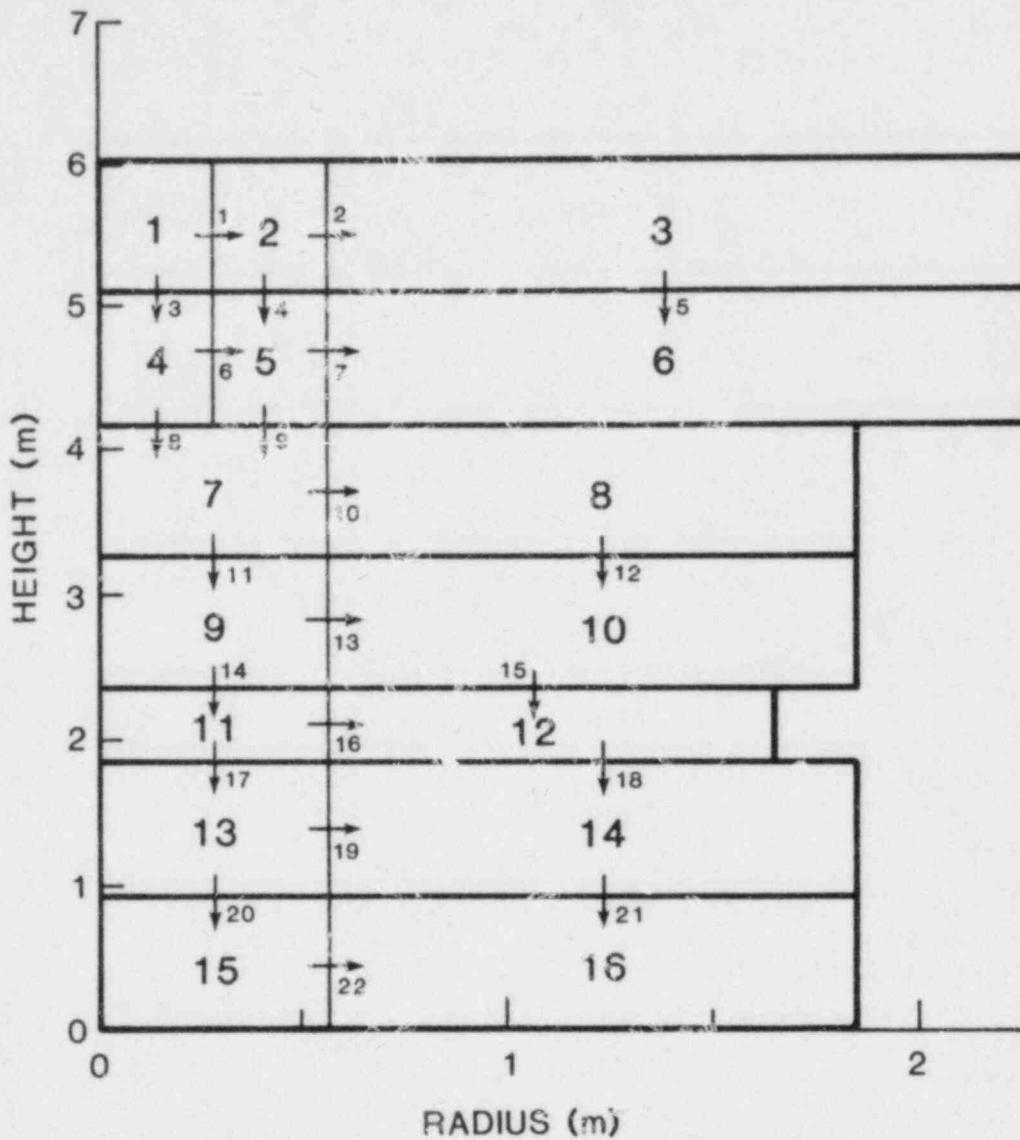
Figure 3.2. HECTR and RALOC Compartmentalization Used for
RF Tests 2 and 6. The arrows indicate flow
junctions where positive flow at a junction is
in the direction of the arrow.

The top room is represented by compartments 1 through 6 and the 1-m² orifice by junctions 8 and 9.

In BF test 2, the rooms were initially isothermal. A total of about 0.27 kg of hydrogen was injected into the bottom of compartments 15 and 16 over a period of more than 3 h. The HECTR and RALOC results calculated for this experiment are compared to the experimental results for compartment 1 in Figure 3.3. The results for other compartments showed HECTR in as good or better agreement with the experimental data.

BF test 6 was similar to BF test 2 except that there was an initial temperature gradient: the top of the experimental facility was approximately 20 K hotter than the bottom. The goal here was to examine the influence of a thermal inversion on the temporal hydrogen distribution. The warm upper layer of air tends to inhibit the convective transport of hydrogen to the top room. Results from HECTR and RALOC are compared to experimental results for compartments 1 and 13 in Figures 3.4 and 3.5. The HECTR results display the same qualitative trends as the data, doing sometimes better and sometimes worse than the RALOC predictons. This case is very difficult to model, and we found that the results were very sensitive to the assumed initial temperature distribution. From the BF report, it appears that some uncertainty exists in both the initial temperature distribution and the hydrogen flow rate.[7] Thus, the HECTR results for test 6 are not unreasonable in light of the known uncertainties and the associated sensitivities.

Calculations for Grand Gulf made with the current version of HECTR agreed well with RALOC calculations (assuming no hydrogen burning occ⁻ However, the version of HECTR used in the earlier ana., is of Grand Gulf did not always agree as well. Although the two versions of HECTR calculated similar results when using the two compartment models, they behaved quite differently when there was a sufficient number of compartments and flow junctions so that natural convective mixing loops could form. Figure 3.6 shows the dome pressure history in the original five-compartment Grand Gulf analysis and Figure 3.7 shows the same pressure history calculated by the current version of HECTR. The mixing was much more rapid in the newer case so that the hydrogen distribution was more uniform throughout the containment. In both cases, the burns generally started in the wetwell, but the more uniform hydrogen distribution in the newer case allowed the burns to propagate upwards further and into higher hydrogen concentrations.

3.1.1.5 Grand Gulf Analysis

The original Grand Gulf analysis did not model the suppression pool, purge/vent system, or drywell. In addition, the
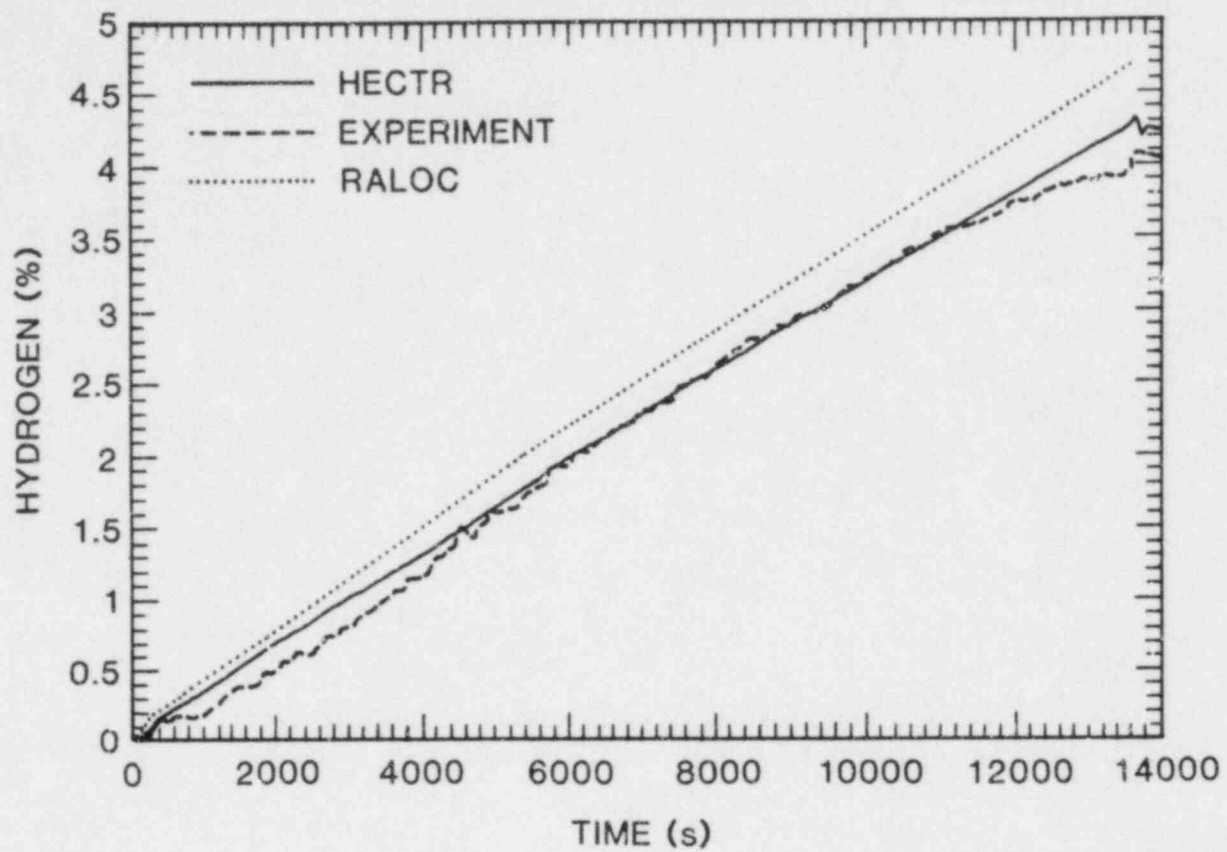
Figure 3.3. Results for BF Test 2 -- Compartment 1
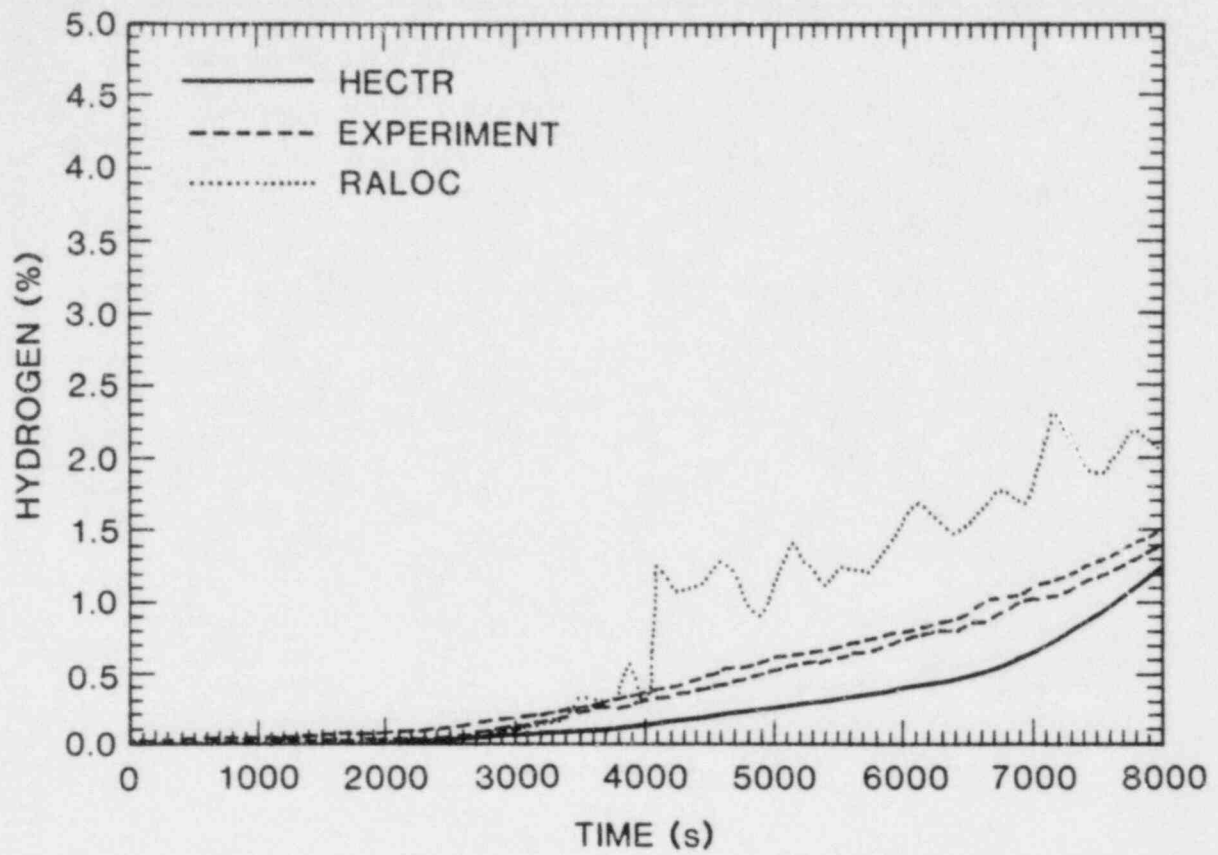
Figure 3.4. Results for BF Test 6 -- Compartment 1
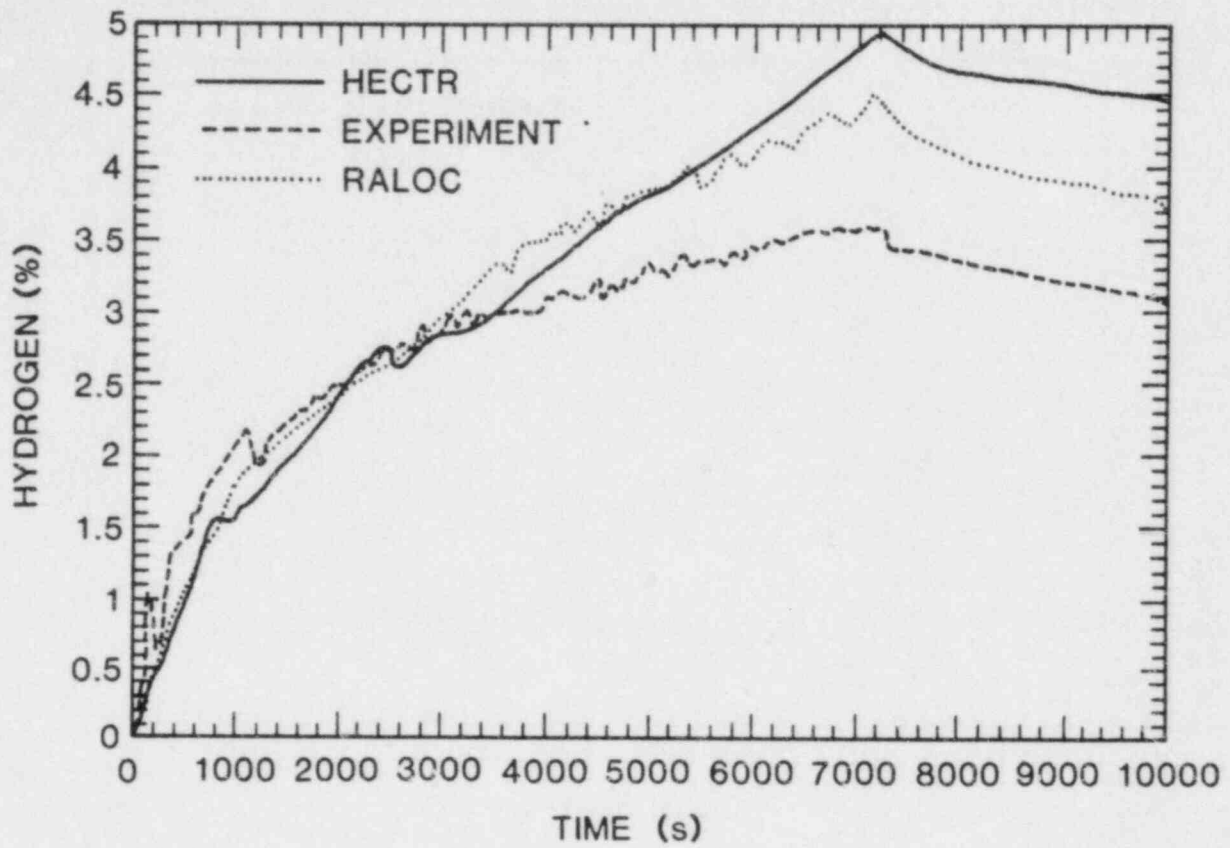
Figure 3.5.   Results for BF Test 6 -- Compartment 13
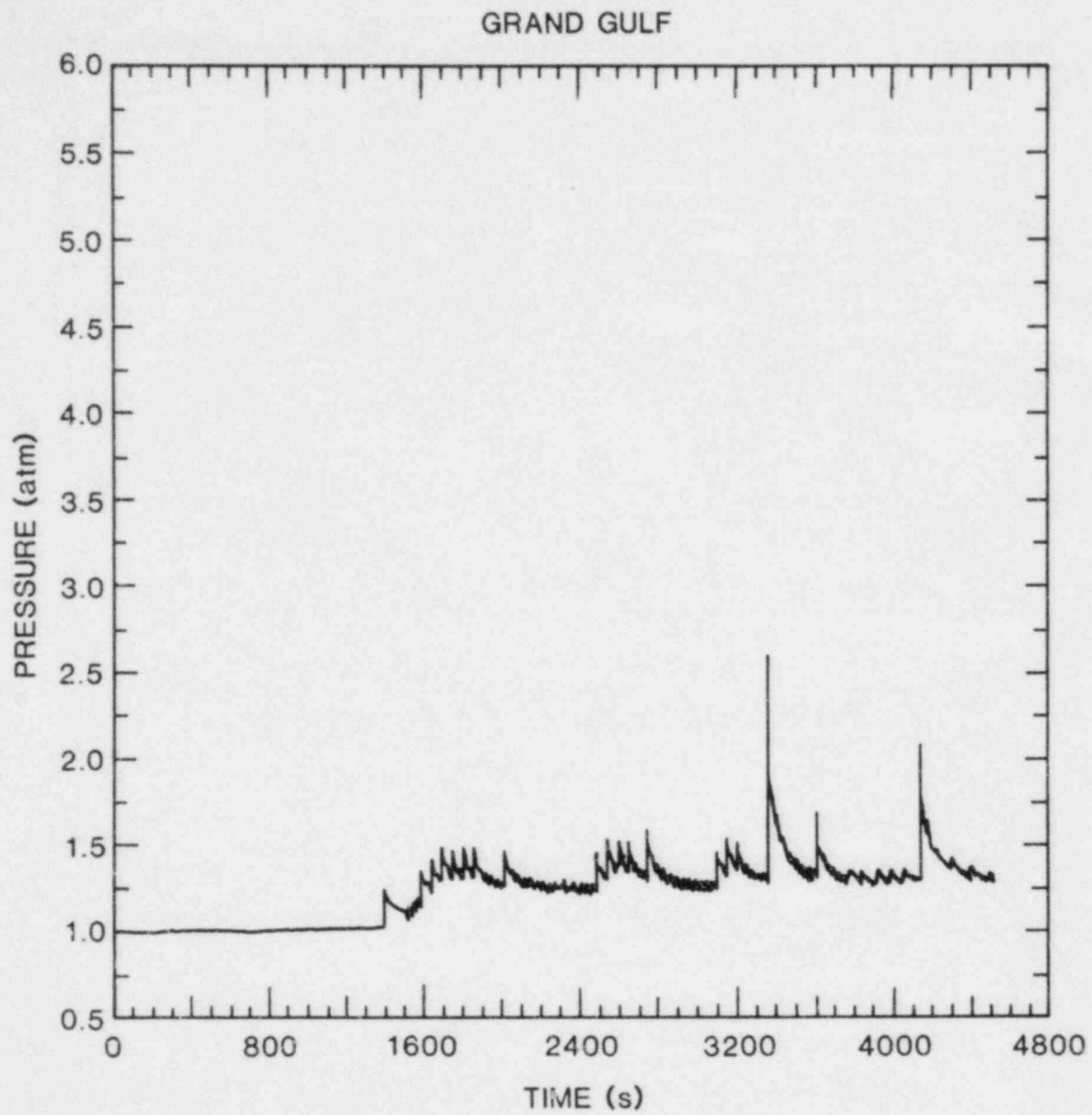
GRAND GULF

Figure 3.6.   Dome Pressure vs Time for the Original Five-
Compartment Grand Gulf Analysis
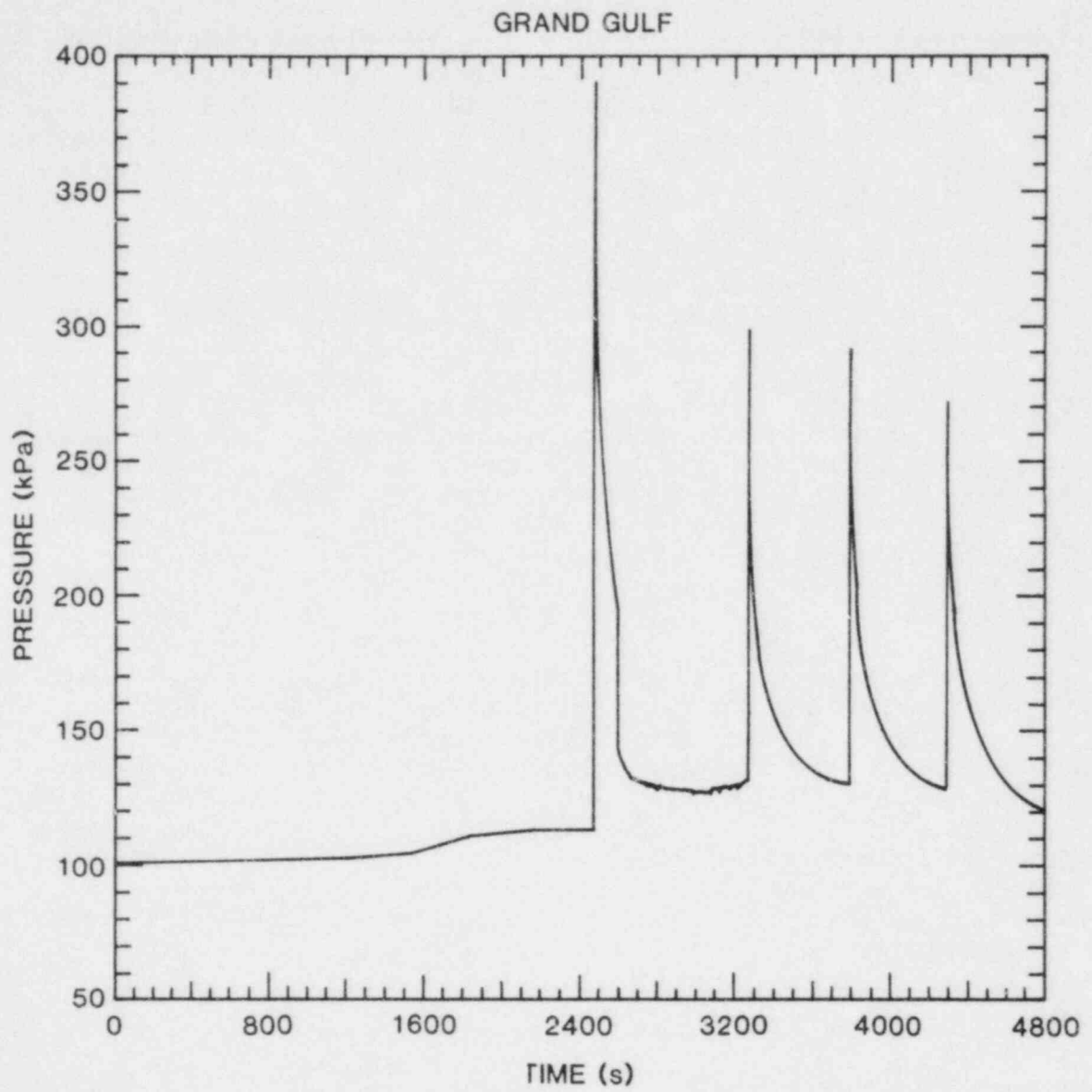
Figure 3.7. Dome Pressure vs Time for the HECTR Code
Analysis

version of HECTR used for the analysis did not treat hydrogen mixing very well (see Section 3.1.4). To address these concerns, we have begun a follow-up analysis of the Grand Gulf reactor. We are currently upgrading the containment model used in the previous analysis to include the drywell. We are also developing models for the suppression pool and the purge-vent system. The suppression pool model will calculate the motion of the pool, the gas flow rate through the vents, and the pool heatup. Changes in the pool mass and temperature due to the upper pool dump, spillover of the pool into the drywell, water removal for spray and the ECC injection, suppression pool cooling, and safety/relief valve discharge will be calculated by the model. We will not attempt to model steam chugging or the pool swell.

3.1.1.6 Support for Other Sandia Programs

The Sequoyah calculations discussed previously are also being used by the Hydrogen Burn Survival program, the Severe Accident Risk Reduction Program, and the Severe Accident Sequence Analysis Program. In addition, we performed several other calculations for the Hydrogen Burn Survival program that are being used to define the environment for equipment in ice condenser containments during transients with significant hydrogen generation. We have also written and reviewed sections for the MELCOR model assessment document.

3.1.1.7 Future Plans

During the next reporting interval, we will complete the HECTR calculations for the Sequoyah containment and the transport and mixing calculations. We will complete the development of the suppression pool and purge-vent system models for the Grand Gulf follow-up analysis and will use these models to perform calculations for Grand Gulf. We will begin assessing the capabilities of HECTR including comparisons with available experimental data. We will also begin an analysis of the Three Mile Island (TMI) hydrogen burn using HECTR.

3.1.2 Vortex Dynamics Modelling of Flame Acceleration
(P. K. Barr, Wm. T. Ashurst & J. F. Grcar)

The initial acceleration of a flame confined in a channel with obstacles has been numerically simulated. A premixed hydrogen-air mixture is assumed, but all chemical kinetics are replaced with a simple flame model that propagates a flame interface into the unburned gas at a specified speed. At the interface, the chemically induced volume expansion is calculated and results in an expanding gas flow past the obstacles. The flow creates turbulent recirculation regions downstream of the obstacles. The turbulence effect is simulated by introducing discrete vorticity into the flow field at the edges of the obstacles. As the flame propagates into

these regions, the surface area increases, which increases the overall burning rate and thus enhances the flow past succeeding obstacles and leads to flame acceleration.

In our computer model, the turbulent flow is simulated with discrete vorticity from which the velocity field can be calculated. This discrete vortex technique has been applied to many different time-dependent flows[8,9] and, more recently, to premixed reacting flows with both a calculated flame structure[10] and with the zero thickness interface model used in this work.[11] Vortex dynamics modelling of flame acceleration began in January 1982. The original form modelled the flame propagation in only one chamber, simulating the effect of the flame propagation in upstream chambers by injecting gas for a specified period of time. This injection flow established the turbulent recirculation regions. In this work, described in a previous report, there was no volume expansion in the flame and thus the enhancement of the burning was due only to the shed vorticity.[12] Those results showed the importance of the large recirculation structures and their ability to distort the flame front. Since the heat release was not included, this version did not simulate all of the acceleration mechanisms, just the possible driving forces.

The next major improvement was the incorporation of the chemically caused volume expansion, assumed to be at constant pressure.[13] The heat release in the combustion is related to an increase in the specific volume of the burned gas. Thus, the chemistry and the fluid flow are coupled, since the expansion of the burning gas is felt throughout the flow field and affects the vortex motion. Because of the constant pressure assumption, no density gradients appear in either the burned or the unburned gases, and the flame "interface" represents a boundary between the different densities. These calculations, restricted to a single chamber, used the same method for modelling the upstream chambers. These results did show acceleration and the experimentally observed dependence on volume confinement.

Current work focuses on extending this model to multichamber configurations. Experimental results by Lee et al., have shown the importance of obstacle-generated turbulent flow in the acceleration of a flame in a tube.[14] In these experiments, the flame first accelerates over a series of obstacles and, under the right conditions, emerges from the obstacle section as a detonation wave. Since the turbulence created in the obstacle region plays a crucial role in the observed acceleration to detonation phenomena, the computer model is being extended to multichambers. To date, we have only calculated geometries composed of 4 chambers, as opposed to the experiments with 20 or more chambers. However, in just these few chambers, the flow accelerates to velocities that violate

our constant pressure assumption. Removal of this assumption is under investigation at this time.

An example of multichamber configurations is shown in Figure 3.8, which shows three frames from a computer-generated movie. In this case, a 160-by-40 mesh is used to compute the flame propagation through three sets of obstacles. The flame "segments" are drawn in each mesh cell that is partially burned. The combustible mixture was ignited along the back wall at the closed end of the chamber. The specified flame parameters are density ratio of 6 and speed of 0.2. As the flame propagates into the unburned fluid, the resulting volume expansion pushes the flow through the obstacles and out the open right end, causing vorticity to be shed off the ends of the obstacles. The discrete vorticity is shown by dashed lines, which are scaled to the vorticity velocity vector. Flame acceleration can be observed in these three plots. The elapsed time after ignition for the flame to reach the open right end is unity but it takes 0.5 time units for the flame to reach the first obstacle. The acceleration of the flame does not begin until the flame passes through the first set of obstacles. The increase of the flame surface due to the area contraction and the interaction of the flame with the shed vorticity causes the flame acceleration to increase, as can be seen from the figure, where the second and third frames are at times of 0.88 and 0.98, respectively. Since the flame front jets through the center of the chambers, leaving much of the fluid unburned, the flame surface, and thus the rate of volume expansion, has increased to many times its original value (at ignition). Preliminary estimates of the flame acceleration, as measured by flame arrival time as well as outlet velocity, indicate that the flame has already exceeded our low-speed flow restriction.

The geometry shown in Figure 3.8 is representative of the complexity which can be included in multichamber calculations. The baffles can be placed symmetrically as shown, to represent flow through orifices such as in the flame acceleration experiments, or the baffles can be staggered, which resembles a containment geometry. We plan to pursue both the question of flame propagation between large chambers for the development of empirical burn-rate models for the HECTR code, and the question of flame acceleration due to obstacle-generated turbulence to compare with results by Lee.[15]

3.1.3 Evaluation of the CONCHAS-SPRAY Computer Code
       (K. D. Marx)

During the past several months, we have been performing an evaluation of the CONCHAS-SPRAY computer code.[16] In addition to gaining experience with the code, we are adding some new features to permit its application to flame acceleration and other problems of interest to the Hydrogen Program. Two
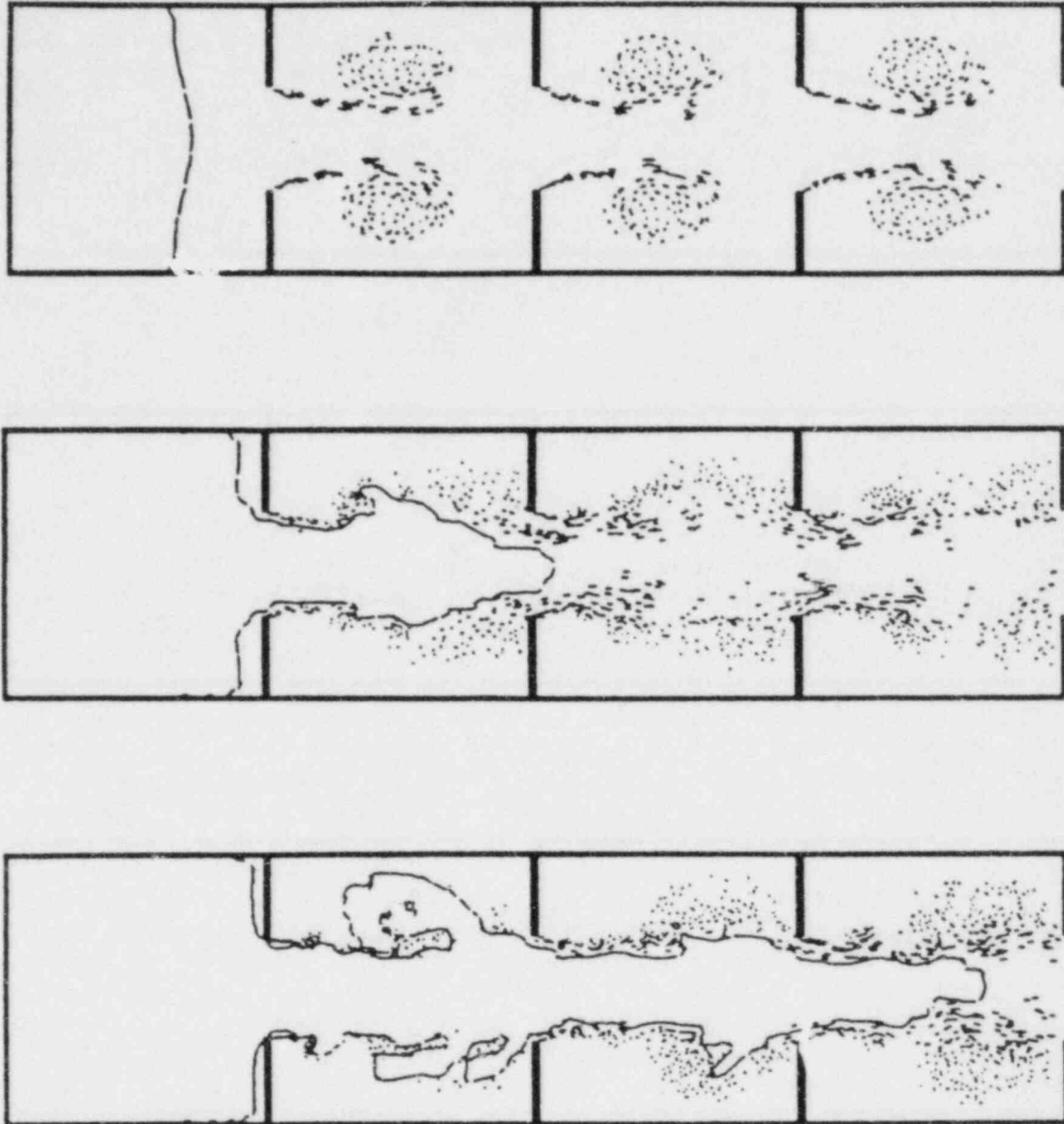
Figure 3.8. Three Frames from a Movie of Flame Acceleration in a Four-Chamber Configuration Created by Four Pairs of Obstacle Plates. Ignition occurred along the left wall and the volume expansion is pushing flow out the open right end. The vorticity shed off the ends of the obstacles (the dashed lines are scaled velocity vectors) helps increase the flame surface and produce the flame acceleration. As an indication of the acceleration effect, notice that the flame advancement is approximately the same from one plot to the next; however, the time interval is not constant: the second interval is three times smaller than the first.

of the more significant modifications that have been installed are the inclusion of outflow boundary conditions and the implementation of artificial flame thickening.

The outflow boundary conditions are an obvious requirement for the simulation of flames propagating in an open chamber. They are not a standard option in CONCHAS-SPRAY. The code was primarily developed for (enclosed) engine geometries; exhaust valves, when required, are so highly problem-dependent that the code designs at Los Alamos National Laboratory deemed it desirable to include them on a case-by-case basis. Guided by information obtained from L. D. Cloutman of LANL, we have supplied the appropriate coding to permit gas flow out of the end of a tube. Similar boundary conditions could be inserted along the walls of a channel to simulate venting.

The artificial flame thickening is necessary to solve problems in which the spatial scales are large compared to the flame thickness. In such cases, it is generally impossible to resolve the flame on the finite-difference grid because the grid spacing must be made larger than the flame thickness. (There are adaptive techniques that could allow resolution of the flame, but their implementation in CONCHAS-SPRAY would require a long-term development project.) The flame-thickening process, referred to as the ß-transformation, consists of increasing the transport coefficients (thermal conductivity, diffusion coefficients, and viscosity) by some factor ß, while decreasing the chemical reaction rate by the same factor. This maintains the same burn velocity for the reacting mixture as would be obtained on a finer grid. A judicious choice of ß results in spreading the flame over the desired number of zones on the grid. It is important that the alteration of the transport coefficients occur only in the region of the flame. Otherwise, significant errors in the computation of the flow could occur. To accomplish this, we make ß proportional to the gradient of temperature.

The ß-transformation has been given some theoretical justification by O'Rourke and Bracco.[17] However, we still must do considerable numerical testing to be assured that it will provide good results in our applications.

Figure 3.9 illustrates a preliminary calculation which simulates a portion of a small-scale experiment such as those performed by Lee and coworkers at McGill University.[18] The computational domain consists of a 5.2-cm-diameter tube, with two chambers separated by an obstacle with a blockage ratio of 0.62. The tube is initially filled with a stoichiometric hydrogen:air mixture. Ignition is accomplished by depositing energy in a ring-shaped region approximately 0.3 cm from the walls in the closed end of the tube. (The energy source is in the lower right corner of the plot frames).
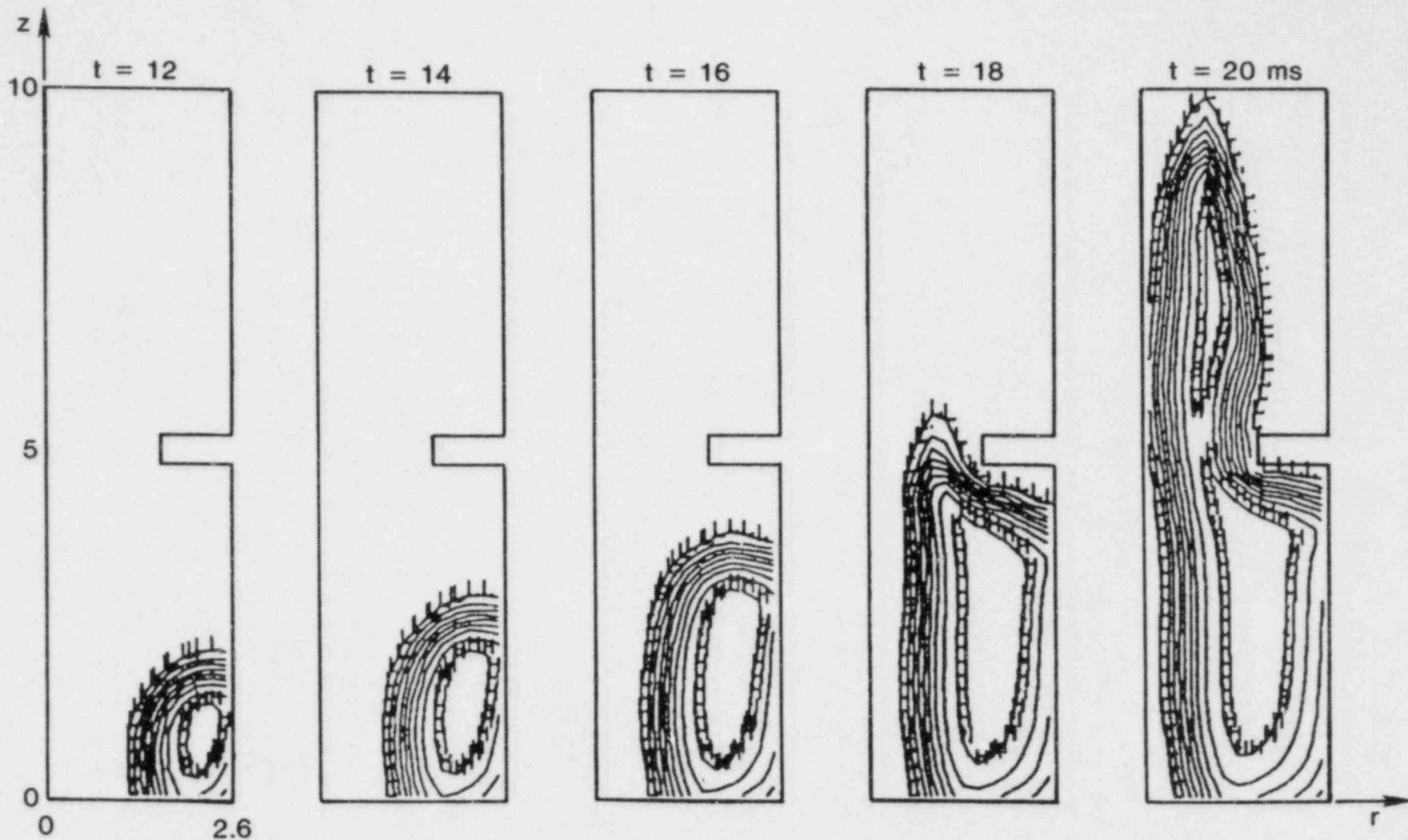
Figure 3.9.   Simulation of a Portion of the Hydrogen Flame Propagation in a Small-Scale Experiment.   The combustion takes place in a tube 5.2 cm in diameter by 10 cm long.   A washer-shaped obstacle of inside diameter 3.2 cm (blockage ratio = 0.62) is placed halfway down the tube.   The plots show isotherms at times (given in s) increasing to the right.   The coordinate system is cylindrical, with radial and axial dimensions given in cm on the first frame.

Isotherms are plotted in Figure 3.9 at various times during the progress of the flame. The letters H and L correspond to the high temperature of approximately 2500 K and the low temperature of 300 K, respectively. In the first frame, the mixture has been ignited and the flame is propagating away from the corner. (The 12 ms that have elapsed prior to this stage were spent in developing a relatively quiet ignition that would not produce unwanted acoustic waves or extreme numerical excursions.) Propagation is essentially isotropic at this time; the rate is the same in both the axial and radial directions. As the burn evolves, the expansion of the gas in the first chamber forces the mixture to jet through the orifice formed by the obstacle, carrying the flame with it. This results in a long tongue of flame extending into the second chamber, as shown in the fifth frame. The propagation of this jet proceeds so rapidly that combustion is not yet complete on the axis of the tube. (This phenomenon is sensitive to the configuration of the ignition source. The ring-shaped source was chosen rather than a point source on the axis because the latter leads to an even greater amount of unburned gas; in that case, the unburned portion is next to the side of the tube.)

This calculation required 20 min on the Cray-1 computer. The finite-difference mesh used here, a 14-by-51 uniform grid, was somewhat coarse; it might be necessary to halve the spacing for suitable accuracy. It may also be necessary to use a variable mesh spacing.

These results should be regarded as very tentative; we would not claim more than qualitative agreement with some of the features of real experiments. Considerable work needs to be done to check the computational accuracy and the numerical models involved. Obviously, a complete simulation of the McGill flame acceleration experiments would require many more chambers. However, since this will undoubtedly be out of reach from the standpoint of computer time, we intend to develop ways to derive useful information from modelling a few chambers at a time. This effort will benefit from the results of vortex dynamics calculations (see Section 3.1.2); in particular, we expect to obtain guidance on the treatment of the effects of turbulence from such results. Conversely, the CONCHAS-SPRAY calculations can provide pressure distributions that may be used in the vortex dynamics calculations. Hence, the two approaches are complementary.

3.1.4 One-Dimensional Flame Propagation Code ODFLAME
       (K. D. Marx and A. E. Lutz)

The ODFLAME code is now capable of providing calculations of the interaction of a laminar flame with evaporating droplets. The major developments over the past few months are as follows:

(1) Derivation of a droplet model and its inclusion in the code.

(2) The use of a detailed chemistry model in hydrogen flame calculations.

(3) The inclusion of detailed transport coefficients.

What follows are brief descriptions of the models used in the present version of the code and a sample calculation.

The code provides an unsteady solution to the basic equations for conservation of a mass and energy and for the transport of chemical species. We neglect the momentum transport equation and consider only ordinary deflagrations slow enough that uniform pressure is a reasonable assumption. Imposition of the constant pressure constraint permits the flow velocity to be determined from the mass conservation equation.

The droplet model that we use accounts for the transport of droplets and for heat and mass transfer between droplets and the combustible gas mixture. When this model is combined with the equations for gas flow, one obtains the following system of K + 6 partial differential equations, where K is the number of chemical species considered:

(a) The equations describing the gas mixture:

$$\frac{\partial \rho_g}{\partial t} + \frac{\partial}{\partial x} (\rho_g u) = - n_d \tilde{\rho} \dot{V}_d \qquad (3-14)$$

$$\rho_g C_{pg} \frac{DT_g}{DT} = \frac{\partial}{\partial x} \lambda \left(\frac{\partial T_g}{\partial x} \right) - \sum_k \dot{\omega}_k W_k h_k - \rho_g \frac{\partial T_g}{\partial x} \sum_k Y_k C_{pk} V_k$$

$$- n_d H_m A_d (T_g - T_d) + n_d \tilde{\rho} \dot{V}_d (h_w - h_w^d) \qquad (3-15)$$

$$\rho_g \frac{DY_k}{Dt} = - \frac{\partial}{\partial x} (\rho_g Y_k V_k) + \dot{\omega}_k W_k + (Y_k - \delta_{kw}) n_d \tilde{\rho} \dot{V}_d, \quad K=1,K \quad (3-16)$$

$$\rho = \frac{\rho_g RT_g}{W} \qquad (3-17)$$

(b) The equations for the droplets:

$$\frac{\partial n_d}{\partial t} + \frac{\partial}{\partial x}(n_d u) = 0 \qquad (3-18)$$

$$\tilde{\rho} V_d C_{pd} \frac{DT_d}{DT} = H_m A_d (T_g - T_d) + \tilde{\rho} \dot{V}_d \Delta h_v \qquad (3-19)$$

3-29

$$\frac{DV_d}{Dt} = \overset{\bullet}{V}_d \tag{3-20}$$

$$\overset{\bullet}{V}_d = \frac{-W_w}{\tilde{\rho}} K_m A_d \left(\frac{x_o - x_\infty}{1 - x_o} \right) \tag{3-21}$$

where the dependent variables required to describe the gas phase alone are density, ρ_g, velocity, u, temperature, T_g, and mass fractions, Y_k; the thermodynamic quantities are pressure, p, specific heats at constant pressure, c_{pg} and c_{pk}, and the enthalpies, h_k; the transport coefficients are thermal conductivity, λ, and diffusion coefficients that are used in determining the diffusion velocity, V_k, (but not shown here); $\overset{\bullet}{\omega}_k$ is is the chemical production rate of species k; and W_k and W are molecular weights and their mean, respectively.

Dependent variables required to account for the droplets are the liquid temperature, T_d, droplet volume, V_d, and droplet number density, n_d; additional quantities relative to the droplets and their interaction with the gas are the heat transfer coefficient, H_m, mass transfer coefficient, K_m, liquid density, ρ, specific heat, C_{pd}, heat of vaporization, Δh_v, and enthalpy, h_w^d of the vapor at the liquid temperature. The droplet surface area is A_d. The index of the droplet species is w; x_o and x_∞ are mole fractions of that species at the droplet surface and in the gas. The symbol δ_{kw} is the Kronecker delta.

These equations may be compared with those given previously for the gas mixture alone.[18] Note that the terms in Eqs. 3-14 through 3-16 involving variables with subscript d are those added to describe the interaction of the gas with the water droplets.

The code has been applied to the problem of a flame in a stoichiometric hydrogen:air mixture propagating through a distribution of water droplets. Figure 3.10 shows the configuration just prior to the collision of the flame with the droplets. The front of the droplet distribution is given a simple, smooth variation from zero up to the value $n_d = n_{di} = 10^5$ droplets/cm³. This value is assumed to extend uniformly to infinity in the positive x-direction. The initial droplet volume V_{di} is the volume of a 20-μm sphere. The volume ratio $Vol(H_2O)/Vol(mixture) = n_{di}V_{di}$ is 4.2 x 10^{-4}. The entire domain is assumed to be filled with a stoichiometric mixture of hydrogen and air. There is sufficient water vapor in the mixture to be in phase equilibrium with the water droplets at the ambient temperature of 300 K. A 13-reaction chemistry model is used to describe the reactions.[19] A new package of subroutines for computing transport properties is used to determine the thermal conductivity and the diffusion coefficients.[20]
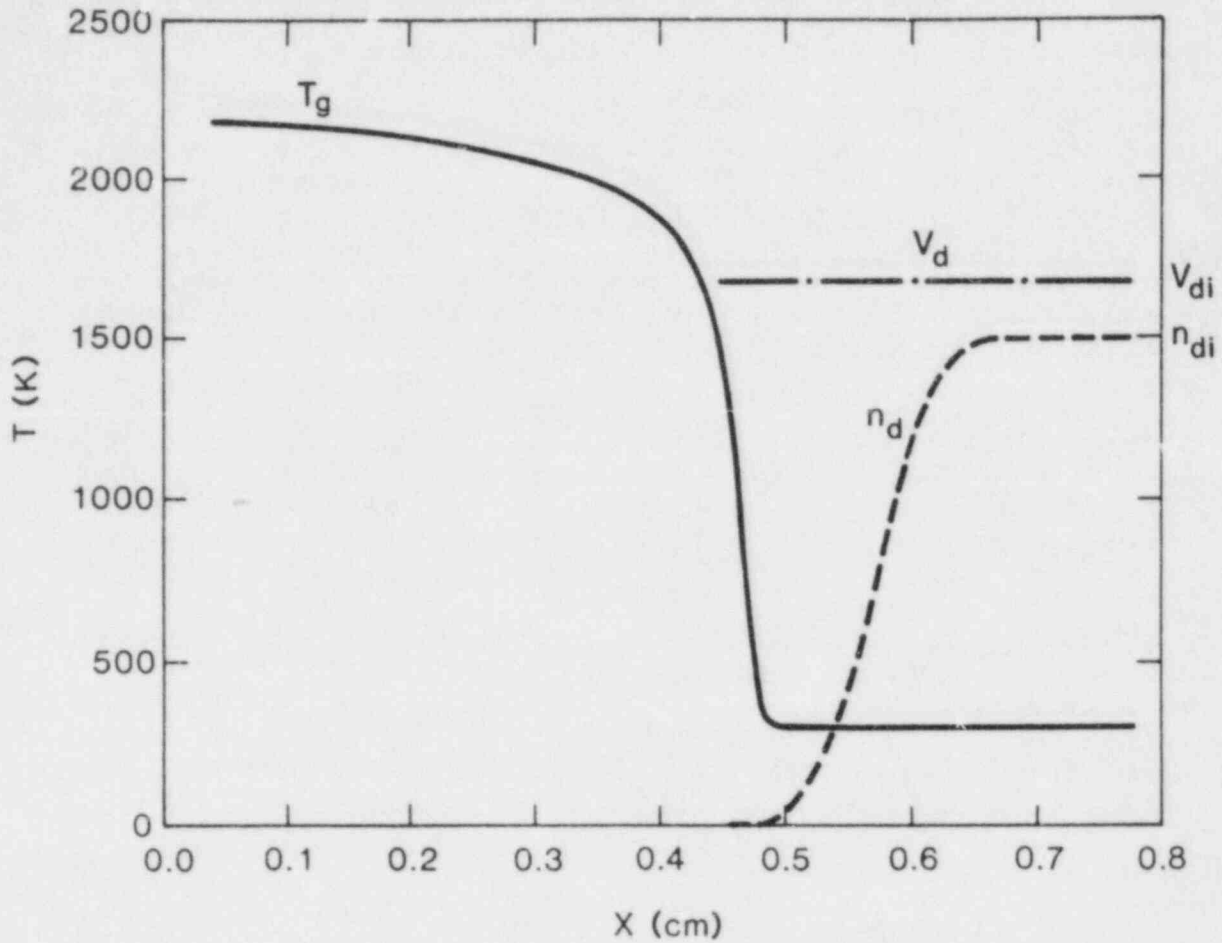
Figure 3.10. Gas Temperature, T_g, Droplet Volume, V_d, and Drop-
let Number Density, n_d, Just Prior to the Colli-
sion of a Stoichiometric Hydrogen:Air Flame with
a Droplet Distribution. The initial droplet
volume, V_{di}, is that for droplets with a dia-
meter of 20 mm. The initial number density,
n_{di}, is adjusted so that the volume ratio is
$Vol(H_2O)/Vol(mixture) = 4.2 \times 10^{-4}$. The flame
is moving toward the droplets at 253 cm/s.

In Figure 3.10, a flame has been ignited at the left. The flame front, identified by the steep gradient in gas temperature, T_g, is propagating toward the droplets at a burn velocity of 253 cm/s. Figure 3.11 shows the same profiles after the flame has passed some distance into the droplet distribution and has established a new steady state. The new burn velocity is 234 cm/s. The gas temperature behind the flame is drastically reduced due to the evaporative cooling by the droplets. The evaporation is evidenced by the decrease in the droplet volume behind the flame.

The position of the flame front in the above calculation is shown as a function of time in curve A in Figure 3.12. Curve B illustrates the result obtained when the volume ratio is multiplied by a factor of 10. In that case, the flame is quenched. The amount of water required to just quench the flame is defined by some volume ratio between these two. We are currently performing calculations to determine such propagation limits.

In the version of the code used to obtain these results, the droplets are assumed to move with the gas without slipping. This is not too severe an assumption for droplet diameters of 20 μm or less. However, it breaks down for larger drops. Procedures are being implemented to relieve this restriction.

The foregoing results demonstrate the capability of the computer code to provide data on burn velocities and propagation limits for flames in mixtures containing water droplets. This has the potential for aiding the design of flame mitigation systems in reactors and for providing a data base for empirical modeling of reactor accident scenarios by large-scale computer codes such as HECTR.[15] These are topics that we will be addressing in the immediate future.

3.1.5 Local Hydrogen Detonation Study
(R. G. Spulak, Jr., and R. K. Byers)

Three NRC-sponsored programs at Sandia contain tasks that address the concerns about local hydrogen detonations in containments after core damage accidents. These programs and their areas of concern are given in Table 3.4.

We have designed and initiated a program to study these concerns with a unified approach. This will avoid duplication of effort among the three NRC programs. This local detonation study will include two major efforts. First, the likelihood of local detonations at various locations in large dry, Mark III, and ice condenser containments will be assessed. Second, the consequences of detonations at the high-likelihood locations will be calculated. (The consequences include effects of equipment destroyed, missile generation, and pressure loading of the containment structure.)
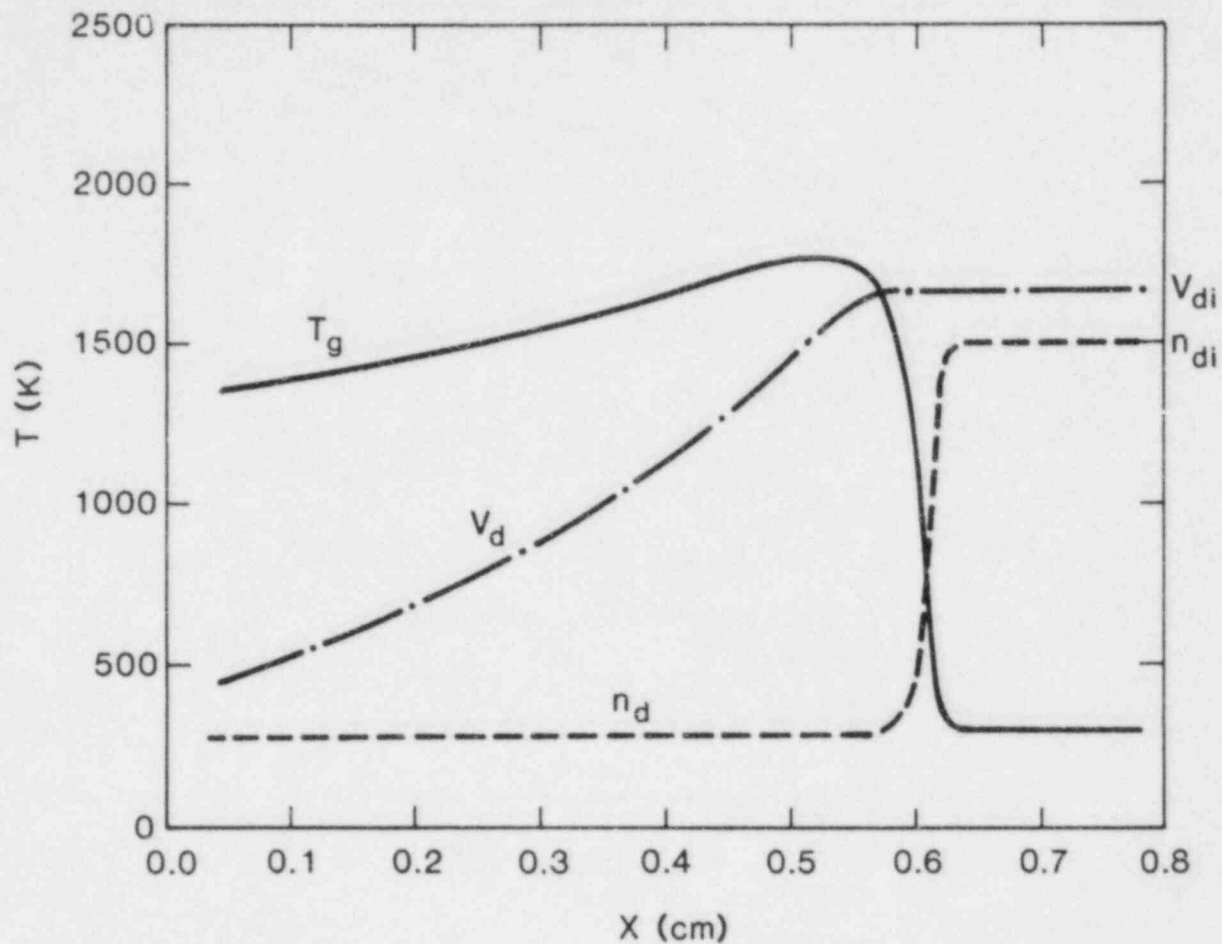
Figure 3.11. Results of the Calculation of Figure 3.10 After
the Flame has Penetrated into the Droplet Dis-
tribution and is Propagating with a New Steady-
State Velocity of 235 cm/s. (The computation
is performed in a coordinate system moving to
the right at 200 cm/s, so the distance scale on
the plot is not indicative of the flame posi-
tion in a stationary system.)
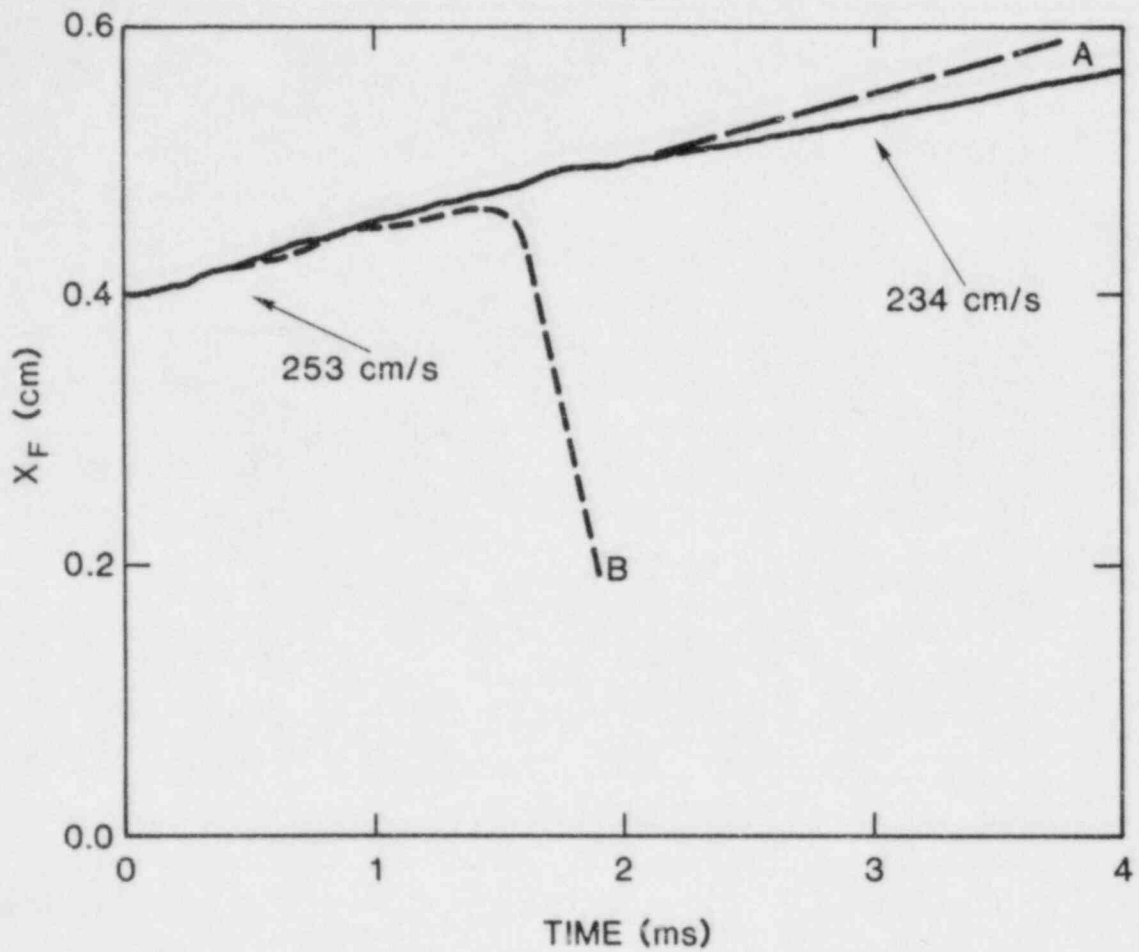
Figure 3.12. Flame Position vs Time for the Above Calcula-
tion (Curve A) and for a Similar One with a
Volume Ratio of 4.2×10^{-3} (Curve B)

Table 3.4

Local Detonation Tasks

NRC Program	Area of Interest
Hydrogen Behavior FIN A-1246	Missile Generation by Local Detonations
Review of the Grand Gulf Hydrogen Ignitor Program II FIN A-1301	Generic Likelihood and Consequences of Local Detonations
Hydrogen Burn Survival FIN A-1306	Effect on Risk of Equipment Destroyed by Local Detonations

The likelihood of local detonations will be assessed using
PRAs of representative plants for each containment type to
determine the most likely core damage accidents, the amount
and rate of generation of hydrogen, the release points of
hydrogen to the containment, and the state of equipment such
as fans and deliberate ignition sources. This knowledge
will be used in conjunction with plant design information to
deduce the transport and mixing of hydrogen inside the con-
tainment with respect to potential locations of locally high
(detonable) concentrations of hydrogen. The existence and
probability of ignition sources at these locations will also
be addressed.

The consequences of local detonations will be assessed by
first determining the safety equipment and potential missiles
at each location. The pressure loading on the containment
structure and forces on the potential missiles will be cal-
culated using detonation and structural response computer
codes. The effects of destroying safety equipment will be
analyzed by modifying the accident sequences of existing
PRAs to include those failures.

We have selected the Reactor Safety Study Methodology Appli-
cations Program (RSSMAP) Oconee, Grand Gulf, and Sequoyah
PRAs as examples of risk analysis of plants with large dry,
Mark III, and ice condenser containments. The other plant
information needed will be gathered by tours of these or
similar plants.

At this time, the major portion of this program, evaluation
of the likelihood and consequences of local hydrogen detona-
tions, has not begun because we have been unable to examine

representative containment designs and obtain the necessary plant drawings. There are two other efforts that merit mention here. The first is performance of a set of CSQ code detonation calculations for arbitrary volumes in the Sequoyah containment, done at the request of Charles Tinkler, Nuclear Reactor Regulation (NRR). The results of these calculations will be reported soon.

The second effort was to perform CSQ detonation calculations for the Nevada Test Site dewar, which will be used as a vessel for hydrogen burn studies. These calculations were done at the request of EPRI, which is sponsoring those studies. Two calculations were performed, with 0.2 hydrogen and 0.5 hydrogen by mole fraction. Table 3.5 gives the thermodynamic states for these mixtures.

The dewar is an 8-m-radius sphere, and the detonation in each case was initiated at a point on the vertical axis 2.4 m above the bottom. The pressure histories at the wall at the top of the sphere (on the vertical axis) are shown in Figure 3.13. For the case with 0.2 hydrogen, the maximum pressure at this point was about 3 MPa (30 atm) at the time of the first arrival of the detonation wave. For the case with 0.5 hydrogen, the maximum was about 6.5 MPa (64 atm), not at the time of the arrival of the detonation, but later due to constructive interference of reflected shock waves on the axis. (The calculation with 0.2 hydrogen was not carried out to a late enough time to observe the second peak.)

The maximum pressures at the wall in both cases were calculated to be 1.75 m above the horizontal "equator" at the time of the first arrival of the detonation wave. This maximum for the 0.2 hydrogen case was 5.4 MPa (53 atm) and for the 0.5 hydrogen case was 10 MPA (99 atm). The results of these calculations have been sent to an EPRI contractor, Structural Mechanics Associates. They will calculate the impulsive loads and structural response from the CSQ results and knowledge of the structure.

3.1.6 Modification of Nuclear Reactor Containment Atmosphere to Reduce Risks from Hydrogen Combustion
(L. S. Nelson, P. G. Prassinos, E. W. Shepherd)

We are investigating several relatively simple and inexpensive schemes to minimize or eliminate threats of failure of nuclear reactor containments during hydrogen combustion situations by partially depleting the oxygen in the containment. We are estimating the worst hydrogen combustion threat for these situations by assuming the maximum possible energy is added to the containment, that is, when the hydrogen concentration is twice the oxygen concentration. By reducing the amount of oxygen available for combustion, it is possible to reduce the containment pressure and temperature rises resulting from a burn.

Table 3.5

Thermodynamic States for Hydrogen:Dry Air Mixtures
(Air Partial Pressure ~0.1 MPa; Initial Temperature = 300 K)

Initial Conditions P(MPa)	ρ(kg/m^3)	Isochoric Burn P(MPa)	T(K)	C-J Detonation P(MPa)	T(K)	Isentrope from C-J State to Initial Density P(MPa)	T(K)
For hydrogen mole fraction = 0.2.:							
0.13	1.20	0.84	2204	1.62	2429	0.81	2136
For hydrogen mole fraction = 0.5:							
0.20	1.26	1.43	2358	2.77	2610	1.38	2280
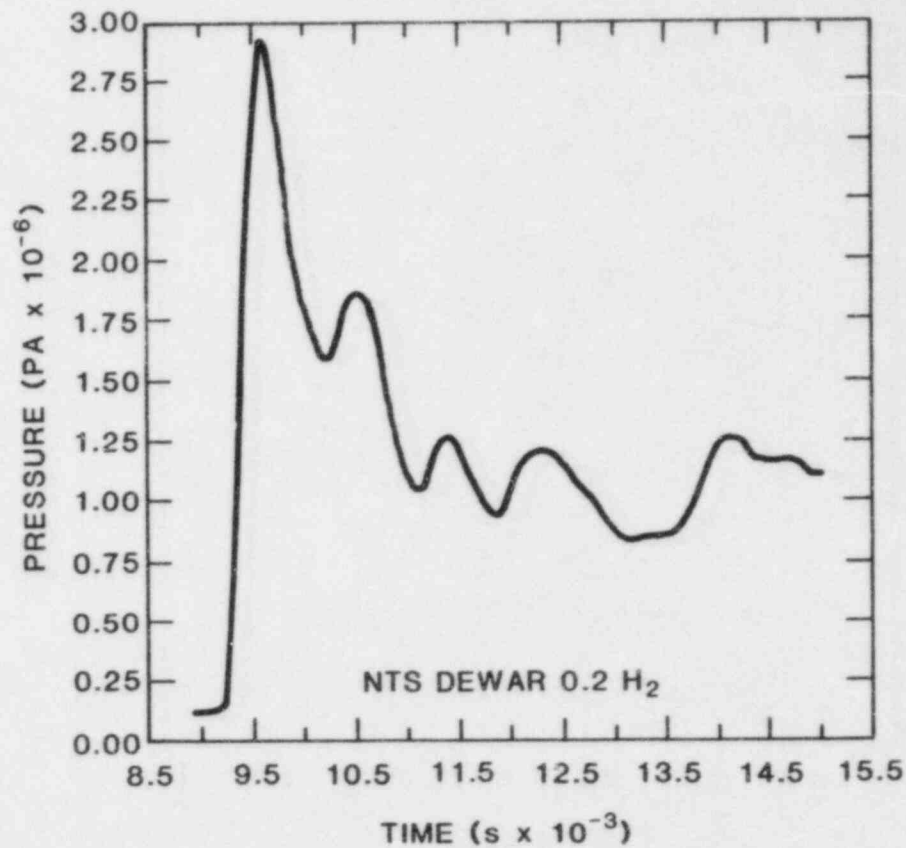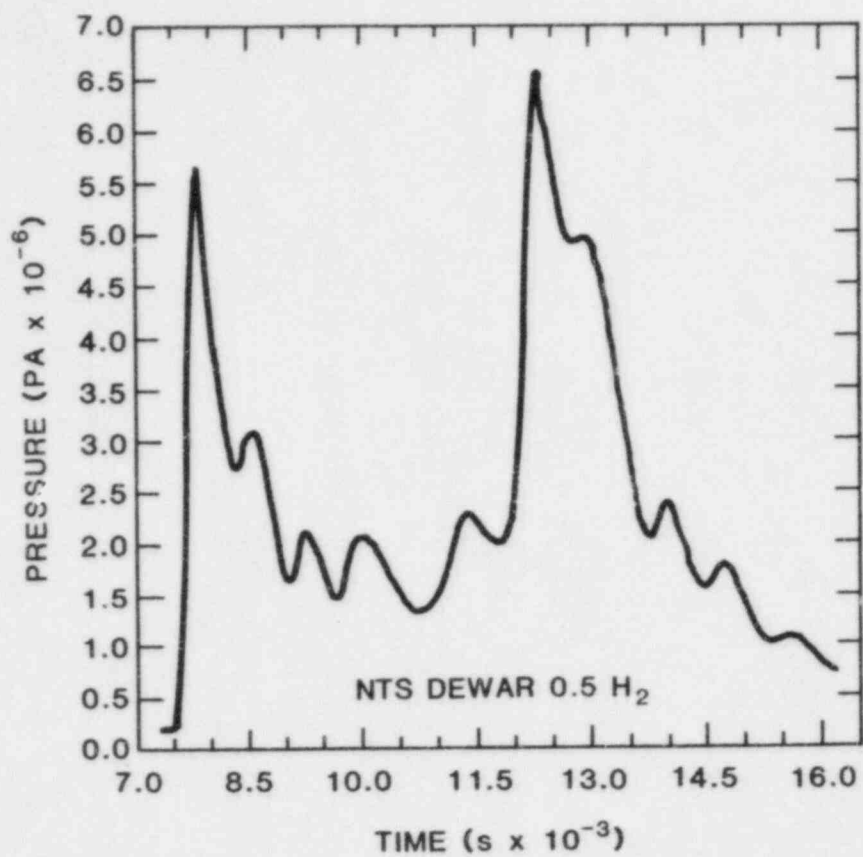
Figure 3.13. Pressure Histories at the Wall on Axis at the Top of the Sphere

In the estimates, we consider the following oxygen depletion schemes:

(1) Initial depletion of the oxygen in the containment atmosphere from 21% (normal air) to 14% (the minimum safe breathing level for sustained working). This depleted air would be obtained by adding nitrogen to the containment until the oxygen concentration was 14% and by venting until the pressure was reduced to 1 atm.

(2) A "bag" rupture method for adding carbon dioxide to the containment to suppress combustion and partially deplete the oxygen. This method involves filling unused volumes in containment with carbon dioxide separated from the working areas by rupturable membranes. A diluent gas of high heat capacity could be added to the containment when necessary without increasing the internal pressure.

(3) A combination of 1 and 2.

In these analyses, we are estimating the peak pressures and temperatures that may result in the containment by using the NASA-Lewis adiabatic isochoric complete combustion (AICC) code. Our analyses have been performed for the Zion containment; however, the concepts are easily extended to other containments by simple proportioning.

3.2 <u>Experimental Facilities, Tests, and Plans</u>

3.2.1 FITS Facility
    (W. W. Marshall, Jr., S. F. Roller)

In October and November, preparations were made for the second series of hydrogen behavior testing and preliminary testing was conducted. Before this test series was begun, the pressure transducers were mounted flush with the tank walls in two ports. Felt metal flame arrestors were used to protect the Kulite pressure gages from any thermal pulses.

In the first part of December, the second series was begun. The instrumentation employed during these tests included:

(1) Thirty-two 12-mil thermocouples.

(2) Four strain-gage type pressure transducers:

    a. Three air-cooled Precise Sensors with operating ranges of 0 to 100 psi and 0 to 200 psi and resonant frequencies of 80 to 125 kHz.

    b. One Kulite pressure gage with an operating range of 0 to 100 psi and a resonant frequency of 130 kHz.

(3) Two thin film heat flux gages (one radiative and one total) with response times of approximately 1 ms.

(4) One radiative and two total thick film calorimeters.

This series of tests attempted to address the following:

(1) The effects of steam and carbon dioxide as diluents in hydrogen:air mixtures.

(2) The flammability limits of hydrogen:air, hydrogen:air: steam and hydrogen:air:carbon dioxide mixtures.

(3) To characterize statistically very lean burns of hydrogen in air.

Test series #2 lasted until the middle of February 1983, consisting of 85 burns (hydrogen volume percentages ranging from 4% to 60%, steam percentages from 10% to 40%, and carbon dioxide percentages from 9% to 40%), at which time site management and planning was taken over by division 9441. Susan F. Roller of division 2513 is presently preparing a report on test series #1 and #2.

In the last part of February, test series #3 began. The test series is presently on-going and attempts to experimentally define the flammability limits of hydrogen:air:steam mixtures with hydrogen volume percentages ranging from 5% to 60% and steam percentages from 0% to 60%. These tests were conducted with air partial pressures equal to 1 Albuquerque atm and initial temperatures of approximately 110°C. The instrumentation used in this test series is the same as that listed above for test series #2.

The preliminary results of the 75 tests completed for the experimental flammability limits of hydrogen:air:steam mixtures in a stagnant (fans off) environment are shown in Figure 3.14. In this figure, "□" represents a no-burn mixture, "O" represents a mixture that ignited. In Figure 3.15, the experimental flammability limits of hydrogen:air:steam mixtures in a turbulent (fans on) environment are shown.

The theoretical maximum pressure for each hydrogen:air:steam mixture in test series #3 was calculated using the "Sandia Simplified AICC code." In Figure 3.16, the ratio of the experimental maximum pressure to the maximum theoretical pressure is plotted against the ratio of the steam volume percentage to the hydrogen volume percentage. It appears from this plot that there is a significant reduction in the percentage burned and therefore the maximum pressures obtained when the steam:hydrogen ratio is approximately 3.5. It should be noted that these points represent a variety of mixtures of hydrogen, air and steam (those plotted in Figures 3.14 and 3.15). Therefore, it appears that if the
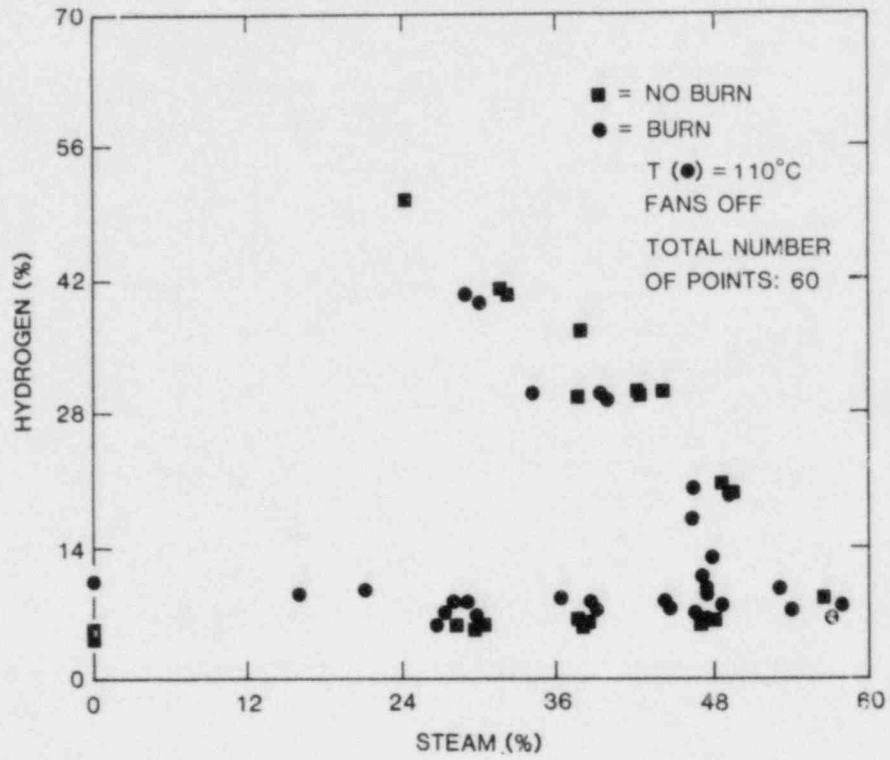
Figures 3.14.   Flammability Limits for Hydrogen:Air:Steam
Mixtures (Stagnant Environment)
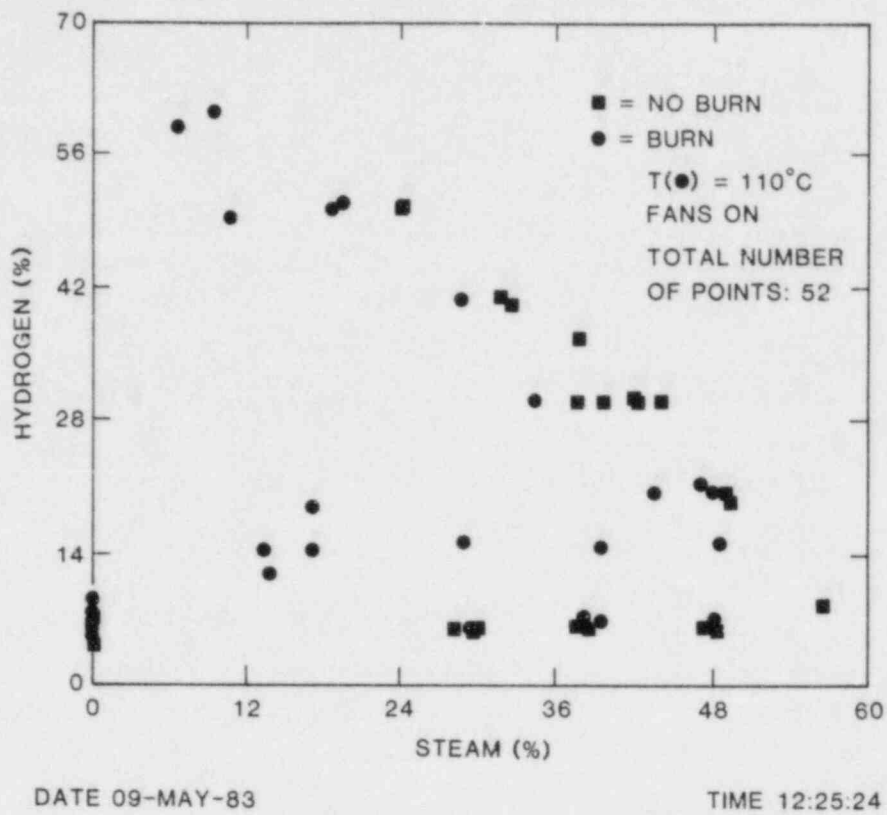
Figure 3.15. Flammability Limits for Hydrogen:Air:Steam
Mixtures (Turbulent Environment)

MAXIMUM PRESSURE RATIO VS. MIXTURE RATIO
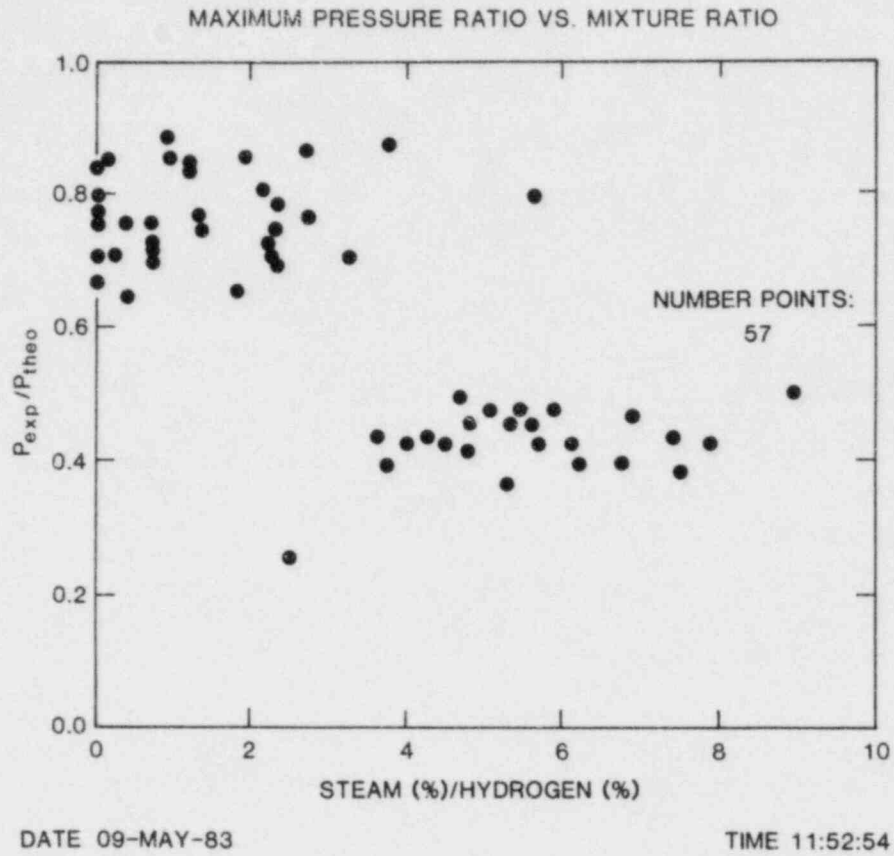
Figure 3.16.   Maximum Pressure Ratio vs Mixture Ratio

steam:hydrogen ratio exceeds about 3.5 for any percentage of hydrogen, the combustion process is significantly inhibited by the steam. Many more data points are needed to confirm this, but there is a substantial difference between the maximum pressures above and below this mixture ratio. This is also shown in Figure 3.17, where the experimental maximum: initial pressure ratio is also plotted against the mixture ratio. As in Figure 3.16, there is a significant difference between the maximum pressures achieved below a mixture ratio of 3.5 to that above a ratio of 3.5. Again, many more data points are needed to confirm this apparent critical mixture ratio.

Testing at the FITS facility during the next semiannual period will include the following:

(1) Complete the hydrogen:air:steam testing (test series #3).

(2) Perform thermal effects testing on the pressure transducers.

(3) Define the flammability limits of hydrogen:air:carbon dioxide mixtures similarly to those of test series #3.

3.2.2 Detonation Propagation from Narrow Channels
(W. B. Benedick, P. G. Prassinos, C. J. Daniel, R. Knystautas)

A hydrogen:air flame started within a confined space with many obstacles in the flame path may accelerate and be detonated. This phenomenon has been observed in many experiments and is a commonly employed method used to obtain a detonation in a closed tube. A short length of copper tubing is wound in a spiral and inserted within the detonation tube. Upon ignition of the gas mixture, the advancing flame is accelerated when passing over the spiral form and reaches detonation velocity in a short distance.

When the detonation emerges from a tube or channel into a larger open volume, the continued propagation of the detonation is dependent upon certain conditions. Experiments with detonations emerging from tubes have been shown to require a minimum of 13 detonation cells, λ, across the diameter of the tube for continued propagation of the detonation. These critical tube diameter data have been reported earlier for both rich and lean hydrogen:air mixtures.

Recent experiments at the McGill University laboratory by John Lee and his coworkers have indicated that detonation propagation from narrow slots require a slot width of only 3 detonation cell widths, i.e., 3 λ. This observation greatly increases the number of places in containment where detonations may emerge from confined areas and continue to
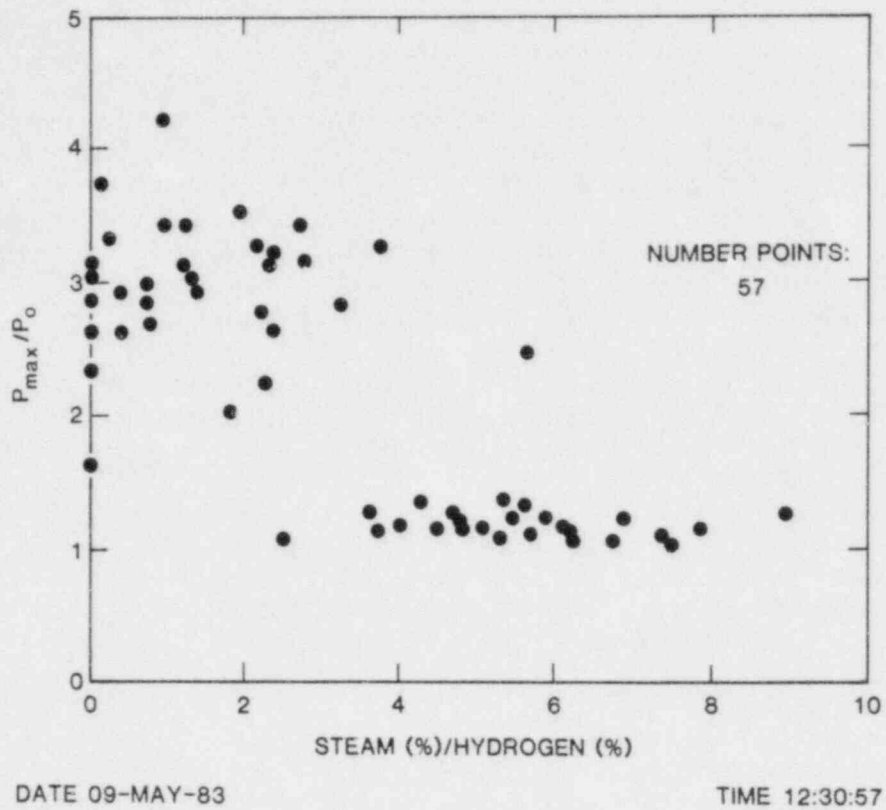
Figure 3.17. Ratio of Maximum to Initial Pressure vs Mixture Ratio

propagate. Consequently, it was desirable to test this phenomenon on a large scale to insure that it is not limited to laboratory-scale apparatus which use sensitive hydrogen:air mixtures.

The large-scale experimental detonation channel consisted of two 25-mm-thick steel plates that were 1.83 m wide and 2.44 m long. The channel height "W" (spacing between the plates) was varied by using four spacer blocks placed at each of the four corners of the plates (Figure 3.18). One of the side walls of the channel is formed by a sheet of clear plastic to permit photographic observations of the detonation propagation in the channel, while the opposite side wall of the channel is simply covered by a plywood sheet. The closed initiation end of this two-dimensional detonation channel is also formed by a sheet of plywood, onto which are taped thin strips of sheet explosive for initiating the gas detonation.

The high-explosive strips are centrally initiated by a detonator. The plastic and plywood side walls and the initiation end of the channel are blown off in the experiment and have to be replaced for each test. The open end of the two-dimensional detonation channel is connected to a large polyethylene bag fabricated from 100-μm-thick sheets that are then taped to the steel plates. The filling procedure consists of first retracting the entire plastic bag into the channel with a vacuum pump thus removing all air in the system. Then a premixed hydrogen:air mixture from a large underground storage tank is introduced into the channel and the plastic bag is thus extruded from the channel as the system is being filled with the explosive gas mixture. The final pressure in system is slightly above ambient so that the plastic bag remains taut. On windy days or when the hydrogen:air mixture concentration is such that the bouyancy of the bag is significant, thin nylon ropes are used to anchor the plastic bag in the horizontal position. The detonation channel and the bag assembly are placed on a thick concrete pad with the plates extended about 0.55 m over the edge of the slab to allow room for the inflated plastic bag. Diagnostics are based solely on high-speed cinematography. Detonation velocity as well as successful transmission or failure can be discerned quite readily from the movie record. Hydrogen:air as well as ethylene:air mixtures have been used, and the desired composition in the mixing tank is obtained by using the method of partial pressures. To measure the detonation cell size, carbon smoke is deposited on a thin aluminum sheet by a welding torch. The smoked aluminum sheet is then taped to the bottom steel plate of the detonation channel. It was found that the "smoked" sheet remains "in place," and cell size can readily be determined from it after the experiment. With this two-dimensional geometry, it is also possible to test the symmetry of the transmission process about the centerline of the channel. By retracting the top plate of the channel relative to the bottom plate and
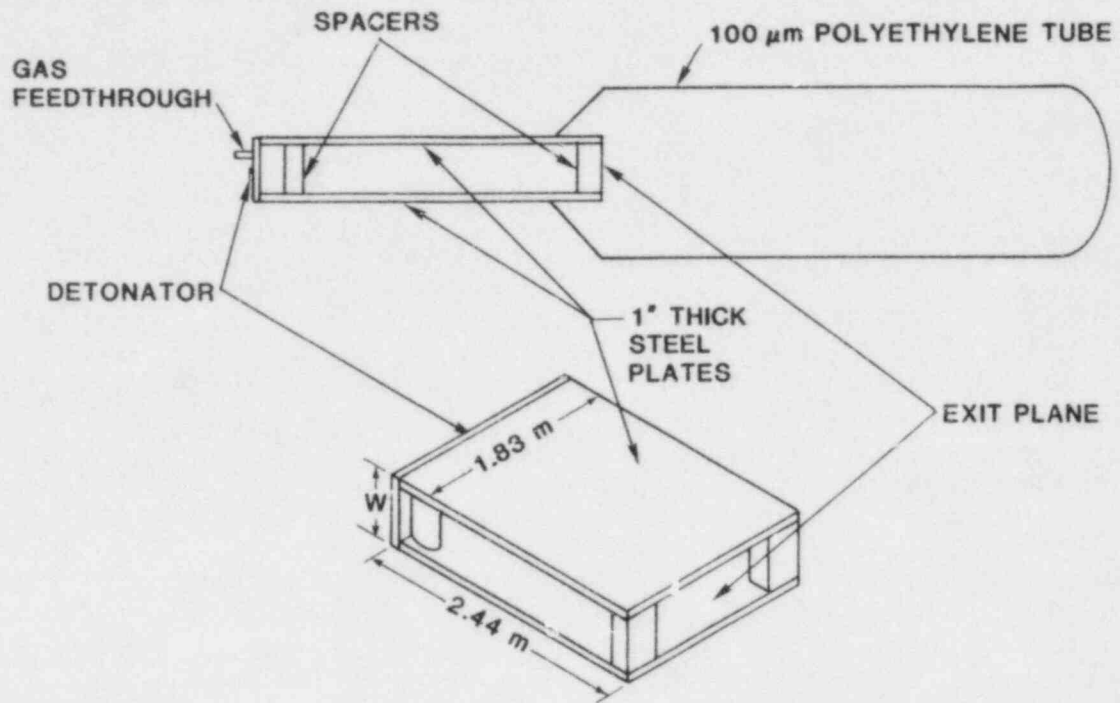
Figure 3.18. Two-Dimensional Channel Apparatus with Unconfined Exit Plane

adding an additional plate to the bottom, it is possible to construct a half channel, and accordingly transmission would now be possible for a spacing between the plates corresponding to only 1.5λ. This experimental system is shown in Figure 3.19.

Rich mixtures of hydrogen:air are not used in the present series of experiments since the objective is simply to verify the empirical law, $W_c \sim 2/\lambda$, for two-dimensional channels into a pen spare (i.e., critical channel height). Extensive experiments have already been carried out for the rich hydrogen:air mixtures for circular tubes and have been reported previously.

The results for the critical channel height for which successful transmission of planar waves from the confined channel to become cylindrical waves in the unconfined mixtures in the plastic bag are given in Figure 3.20. The critical channel height, W_c, is normalized with respect to the characteristic cell size, λ, of the mixture, and W_c/λ is plotted against the aspect ratio of the channel L/W. For large aspect ratios (L/W > 10), the present results give a value, $W_c/\lambda \simeq 3$, which agrees with the results obtained at McGill University by Liu using rectangular orifices instead of a full two-dimensional channel. Experiments up to <u>very</u> large aspect ratios, ie., L/W > 30, yield the same value for $W_c/\lambda \simeq 3$, indicating that the critical channel height, W_c, scales according to the cell size, λ, and within the present experimental accuracy, W_c does not depend explicitly on the Chapman-Jouguet states. An experiment is also carried out for a fuel other than Hydrogen (i.e., C_2H_4) at an aspect ratio, L/W $\simeq$ 18. Again, the result of $W_c/\lambda \simeq 3$ is obtained for ethylene as well, strengthening the argument that the scaling law is based only on the cell size, λ, as observed for circular tubes.

For aspect ratios, L/W < 10, the present results indicate that the value for W_c/λ rises sharply. A similar trend was also obtained by Liu for the case of transmission through rectangular orifices. However, for the smaller scale orifice experiments of Liu, the increase does not occur until L/W < 5. For the square orifice (L/W $\simeq$ 1), the data points obtained by Liu indicate that $W_c/\lambda \simeq 10$. The reason three-dimensional effects begin to become important at larger aspect ratios for channels (L/W < 5) is not apparent at present. Boundary layers on the two side walls of the present channel, as well as the rarefaction waves produced by the side relief as the plywood and plastic side walls of the channel are being blown apart by the detonation propagating in the channel, could account for the earlier onset of three-dimensional effects. Qualitatively however, the present channel experiments agree with the rectangular orifice plate experiments of Liu.

To test the symmetry of the two-dimensional transmission about the centerline, several experiments using 20 to 20.5 hydrogen:
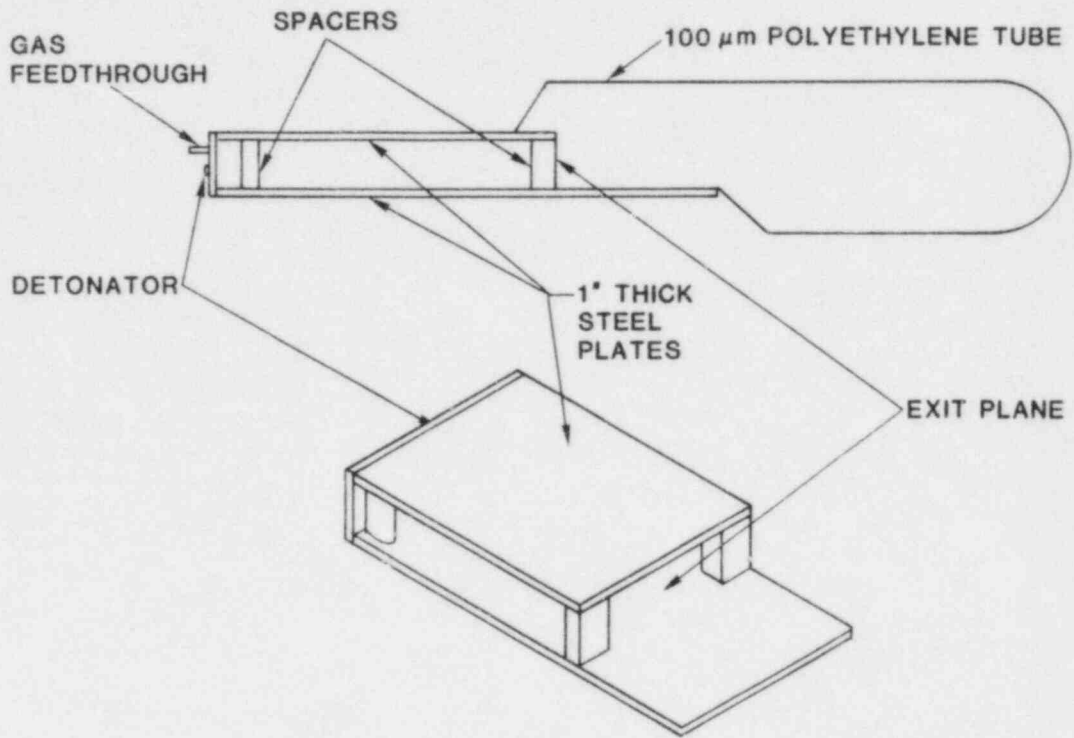
Figure 3.19. Two-Dimensional Channel Apparatus with "One Degree of Confinement" at the Exit Plane
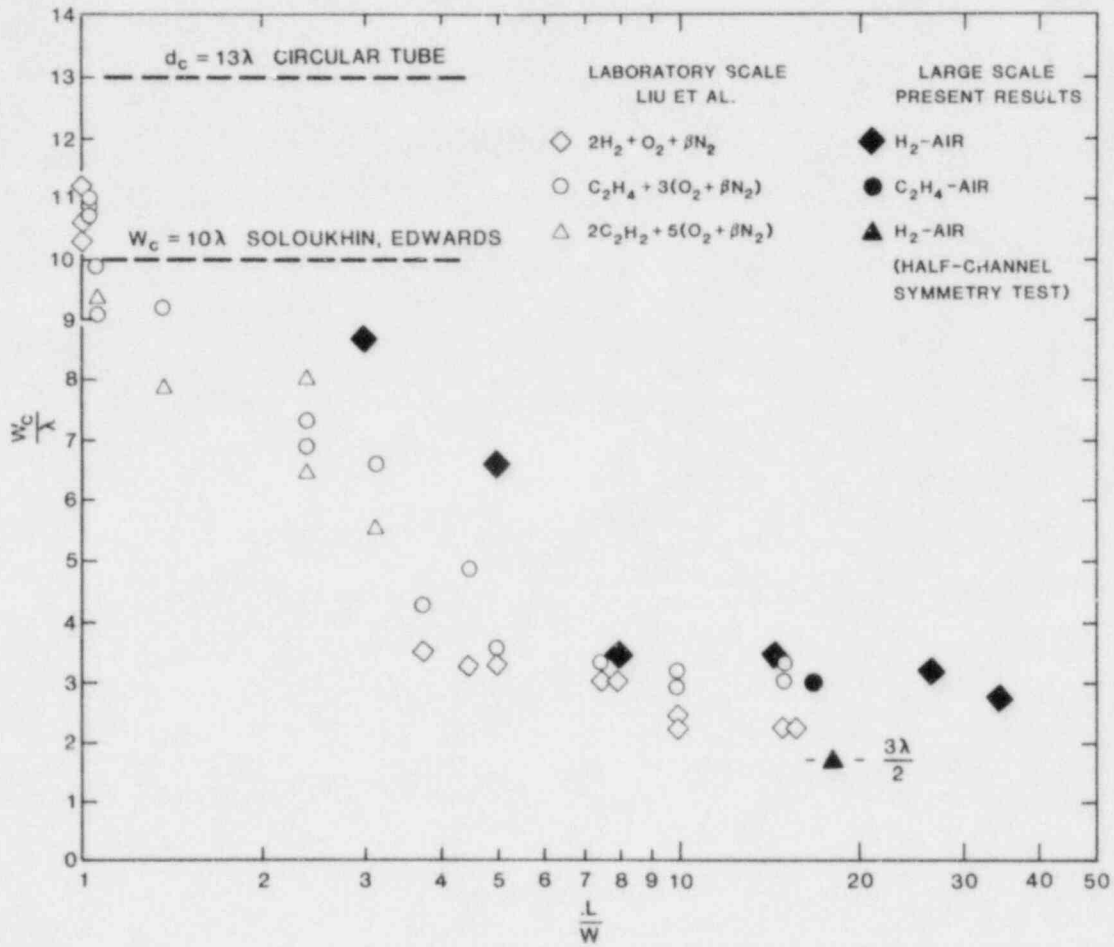
Figure 3.20. Critical Channel Height vs Aspect Ratio of Detonation Propagation

air mixtures with W = 10 to 10.5 cm, L = 1.82 m, and L/W = 17.5 to 18.2 were performed. The results yield a critical spacing between the plates of close to 1.5λ (Figure 3.20).

The present series of large-scale tests confirms the smaller laboratory experiments of Liu that transmission from confined planar detonations to unconfined cylindrical detonations requires a critical channel height of approximately three cell diameters (i.e., $W_C \simeq 3\lambda$). Also, the two-dimensional transmission phenomena appears to be symmetrical about the central plane; thus, a spacing of only about 1.5λ is required when supported by one plane. Furthermore, the channel results are similar to the results from a rectangular orifice. This suggests that the re-initiation mechanism is very local and does not depend strongly on the flow structure of the product gas emerging into confined space behind the leading front.

3.2.3 Combustion of Hydrogen:Air Mixtures Encased in Aqueous Foams
(W. B. Benedick, P. G. Prassinos, C. J. Daniel)

This experimental series for combustion of hydrogen:air mixtures encased in aqueous foam has been completed. We previously reported that when 10% and 15% hydrogen:air mixtures were encased in a 620:1 expansion foam (H_2O = 1.57 kg/m³), both peak pressure and temperature were reduced when compared to burning the same mixture without foam. The first experiment using 20% hydrogen:air mixture encased in foam indicated that an accelerated flame velocity was obtained. However, the data sampling rate was too low (5 ms) to obtain a good velocity measurement.

Experiments with the 20% hydrogen:air mixture were repeated using a faster sampling rate to better resolve the flame velocities. Figure 3.21 shows the data obtained from this series of experiments. The flame velocity for the foam-encased 20% hydrogen:air mixture was more than six times the velocity of the nonfoamed mixture. The best explanation for this observed phenomena is that the initial rapid burning velocity results in a rapid rise in pressure, which causes the bubbles to collapse far ahead of the advancing flame. Bubble collapse leads to flame propagation into a turbulent mixture, which causes further flame acceleration. For the leaner mixtures, the flame velocity is much lower and hence the rate of pressure rise is lower. The lower rate of pressure rise allows time for the foam bubbles to change dimension without collapsing and generating turbulence.

For both experiments in which an accelerated flame was observed, the foam generator was severely damaged. An accelerated flame produces a sufficiently strong shock to result in damage to equipment. For lean hydrogen:air mixtures,
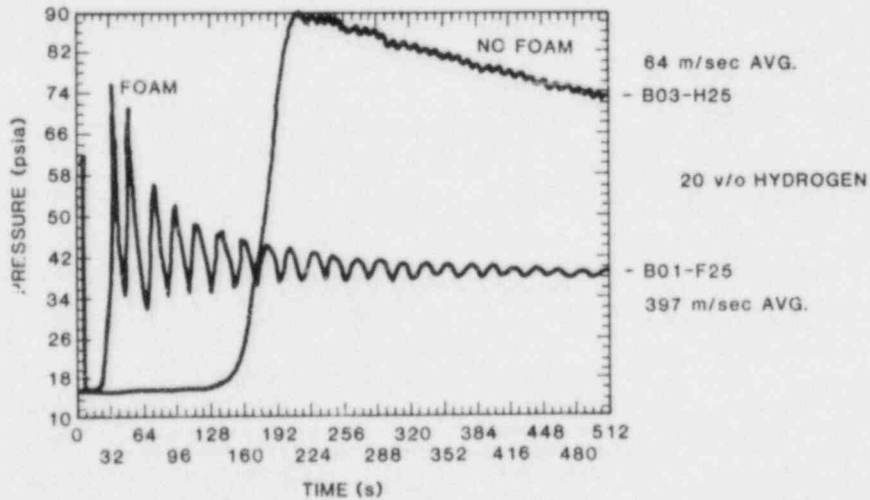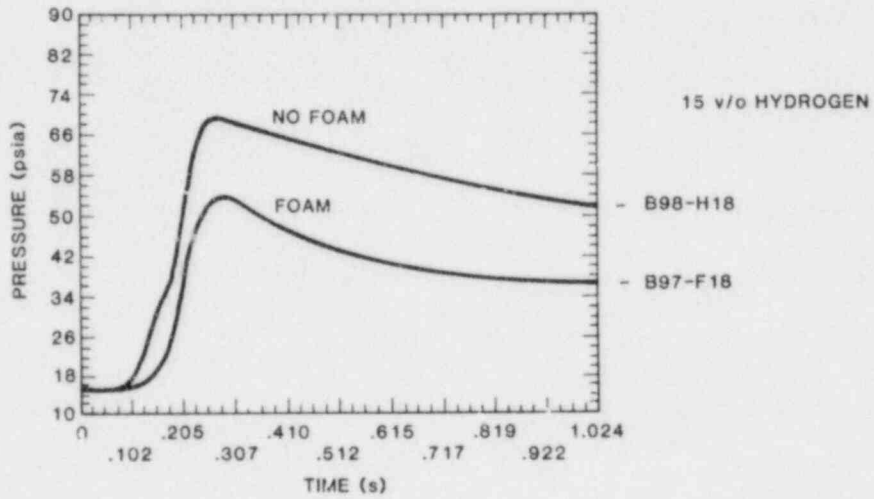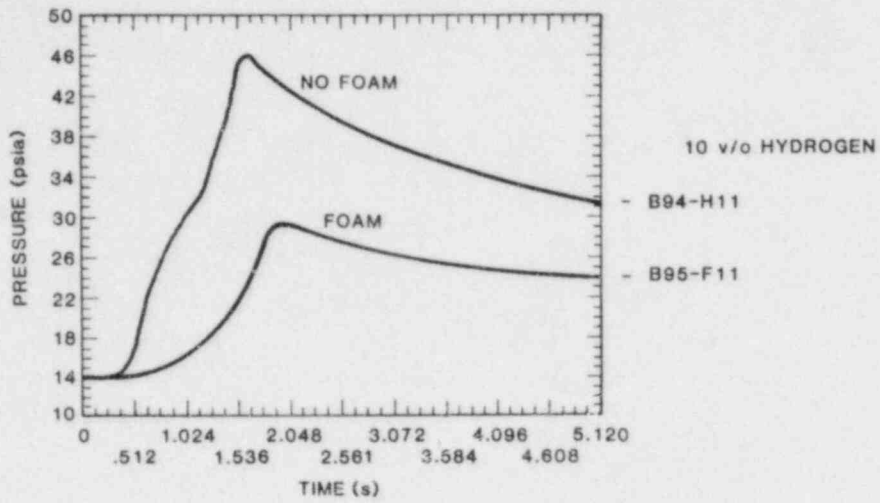
Figure 3.21.   Pressure vs Time for Combustion of Hydrogen:
Air Mixtures Encased in Aqueous Foam

aqueous foam encasement is certainly beneficial. However, use of foam as a mitigant would have to be limited to only those instances where a lean hydrogen concentration could be assured.

3.2.4 Flame Facility
(J. W. Fisk, M. P. Sherman, S. R. Tieszon)

Five contractors submitted bids on 21 October 1982 for the construction of the FLAME facility. These bids were individually reviewed and evaluated by selection panel members. The members met on October 28, 1982 to submit their findings and choose the winning contractor. The contract was officially awarded to Cardenas Construction Company of Albuquerque, New Mexico, on November 11. A preconstruction conference was held on November 16 at Sandia National Laboratories Plant Engineering to discuss the FLAME facility construction, assign inspectors, and introduce key personnel. Work on the facility began on November 26 with first ground breaking on December 3.

The projected facility completion date was January 25, 1983, 60 days after work on FLAME began. The groundwork, footing preparation, embed alignment, and strain gage installation were completed in December and early January. The footing was poured on January 11. Inclement weather, erroneous bending of reinforcing steel, and the Christmas holidays caused the delay. The walls for FLAME were poured in four sections. The first pour was on February 22, and the fourth and last pour was made on March 28. The contractor badly underestimated the amount of time and effort required to install the reinforcing steel, the access pipes, the viewports, and the fixtures to hold the embeds in place. Additionally, this crew had not previously used plasticizer in concrete and consequently did not vibrate the concrete sufficiently to fill all gaps and voids in the wall of the first pour. This "honeycombing" occurred on the exterior surfaces and near the base where the vibrator could not easily reach. This situation was remedied by using a smaller diameter hose to pour the concrete nearer the bottom of the wall and by cutting portholes in the form to allow the vibrators access to the bottom and sides of the wall. All subsequent wall pours did not suffer the severe honeycombing of the first wall pour. The honeycombing was repaired by using a high-compressive-strength nonshrink grout bonded to the concrete by an epoxy adhesive.

The contractor provided all 38 steel top plates and 1 end plate. The contractor has installed one-half of the top plates, evenly spaced, to set up for the configuration required for the shakedown tests. Installation of scaffolding, ground contouring around FLAME for watershed purposes, and general cleanup of the site should be completed in April. The steel channels for reinforcing the end plate and the top

plates were delivered in March and will be installed prior to the shakedown tests. All of the structural components needed to run open-ended tests in FLAME are on hand.

Since some tests are desired with both ends of FLAME closed, a second end plate and steel reinforcing channels will be ordered in April. These types of tests will necessitate reinforcing the unsupported top of the end plate with steel angles or their equivalent.

FLAME will incorporate several operating systems: a data acquisition system, a bag extension system, a hydrogen transfer and mixing system, a gas sampling system, and an ignitor system. The data acquisition system hardware has all been received and installed. The RG-174/U coaxial cable came in, and several cable assemblies have been made to interface the digitizers, the clock generators, the trigger generators, the amplifiers, and the patch panels. The final link between FLAME and the instrumentation cabinet will be the multipair cables. A work order for instrumentation/power cable pits/ trenches and junction boxes from VGES, FLAME, and the Detonation Tube to the blockhouse was placed with Sandia plant engineering as of February 7. This work is not expected to be completed until after June 1.

In the course of the development of the computer software, hardware problems with the data acquisition system have been discovered. At present, the problems have been solved except for newly discovered ones in the trigger generators. Two LeCroy 8610B trigger generators have been sent back to the factory for repair. We have begun to test the use of the system and gain experience operating it.

The bag extension system consists of some plastic sheets to enclose the ceiling and end plate, a collapsible plastic bag at the open end of the facility to allow addition of hydrogen to the facility, a bag guiding system to hold the bag in place as the bag extends, and a windbreak to protect the bag during and after filling prior to a burn. The plastic sheet and bags are on hand. The parts for the bag extension system and the windbreak are also on hand. The poles to anchor the windbreak and the bag extension system will be installed in April.

The hydrogen-transfer system consists of a 943-m^3 trailer, remotely operated valves, grounding wires, piping, check valves, a mass flowmeter, and some flame arrestors.

The gas sampling system consists of a gas sampling bottle, sandwiched between two solenoid valves, a vacuum bottle to provide flow, and the miscellaneous piping. There are five sets of these sampling systems spaced along the 30-m length of FLAME. All samples will be taken simultaneously by opening the solenoidal controlled valves and letting gas mixtures

pass through the sampling bottle to the vacuum bottles. Shutoff will occur before the vacuum bottles are filled to capacity.

FLAME will incorporate a ternary ignitor system consisting of a spark gap device, an exploding bridge wire, and a Tayco 120-VAC glow plug. These three systems will have independent firing circuits. Most of the parts are on hand awaiting assembly.

An additional video camera has been purchased as a safety feature. It will provide a visual check of the far side of the FLAME Facility and the detonation tube that cannot be observed by a camera mounted on the main building by the blockhouse. The new camera will be mounted on a tower that will be located southwest of the FLAME facility and the detonation tube. This camera should be operational in May.

Lift devices must be designed and built to remove and install the steel end plate and to adjust the spacing of the top plates for different tests. The fabrication and assembly of these devices should be completed by June.

Basic instrumentation devices include pressure transducers, germanium photodiode systems, lithium niobate gauges, thermocouples, ionization gauges, and possibly hot wire anemometers and heat flux gages.

Eight Kulite gages are now on hand. A voltage regulating circuit has been assembled and checked for sensitivity to temperature variations. These new circuits will be used to provide the constant voltage excitation required by the Kulite gages. The parts for these new circuits will be ordered in April and assembled upon receipt. The Kistler piezoelectric pressure transducers have been received. These have a faster response time than the Kulite gauges and will be used in FLAME to measure pressures under fast deflagration and detonation conditions. Two more pressure transducers of the piezoresistive type have been ordered from Kistler. This type has sensors that are immersed in a silicone oil bath and are supposed to be insensitive to flash temperatures. They will be checked in VGES after delivery.

The germanium photodiode detector (GPD) was used in VGES tests on February 28 and March 1. Tests were conducted for hydrogen:air percentages of 10%, 15%, and 20%. The GPD measures steam radiation primarily at 1.38 μm wavelength. The results show that the GPD is sensitive to a line-of-sight leading edge of the flame front as well as indicating a maximum intensity across its field of view when the bulk of the flame front goes by. When compared to chromel-alumel thermocouple results at the same distance from the ignition source (2.5 m), the GPD is slightly more responsive at all mixtures. Seven of these systems will be used in FLAME. Each of five

viewports will have a GPD installed, and in addition, the last viewport before the exit end of FLAME will have a GPD installed in the upper and lower access pipes providing a cross-sectional mapping of FLAME at that location.

Different types of lithium-niobate gages are still being checked in VGES. These crystals appear to be extremely susceptible to cracking with or without a protective cover. It appears that these gages can still produce a substantial but reduced signal even when cracked. These gages will be used to signal the flame arrival time at given points and/or as a feedback signal to change digitizer sampling rates in the five sections of FLAME.

As an alternative to the lithium-niobate gages, chromel-alumel thermocouple arrays are presently being fabricated for mapping the flame front arrival times at various points in FLAME. Forty ot these thermocouples, evenly divided between 0.05- and 0.14-mm sizes, will be installed at desig-nated access pipe locations along the length of FLAME.

Ionization probes will be built to measure fast deflagration and detonation flame front time of arrival and as a possible tool for measuring deflagration-to-detonation transitions.

Hot-wire anemometers are being considered as a means of mea-suring turbulence in the region of obstacles. Coordination with Sandia, Livermore, will determine the number and loca-tion of these devices to correlate with models that are being developed.

Heat-flux gages are presently being checked in FITS and in the EPRI large dewar in Nevada. Installation of these gages in FLAME will depend on the results obtained in these other experiments.

Current priorities are the completion of FLAME, lay g tem-porary cables for operation of FLAME, siting of the hydrogen trailer and installation of the hydrogen transfer system, installation of the operating systems, design and fabrication of plate lifting devices, installation of instrumentation, writing of a standard operating procedure (SOP) for FLAME, and preparation for the shakedown tests for FLAME.

3.2.5 Heated Detonation Tube
       (M. P. Sherman, J. R. Tieszen, W. B. Benedick)

In the previous semiannual report, the purpose of the heated detonation tube, the determination of hydrogen:air:steam mix-ture detonation properties, was discussed. In this report, we will describe the development of the hardware and the test program.

The heated detonation tube hardware can be considered in the following categories:

(1) the two 18-inch-diameter stainless steel tubes, driver section and end plates,

(2) the gas injection and recirculation system,

(3) the tube supports,

(4) the tube heating and insulation system,

(5) the transducers,

(6) the cables from the tube to the blockhouse, and

(7) the data acquisition system.

We will consider the progress made in the development of each of these categories.

During this period, it was decided that the design of the heated detonation tube had become too complex and potentially expensive. The design was simplified, completed, and sent out for fabrication. The general configuration of the two detonation tubes and driver section is shown in Figure 3.22. The initiation of the detonation will be done just inside the end plate at the driver section. After competitive bidding, Gadius Manufacturing Company was given the job of fabricating the flanges, transducer ports, etc., onto the detonation tubes and manufacturing the driver section and end plates. The work was completed in mid-April.

The tube support design was greatly simplified. The design selected is shown in a sketch in Figure 3.23. The tube supports were fabricated by our group, and concrete was poured to complete the structures. The cost of materials in the simple design was small. For example, used 55-gal drums, costing $5 each, were used as a main structural piece.

A gas injection and recirculation system was designed to perform several functions: inject hydrogen, inject steam, and recirculate the gas mixture from one end of the tubes to the other to insure the mixture was homogeneous. A bellows pump with an explosionproof motor was ordered and delivered. The tubing, valves, and fittings for the system were ordered.

Electric resistance heating tapes were ordered. The earlier design for enclosing insulation in a plywood box was discarded. The insulation will simply be wrapped around the tube.

The location of the detonation tube and the path of the cables from the tube to a cable pit were selected. The cable
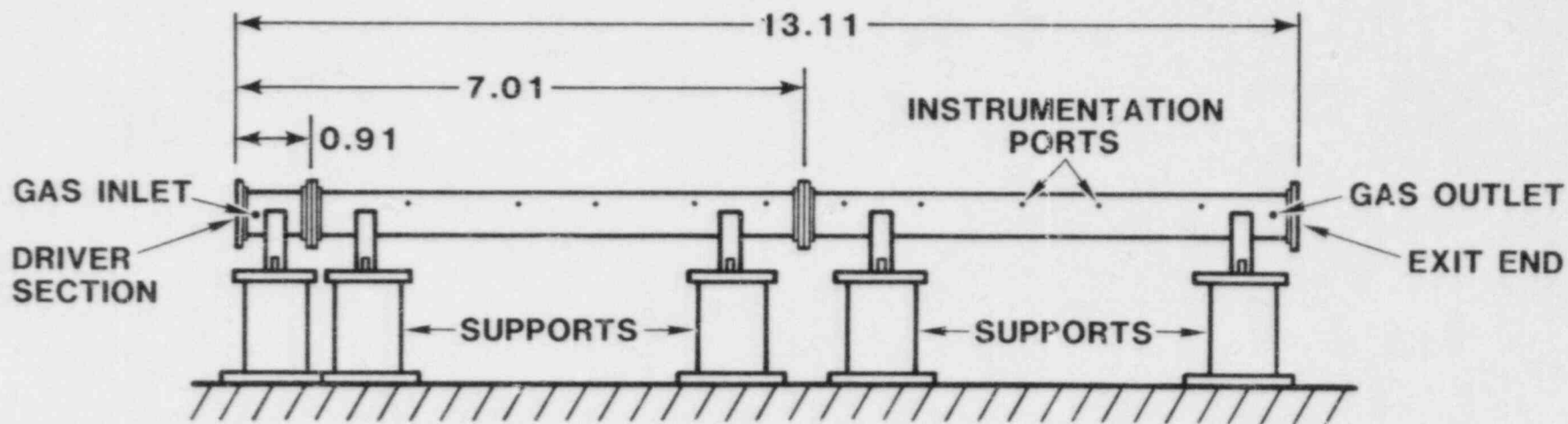
(DIMENSIONS IN METERS)

Figure 3.22. Configuration of the Detonation Tubes and Driver Section

DETONATION TUBE

WOOD INSULATION

4" CHANNEL

6" CHANNEL

55 GAL. BARREL

LIFTING BAR
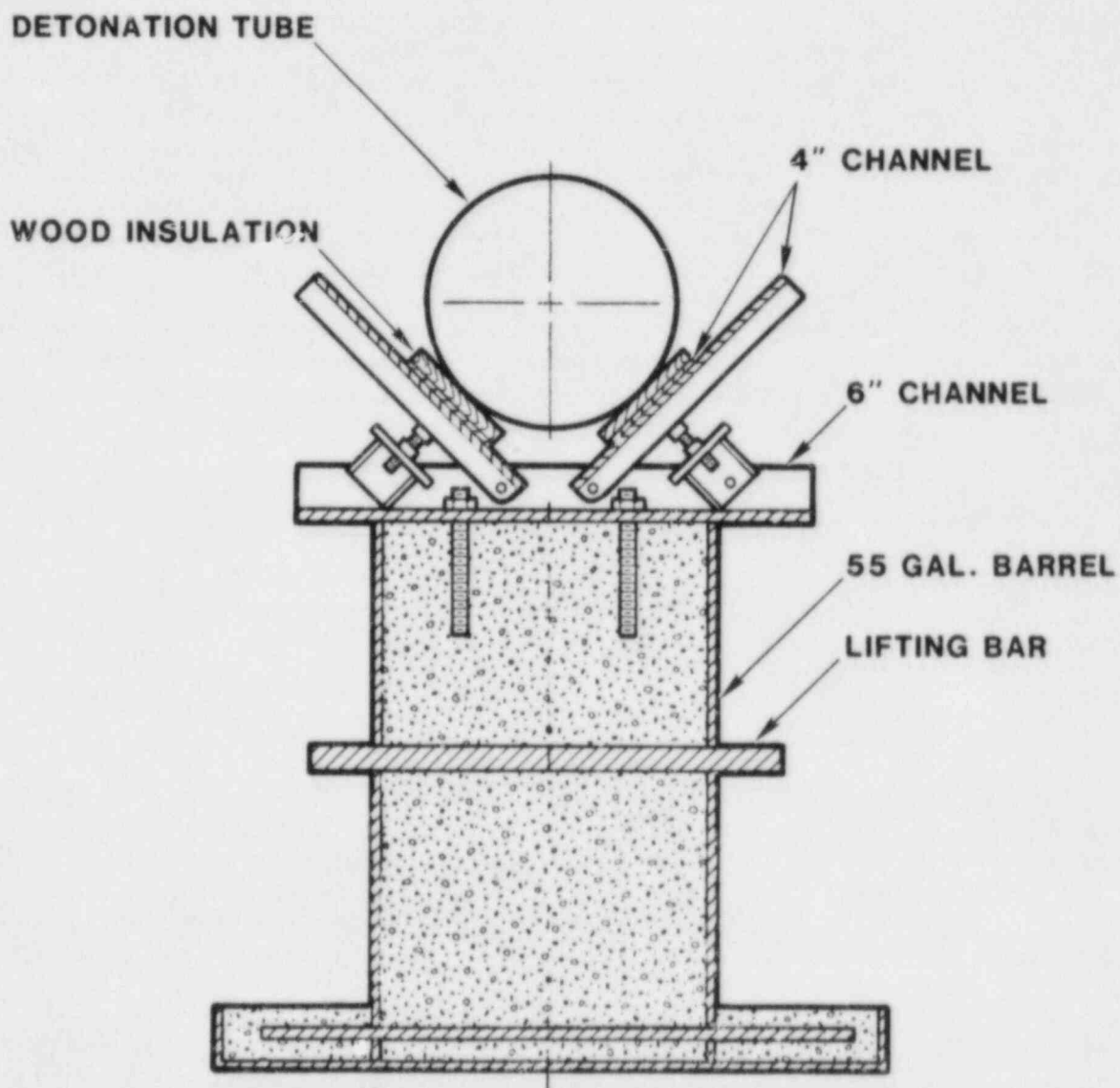
Figure 3.23.   Detonation Tube Support

pit will connect cables from the heated detonation tube, FLAME, and VGES to the blockhouse. A common data acquisition system will be used for FLAME and the heated detonation tube. The system hardware is functioning. Some added software will be required for the heated detonation tube.

Various pressure transducers to be used in the heated detonation tube and in FLAME are being tested in the VGES tank. It is expected that Kistler piezoelectric transducers will be used in the detonation tube.

A test program was developed. The first runs will be carried out at ambient temperature to check out the procedures for filling the tube with hydrogen:air mixtures, detonation initiation, and data acquisition. After these "shakedown" runs, a series of runs at various hydrogen concentrations will be run at ambient temperature. The purposes of these runs will be to develop the technique of reading the detonation cell size from smoke foils used in the tube and to compare the results with those found in the work of other researchers. It may be possible to achieve a stable detonation with a value of hydrogen mole fraction below that previously achieved in smaller diameter tubes (13.8%).

The next set of runs will be carried out at one or two elevated temperatures. The purposes of these runs will be to test out the tube heating system and to determine the effect of initial temperature on hydrogen:air detonations.

The main objective of the tube will be achieved in the next set of tests using hydrogen:air steam mixtures at elevated temperatures.

3.2.6   Interactions Between Aerosols and the Combustion of
        Hydrogen:Air Mixtures
        (L. S. Nelson)

3.2.6.1 Background

There is reason to believe that the aerosols produced during LWR core melting or core degradation may affect the combustion of hydrogen situations. We have defined an experimental program to learn quickly and inexpensively whether such interactions exist and whether they are benevolent, malevolent, or insignificant.

We expect to learn whether the hydrogen burn characteristics are modified by the presence of the aerosol. These modifications might affect the deflagration-detonation limits, the limits of ignition and performance of igniters, flame velocities, and pressure and temperature profiles produced during the combustion. Also, we expect to learn whether there is modification of the aerosols by the hydrogen combustion.

This might change particle concentrations, particle morphology, the chemistry of the particles, and possible adsorption or desorption on the particles. Of importance here are the airborne fission products, particularly cesium iodide.

The background for these studies is not extensive. The most significant literature surrounds the use of dry powders for fire extinguishment[21] and explosion suppression.[22] The literature is devoted mostly to the effects of alkali metal salts on hydrocarbon-air combustions. There are related heterogeneous combustion processes, however, that involve powder explosions (coal, grain, and metal dusts), the formation of soot and its catalytic effects during combustion, the effect of organometallics on engine combustion, and gnition of gaseous mixtures by radiatively heated particulate material.

We have looked at the amount of aerosols required to simulate aerosol generation in core melt or core degradation accidents. Concentrations on the order of 100 g m^{-3} may be generated early in CMCIs.[23]. Later on, this generation rate is thought to drop to produce aerosols with concentrations on the order of 10 g m^{-3}. Concentrations in the range 1 to 100 g m^{-3} seem likely in most core degradation situations.

We have surveyed some of the methods for generating nuclear aerosols, primarily those evolved at Oak Ridge National Laboratories.[24] These methods involve high-current electrical heating, the use of plasma torches, and radio-frequency induction heating. At Sandia, Brockmann is working on several metallothermic and pyrotechnic ways to produce aerosols.[25]

High-energy, high-temperature techniques such as these would be difficult (but not impossible) to adapt to premixed combustible mixtures of hydrogen and air. Therefore, we have turned to dry-powder fire extinguishers in which powder suspensions with instantaneous concentrations of up to 300 g m^{-3} have been reported. These concentrations are achieved by dispersing fine powders through orifices with bursts of pressurized gas. In addition to the common dry-powder extinguishers, there is a commercial, detonator-operated disperser that uses a gas pressure higher than regular extinguishers and can disperse powders more rapidly.[22] Both the dry-powder fire extinguisher and the commercial disperser have been tested with decomposable alkali metal salts for fire extinguishing, but it has been reported that the use of decomposable materials is not necessary.[21] A number of papers stress that catalytic, free radical chain-breaking effects are also important. For example, it has been shown that finely divided silica can strongly affect the detonability of a gaseous mixture.[26] There also is evidence that dispersed iron oxide powders may have a catalytic effect on hydrogen-air combustion.[27-29]

3.2.6.2 Experimental

In some simple outdoor experiments, we confirmed that commercial dry-powder fire extinguishers can produce dispersions of airborne solids at concentrations of 100 to 200 g m^{-3}. These concentrations were determined from the weight lost by the extinguisher over a measured discharge interval and from the volume of the plume determined photographically (Figure 3.24).

We did other gas burst experiments indoors in a transparent, plastic-walled aerosol chamber with the dimensions of the VGES tank (4.9 m tall, 1.2 m square) (see Figure 3.25). The dry-powder fire extinguisher used to disperse the powders is shown in Figure 3.26; it was placed beneath the chamber on the vibrating support as shown. Since the chamber was located in a manned area, it could not be used for combustion experiments.

We made seven indoor shots, five instrumented for aerosol measurements. The first two were made by discharging the original filling of the extinguishers, Purple-K powder, nominally potassium bicarbonate; no aerosol measurements were attempted with this material. One experiment was done with one discharge fired downward and a second, upward. Since the dispersion of the powder throughout the chamber appeared to be much more uniform with the upward discharge, all subsequent discharges have been fired upward.

Next, three experiments were performed with commercial deagglomerated gamma-alumina polishing powder, with a nominal particle size of 0.05 μm. For each experiment, the fire extinguisher (4.5-kg capacity) was loaded with 600 g of the powder and pressurized with dry nitrogen or argon to 1.33 MPa. Aerosol measurements were made as follows: four total filters were suspended at the center of the chamber, along with four collector tubes (filters and collector tubes are shown in Figures 3.27 and 3.28); each tube was evacuated through a four-stage Andersen impactor. The collector tubes were 3.8 cm in diameter and approximately 1.5 m long. The results of the alumina aerosol sampling are presented in the histograms shown in Figures 3.29 and 3.30.

Finally, two experiments were conducted with powdered iron oxide. This material is a commercial jeweler's rouge of 3 μm nominal particle diameter. One discharge was performed identically to the alumina discharges, while the other was performed with two fire extinguishers simultaneously discharged upward in the attempt to increase the concentration of total airborne solids. The results for the single iron oxide discharge are also shown in Figures 3.29 and 3.30.
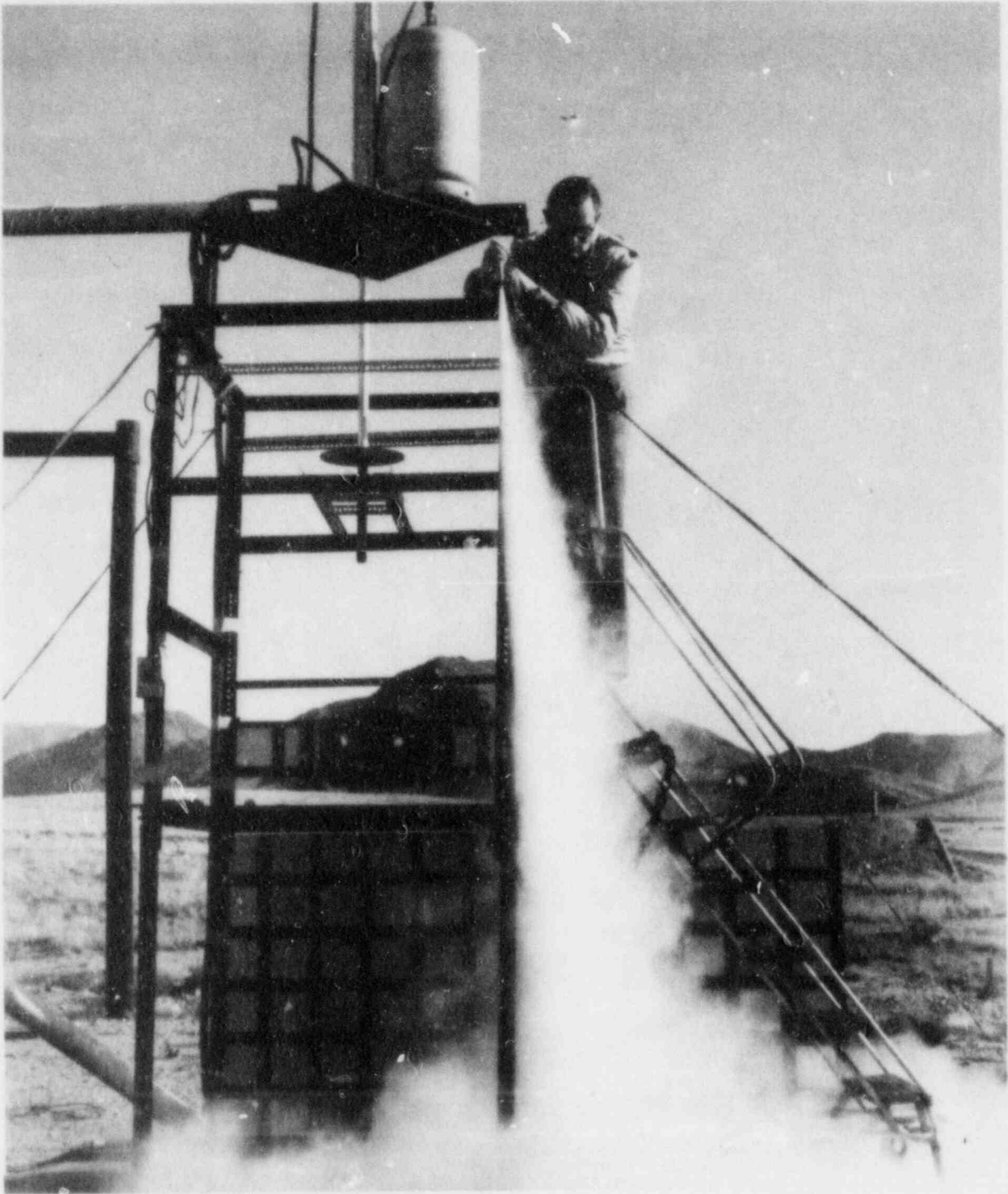
Figure 3.24. Gas Burst Dispersal (downward, 14-27-1) of a Commercial Fire-Extinguishing Powder. A concentration ~125 g cm³ of airborne solids was obtained in the upper part of the plume. Light squares on the stadia board are 15 cm across.
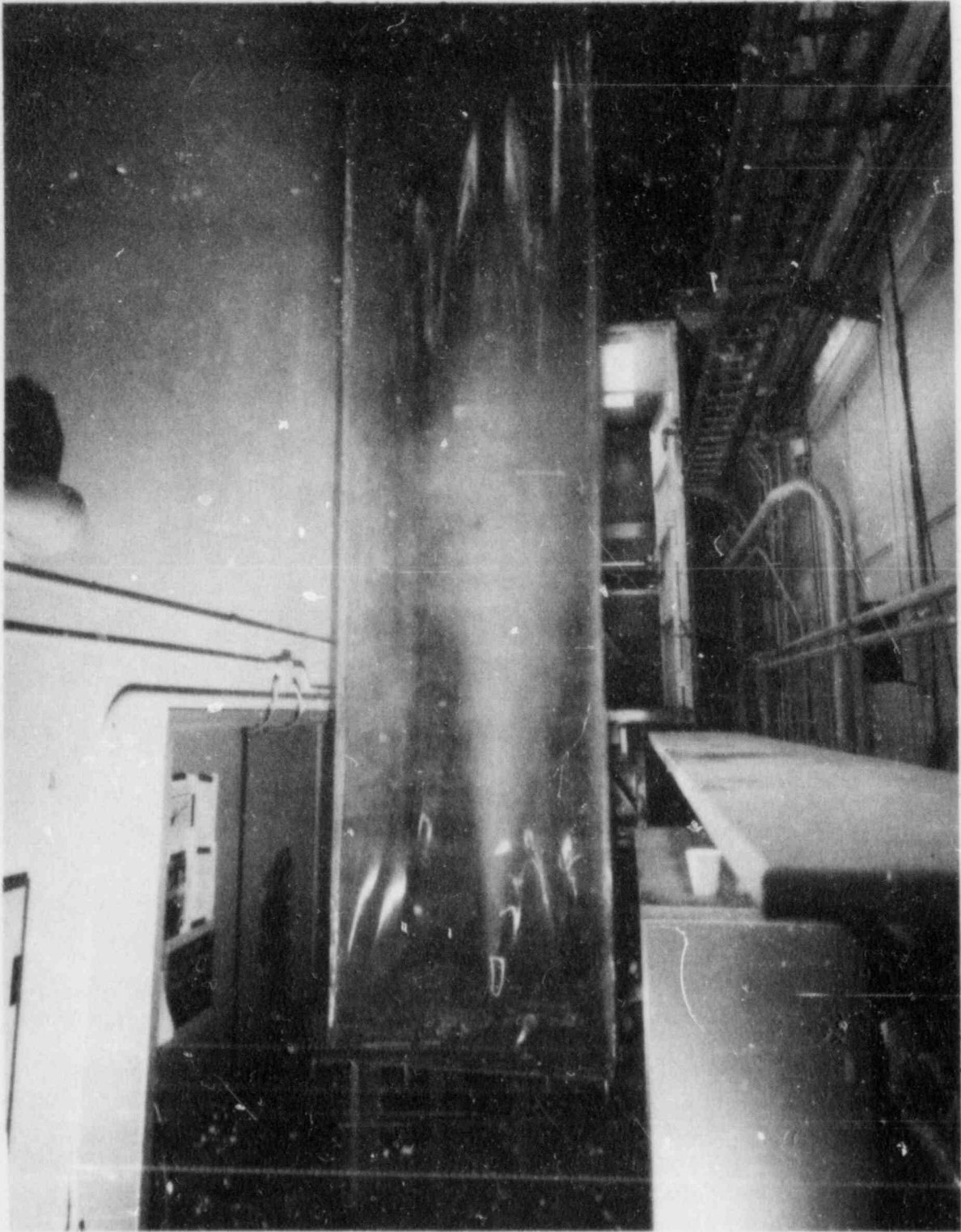
Figure 3.25. Upward Dispersal of Gamma-Alumina Powder in a
Plastic-Walled Aerosol Chamber. Chamber is
4.9 m tall and 1.2 m square (17-7-1-V).
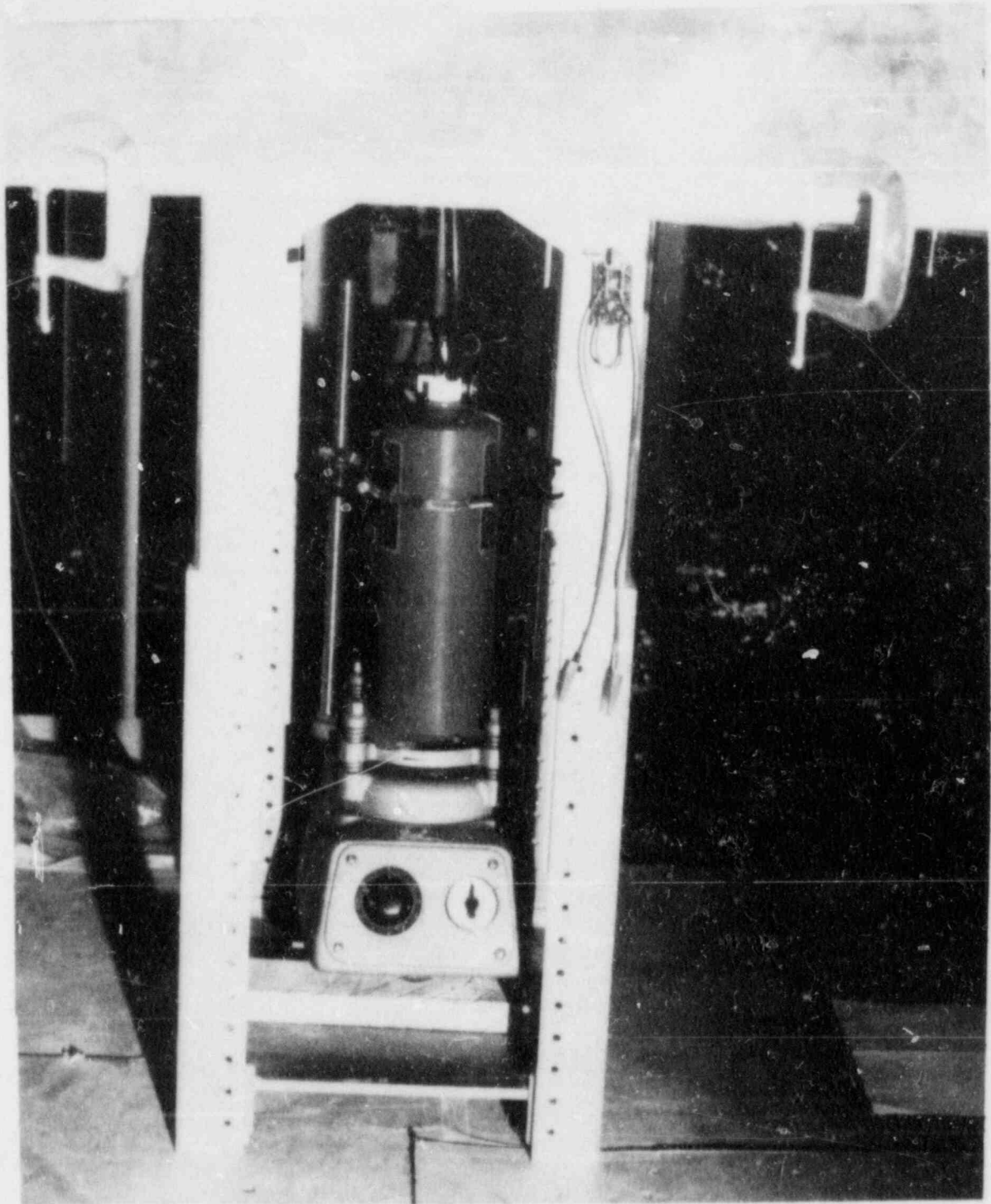
Figure 3.26. Dry-Powder Fire Extinguisher Used to Disperse Powders in the Aerosol Chamber Shown in Figure 3.25. The electrical vibrator beneath the tank is used to enhance powder discharge (17-7-2-4).
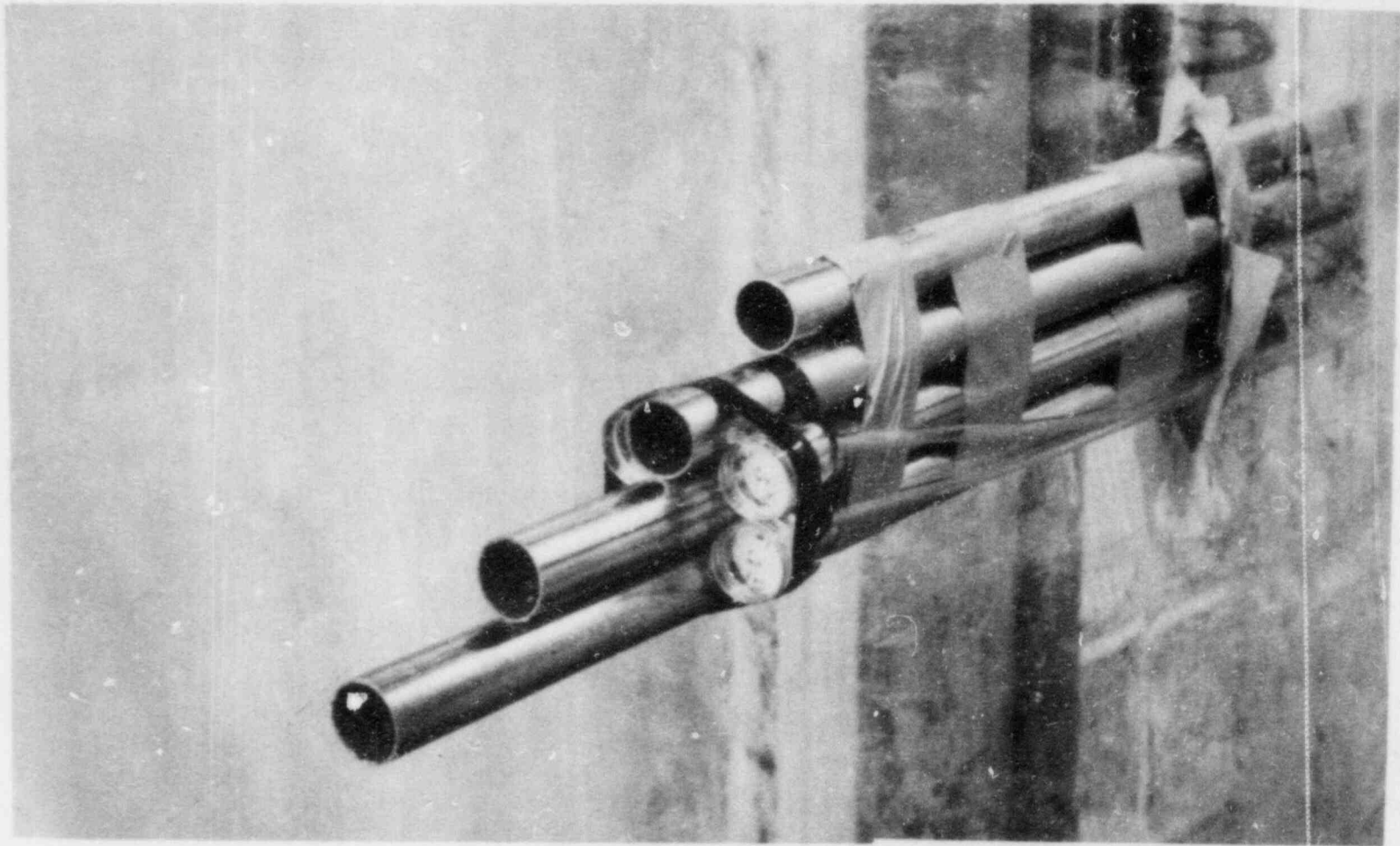
Figure 3.27.   Aerosol Collection Equipment Placed Centrally in the Chamber Shown in
Figure 3.25.   The tubes, 3.8 cm in diameter, are exhausted sequentially
through the cascade impactors shown in Figure 3.28.   The smaller col-
lectors are total filters, exhausted sequentially through the plastic
tubes.
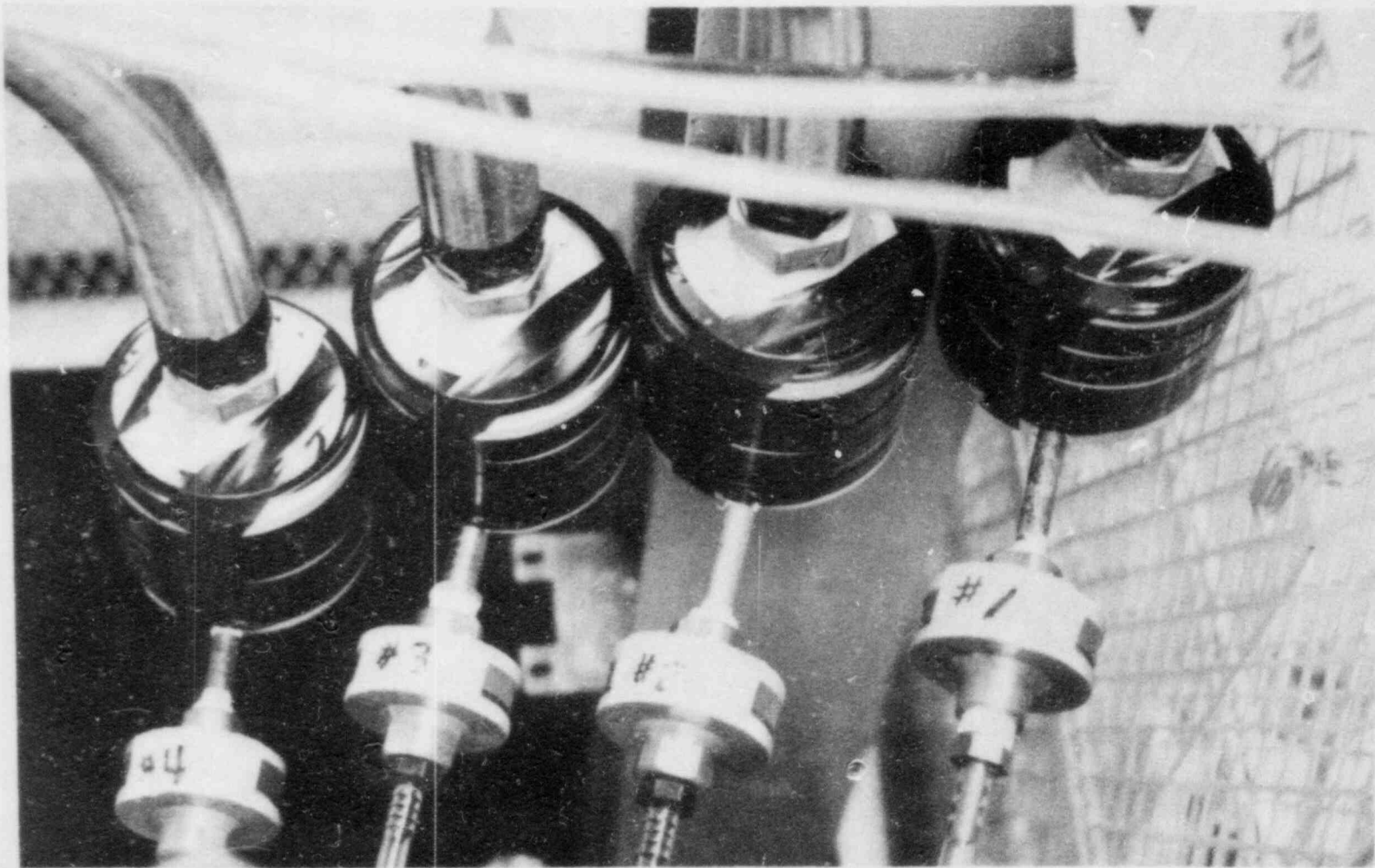
Figure 3.28. Four-Stage Cascade Impactors Attached to the Collector Tubes Shown in Figure 3.27. Each impactor is exhausted through the final filters (with numbers).
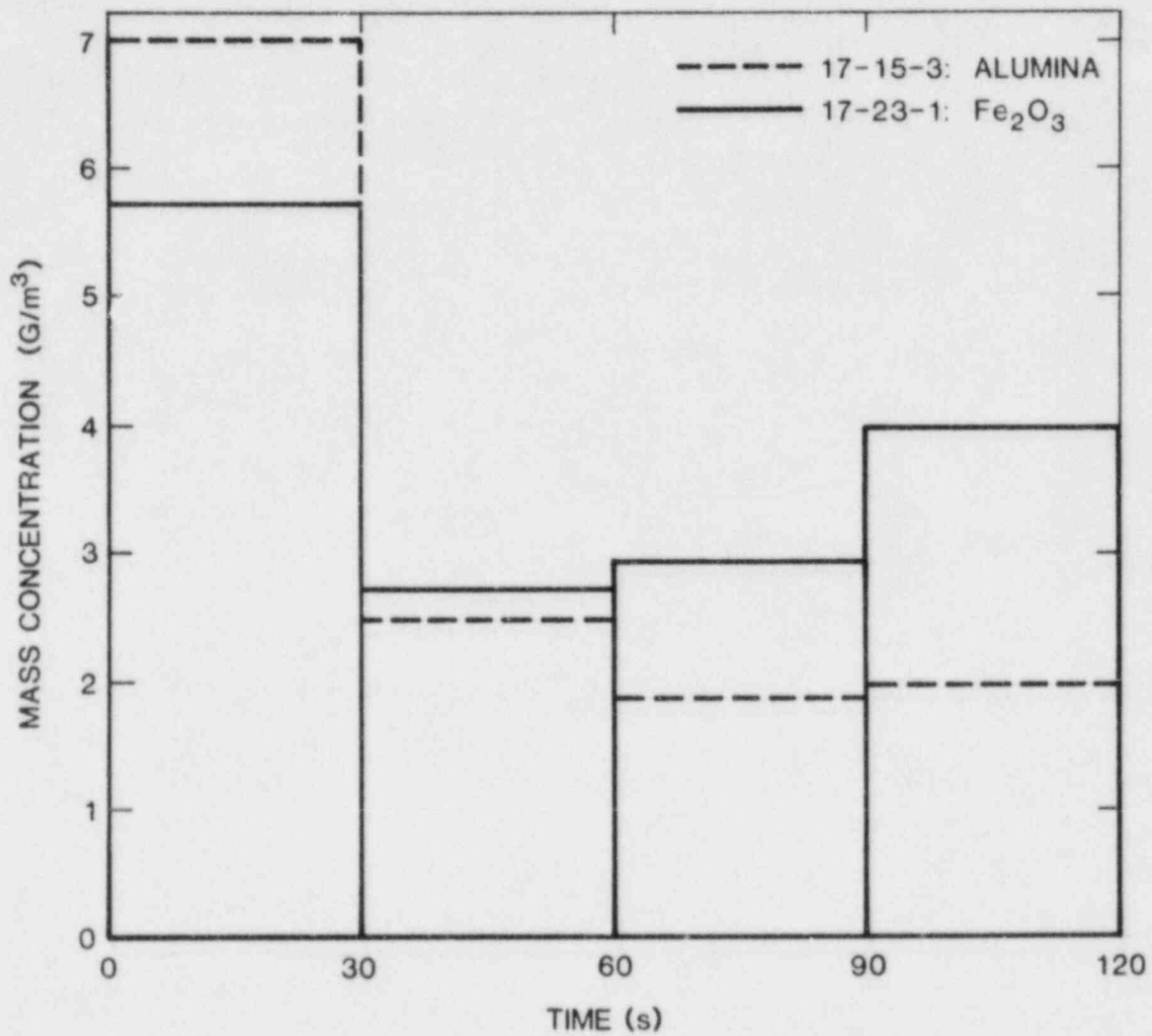
Figure 3.29.   Mass Concentration of Al_2O_3 and Fe_2O_3
                Aerosols Produced in Chamber of VGES Tank
                Dimensions vs Time
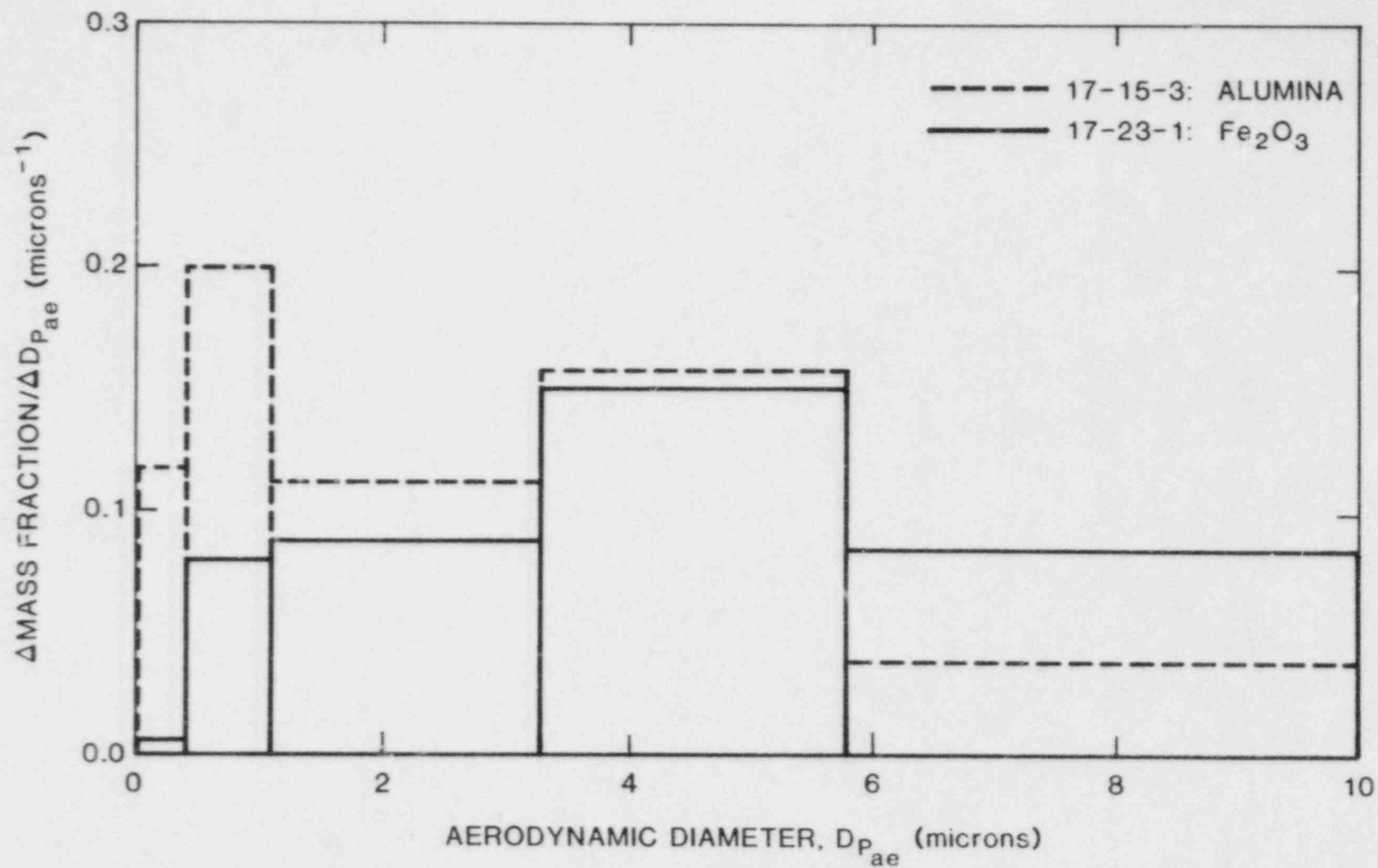
Figure 3.30. Normalized Weight Fractions of Al_2O_3 and Fe_2O_3 Aerosols Produced in Chamber of VGES Tank Dimensions vs Thermodynamic Diameter

3.2.6.3 Results

So far, we have produced aerosols of iron and aluminum oxides with initial total concentrations estimated to be 5 to 7 g m^{-3} with a single discharge. (When we used two discharges with the iron oxide, we may have reached 10 g m^{-3}; we estimated this latter concentration indirectly because we lost our initial total filter measurements). Between 30% and 50% of the total mass of the alumina aerosol particles collected had aerodynamic diameters of 3 μm or less; only 20% to 30% of the mass of the iron oxide aerosol particles was in this range, presumably due to the larger initial particle size of the powder.

The use of gas burst dispersal to simulate nuclear aerosols seems to be a useful technique, particularly in light of the simplicity and low cost of the generating equipment. There is still considerable room for improvement, however, because we are only discharging from one-third to one-half of the powder we place in the extinguisher. This has limited the maximum possible aerosol concentration in the chamber to 30 to 40 g m^{-3}. Moreover, only about 20% of this maximum concentration is being collected on our total filters. We are currently conferring with both aerosol and powder technology personnel at Sandia to improve the quality and concentration of the aerosols.

Plans are being made for several preliminary experiments in the VGES tank early in the next reporting period. Control experiments with and without powder will be performed initially to determine (a) baseline combustion conditions and (b) whether the discharge itself ignites the hydrogen:air mixture via static electricity. The latter is being considered because ignitions attributed to static discharges have occurred occasionally during manipulations of hydrogen:air mixtures in large plastic bags at the VGES site. Also, static electrical sparks produced by a discharging carbon dioxide fire extinguisher have been reported.[30]

If it can be shown that the powder discharges do not ignite the combustible mixtures, we will attempt to prepare aerosols with concentrations up to 50 or 100 g m^{-3} in hydrogen:air mixtures in the VGES tank. Ignition will be induced with exploding bridgewires, sparks, or glow plug igniters. Several initial experiments will be performed with an iron-oxide aerosol to examine the effects of this aerosol on the pressure and temperature transients produced during the hydrogen combustion.[27-29] Later, experiments will be performed with cesium iodide-containing aerosols to look for the production of gaseous iodine compounds during the hydrogen combustion.

3.2.7 Water Droplet Studies
       (L. S. Nelson, C. J. Richards)

3.2.7.1 Objectives

The effects of water droplets on hydrogen:air combustion
have been discussed in an earlier report.[31] It was shown
that significant reductions in both peak pressure and peak
temperature can be achieved by dispersing 0.01 to 0.05
volume-percent of water as droplets throughout the preburn
gases; optimum droplet sizes were on the order of 100 μm.
On this basis, a research plan was initiated to study the
effect of water drops on hydrogen combustion behavior, to be
performed in the FITS facility. This sequence of experiments
had been planned for the current fiscal year (FY 1983).
However, during this reporting period, a request was initi-
ated by the Nuclear Regulatory Commission (NRC) for Sandia
to perform a short series of experiments to test the opera-
bility of igniters in water spray environments that would
simulate these expected in several reactor containments in
the event of a hydrogen-generating accident. These tests
are now being planned for the VGES facility and are expected
to last approximately 1 month.

3.2.7.2 Need for Information about Water Droplets

In order to carry out and properly analyze the experiments
proposed for both the FITS and VGES tank experiments, we
need to know and understand the following characteristics of
the water droplets that are present during the combustion:

(1) Diameter distributions and how they can be characterized
    (e.g., can they be described with a log-normal distri-
    bution by a mean diameter and standard deviation).

(2) Fluxes and their uniformity in the tanks.

(3) Velocities, in particular, if the drops have reached
    terminal velocity.

(4) The coalescence of the drops as a function of time,
    experimental conditions, and droplet diameter distribu-
    tion.

We need this information to provide interpretable and
reproducible results in the hydrogen combustion behavior
experiments to generate desired droplet distributions and
fluxes (e.g., nozzle types are interchanged) and to investi-
gate droplet diameter stabilization schemes (e.g. the use of
charged, monodisperse droplets or the addition of chemicals
to the water).

3.2.7.3 Water Droplet Diagnostics

During this reporting period, we have constructed two fast-shuttered droplet samplers according to the design shown in our previous semiannual report.[1] The open time of the sampler vs driving gas pressure is shown in Figure 3.31. On the basis of preliminary testing with these samplers, a design modification is being made to place a second movable shutter above the droplet opening to prevent flooding in high-flux situations.

We have improved the quality of the sampling substrate, which is basically the polyvinyl alcohol-coated microscope slides described by Tanaka.[32] Our improvements have involved the addition of a tinting agent to the coating solution, careful filtration of the solution, and deposition of the films under clean bench conditions. A typical image of water droplets as photographed from the screen of the Quantimet system is shown in Figure 3.32.

The automatic image analysis by the Quantimet system readily produces droplet diameter distributions similar to the preliminary distribution shown in the previous semiannual report. We have studied the reproducibility of the droplet diameter measurements using a spray produced by a single Spraco-type 1106-2004 nozzle used under the conditions reported by Camp.[33] The mean diameters of droplets collected at various distances beneath the nozzle in are shown in Table 3.6. It can be seen that there is considerable variation between shots even though drop generating conditions are identical in all experiments.

3.2.7.4 Igniter Studies

In response to the NRC request, we are undertaking a short series of experiments designed initially to test the operability of Tayco igniters in a water spray environment equivalent to that of the Sequoyah containment. Our program plan was submitted to the NRC in memorandum form.[34] The basic objective of these studies is to provide backup information for a test plan generated by the Tennesee Valley Authority as required by modified licensing procedures.[35-37]

We have started the experimental preliminaries for these studies in the VGES tank, which include plans for tank modifications and installation of new air-drive fans. We have also obtained Tayco igniters for the tests and have spot-welded thermocouples to their surfaces.

We have explored the possiblity of using Spraco-type 1713A nozzles, used as standard in reactor containments in these tests. However, a major difficulty arises with this nozzle because it is a massive, hollow-cone nozzle that produces a large-diameter spray distributed as shown in Figure 3.33.
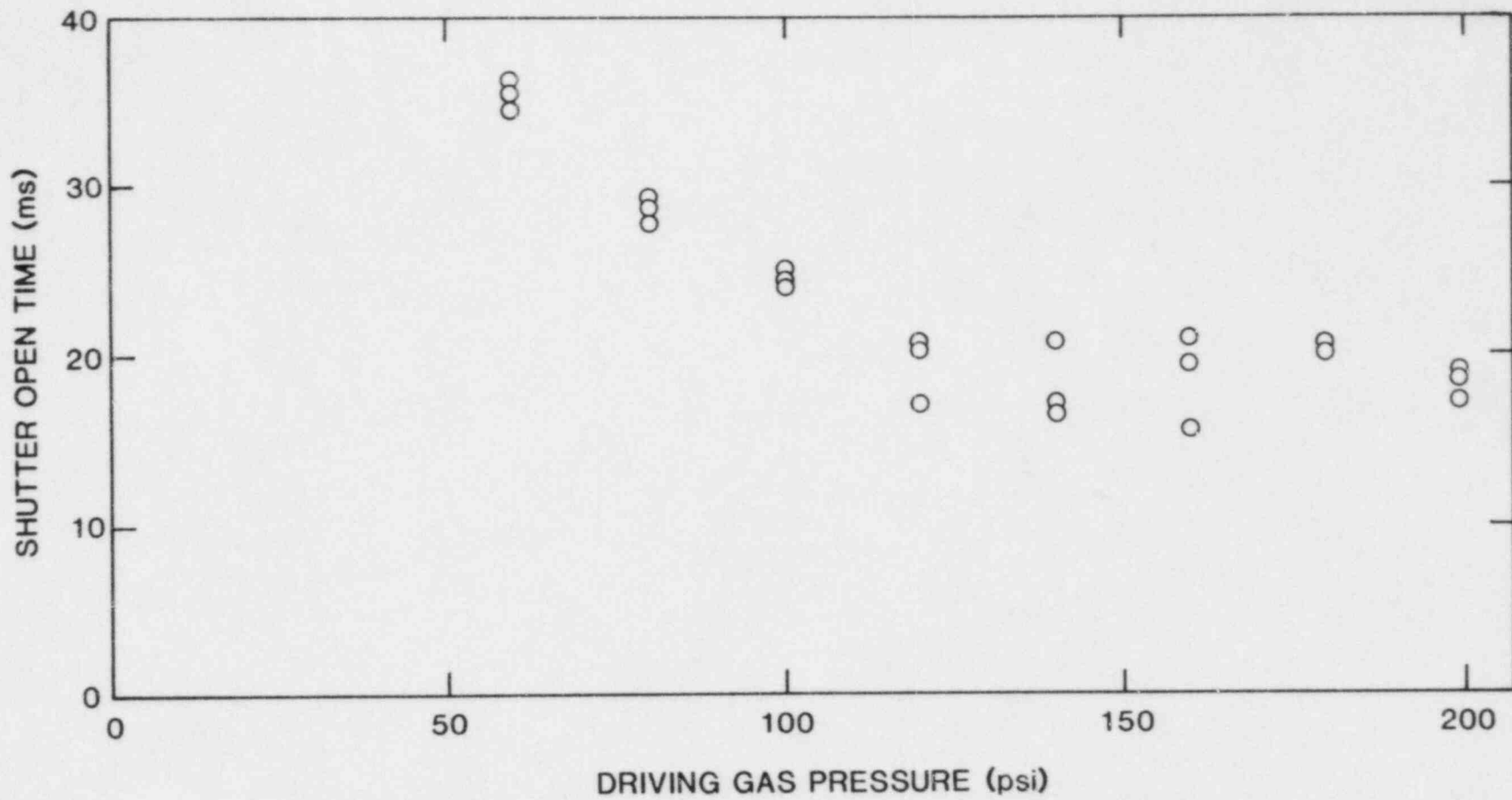
Figure 3.31. Open Time of the Pneumatically Operated Water Droplet Sampler as a Function of Driving Gas Pressure
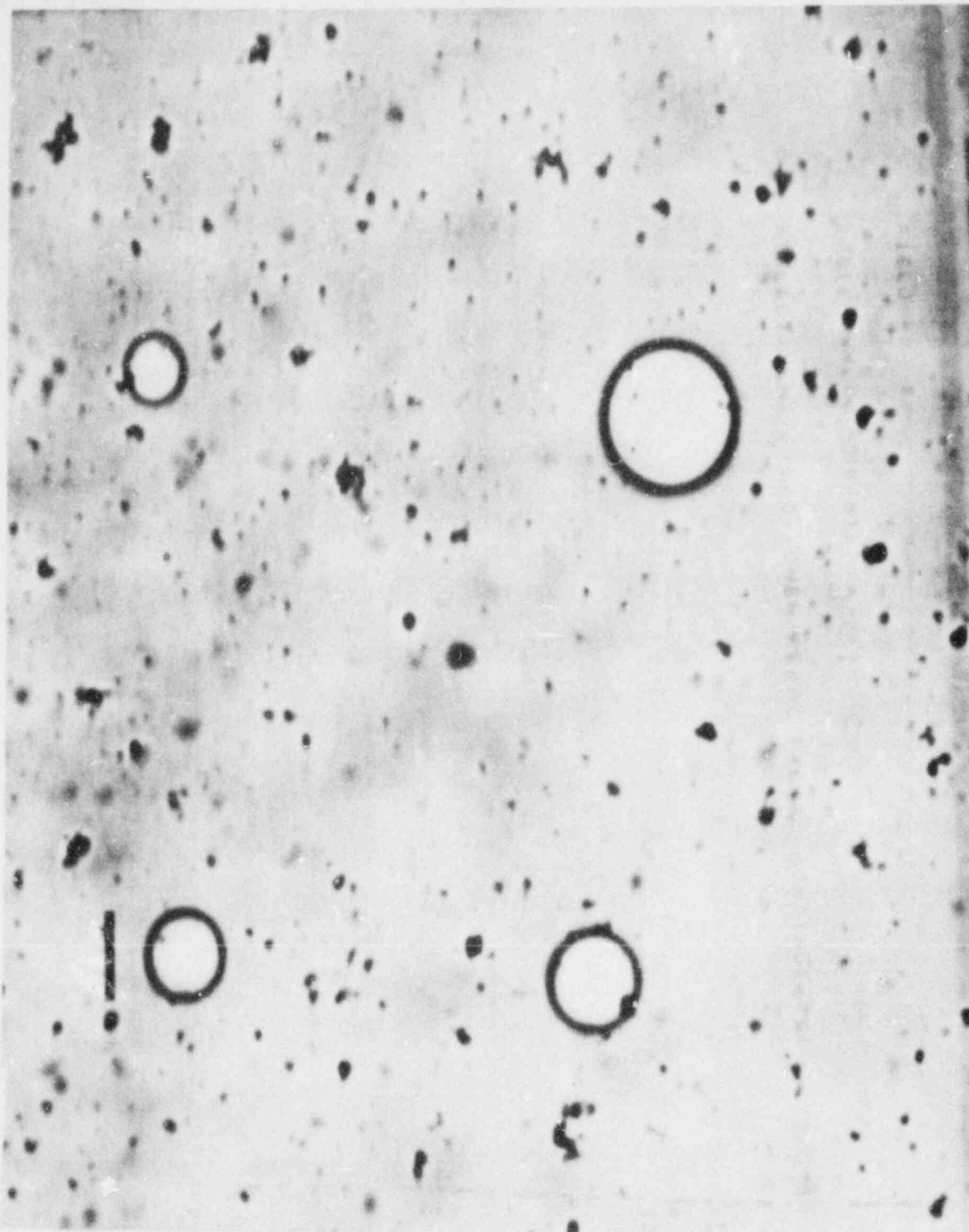
Figure 3.32. Photograph of the Quantimet Screen Showing
Images of Four Water Droplets Captured on a
Microscope Slide Coated with a PVA-Ink Solu-
tion. Bar at upper right is 25 μm long.

Table 3.6

Direct Water Droplet Sampling--One No. 11062004
Spraco Nozzle Centered Above PVA-Coated Slides

Nozzle – Sampler Distance (cm)	Shutter Open Time (ms)	No. Drops Counted	Median Diameter (μm)
77	22	269	155
77	22	378	147
100	55	367	145
100	55	309	181
103	22	56	126
103	22	54	133
125	48	90	225
125	48	254	166
125	48	193	175
129	22	24	107
129	22	42	116
159	22	90	137
159	22	159	214

SPRAY DISTRIBUTION CHART
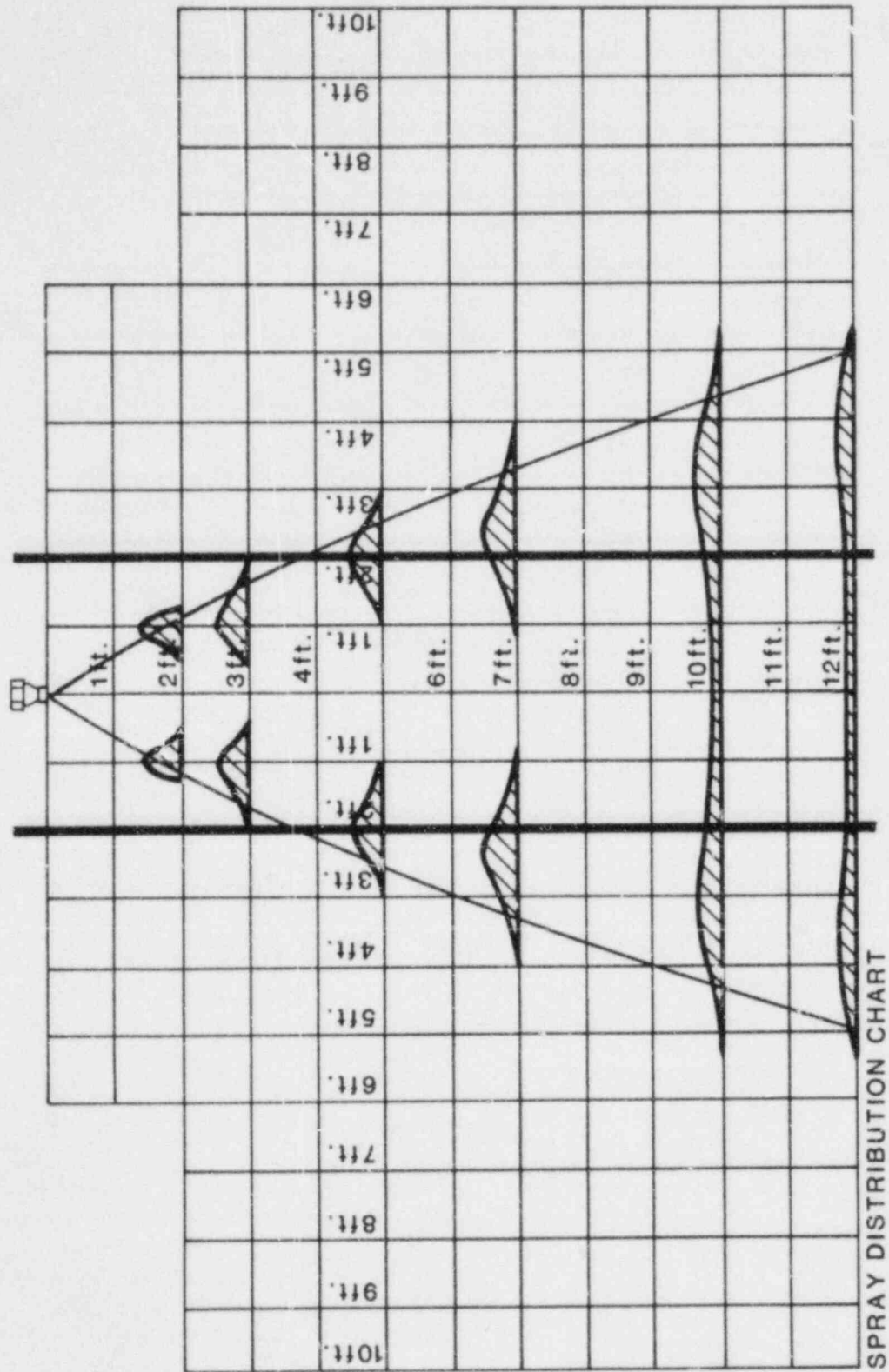
Figure 3.33. Distribution of Spray Produced by the Spraco 1713A. Hollow Cone Nozzle operated at 40 psi (data supplied by the manufacturer). Width of the VGES tank is indicated by the two heavy vertical lines.

3-76

On this figure, we have superimposed the dimensions of the side walls of the VGES tank, shown as heavy vertical lines. It can be seen that the bulk of the water will strike the walls of the chamber, subsequently flooding downward and splashing inward. To obtain more representative spray conditions, we plan to substitute a full-cone nozzle reported by the supplier to produce a droplet distribution similar to the Spraco 1713A. A photograph of the 1713A nozzle and a candidate full-cone nozzle is shown in Figure 3.34. It will be necessary to measure water droplet size distributions and fluxes to compare the various nozzles.

3.2.7.5 Water Fog Production and Maintenance

3.2.7.5.1 Background and Objectives

Previous work by Berman et al. has shown that the use of a dense water fog (~0.05 percent by volume) decreases by a significant amount (a factor of 3) the pressure and temperatures in containment caused by a hydrogen combustion event.[31] Because of this suppression effect, the use of water fogs generated in containment appears to be an attractive mitigation scheme. Although high-volume production of small drops is possible using conventional spray nozzles (high-pressure or pneumatic), maintenance of these high-density fogs is difficult due to self-agglomeration of the water droplets, which causes large fog-settling loss rates. The self-agglomeration of the water droplets is due to the fact that larger droplets have a larger fall velocity than smaller droplets, which causes the larger droplets to overcome the smaller ones, increasing their fall velocity further, etc. The polydisperse nature of fogs from conventional spray nozzles (ratio of maximum droplet size to minimum droplet size typically greater than 20) compounds this problem.

In order to utilize the beneficial features of water fogs, a method for maintaining the fog needs to be developed, i.e., the method must prevent droplet agglomeration. There are two ways to prevent droplet agglomeration:

(1) Produce a monodisperse (uniform droplet size) fog.

(2) Electrically charge the droplets (same polarity).

There are methods for producing monodisperse droplets (such as those used in ink-jet printers), but none of these methods can produce the copious number of droplets necessary for this application. There is, however, a well-known practical method for producing copious amounts of electrically charged fog droplets of nearly uniform size. This method, which is described in detail in the following section, consists of spinning disc-type sprayers fitted with induction-charging electrodes. Spinning disc-type sprayers have long been used (since ~1950) to produce sprays for various industrial
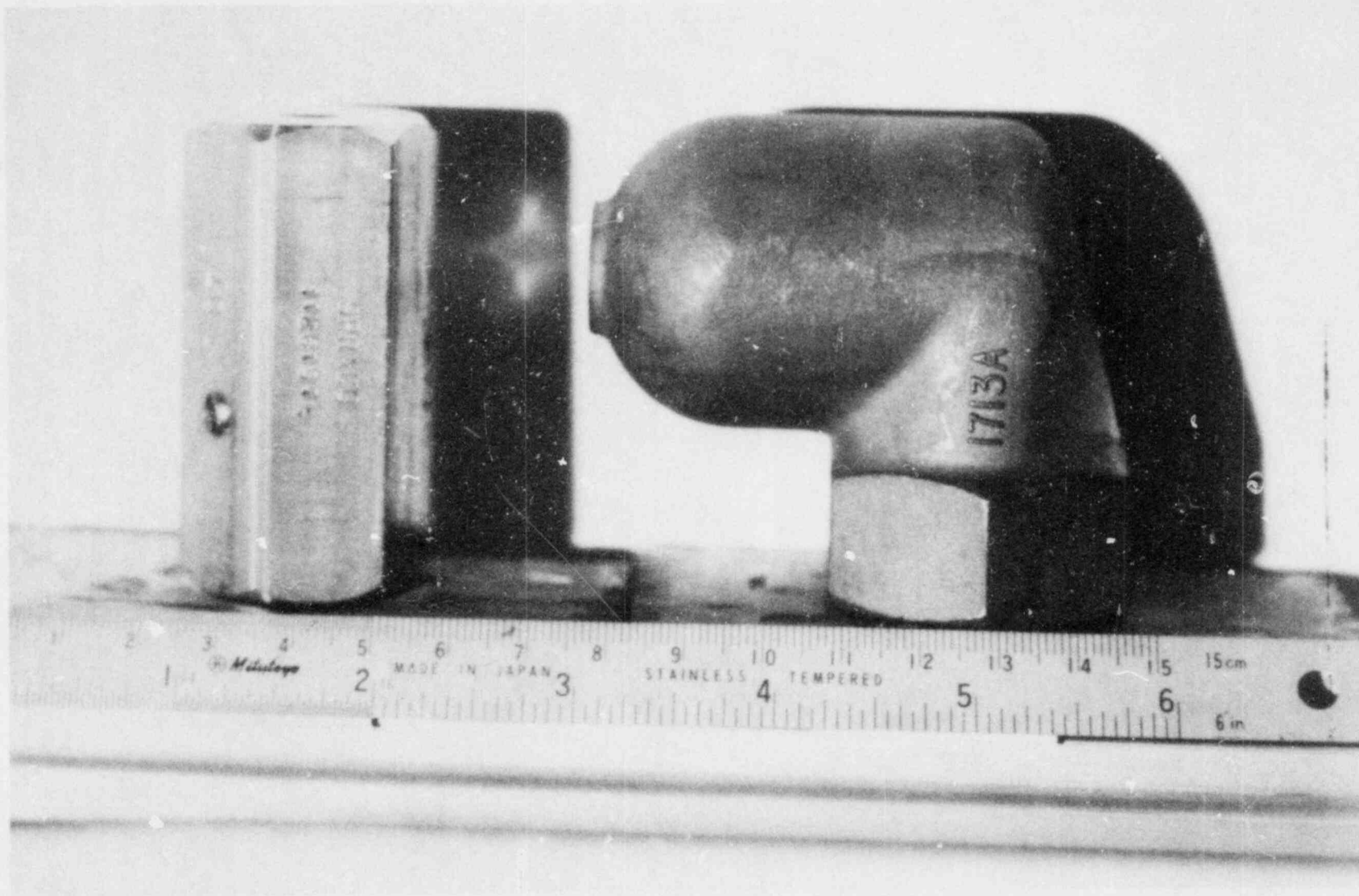
Figure 3.34. Photograph of the Spraco 1713A Hollow Cone Nozzle (Right) and a Candidate Substitute Solid Cone Nozzle (Left) for Use in the VGES Tank

processes, such as air humidification, spray drying, insecticide sprayers, etc.[38]

The spinning disc-type sprayers produce almost uniform droplet sizes (ratio of maximum droplet size to minimum droplet size less than 2) and can be designed to produce droplets as small as 15-µm diameter.[38-42]

When fitted with induction-charging electrodes, the disc sprayers can produce droplets that are electrically charged to within 10% of the theoretical maximum charge (the so-called Rayleigh limit) that a droplet can hold.[43] Such devices are used extensively in scrubbing toxic gases and aerosol particles from industrial effluents. More than a half-dozen patents have been granted since 1931 for spinning disc-type sprayers with induction-charging electrodes (see References 44-47 for example).

A very important side benefit of this method is its ability to scrub the fission-product aerosols from the containment chamber. The use of highly charged droplets is one of the few ways known to remove submicrometer aerosol particles efficiently. Even uncharged particles are attracted (via an induced dipole interaction) to the droplets as they drift through the aerosol.[48,49]

3.2.7.5.2 Program Status and Plan

As is shown by Walton and Prewett [38], the size of the droplets produced by spinning disc-type sprayers is accurately predicted by

$$d = 3.8(\sigma/D\rho)^{1/2}/\omega \qquad\qquad (3-22)$$

where

σ = surface tension of the liquid
D = diameter of the disc
ρ = density of the liquid
ω = angular speed of the disc
d = diameter of the droplets produced

The charge on each droplet is proportional to the voltage applied to the induction electrode (and of opposite polarity).[43]

It appears well-established then that the spinning disc-type sprayers fitted with induction-charging electrodes are the best and most well-developed, practical devices for producing easily maintained fogs (minimal self-agglomeration).

Given that these devices can produce droplets of near uniform size, from 3-mm to 15-µm diameter, each with a charge of up to 10% of the Rayleigh limit (either polarity), the next

question to be answered is, What size droplet and electrical charge is optimum (within the limits set forth by Berman et al. for effective hydrogen burn mitigation [31]) for maintaining the dense fog?

In order to answer this question and thus put limits on the range of disc diameters, rotational speed, charging voltages, etc., for the disc sprayers, a computer study has been initiated to model the interaction of charged fog droplets. The part of the computer model that calculates the effect of the electrical charges and electric fields on droplet interaction has been completed. The remaining part of the computer model, scheduled for completion within 3 months, will calculate the hydrodynamic and gravitational effects on droplet interaction, thus providing the tool necessary to completely specify disc sprayer.

This computer model will also provide the operating parameters such as rotational speed and charging voltage (controlled remotely) that are optimum for scrubbing fission-product aerosols from containment.

Upon the specification of the disc spray, a series of small-scale tests is planned that will consist of fabrication of a disc sprayer of only a few (~ four) discs, and operating it in a small (~50-m³) volume to verify that the self-agglomeration has been reduced to an acceptable level. These tests will also include demonstration of fission-product scrubbing efficiencies, using the same dics sprayer assembly.

3.2.8 Catalytic Mitigation Evaluation Program
(M. L. Koszykowski, R. W. Schefer, and W. J. McLean)

The promotion of hydrogen oxidation by noble metal catalysts such as platinum has been known for well over a century, and in fact, commercial systems for catalytic recombination of hydrogen are already available for use in nuclear power plants.[50] These commercial systems are designed to remove relatively small quantities of radiolytically-produced hydrogen by pumping dry containment gases through external systems containing packed bed catalysts. In considering relatively large releases of hydrogen from metal-water interactions during a reactor accident, a catalytic mitigation (deliberate ignition) system would have to be designed to handle mixtures with larger fractions of hydrogen, as well as mixtures containing relatively high quantities of water vapor. The system would be designed to ignite relatively weak flammable mixtures, thereby preventing buildup of higher concentrations of hydrogen. If catalytic activity at normal operating temperature is sufficiently fast, such a catalytic ignition

system would have the advantage of being electrically passive, no external power being required. We note that a passive ignition system based on hydrogen oxidation over a platinum catalyst has been developed successfully by the Institute of Gas Technology.[51]

Researchers at the Lawrence Livermore Laboratory and Sandia's Combustion Research Facility (CRF) in Livermore have been carrying out detailed experimental and theoretical studies of the oxidation of hydrogen in the presence of catalytic surfaces.[52-56] The most recent results from these studies illustrate the need for developing more detailed models for the surface reaction processes.

With respect to the NRC Hydrogen Mitigation Program, the expertise available at the CRF is being applied to the problem of catalytic oxidation of hydrogen:air:steam mixtures characteristic of reactor accident scenarios. Physical chemists, familiar with surface processes, are providing a more detailed physico-chemical model for the surface conditions used in the existing model. Comparisons are being made between model calculations and existing experimental data taken at Sandia's CRF during catalytic oxidation of hydrogen: air mixtures in a flat-plate boundary layer. The objective of this program is to improve the model and apply it to the conditions of interest to the NRC program so that an evaluation of the potential for catalytic ignition can be made.

An initial critical review of the literature has resulted in the reactions and rate constants, shown in Table 3.7, which most appropriately represent the surface-reaction process. The data support a Langmuir-Hinschelwood type of reaction mechanism (i.e., one in which reactants must both adsorb prior to reaction) that then proceeds via formation of an unstable adsorbed hydroxyl intermediate. The following conclusions have been drawn, based upon this model:

(1) Under the conditions of the CRF experiments (relatively high temperatures), adsorption of hydrogen is rate limiting in production of H_2O.

(2) The model predicts that the Pt surface acts as a sink for OH radicals that are produced by the gas phase r _-tion, under the conditions of the CRF experiment, (_u-sistent with observation.

(3) The model is also consistent with the absolute pressure of H_2 at which the maximum rate of OH production from surface reaction is observed.

Table 3.7

Rates and Mechanisms for the Catalytic Oxidation of Hydrogen on Platinum*

Reactions and Rate Expressions	S^o	ν	E, cal/mole
1. $H_{2,g} + 2X_H \rightleftarrows 2H_a$			
$R_{1f} = S^o_{H2}(1 - \theta_H)^2 P_{H2}(2\pi m_{H2}k'T_g)^{-1/2}$	10^{-1}		
$R_{1r} = \nu_{1r}\theta_H^2 N_H^2 \exp(-E_{1r}/CT_s)$		$10^{-3}cm^2s^{-1}$	1.8×10^4
2. $O_{2,g} + 2X_O \rightleftarrows 2O_a$			
$R_{2f} = s^o_{O2}(1 - \theta_O)^2 P_{O2}(2\pi m_{O2}k'T_g)^{-1/2}$	$\sim 10^{-1}$		
$R_{2r} = \nu_{2r}\theta_O^2 N_O^2 \exp(-E_{2r}/CT_s)$		$2 \times 10^{-2}cm^2s^{-1}$	4 to 7×10^4
3. $O_a + H_2 \rightleftarrows OH_a$			
$R_{3f} = \nu_{3f}\theta_O N_O \theta_H N_H \exp(-E_{3f}/CT_s)$		$10^{-1}cm^2s^{-1}$	1.2×10^4
$R_{3r} = \nu_{3r}\theta_{OH} \exp(-E_{3r}/CT_s)$		$10^{13}s^{-1}$	1.2×10^4
4. $H_a + OH_a \rightarrow H_2O_a$			
$R_{4f} = \nu_{4f}\theta_H N_H \theta_{OH}N_{OH} \exp(-E_{4f}/CT_s)$		$10^{-1}cm^2s^{-1}$	0.85×10^4
5. $OH_a \rightleftarrows OH_g$			
$R_{5f} = \nu_{5f}\theta_{OH}N_{OH} \exp(-E_{5f}/CT_s)$	$\sim 10^{-1}$	$10^{13}s^{-1}$	2.8×10^4
$R_{5r} = S^o_{OH}(1 - \theta_{OH})P_{OH}(2\pi m_{OH}k'T_g)^{-1/2}$			
6. $H_2O_a \rightleftarrows H_2O_g$			
$R_{6f} = \nu_{6f}\theta_{H2O}N_{H2O} \exp(-E_{6f}/CT_s)$		$10^{15}s^{-1}$	1.0×10^4
$R_{6r} = S^o_{H2O}(1 - \theta_{H2O})P_{H2O}(2\pi m_{H2O}k'T_g)^{-1/2}$	1		

*Nomenclature given on attached appendix.

Appendix to Table 3.7

Symbols, Units, and Values of Constants

Symbol	Meaning	Value	Units
X_Z	Adsorption site of adatom Z		
R	Reaction rate		$cm^{-2}s^{-1}$
k	Reaction rate constant:		
	First-order:		s^{-1}
	Second-order:		cm^2s^{-1}
θ_Z	Coverage of species Z, relative to its maximum (saturation) value		
S_{Z2}	Sticking (adsorption) probability of molecule $Z_{2,g}$		
S_{Z2}^O	Initial adsorption probability of molecule Z_2, i.e. S_{Z2} in the limit as $\theta_Z \rightarrow 0$.		
	Clean-surface values: $S_{H2}^O \sim 10^{-1}$		
	$S_{H2}^O \sim 10^{-1}$		
P_{Z_2}	Pressure of molecule Z_2		
	Experimental values:		
	P_{H2} =	80	torr
		10^5	$g \cdot cm^{-1} \cdot s^{-2}$
	P_{O2} =	680	torr
		9×10^5	$g \cdot cm^{-1} \cdot s^{-2}$
k'	Boltzmann's constant	1.38×10^{-16}	$g \cdot cm^2 \cdot s^{-2} \cdot K^{-1}$
C	Gas constant	1.987	$cal \cdot mole^{-1} \cdot K^{-1}$

Appendix to Table 3.7
(continued)

Symbols, Units, and Values of Constants

Symbol	Meaning	Value	Units
N_Z	Density of adsorption site of particle Z at $\theta = 1$ on Pt(111)		
	$N_H =$	1.5×10^{15}	cm^{-2}
	$N_H =$	4×10^{14}	cm^{-2}
m_{Z2}	Mass of particle Z_2		
	$m_{H2} =$	3×10^{-24}	g
	$m_{O2} =$	5×10^{-23}	g
T_g	Gas temperature		K
T_s	Surface temperature		K
E	Energy		cal/mole
υ	Pre-exponential (frequency) factor in the rate constant		
	First-order:		s^{-1}
	Second-order:		$cm^2 s^{-1}$

(4) The Pt catalyst is certainly a promising candidate, with reaction probabilities per hydrogen-metal surface collision reported on the order of unity for metal wires, foils, and single crystals, in the temperature range 300-450 K and under conditions where adsorption of oxygen is not rate limiting.

This model has also been used to study the bulk rate of production of water from the surface under a variety of conditions. The assumption made was that the gas-phase concentrations were constant (that is, the rate limiting process is the surface chemistry and not the transport of the gas). A typical result for a 10% hydrogen mixture is shown in Figure 3.35. The results are consistent with bulk rate measurements made previously for the production of water. Preliminary calculations also indicate that the rate is linear in the gas-phase hydrogen concentration in the intermediate temperature range.

An important observation about the mechanism can be drawn from the calculations and the figure. There are really three separate regimes with different rate limiting factors. At low temperatures, the water product does not desorb rapidly and the water blocks oxygen sites and significantly reduces the reaction rate. At intermediate temperatures, no single process dominates and a linear rate is observed, while at higher temperatures, desorption of reactants becomes important and the rate again slows.

The detailed surface reaction mechanism for catalytic oxidation of hydrogen on platinum has been included in an existing model for boundary layer combustion. The model utilizes a finite difference scheme for solving the laminar boundary layer equations for flow past a heated plate surface. Gas-phase reactions are modeled using a detailed kinetic scheme involving 17 reactions and 8 species (H_2, O_2, H_2O, O, H, OH, and HO_2). The object of these calculations is to assess the temperature rise under reaction conditions and to examine the progress of reaction from the surface to the gas phase. Comparisons with experimentally measured surface heat release rates and OH and temperature distributions over a platinum plate are being made to validate the surface reaction model and rate constants.

A comparison between experimentally measured and predicted surface heat release rates is shown in Figure 3.36 as a function of distance along the plate surface. The predicted heat release rates were obtained using the surface reaction mechanism and estimated rate constants of Table 3.7. Near the plate leading edge, where surface reaction rates are kinetically limited, the calculations underpredict the measured heat release rates. Farther downstream the reaction rate is limited by diffusion of reactant species to the surface, and predicted results agree well with measured values.

HYDROGEN OXIDATION RATE ON PLATINUM
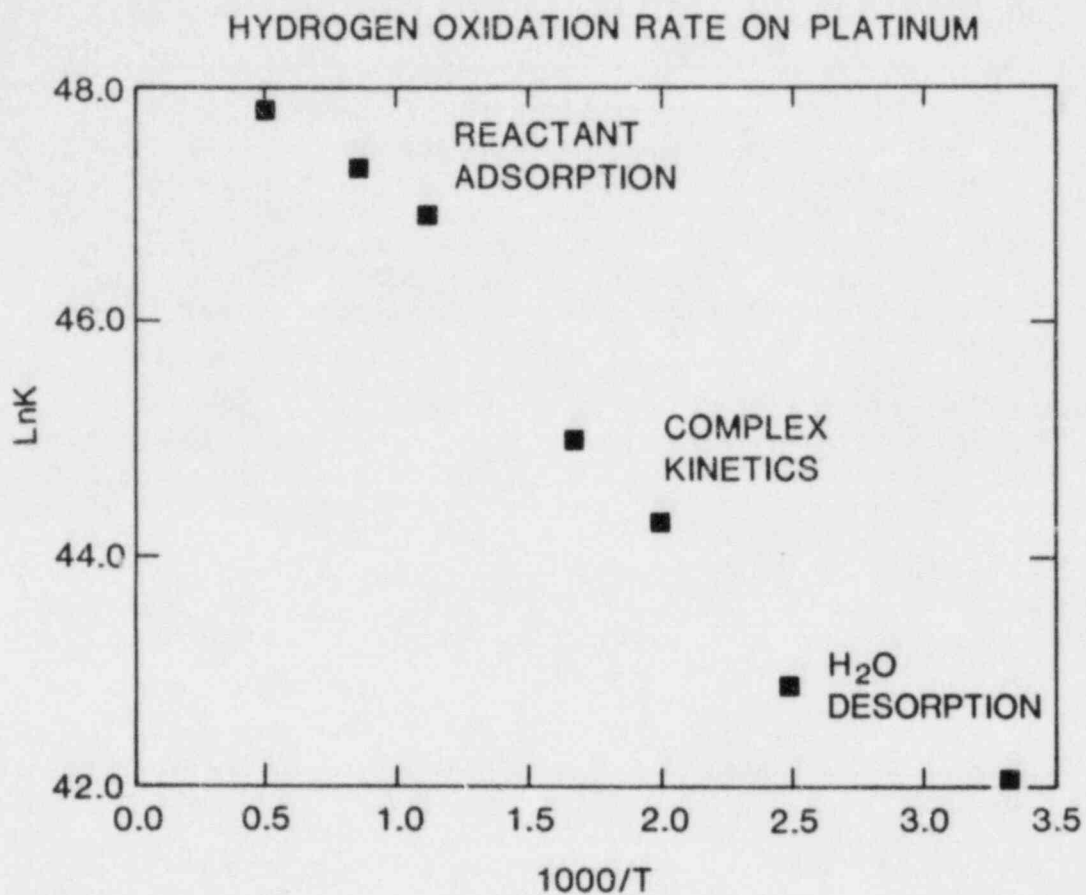
Figure 3.35. Hydrogen Oxidation Rate on Platinum Surface
Based on Rates and Mechanisms of Table 3.7,
Assuming 80-torr Gas-Phase Hydrogen Pressure

SURFACE ENERGY RELEASE RATE
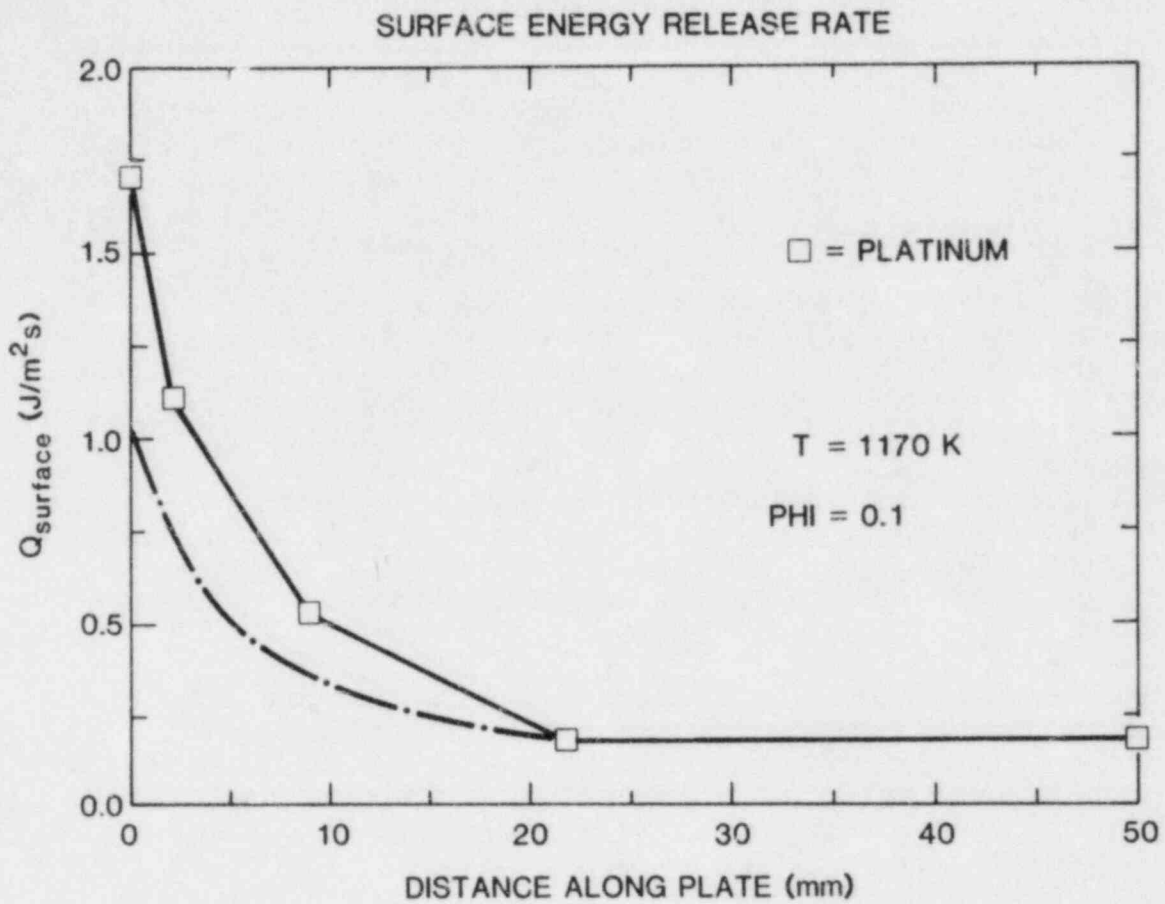
Figure 3.36.   Comparison of Computed and Measured Surface
Heat Release Rates for 3% Hydrogen in Air
(ϕ = 0.1) and Surface Temperature of 1170 K

Experimental and predicted OH concentration profiles are shown in Figure 3.37 as a function of distance above the platinum surface at 5 mm from the plate leading edge. In both cases maximum OH concentrations occur in the high temperature region near the surface and decrease across the boundary layer due to gas phase recombination reactions. Maximum predicted concentrations are significantly lower than measured experimentally, and the model is being examined to ascertain the reason for this difference.

It is expected that the observed discrepancies between experimental and predicted results are due primarily to uncertainties in the surface reaction rate constants, which were estimated based on best values obtained from the literature. An additional source of error arises from the simplified method used to estimate the surface adsorbed species concentrations. This approach assumes a constant value for the surface concentrations based on the initial gas phase reactant concentration while in fact the surface concentrations are dependent on local gas phase concentrations which vary along the surface. A more exact approach in which a steady state assumption for the surface species is used to calculate the surface concentrations as a function of local gas phase composition is being developed and incorporated into the model. The surface reaction rate constants can then be modified to obtain agreement with experimental results.

Based on the modelling studies to date, we conclude that there is good evidence for catalytic oxidation of weak (lean) hydrogen:air mixtures at temperatures as low as room temperature. A successful passive ignition device would require the surface of the igniter to become sufficiently hot due to such catalytic activity that initiation and propagation of a gas phase flame would result. While it may be possible to construct an approximate model of the initiation process, it is also necessary to test various configurations and materials for ignition devices in the laboratory under appropriate gas concentration and gas velocity conditions. Such experiments must also be complemented by experiments that examine the catalytic activity of various materials in the presence of adsorbed water vapor or other contaminants.

3.2.9   Steam:Hydrogen Flame-Jet
        (J. E. Shepherd and O. B. Crump, Jr.)

During the October 1982 to March 1983 period, we have carried out several new types of experiments and measurements in the facility. We have concentrated on measuring heat flux from the flame and developing improved flow visualization using video (TV) cameras.

Simultaneous measurements of centerline flame temperature and heat flux have been obtained for steam:hydrogen ratios
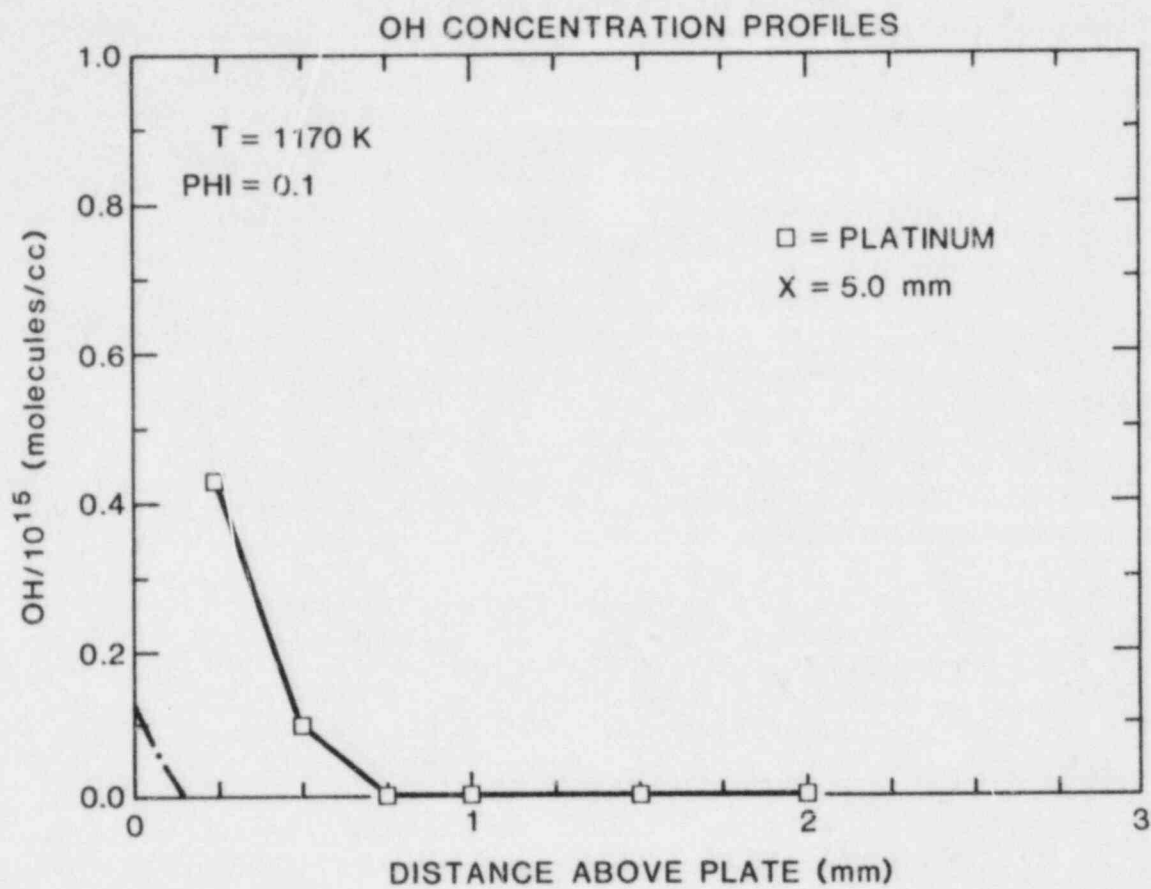
Figure 3.37. Comparison of Computed and Measured OH Concentrations Near the Surface Leading Edge for Same Conditions as Figure 3.36

of 0 to 6 and an exit temperature of 200°C. Two different types of gages have been used to measure heat flux. The first is a water-cooled Gardon (circular-foil) gage manufactured by the HYCAL Corporation. The face and sensitive element of this gage is directly exposed to the flame and is placed parallel to the flow direction approximately 0.5 in. from the centerline. The gage is coated with a highly absorptive black paint so that the total flux is measured. The second gage is our own design, a small diameter stainless-steel tube through which a slow flow of water is maintained. The tube is oriented perpendicular to the jet flow and passes through the jet centerline. Both the cooling water flowrate and the tube inlet and exit water temperatures are measured; the tube surface remains cool during operation and appears fairly reflective.

Each probe and a Pt/Pt-Rh thermocouple mounted nearby have been simultaneously traversed along the centerline of flames with a variety of steam:hydrogen ratios in the jet. Data from a traverse with the Gardon gage is shown in Figure 3.38; the hydrogen flowrate was 60 SLPM and the steam flowrate 80 SLPM with an exit temperature of 200°C and a nozzle diameter of 0.25 in. During operation, a substantial amount of water is observed to condense on both types of probes.

Comparison of heat-flux profiles from nitrogen- and steam-diluted flames with the same parameters shows that the steam-diluted flames transfer heat at approximately four times the rate of the nitrogen-diluted flames. The temperature profiles are almost identical for the two flames except that the nitrogen-diluted flame is slightly shorter since nitrogen is heavier than steam, increasing the jet momentum flux and entrainment. The enhanced heat transfer can be attributed to the condensation of the steam on the cool heat-transfer gages.

In future experiments, we will attempt to operate with lower cooling-water flowrates in order to eliminate this effect and determine the difference in the heat transfer. Measurements at higher exit temperatures and different steam: hydrogen ratios will be performed next. In addition, the Gardon gage will be installed in a false ceiling that can be traversed above the flame. The stagnation heat flux measured in this configuration has been studied extensively by other investigators and is much easier to analyze than the present measurements.

A brief literature search has turned up several papers on heat transfer from impinging flames. The most comprehensive of these is You and Faeth's paper on fire plume impingement.[57] Unfortunately, no work of a similarly comprehensive nature has been located for flame-jets. Experimental results for fuel-oxygen flame-jets have been reported by
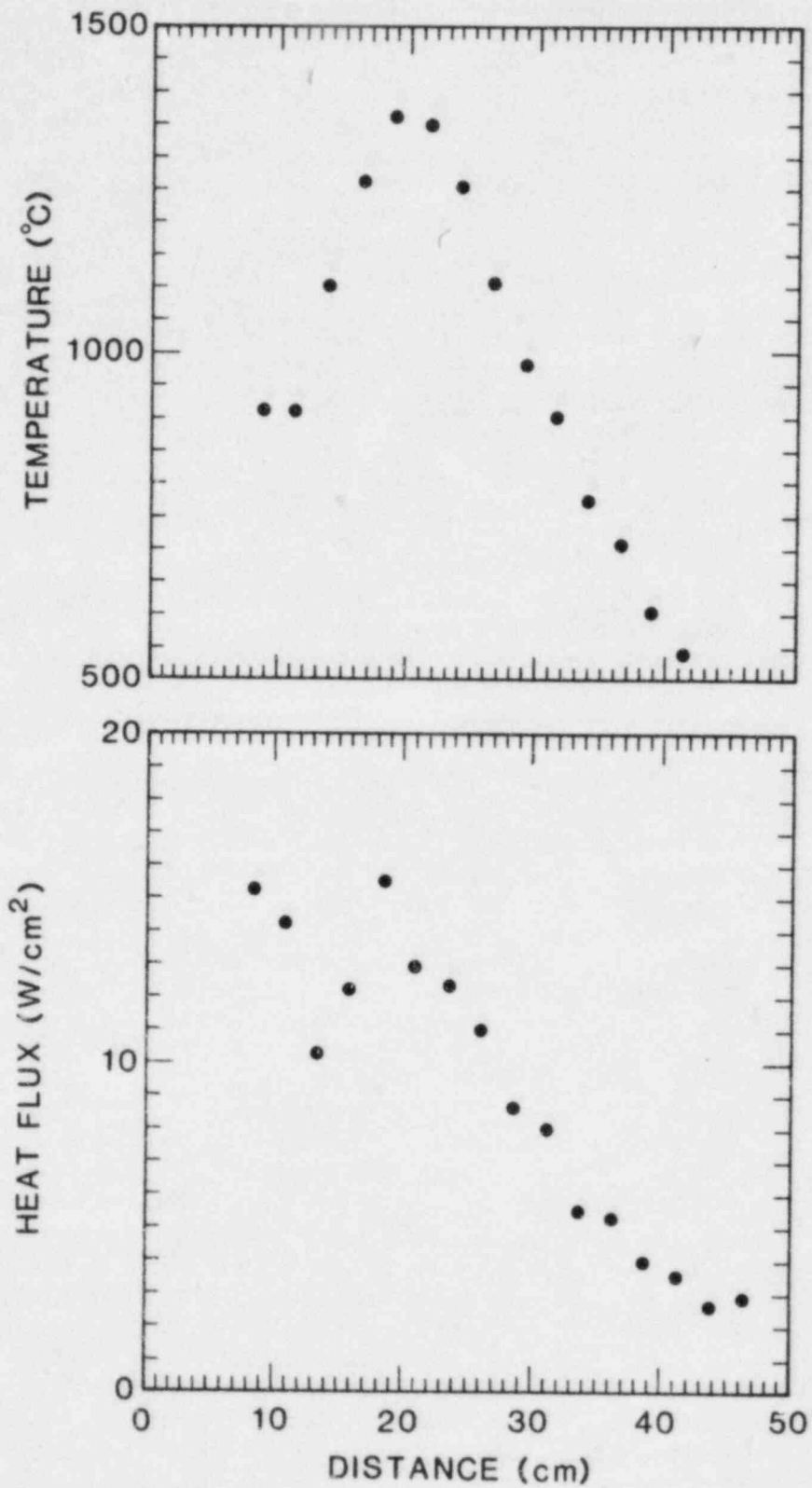
Figure 3.38. Centerline Temperature and Total Heat-Flux
Profiles for a 60-SLPM Hydrogen and 80-SLPM
Steam Flame-Jet, Initial Temperature 200°C,
0.635-cm-Diameter Nozzle

Connoly and Davies [58] and Kilham and Purvis[59], but scaling information was not reported. It may be possible to use the extensive literature on heat transfer from noncombusting jets (cf Donaldson et al. [60]) to estimate the heat transfer from flame-jets. In fact, this is the approach used to correlate the experimental results in the references given above.

Results of heat-flux measurements in the flame with the Sandia-designed probe are shown in Figure 3.39. This probe is a 1.7 mm-diameter stainless steel tube 15 cm in length through which a slow flow of water (about 0.5 cc/s) is maintained. The total heat input to the tube is calculated from the temperature rise, $T_2 - T_1$, in the water,

$$Q = M_{H_2O} C_p (T_2 - T_1) \tag{3-23}$$

where M_{H_2O} is the cooling water flowrate and C_p is the heat capacity of water. Typical temperature rises are about 50°C yielding Q's of about 100 W. This heat input can be compared to the total heat output of the flame,

$$Q^* = M_{H_2} h_c \tag{3-24}$$

where M_{H_2} is the hydrogen flow rate and h_c is the heat of combustion of hydrogen, 57 kcal/mole (0.177 kW/SLPM) or in reactor-scale units, 96.2 MW per kg/s of H_2. For the flame used in the present experiments (a 60:40 ratio of steam to hydrogen at 200°C, total flowrate of 80 SLPM), $Q^* = 11.5$ kW and $Q/Q^* = 0.02$. That is, the heat absorbed by the probe is about 2% of the total flame power output.

A commercially available TV camera equipped with a low-light-level-sensitive tube (newvicon) has been used to visualize the flame without the aid of seeding the flow. The technique looks very promising for possible use in large-scale experiments such as the EPRI NTS tests or the FLAME facility. The camera contains commercially available optics and as such is not sensitive in the infrared. Therefore, the optical signal must be due to the luminescence of the inevitable impurities present in the flow. It may be possible to enhance the effect and increase contrast by the addition of small amounts of impurities (i.e., sodium) to the flow upstream. A videotape recording has been made to demonstrate both the technique and several flame-jet phenomena.
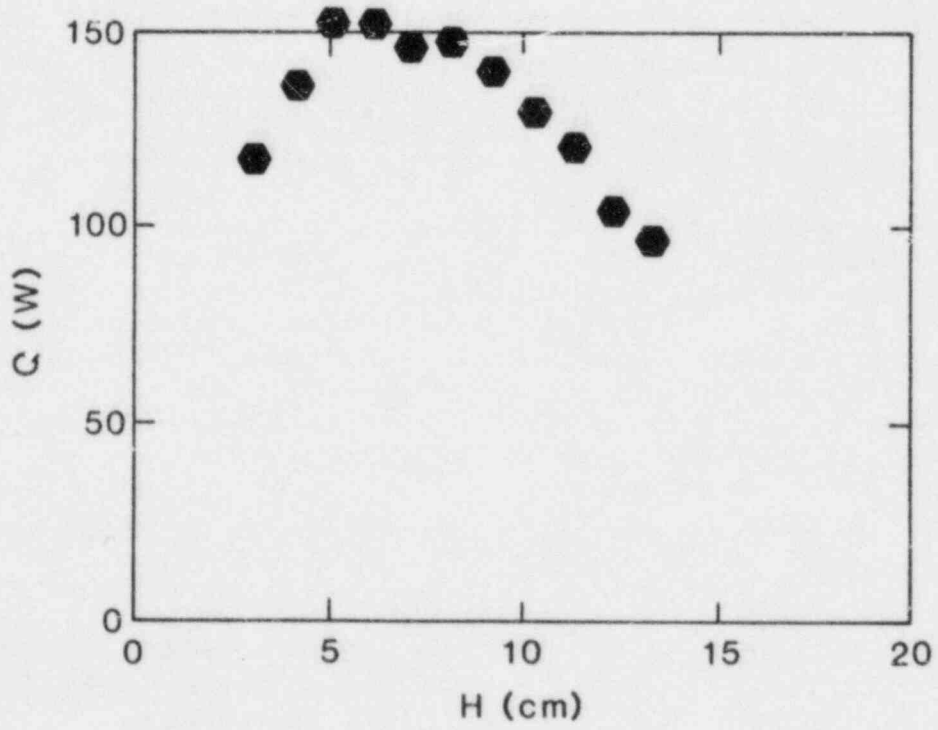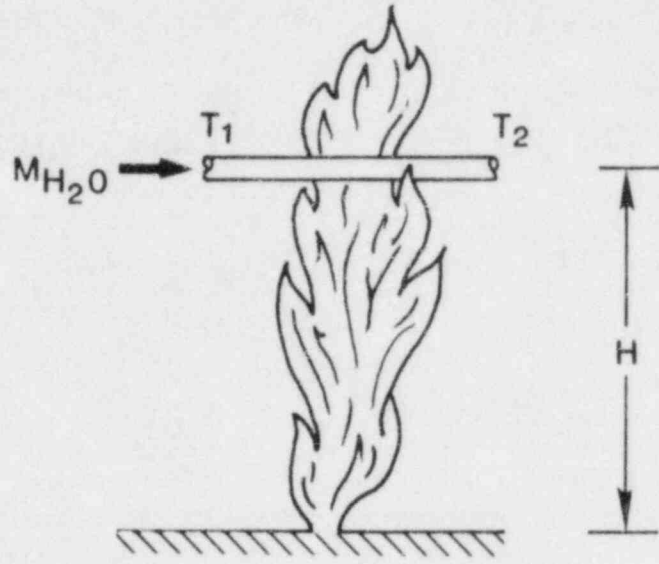
Figure 3.39.   Heat Transfer Along the Centerline of a 10 kW
              60:40 Steam:Hydrogen Flame-Jet to the Sandia
              Water-Cooled Probe

3.2.10 Heat-Flux Measurements and FITS Data Reduction
        (J. E. Shepherd, O. B. Crump, S. N. Kempka,
         A. C. Ratzel)

Thin-film gages and slug (capacitance) calorimeters have been
in use at the FITS tank since December 1983. Data from over
100 burns have been successfully recorded. Several problems
with the gages occurred and have been solved. As a result of
these problems, a new window holder design for the radiative
gages will be used in the EPRI NTS tests and the calorimeter
design will also be modified. Both problems were the result
of adhesives failing after prolonged use at 120°C and windows
or calorimeter disks detaching from their mounting surfaces.

Preliminary data reduction has been carried out on four dry
burns with nominal hydrogen concentrations of 10%, 15%, 20%,
and 30% by volume. This initial data reduction assumes con-
stant and uniform thermal properties of the gage substrate.
Front-surface temperature rises of over 200°C were recorded
on the 30% burn, so these property variations can be impor-
tant at the higher concentrations and the present method
will be inaccurate. Radiative and total fluxes for the 15%
and 20% burns are shown in Figure 3.40.

The radiative fluxes have been corrected for the transmission
and reflection (Fresnel) losses of the sapphire window (about
15%) and the cutoff in transmission at wavelengths longer
than 6 μm. The magnitude of the latter effect depends
primarily on the temperature of the product gases and ranges
from about 20% lost at 2800 K to over 70% at 1200 K. This
correction was computed by using the measured pressure his-
tory and calculated AICC density to compute an effective gas
temperature and then using Edwards' wide-band radiation model
to compute the fraction of radiation emitted by the water
vapor at 6 μm and longer wavelengths. Both radiative and
total gages have essentially the same viewfactor except for
the vignetting effect of the window on the radiative gage.
We estimate this effect to be about 3% at most.

There are several interesting features in the measured fluxes
shown in Figure 3.40. Comparison with the pressure signals
shows that the peak total fluxes occur just before the end
of the burn (both gages were mounted near the top of the
tank). The peak total fluxes are approximately 2.5 times
higher than the peak radiative fluxes. The maximum specific
energy deposition (J/cm^2) is a factor of 2 higher for the
total flux gage than for the radiative gage.

A method to transfer FITS data to the Building 634 VAX has
been established. An LSI 11 minicomputer equipped with a
floppy disk drive has been connected to the VAX. Copies of
the data diskettes and test data sheets from test series 1
and 2 have also been stored with the LSI 11. A set cf pro-
grams and data files has been developed on the VAX to reduce
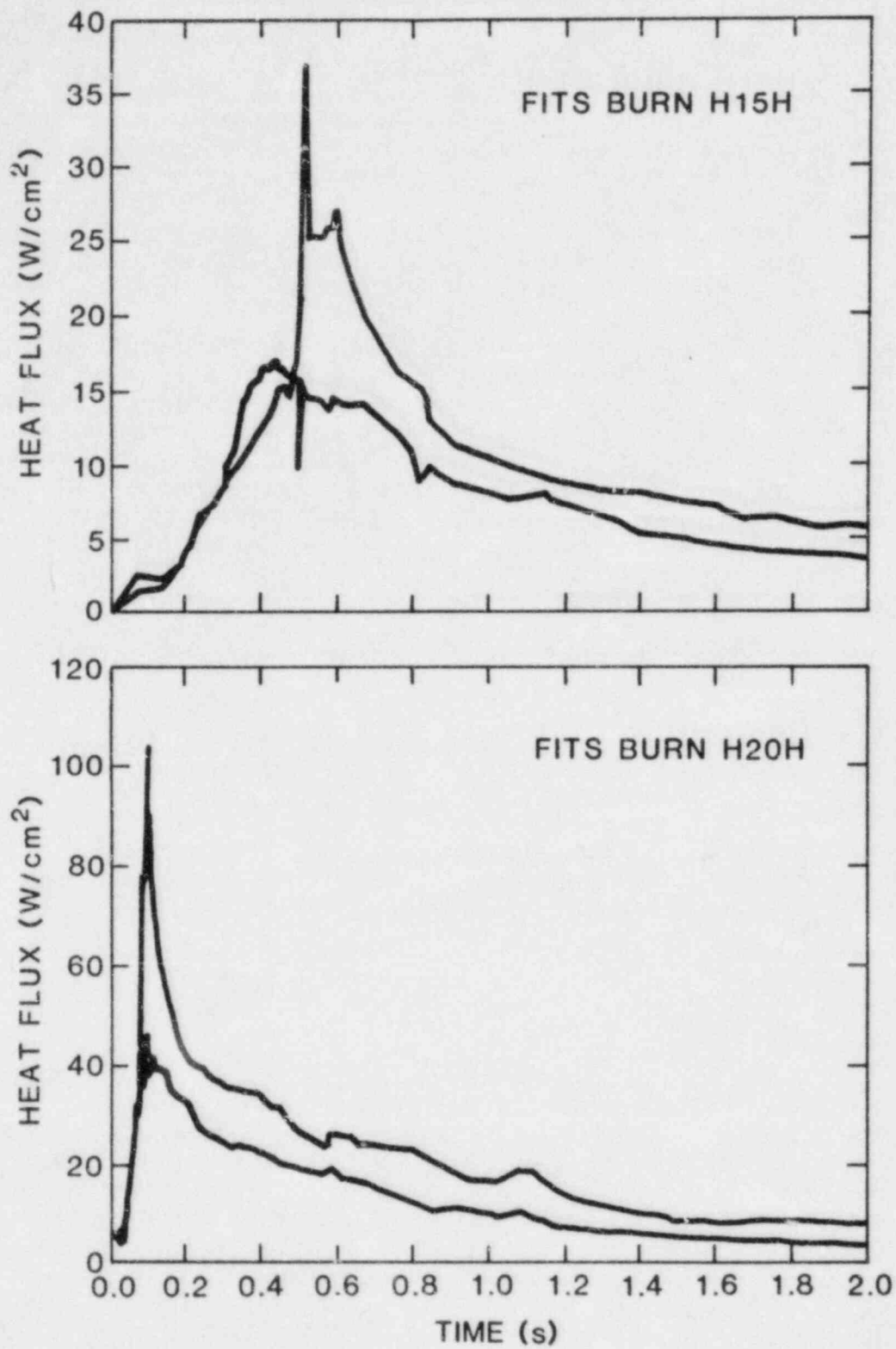
Figure 3.40.   Total and Radiant Heat Fluxes Measured in Two
Dry Hydrogen Burns in the FITS Tank: Burn
H20H, 20% Hydrogen; Burn H15H, 15% Hydrogen

pressure, thin-film and slug calorimeter data. These programs have been integrated into an automatic data reduction system that uses the raw data transferred from the LSI 11 and produces plots and reports on computed heat fluxes, energy depositions, gas temperatures, and pressures. Adiabatic, isochoric conditions, gas emittance, and window cutoff corrections are automatically computed as part of this package. Data from about 20 tests have been completely reduced at this time. This includes some pressure data from the HBS tests last summer.

Since much more complex (and necessarily larger) routines can be used on the VAX than on the LSI 11, a greater amount of information can be extracted from the pressure signals than has been done in the past. After the burn is complete, the mean gas temperature can be estimated from pressure using the calculated (or measured) postcombustion composition and the ideal gas law. The mean gas temperature, pressure, and steam fraction are used to compute the emittance of the gas as a function of time. The radiative heat flux, q_r, from the combustion products to the vessel walls can be estimated by

$$q_r = e * \sigma * T^4 ,\qquad (3-25)$$

where e is the emissivity computed with a beam length appropriate for radiative transfer to the enclosure, σ is the Stefan-Boltzmann constant, and T is the temperature.

The total heat flux to the vessel walls, q_t, can be estimated by calculating the mean energy loss rate from the gas per unit surface area of the vessel;

$$q_t = \frac{VC_v}{A} \frac{dT}{dt}\qquad (3-26)$$

where V/A is the volume-to-surface-area ratio of the vessel, C_v is the specific heat at constant volume, and dT/dt is the time-rate-of-change of the mean gas temperature. The time-rate-of-change of the mean gas temperature can be determined from the derivative of the pressure cooldown curve and the ideal gas law. Both the total and radiative fluxes can be integrated with respect to time to obtain specific energy depositions. Plots of each type of computed information are shown in Figures 3.41 and 3.42 for FITS test H10H. This test was performed on January 7, 1983; the initial conditions were: pressure, .93 atm; temperature, 352 K; and hydrogen concentration, 10.0%. No steam or carbon dioxide was added. A beam length of 1 m was used in the emittance calculations and a volume-to-surface area ratio of 28.6 cm was used in the total heat-flux calculations.

GAS TEMPERATURE
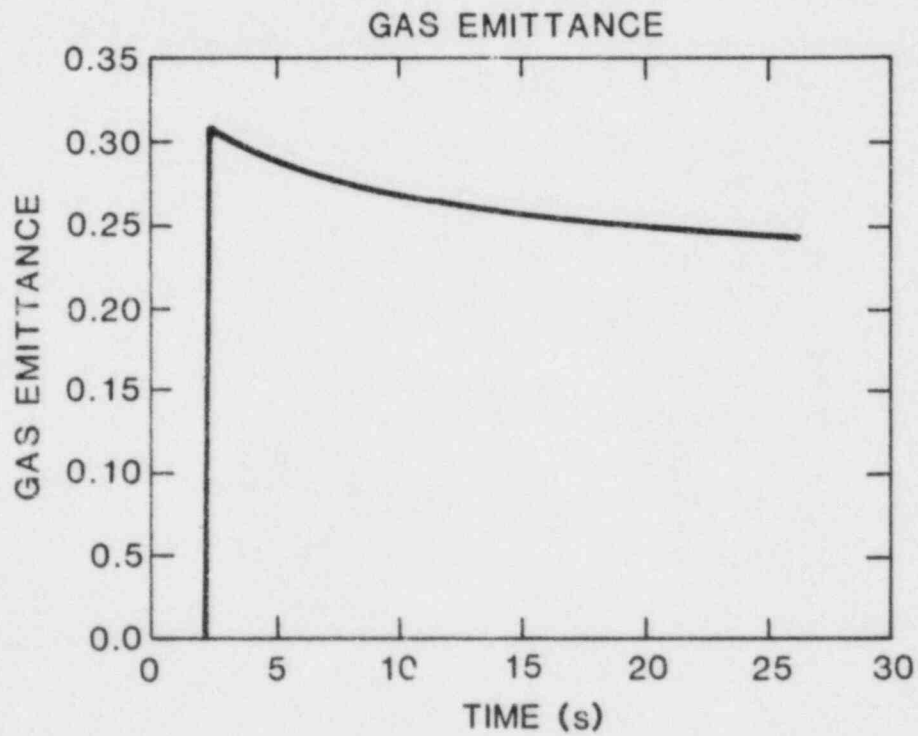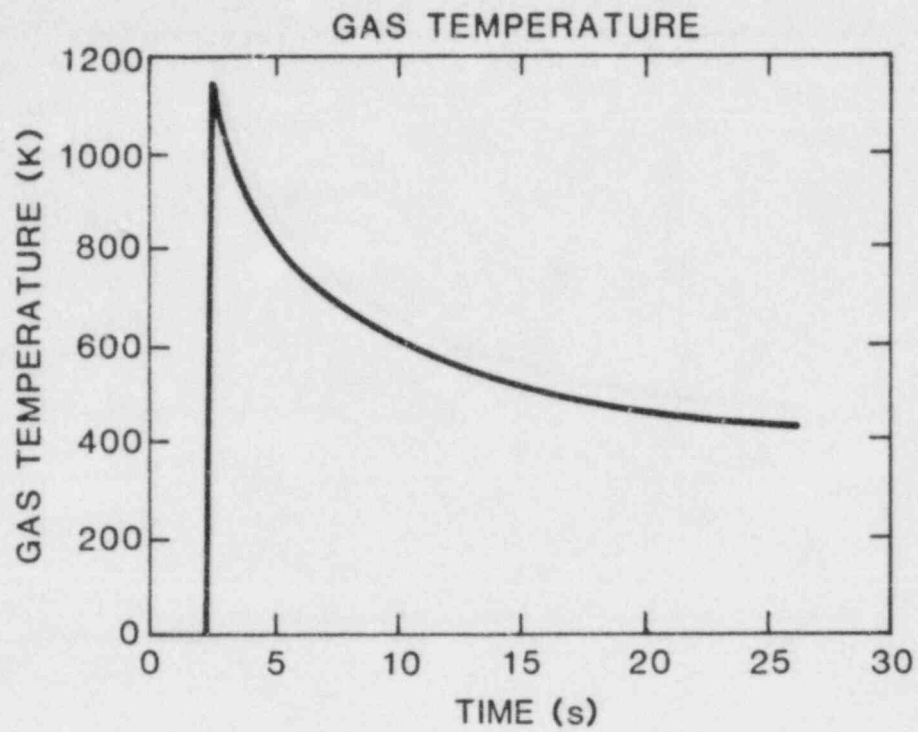
GAS EMITTANCE

Figure 3.41.   Mean Gas Temperature and Emittance Calculated from the Pressure Signal of FITS Test H10H
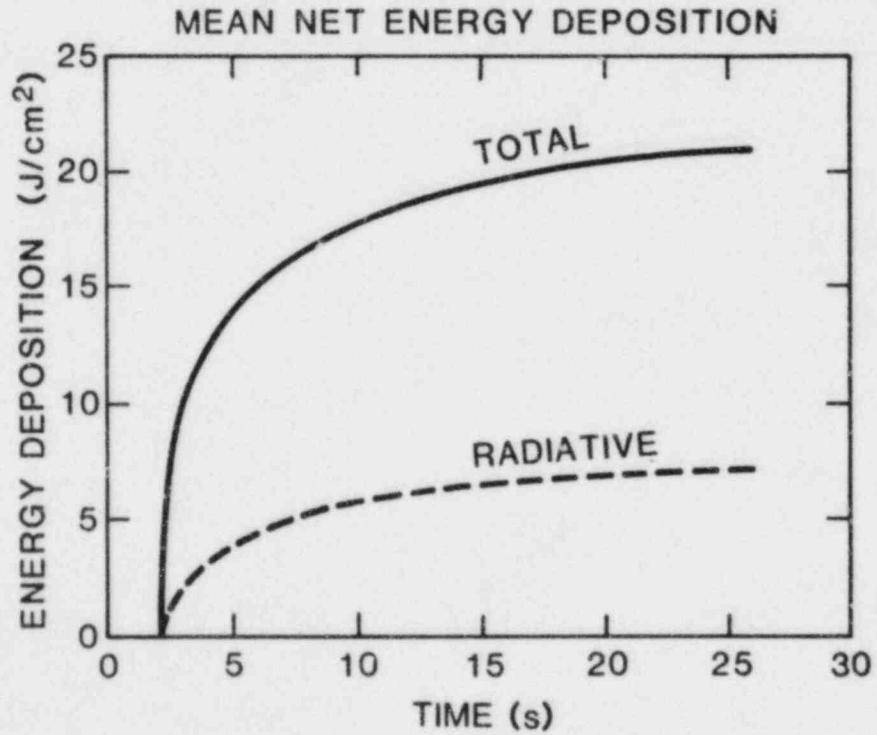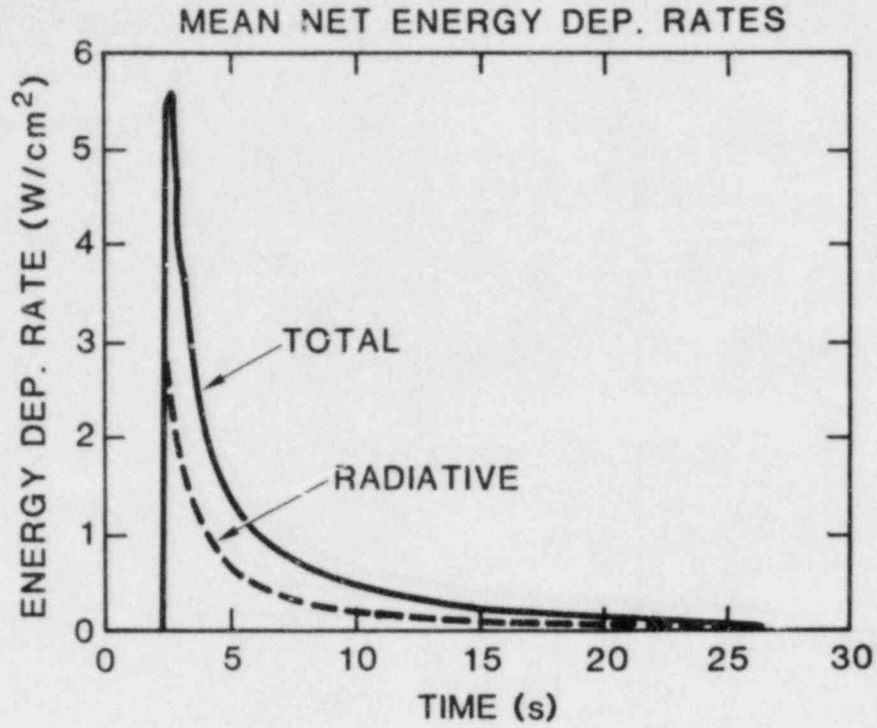
Figure 3.42. Radiative and Total Heat Flux and Energy Deposition Calculated from the Pressure Signal FITS Test H10H

3.2.11 Sandia Participation in EPRI NTS Tests
        (J. E. Shepherd and O. B. Crump, Jr.)

Following discussions with EPRI and EG&G, an agreement was
reached for Sandia to place some instrumentation inside the
dewar being used by EPRI at NTS. The instrumentation is
similar to that developed at Sandia for use in the FITS tests
and includes two thin-film heat-flux gages, two slug calori-
meters and two pressure transducers. The equipment was
ordered and constructed during the winter and was installed
during several trips to the NTS in March 1983. Each instru-
ment is described in detail below. Besides supplying equip-
ment, we have participated in the design and safety reviews
of the facility and made estimates of combustion overpres-
sures and flame lengths for the proposed test series. We
are also supplying EG&G with an equilibrium computer code to
do calculations of adiabatic combustion final states for
general hydrogen:air:steam mixtures.

We have supplied two heat-flux gages that have been developed
especially for transient measurements in a combustion envi-
ronment. The gages were designed and constructed at Sandia
and several models have been in use in combustion experiments
at Sandia during the last 6 months. Each gage consists of a
300 angstrom thick platinum resistance element (about 100
ohms) that is vapor deposited on the polished front surface
of synthetic glass ceramic (MACOR) substrate, 10 cm in diame-
ter and 5 cm thick. The front surface of the gage is covered
by a protective coating of Al_2O_3 and then a layer of NEXTEL
paint. NEXTEL is a highly absorptive, spectrally flat, black
coating with an emissivity of 0.98. The MACOR substrate is
mounted in a protective stainless-steel housing with only
the front surface exposed. A constant current of 10 mA is
passed through the resistance element and the voltage drop
across the gage is recorded. From the voltage drop, the
resistance of the element can be determined and having pre-
viously calibrated the resistance-temperature characteris-
tics, we can determine the gage front surface temperature.

One gage, referred to as the "total flux gage" is directly
exposed to the combustion environment and measures the net
total heat flux to the gage. The other gage, referred to as
the "radiative flux gage" is covered by a 0.635 cm thick
sapphire window separated by a vacuum space from the MACOR
substrate. After correcting for the losses in the window,
the output of this gage can be interpreted as the net radia-
tive heat flux to the gage. The pair of gages are mounted
near the top of the dewar, about 1 m from the centerline
rake.

The theory behind the gage operation is outlined below. Due
to its small mass, the thin-film resistance element has an
extremely fast response time (microseconds) and a negligible

effect on the heat transfer into the MACOR. Also, the MACOR substrate is made large enough so that, for the purposes of heat transfer, it appears semi-infinite on the time scale of the experiment, typically 20-100 s. Using the measured front-surface temperature of the substrate and the thermal properties of MACOR, the front surface heat flux can be calculated from the known solution to the heat transfer problem in a semi-infinite, one-dimensional slab.

A signal processing unit has been supplied by Sandia to precondition the signals from the thin-film heat-flux gages before digitizing by the NEFF system. The processor consists of two identical and completely independent channels for each of the two gages. Each channel contains a constant-current source, a sample-and-hold circuit, and three instrumentation amplifiers. The main purpose of the processor is to generate the main gage output signal. This signal is obtained by amplifying the difference between the voltage drop across the gage during the experiment (burn and cooldown of the combustion products) and the voltage drop that was present at the static conditions just prior to the burn.

Sandia has supplied two strain-gage type pressure transducers manufactured by Precise Sensors. These gages will be mounted inside the dewar and used to monitor both static and dynamic pressure during the combustion experiments. These gages are both of the same design (model 141-3), but with differing sensitivities; one has a 100 psi full scale range, the other has a 200 psi full scale range. The 100-psi range gage has been mounted at the top of the dewar next to the thin-film gages, and the 200-psi gage will be mounted at the bottom of the vessel about 30 cm above the nominal water level.

The gages were supplied with factory calibrations and were tested at Sandia in about 30 hydrogen:air:steam combustion experiments in the FITS tank. Gage responses agreed well with each other and with other Precise Sensors that had air-cooled diaphragms. From this, we concluded that these gages were fairly insensitive to the combustion environment and should function properly inside the dewar. After the combustion testing, the gages were recalibrated at room temperature (about 23°C) and at 80°C.

Sandia has supplied two slug calorimeters to be used in the experiments. These calorimeters consist of a 3.5 cm diameter OFHC copper disk mounted in an insulating substrate (MACOR). The front surface is coated with NEXTEL paint and a type K intrinsic thermocouple has been constructed on the back surface by brazing two .25-mm thermocouple wires to the copper about 4 mm apart near the center of the disk. Both gages are mounted inside the dewar near the off-axis rake. One gage, the "total flux calorimeter", is directly exposed to the flow. The other gage, the "radiative flux calorimeter",

3-100

is protected from the environment by a 0.635-cm thick sapphire window and a vacuum space.

The total flux gage is about 1.5-mm thick in the center and has a mass of 16.00 g; the specific energy deposition constant is 0.743 J/K-cm². The radiative flux gage is 0.5 mm thick in the center and has a mass of 4.24 g; the specific energy deposition constant is 0.197 J/Kcm². We expect that the maximum temperature the copper will reach is about 10 times that reached in our medium scale experiments at Sandia. This means that for a dry burn, 10% hydrogen, we expect to see a maximum temperature rise of 250°C for the total gage and 100°C for the radiative gage.

Sandia has supplied a simple code to perform on-line calculations of adiabatic, constant-volume, or constant-pressure combustion final states. This code solves for the equilibrium state of the combustion products and prints out or displays the final pressure, temperature, density, molecular weight, isentropic index (ratio of specific heats), and composition. Eleven species are included in the products: H_2, H, O_2, O, H_2O, OH, N_2, AR, CO, CO_2, NO. All of the major species and liquid water can be included as reactants.

A document that describes the Sandia instrumentation has been prepared and will be distributed to EG&G, EPRI, and Sandia personnel involved in the tests. We plan to process data from some tests at Sandia as a cross-check on the reduction at the NTS.

3.2.12 McGill Research on Hydrogen Combustion
(J. Lee, R. Knystautas, C. Guirao, C. Chan)

3.2.12.1 Hydrogen Deflagration Studies

The deflagration mode of combustion is by far more probable than the detonation mode in accidental situations. In any probability risk assessment, it is important to have a realistic estimate of the burning rate. Although a laminar burning velocity can readily be measured or calculated theoretically with a fair degree of accuracy for any given explosive mixture, this parameter does not represent the burning rate under actual conditions. This is due to the fact that the freely propagating flame in an explosion is very sensitive to the gas dynamic flow structure that it generates. Thus, ignition criterion, flammability limits, turbulent burning velocity, etc., are all strongly coupled to the gas dynamic flow parameters (i.e., velocity gradient field, turbulence intensities, and scales, etc.) in the unburnt mixture, much more so than the chemical and physical properties. This intercoupling between gas dynamics and combustion for transient deflagrations is far from understood. The objectives of the research conducted at McGill are to elucidate these

coupling mechanisms and deduce empirical relationships and
scaling laws for hydrogen:air deflagrations.

3.2.12.1.1 Flame Acceleration Due to Repeated Obstacles

The first study investigates the influence of repeated obsta-
cles on flame acceleration. It is by now well known that
obstacles in the path of a propagating flame create turbu-
lence resulting in flame acceleration and high turbulent
flame speeds.[61] Hydrogen:air mixtures are particularly
sensitive, and transition to detonation can easily occur
under appropriate confinement and boundary conditions. The
objectives of the study are to investigate flame acceleration
rates, transition to detonation, maximum turbulent flame
speeds, and detonation states under different obstacle envi-
ronments. The experiments are performed in long circular
tubes of various diameters (5 cm and 15 cm). Spiral coils
or repeated circular orifice plates of different blockage
ratios (BR = 1 - $(d/D)^2$) are inserted into the tube as turbu-
lence generators. The flame speeds (relative to laboratory
coordinates) and pressure-time histories are measured for
a wide range of hydrogen concentrations in air (10% $\leq$ hydro-
gen $\leq$ 55%).

For all hydrogen concentrations, rapid flame acceleration to
steady state conditions within the 3 m length of the obsta-
cle region are observed. Figure 3.43 shows the steady state
flame speed in the obstacle section of the 5 cm diameter
tube for various hydrogen concentrations. Results for three
different obstacle configurations are plotted: (i) spiral
BR = 0.44, (ii) orifice plates BR = 0.44, (iii) orifice
plates with BR = 0.60, and the pitch or plate separation is
5 cm for all three configurations. It is of interest to note
that a sharp jump in the steady-state turbulent flame speed
occurs around 13% hydrogen. For hydrogen $\lesssim$ 13%, the flame
speeds are < 200 m/s and not particularly sensitive to obsta-
cle configuration. For hydrogen $\lesssim$ 13%, the flame speeds jump
up sharply to values of the order of the sound speed of the
mixture, i.e., ~400 m/s. For 13% $\lesssim$ hydrogen $\lesssim$ 25%, a small
dependence on the blockage ratio of the obstacles (i.e., pres-
sure losses) is observed, but the flame speed increases relat-
ively slowly with increasing hydrogen concentration. Depen-
ding on the blockage ratio of the obstacles, another sharp
jump to quasi-detonation velocities (1300 m/s $\lesssim \dot{R}_f \lesssim$ 1700 m/s)
occurs at hydrogen concentrations between 25% and 30%. Tur-
bulent flames and quasi-detonation velocities depend on pres-
sure losses (i.e., blockage ratio). However, it should be
pointed out that although the spiral coil and orifice plates
may have the same blockage ratio based on the ratio of the
open core to the tube area, the spiral in effect causes a
smaller pressure loss to the flow. For the smallest block-
age ratio (BR = 0.44), quasi-detonation was achieved for
hydrogen concentrations ranging from 25% hydrogen to 45%
hydrogen for the spiral obstacle and from 30% hydrogen to
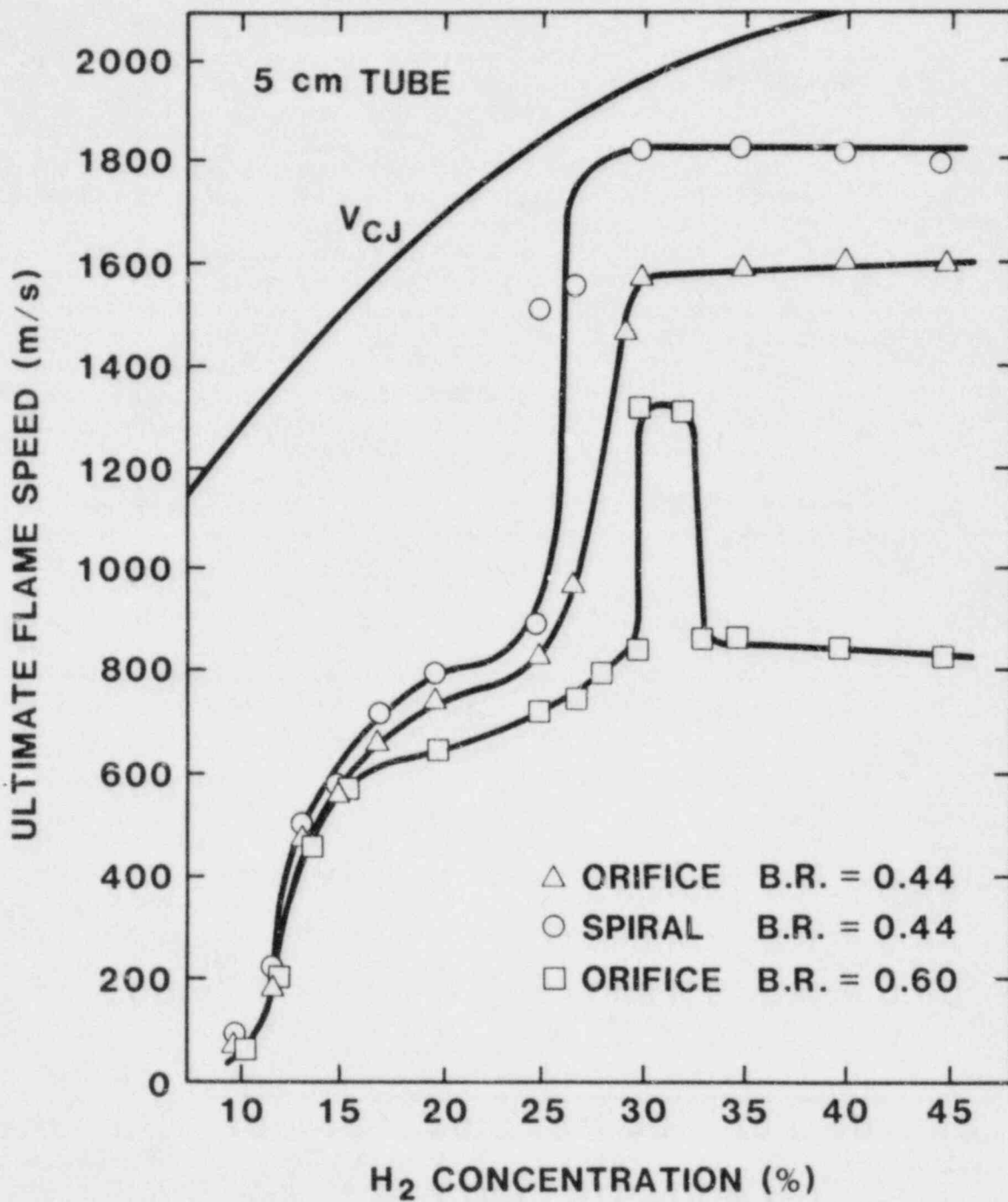
Figure 3.43.   Ultimate Flame Speeds for Hydrogen:Air Mixtures in a 5-cm Diameter Tube

45% hydrogen for the orifice plate. On the other hand, for the highest blockage ratio BR = 0.60, only strong turbulent deflagrations occur for hydrogen concentrations greater than about 33% hydrogen. For the smallest blockage ratio, it is expected that the quasi-detonation regime should also eventually terminate at the rich end when the mixture becomes less sensitive. For all obstacle configurations studied, the turbulent flame speed in which transition occurs is around 800 m/s. For an obstacle configuration where the pressure losses are less severe, this flame speed can be attained at lower hydrogen concentrations (e.g., hydrogen ≃ 26% for spiral). For high-pressure loss configurations, transition is delayed since the critical value of the flame speed is achieved for more sensitive mixture compositions (hydrogen ≃ 30% for orifice plates with BR = 0.6). Detonations in the obstacle region are characterized by detonation velocities significantly below that of the normal C-J values in smooth tubes with no pressure losses. For a given obstacle configuration, transition to the quasi-detonation regime occurs in a region around stoichiometric composition extending more to the rich side since hydrogen:air mixtures are more sensitive for high hydrogen concentrations. The width of this detonation regime depends on pressure losses.

To investigate the effect of scaling, the same experiments were repeated in a 15 cm diameter tube. As shown in Figure 3.44, the ultimate flame speed achieved with orifice plates (BR = 0.3875) as obstacles in both 5 cm and 15 cm diameter tubes is almost identical. In both tubes, two sharp jumps in flame speed occur at about 13% hydrogen and also around 25% hydrogen where transition to quasi-detonation occurs. The turbulent flame speeds are almost identical, although for the case of the larger tube, the quasi-detonation velocity is found to be below that of the smaller tube.

The results obtained thus far for both tubes indicate that larger scales appear to increase the acceleration rate, but the influence on the final steady-stage turbulent flame speed is minimal. Large eddies with longer lifetimes generated in future experiments in the 30 cm diameter tube and in the 4 ft diameter VGES facility at Sandia should have a more significant influence on the burning rate, especially for lean mixtures (hydrogen ≤ 13%).

3.2.12.1.2   Influence of Confinement on Flame Acceleration

The investigations on flame acceleration described in the previous section were performed in experimental situations where the flame propagation progressed in a fully enclosed environment of a long confining tube. In such a fully confined geometry, the flow of the unburnt gases that develops due to the displacement effect resulting from the increase in the specific volume across the flame zone is maximum. In most practical situations, explosion occurs under partially
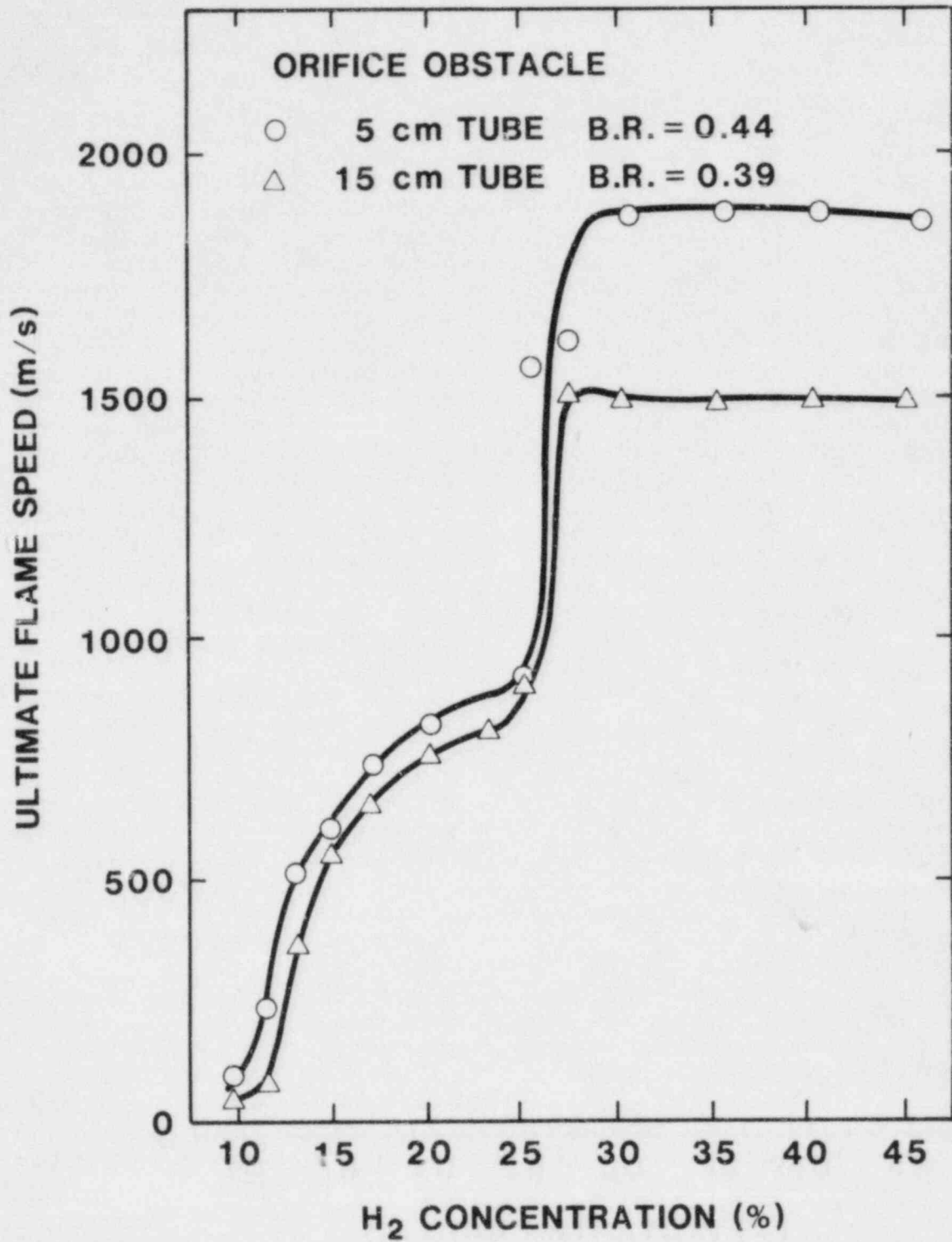
Figure 3.44.   Ultimate Flame Speeds for Hydrogen:Air Mixtures in a 15-cm Diameter Tube

confined conditions. Confinement here may be defined in terms of the available degree of venting of the gases normal to the direction of flame propagation (e.g., a tube with porous walls). The consequence of side relief by venting is a reduction of the mean flow velocity in the unburnt mixture ahead of the flame, thus rendering the turbulent flame acceleration mechanism less effective.

Experiments were carried out in a rectangular channel with one porous wall to determine the effectiveness of side relief on flame acceleration by repeated obstacle arrays. The channel is 12.7 cm x 20.3 cm x 1.22 m long with the top wall of the channel being removable so that it can be replaced by a porous plate of different degree of porosity. The degree of confinement is henceforth defined as the ratio of the closed area to the total area of the top plate (i.e., 100% confinement denotes a solid plate, while 0% confinement refers to complete removal of the top plate itself). Obstacles are in the form of baffle plates (12.7 cm x 5.0 cm) spaced 10 cm apart. Three different obstacle configurations are studied: (i) baffle plates mounted on the bottom of the channel, (ii) plates mounted on the centerline, and (iii) plates (20.3 cm x 3.1 cm) staggered alternately along both side walls of the flame channel. Typical results for the variation of flame speed with distance are shown in Figure 3.45 for the staggered obstacle configuration in 12.7% hydrogen: air mixtures. With a solid top plate (i.e., 100% confinement), the flame speed increases exponentially; however, steady state is not reached within the first meter of available travel. The maximum flame speed obtained is about 200 m/s. Replacing the solid top plate by a porous one of only 8% porosity (i.e., 92% confinement), a drastic reduction in flame speed is noted. The flame reaches a steady state in about 0.5 m, and the maximum steady turbulent flame speed corresponding to 92% confinement is only 14 m/s. Further increase in porosity of the top plate (e.g., 23% porosity or 77% confinement) gives only a slight further reduction in the steady state turbulent flame speed (i.e., 8 m/s). Figure 3.46 summarizes the results for different obstacle configurations, hydrogen concentration and degrees of confinement. The maximum flame speed at 1 m is plotted for different conditions. For 100% confinement, results for different obstacle configurations indicate that the staggered obstacle arrangement is the most effective giving maximum flame speeds of about 200 m/s as compared to only 50 m/s for the configuration when the baffle plates are mounted on the bottom of the channel. A reduction in hydrogen concentration by only 2% (from 12.7% to 10.6%) gives a large reduction in the maximum flame speed (e.g., 200 m/s to 53 m/s for the same staggered obstacle configuration). Significant decrease in flame speed for only slight decrease in the degree of confinement is illustrated for the particular case of the staggered obstacle arrangement and for 12.7% hydrogen. The
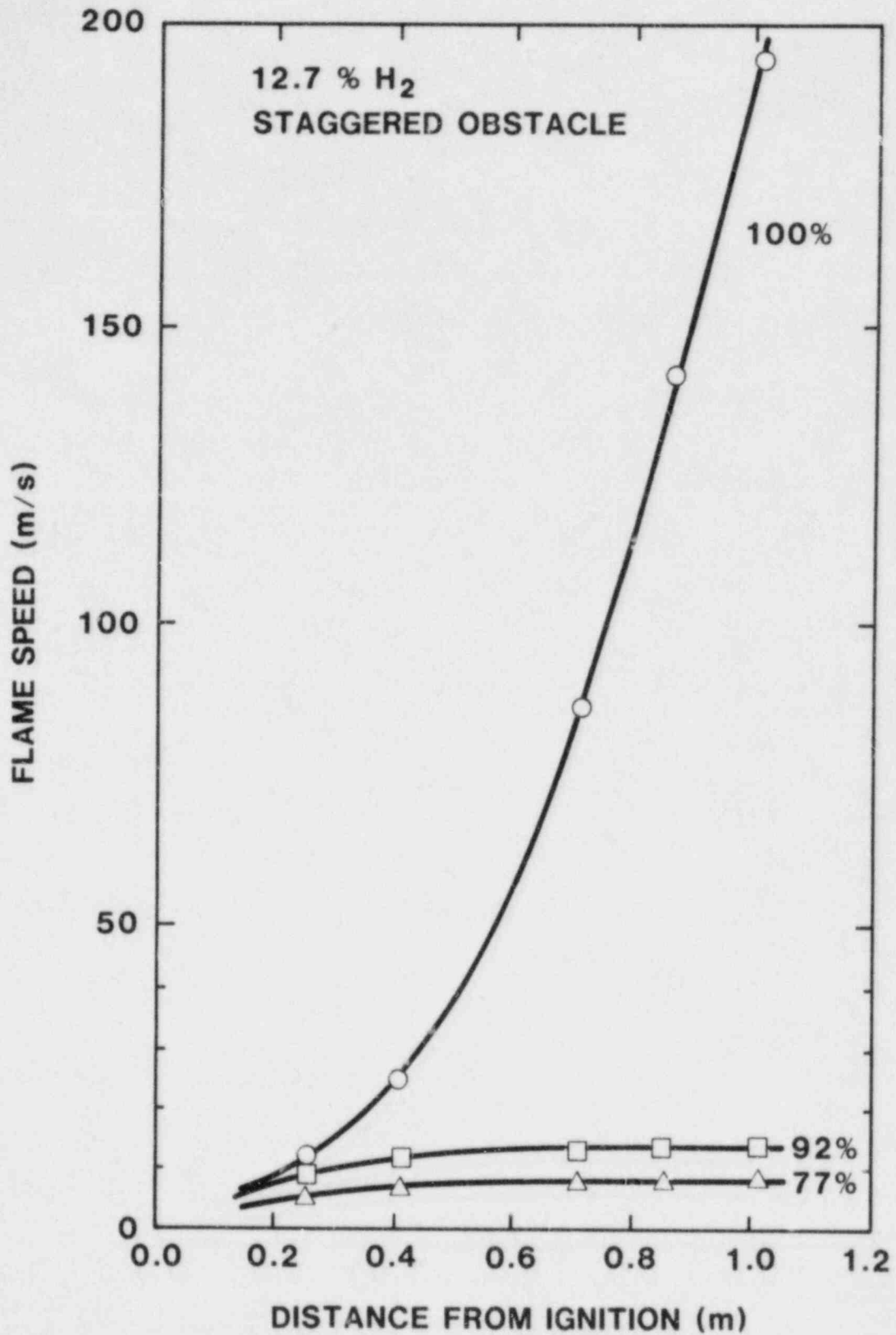
Figure 3.45. Flame Speed Profiles for 12.7% Hydrogen:Air Mixture under Various Degrees of Confinement
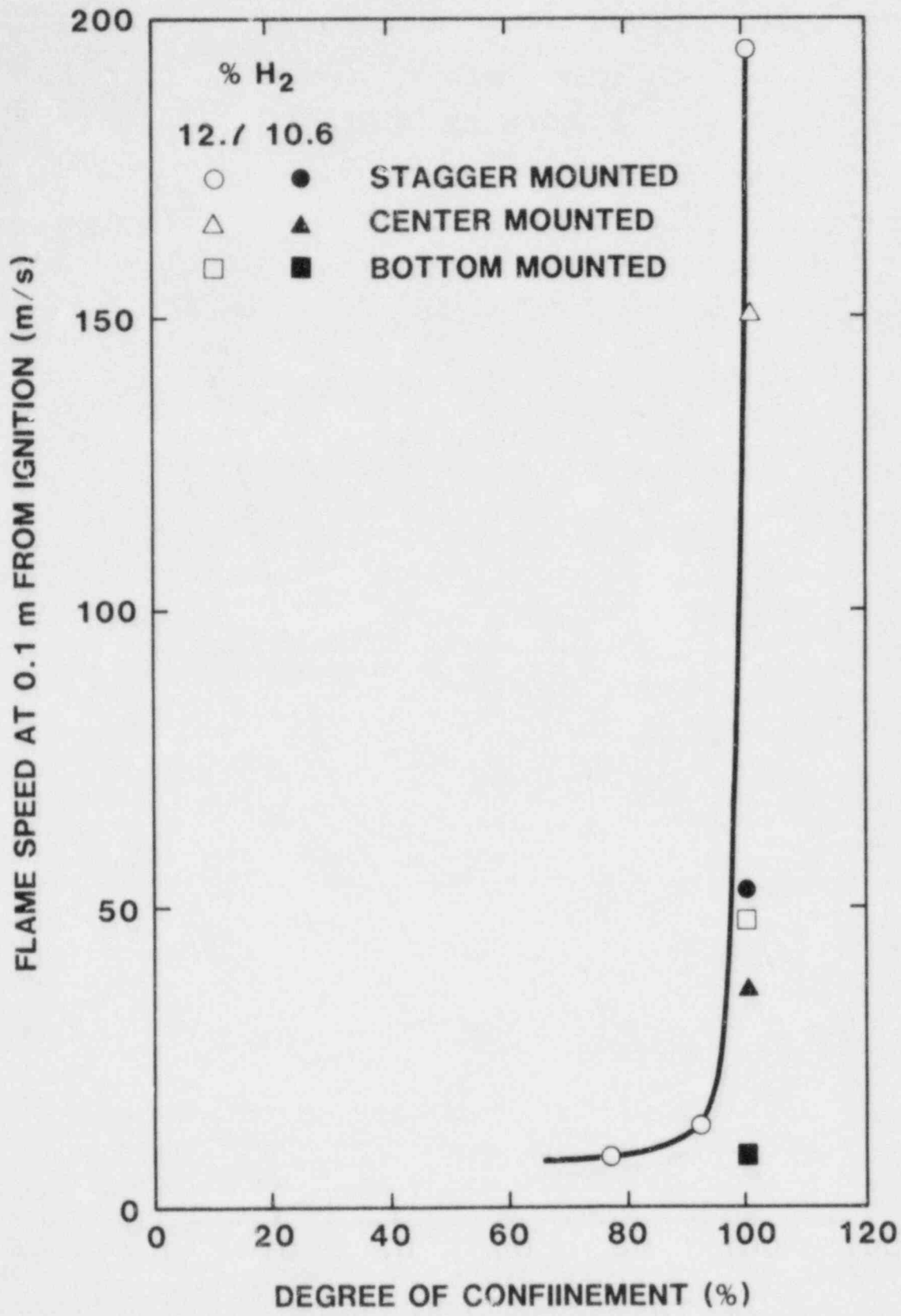
Figure 3.46. Influence of Confinement on Flame Acceleration for Various Obstacle Configurations

result from this study clearly indicates the effectiveness
of side relief or venting in reducing flame acceleration.
It should also be pointed out that this conclusion is based
on very lean mixtures only. For higher hydrogen concentra-
tions, the side relief may not be as effectve. Once the
flame accelerates to sufficiently high speeds so that the
pressure build-up can cause choked flow conditions through
the porous plate openings, venting becomes ineffective. It
should also be pointed out that scale will play an important
role for lean mixtures. Under large scale conditions, lean
mixtures may attain sufficiently high acceleration rates and
turbulent flame speeds to cause choking of the vents. When
this happens, the side relief provided will become ineffec-
tive. Future experiments in the large scale FLAME facility
at Sandia will provide more information on the importance of
scale.

3.2.12.1.3 Influence of Fuel-Air Composition on Flame Accel-
eration

Most of the turbulent flame acceleration tests have been
carried out with stoichiometric mixtures which, in general,
represent the optimum burning rate for a given fuel. In
practical situations, the explosive mixture under considera-
tion may often be far from the stoichiometric composition.
Thus, it is of importance to establish the sensitivity of
off-stoichiometric mixtures to turbulent flame acceleration
by obstacles.

Experiments have been carried out in a rectangular vessel
(0.13 m x 0.20 m x 1.2 m long) containing obstacles in the
form of baffle plates placed at the bottom of the vessel to
induce turbulence. Near lean limit hydrogen:air mixtures
as well as methane and propane mixtures were tested. The
results are shown in Figure 3.47 where the normalized flame
speed $\overset{\bullet}{R}_f/(\rho_u/\rho_b)$ S_u (or equivalently the burning velocity
ratio S_T/S_L with subscripts "T" and "L" denoting turbulent and
laminar flames, respectively) is plotted against the equiva-
lence ratio "ϕ" for the three fuels ($\phi = 1$ corresponds to stoi-
chiometric composition). The turbulent flame speeds in Figure
3.47 corresponds to values after 1 m of flame travel. The
results indicate a sharp decrease towards the lean and rich
limits as would be expected.

To examine the sensitivity of various fuel-air mixture on
flame acceleration, Figure 3.48 shows the flame speeds at
0.6 m, 1.0 m, and 1.1 m from ignition for various CH_4, C_3H_8,
and hydrogen:air mixtures as a function of the Reynolds number
defined as $(S_L(\rho_u/\rho_b - 1)/\upsilon)x$. S_L is the laminar burning
velocity, ρ_u and ρ_b are the density of the unburned and burned
gas, respectively, and υ is the kinematic viscosity. This
Reynolds number characterizes the flow generated by a planar
laminar flame and correlates reasonably well with experimental
data. The scatter in Figure 3.48 is believed to be due to
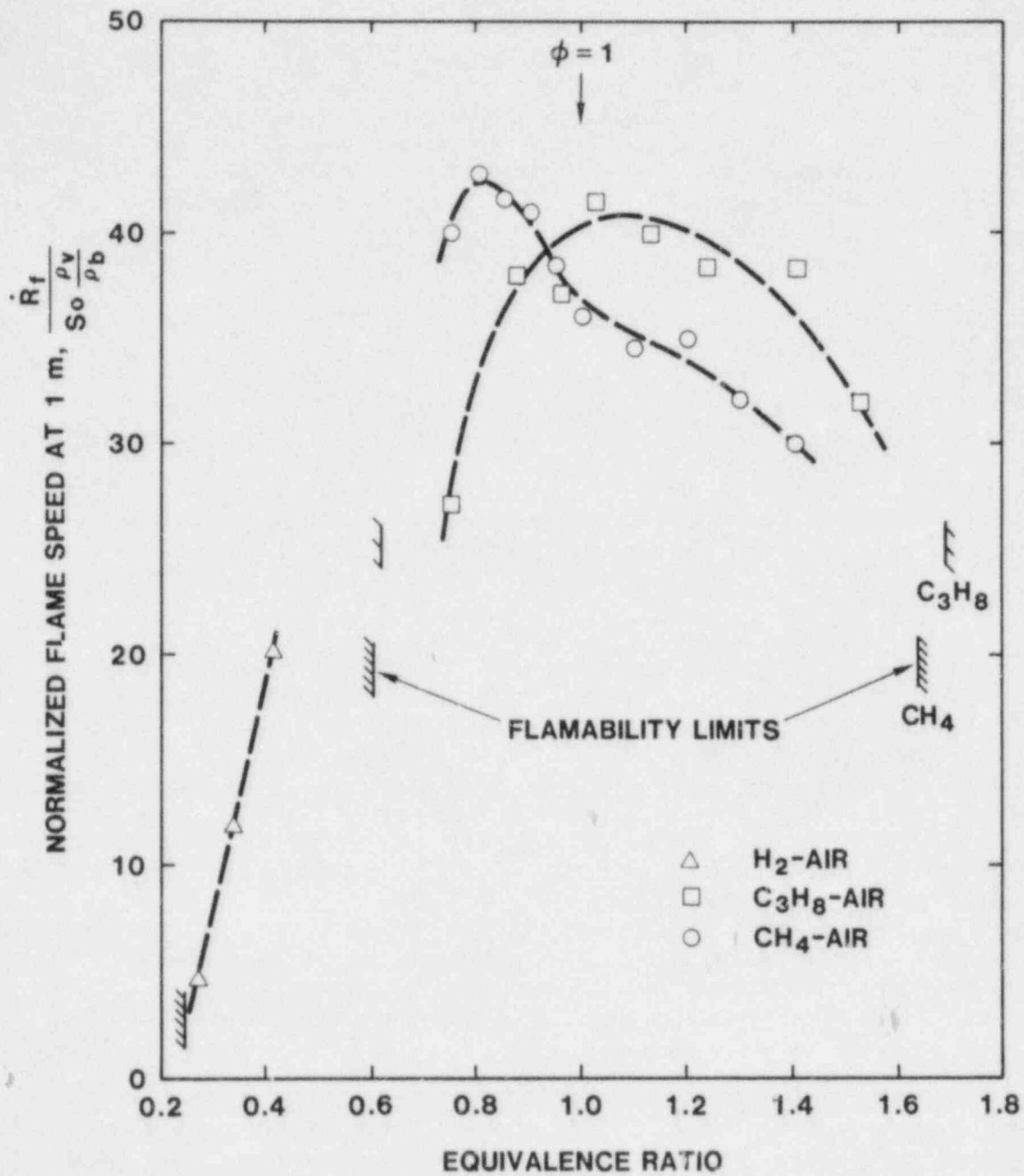
Figure 3.47. Normalized Flame Speed for Various Mixtures of H_2, CH_4, and C_3H_8, with Air
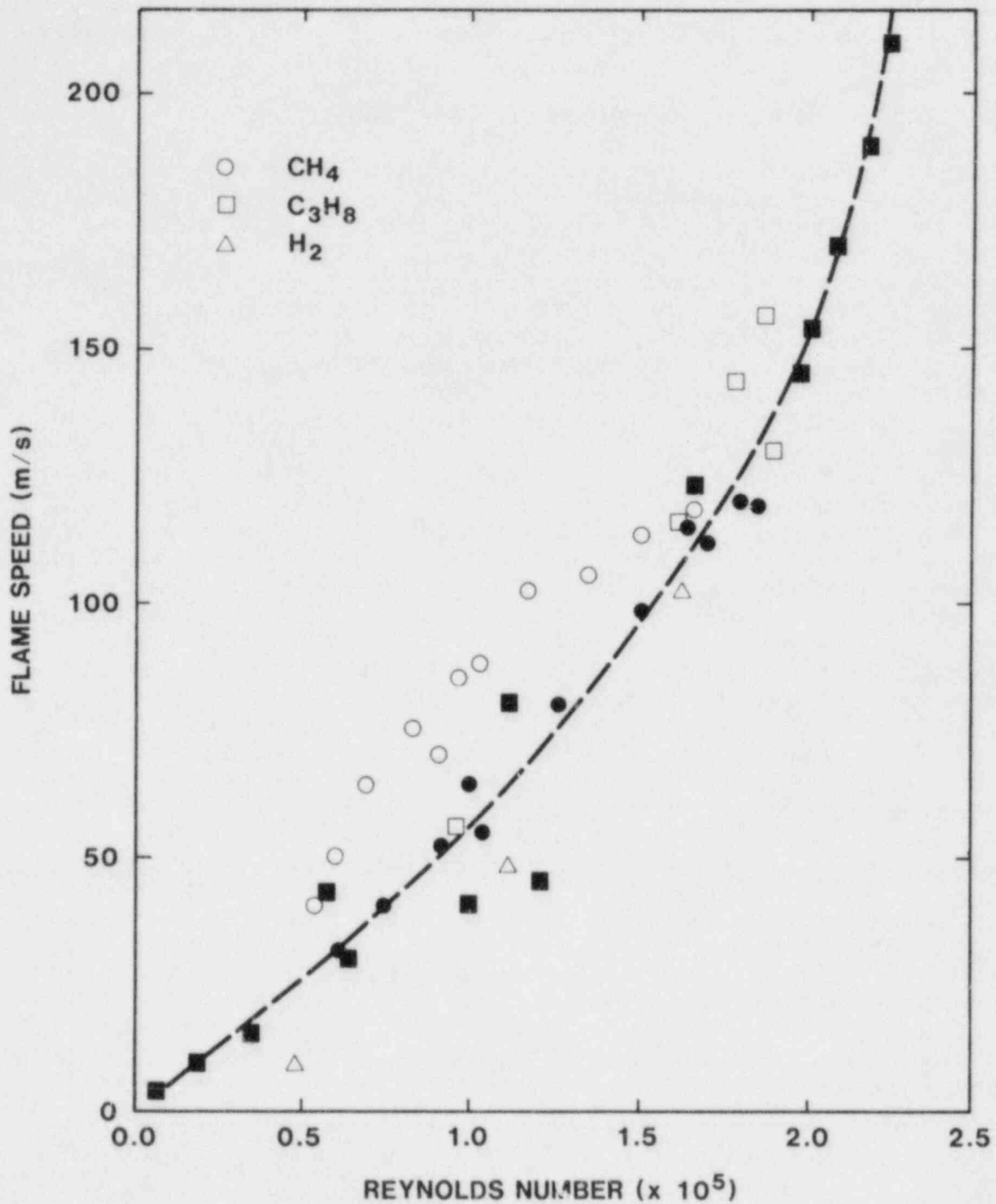
Figure 3.48. Flame Speed Profiles for Mixtures of H_2, CH_4, and C_3H_8 with Air as a Function of the Reynolds Number

the secondary effect of intrinsic cellular flame instability.
These results suggest that for the initial phase of flame
acceleration, one can use $(S_L(\rho_u/\rho_b - 1)/\nu)$ as a criterion
to rate the sensitivity or the hazardous level of every mix-
ture.

3.2.12.1.4 Quenching Diameter for Jet Ignition

A common scenario in an accidental explosion is the transmis-
sion of the explosion from one chamber to another. For exam-
ple, an explosion may start in a closed-in switch box or
motor casing, and the subsequent venting of the combustion
products via small openings can cause ignition of the explo-
sive mixture in the surrounding containment structure or
vessel. The problem of the transmision of explosion through
a small opening is a complex one consisting of different
regimes depending on the initial conditions. For example, if
combustion occurs sufficiently slowly in the first chamber
so that the pressure difference across the opening is negli-
gible, the transmission is essentially via laminar flame
propagation through the opening. The quenching mechanism is
based on heat and free radical losses to the wall of the
opening and the criterion for the quenching diameter is found
to correlate quite well using the Peclet number $Pe = SD/\alpha$
(where S is the laminar burning velocity, D the quenching
diameter, and α is the thermal diffusivity). For a small
pressure build-up across the opening, the transit time for
the flame through the opening is reduced. Thus, losses to
the wall are reduced and re-ignition past the opening can
occur for smaller opening than indicated by the Peclet num-
ber. Transmission for this regime is given by the so-called
maximum experimental safety gap (MESG) values and a standard
apparatus, agreed upon internationally, is used to determine
MESG values for different explosion gases. In general, MESG
values are slightly smaller than quenching diameters from
the Peclet regime. However, hydrogen:air mixtures for exam-
ple, are sufficiently sensitive so that confined explosions,
even with fairly large vents, give rise to large pressure
differences across the opening. In fact, except for near-
limit mixtures, pressures of the order of the constant volume
explosion pressure are usually attained. Quenching condi-
tions corresponding to such large pressure differences where
the venting is in the form of an underexpanded supersonic
turbulent jet are not well established. In view of its prac-
tical significance in accidental hydrogen:air explosions, a
study was carried out to establish the quenching criterion
for this supersonic jet ignition regime.

The experiments are carried out in a cylindrical explosion
chamber 25 cm diameter and 35 cm long with a smaller ignition
chamber (5 cm diameter and 48 cm long) connected to it via a
small orifice. Combustion is initiated by a spark in the
ignition chamber, and the mixture composition is varied for
a given orifice diameter until quenching (i.e., no ignition

in the main explosive chamber) is obtained. For orifice diame-
ters up to 35 mm, and 13% ≤ hydrogen ≤ 60%, the pressure
build-up in the ignition chamber is close to the constant
volume explosion value and a strong supersonic jet discharges
hot combustion products for the ignition of the mixture in
the main chamber. The variations of quenching diameter with
hydrogen concentration are shown in Figure 3.49. Also shown
is the corresponding overpressure developed across the ori-
fice. In all case, the overpressure ratio is greater than
the critical value of about 0.8 required for a choked dis-
charge. The variations of quenching diameter with hydrogen
concentration are in the familiar form of a U-shaped curve.
In the range of hydrogen concentration from 25% hydrogen to
45% hydrogen, the quenching diameter takes on a more or less
constant value of 1.2 mm and a sharp increase occurs at about
13% hydrogen and 60% hydrogen on the lean and rich sides,
respectively.

3.2.12.1.5 Influence of Strong Jet Ignition on Rate of Pres-
           sure Rise

The mechanism of strong ignition by a jet of hot combustion
products is fairly well understood qualitatively. The hot
jet entrains the cold explosive mixture and ignition results
in the mixing zones of the jet. Subsequent propagation of
the flame from this large turbulent flame kernel is very
rapid. It is also demonstrated that significant overpres-
sures can be developed even in fully vented vessels when the
ignition jet is sufficiently large and intense. A more sys-
tematic study of the overpressure development in a closed
vessel by jet ignition has been carried out.

The apparatus consists of a main explosion vessel connected
to a smaller ignition tube via an orifice. The volume of
the ignition tube is of the order of 10% of the volume of
the main vessel. The ignition jet diameter is controlled by
the size of the interconnecting orifice of the two chambers
and the jet intensity is varied by changing the vent area
(i.e., orifice opening) to volume ratio of the ignition tube
as well as the turbulent flame speed in the ignition tube
via the use of obstacles. Figure 3.50 shows the maximum
rate of overpressure rise in the vessel as a function of the
jet diameter normalized by the cube root of the vessel vol-
ume. The maximum rate of overpressure rise is normalized
with respect to the initial rate of overpressure rise due to
the growth of the flame kernel when the hot jet discharges
into the vessel. The results indicate that for CH_4 and C_2H_4
fuels, this normalized rate of the maximum overpressure rise
remains fairly constant with the size of the ignition jet,
suggesting that this maximum rate of overpressure rise in the
vessel is directly proportional to the initial rate when the
flame kernel size (i.e., jet size) increases. In other words,
the larger the size of the ignition jet, the higher will be
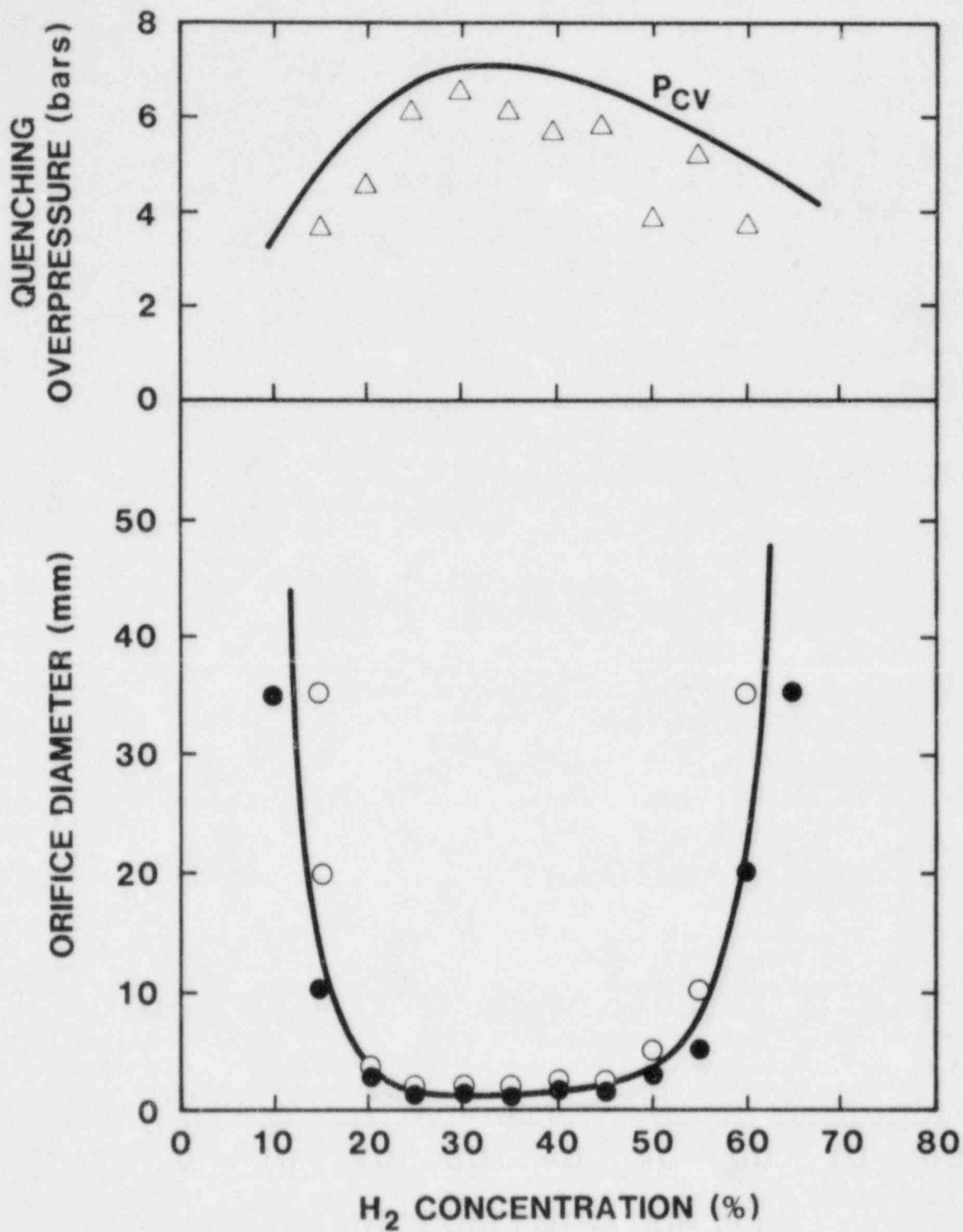
Figure 3.49. Quenching Diameters for Hydrogen:Air Mixtures
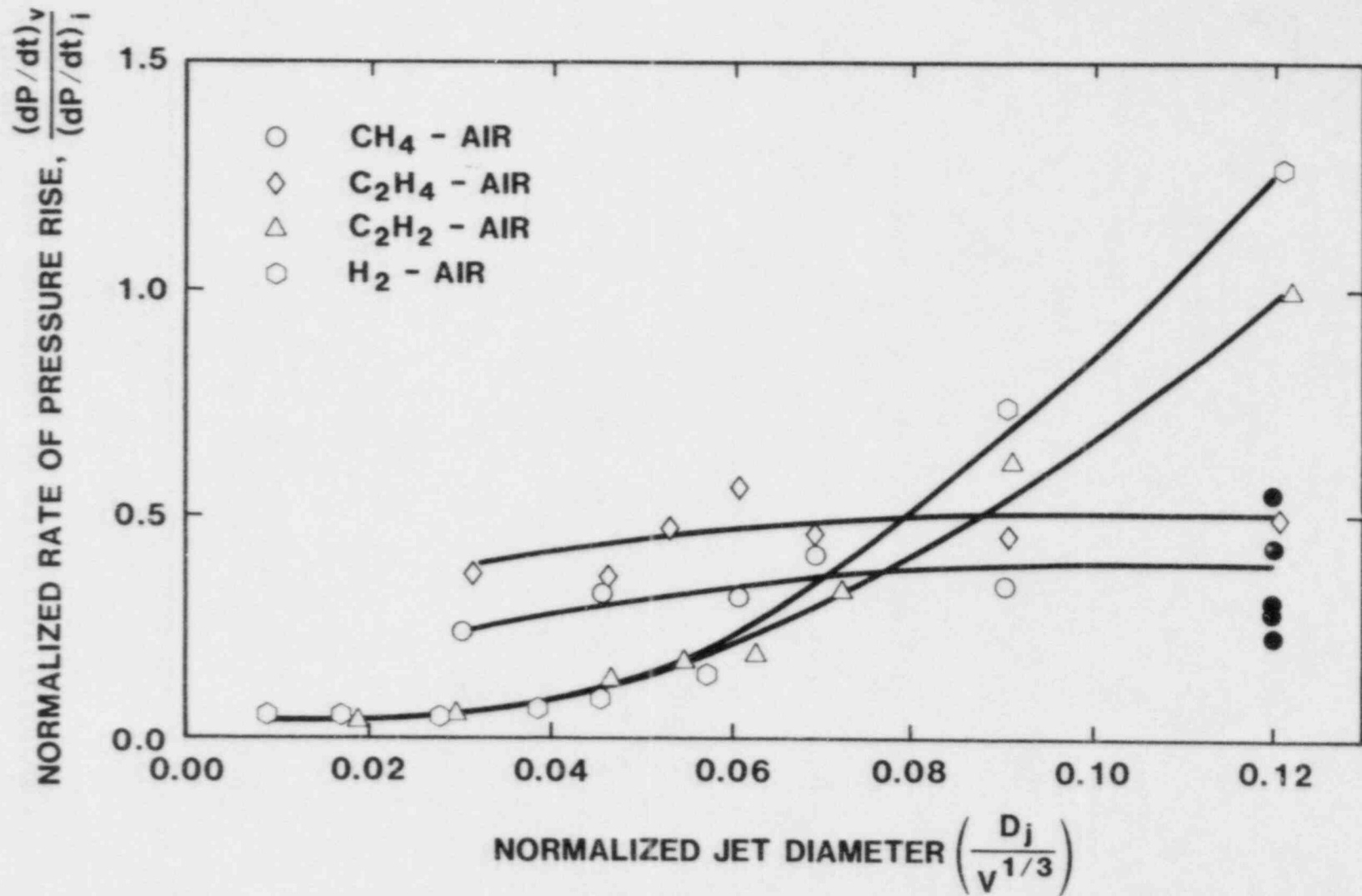
Figure 3.50.   Normalized Rate of Pressure Rise vs Normalized Jet Diameter

the subsequent maximum overpressure rise in the vessel. However, for the more sensitive fuels such as C_2H_2 and H_2, the maximum rate of overpressure rise in the vessel increases with the jet diameter after some critical value. Hence, some other flame acceleration mechanisms are triggered when the initial flame growth is sufficiently intense. Examination of the pressure records indicates that the mechanisms responsible are acoustic and Taylor instabilities due to the pressure wave interaction with the developing flame ball. The strong pressure waves generated by the initial growth of the flame kernel formed by the turbulent jet reflect off the vessel walls and interact with the expanding flame. Thus, the subsequent growth rate is increased significantly due to the intense turbulent flame structure developed as a result of these acoustic and Taylor instabilities. For these sensitive fuels, a sufficiently large intense turbulent jet may even result in the formation of detonation waves in the vessel.

3.2.12.1.6   The Taylor-Markstein Instability Mechanism on Flame Acceleration

Flame propagation inside a closed vessel is characterized by a cellular structure resulting from the coupling effect with the acoustic mode of the vessel. This cellular structure can give rise to very high burning rates. The intense combustion leads to the formation of shock waves from the coalescence of pressure waves in the system and gives rise to the Taylor-Markstein interfacial instability mechanism when head-on interaction of the shock with a flame occurs. Gross distortion of the flame resulting from Taylor-Markstein instability further augments the overall burning rate. Providing proper boundary conditions and sufficient time for the pressure waves to develop into strong shock waves, the Taylor-Markstein instability can be a strong flame acceleration mechanism. In small-scale laboratory experiments, the time scale may not be sufficient to manifest itself naturally prior to the completion of the combustion process. However, in large-scale experiments, the time scale for combustion process is longer. The Taylor-Markstein instability can be expected to play an important role in flame propagation.

A study of the role of Taylor-Markstein instability on flame propagation was recently conducted. The apparatus consists of a 0.96 m diameter spherical combustion chamber with a small cylindrical pressure vessel (13 cm long and 4 cm diameter) attached at the top. They are separated by a film of mylar (0.13 mm thick). The volume ratio between the main chamber and the vessel is 1 to 2800. The combustion chamber is filled with a fuel-air mixture (14% hydrogen) at atmospheric pressure, while the pressure vessel is filled with compressed air (150 psi). Moments after the mixture is ignited at the center of the chamber, the expanding flame kernel is perturbed by a blast wave resulting from bursting

the mylar film with a pin. The subsequent interaction between the pressure wave and the flame is monitored by measuring the pressure development within the chamber.

Assuming the flame kernel expands spherically and the gases within the chamber are compressed isentropically, the burned mass fraction $\lambda = m_b/m_0$, the normalized flame kernel size R_f/R_0, and the effective burning velocity S can be calculated based on the pressure development. m_0 is the initial mass of unburned mixture and R_0 is the radius of the combustion chamber. Figure 3.51 shows such a record for the centrally ignited 14% hydrogen:air mixture with no blast wave perturbation. It is interesting to note that when the kernel is about half the size of the chamber, only about 10% of the fuel has been consumed and almost half of the fuel is consumed during the last 10% of flame travel. The flame speed (relative to the chamber coordinate) remains almost constant throughout the whole combustion process. However, the effective burning velocity responds quite differently. It increases sharply as the flame gets closer to the wall. Oscillations on the pressure records suggest that the strong acoustically coupled pressure waves may have manifested themselves within the chamber and triggered the Taylor-Markstein instability mechanism. It should also be pointed out that part of the increase in burning velocity may be due to the increase in pressure inside the vessel.

To examine the shock wave-flame interaction, the expanding flame is perturbed by a shock wave generated by bursting the diaphragm in the pressure vessel. The results are shown in Figure 3.52. The delayed time in this experiment is 14 ms and the initial flame kernel size is 0.045 m in radius. Based on the pressure development, the effective burning velocity increases to about 6.0 m/s within 10 ms and decays rapidly back to its laminar value. The flame front is found to accelerate very rapidly right after the perturbation. The combustion process is completed within the next 90 ms. Without external perturbation, the process takes almost 180 ms. It was found that pressure oscillation resulted from the blast wave decay very rapidly. The subsequent low burning velocity indicates that the pressure waves fail to "hook" on to the acoustic frequency of the chamber and amplify themselves. The rapid decay of the burning velocity after perturbation also suggests that the lean hydrogen:air flame (14% hydrogen) is quite stable and does not create avalanche effects once perturbed. To examine the influence of the size of the initial flame kernel at the time of perturbation on subsequent flame development, similar experiments are performed with various delayed times. It is found that the subsequent burning differs significantly. Figure 3.53 shows the effective burning velocity development for various initial flame kernel sizes. With the same initial perturbation, the resultant peak burning velocity right after the perturbation decreases as the flame kernel gets larger. This result
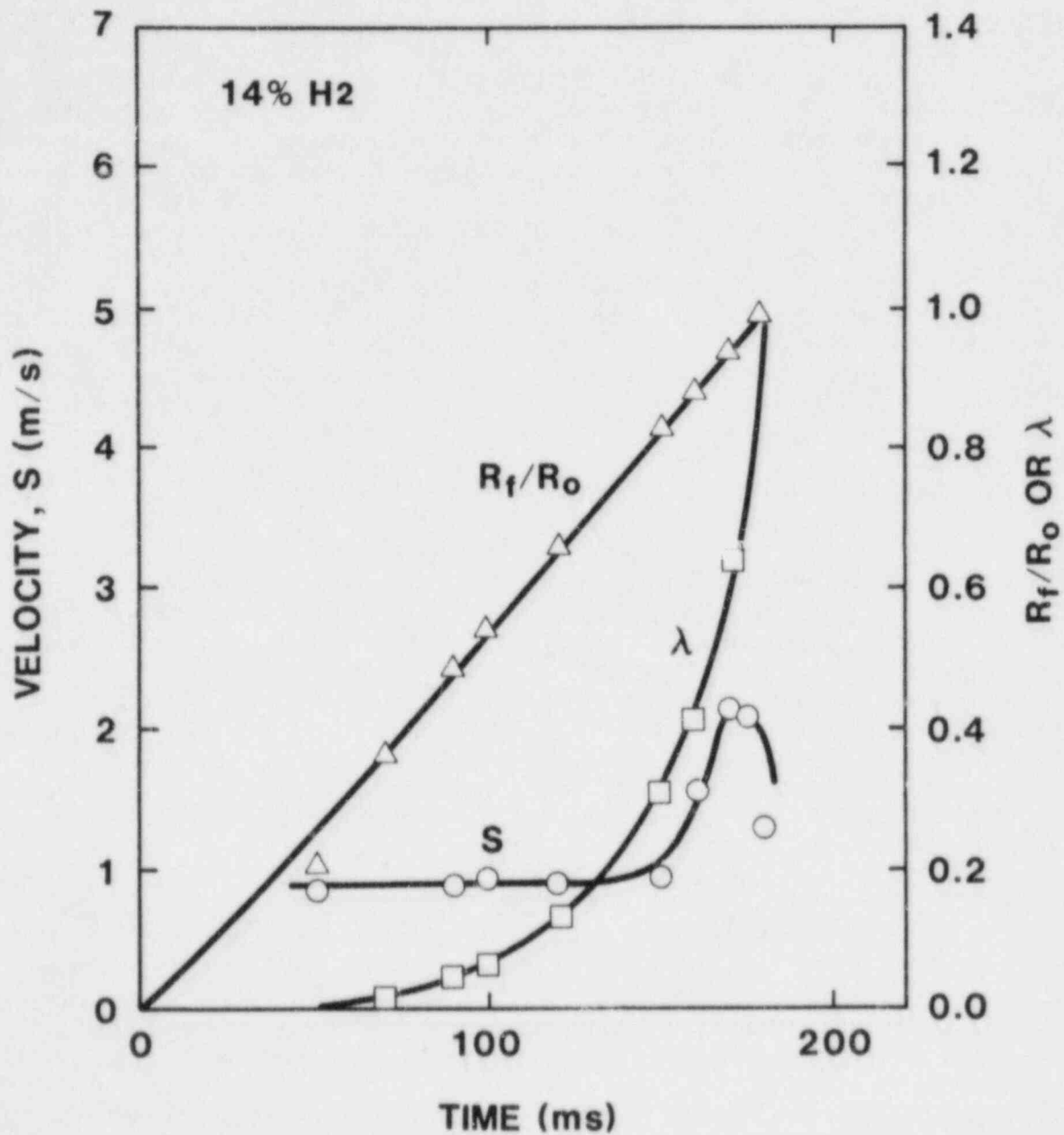
Figure 3.51. Flame and Effective Burning Velocity Development for 14% Hydrogen:Air Mixture without Perturbation
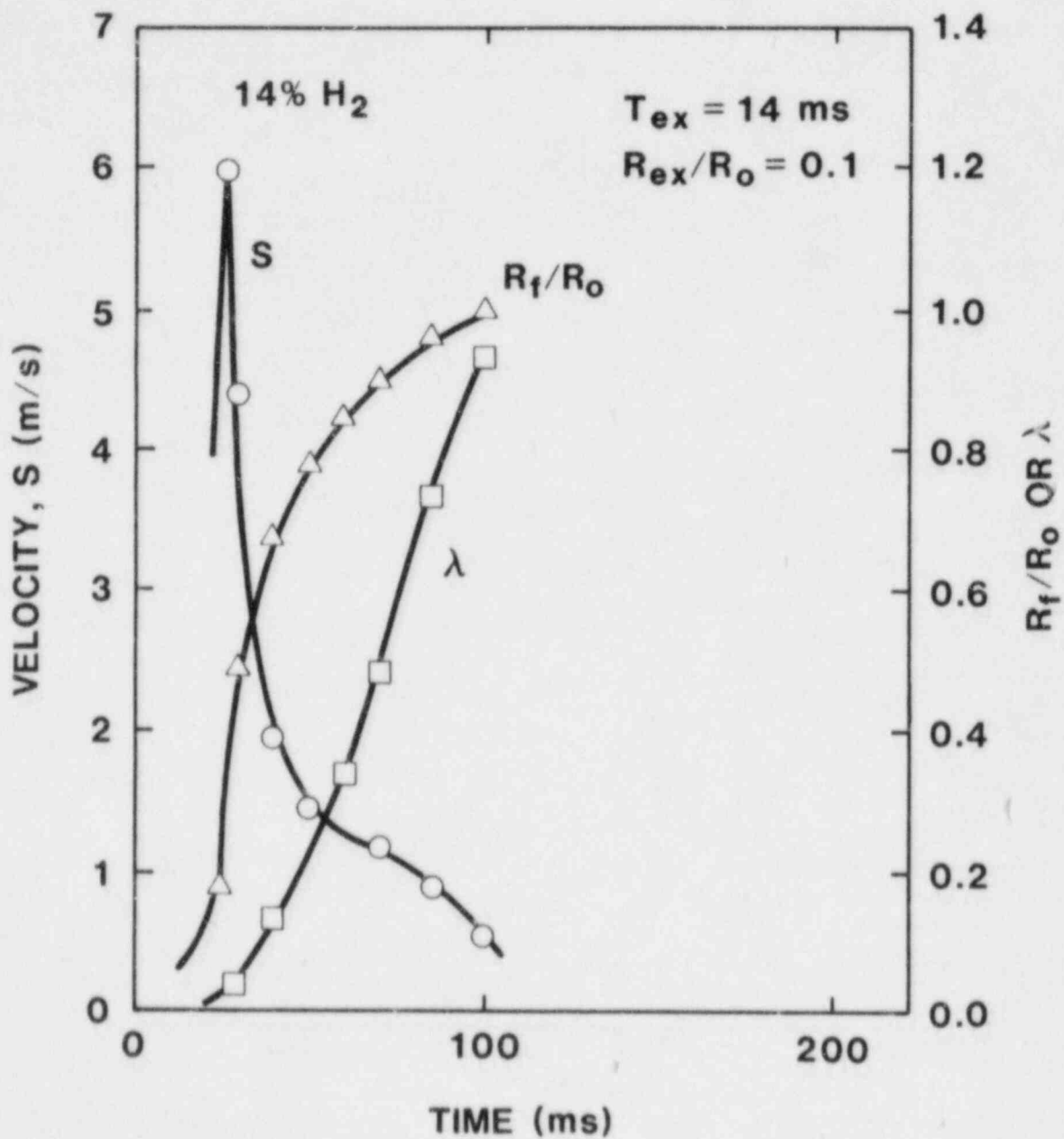
Figure 3.52. Flame and Effective Burning Velocity Development for 14% Hydrogen:Air Mixture with Perturbation
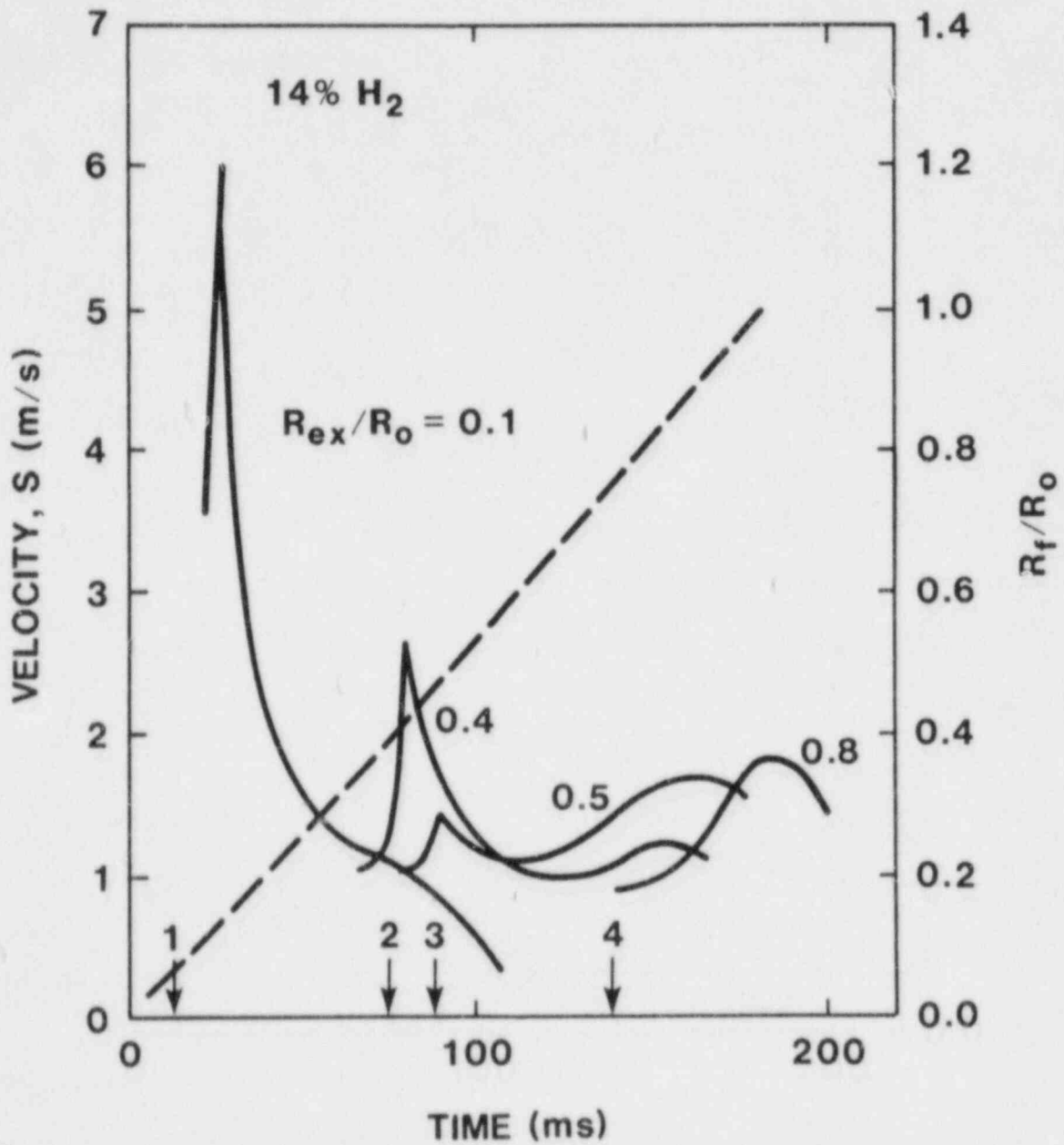
Figure 3.53. Effective Burning Velocity Development for Various Initial Flame Kernel Sizes

is expected. Due to the geometry of the chamber, the pressure waves after a few reflections off the wall coalesce more around the center of the chamber. This implies that the intensity of the perturbation is the highest around the center and decreases towards the wall. The second peak found in most of the records can be explained as a result of acoustic perturbation. If the burning process is long enough and the Rayleigh criterion is satisfied, the acoustic waves can grow into strong pressure waves and trigger the Taylor-Markstein instability mechanism. It should be noted that due to the large difference in the acoustic impedance for the burned and unburned gases, the acoustic frequency in the chamber changes during the combustion process. Thus, it is reasonable to expect the manifestation of strong acoustic waves in large-scale experiments as a rule rather than an exception. This study has demonstrated that the Taylor-Markstein instability mechanism is a powerful one, particularly when the pressure waves are strong. For sensitive mixtures, the instability mechanism can lead to an "avalanche effect" resulting eventually in transition to detonation.

3.2.12.2 Detonation Studies

In the present studies, both CO_2 and water vapor dilutions have been investigated as possible mitigative schemes to reduce the sensitivity of hydrogen:air detonations in the event of a LOCA incident at a nuclear plant.

3.2.12.2.1 Hydrogen:Air:CO_2 Detonations

Detonation cell sizes have been measured over a wide composition range in hydrogen:air:CO_2 mixtures. From these cell size data, all important dynamic detonation parameters (i.e., critical tube diameter, initiation energy, and detonability limits) can be deduced from existing empirical laws.

Apparatus--Detonation cell sizes were measured to two detonation tubes 15 cm diameter x 6 m long and 30 cm diameter x 16 m long. The mixture was introduced in the detonation tube by coflowing streams of the constituent gases (hydrogen, air, and CO_2) via individually calibrated rotameter type flowmeters. Direct initiation of detonation was achieved using a solid explosive charge. The diagnostics consisted of (i) average wave velocity measurements via four ionization gauges located along the detonation tube, (ii) detonation overpressure measurements using a piezoelectric transducer, and (iii) detonation cell diameter measurements using the smoked foil technique.

Results--Detonation cell diameter data for hydrogen: air:CO_2 mixtures are compared in Figure 3.54 with cell data for undiluted mixtures.[62] For meaningful
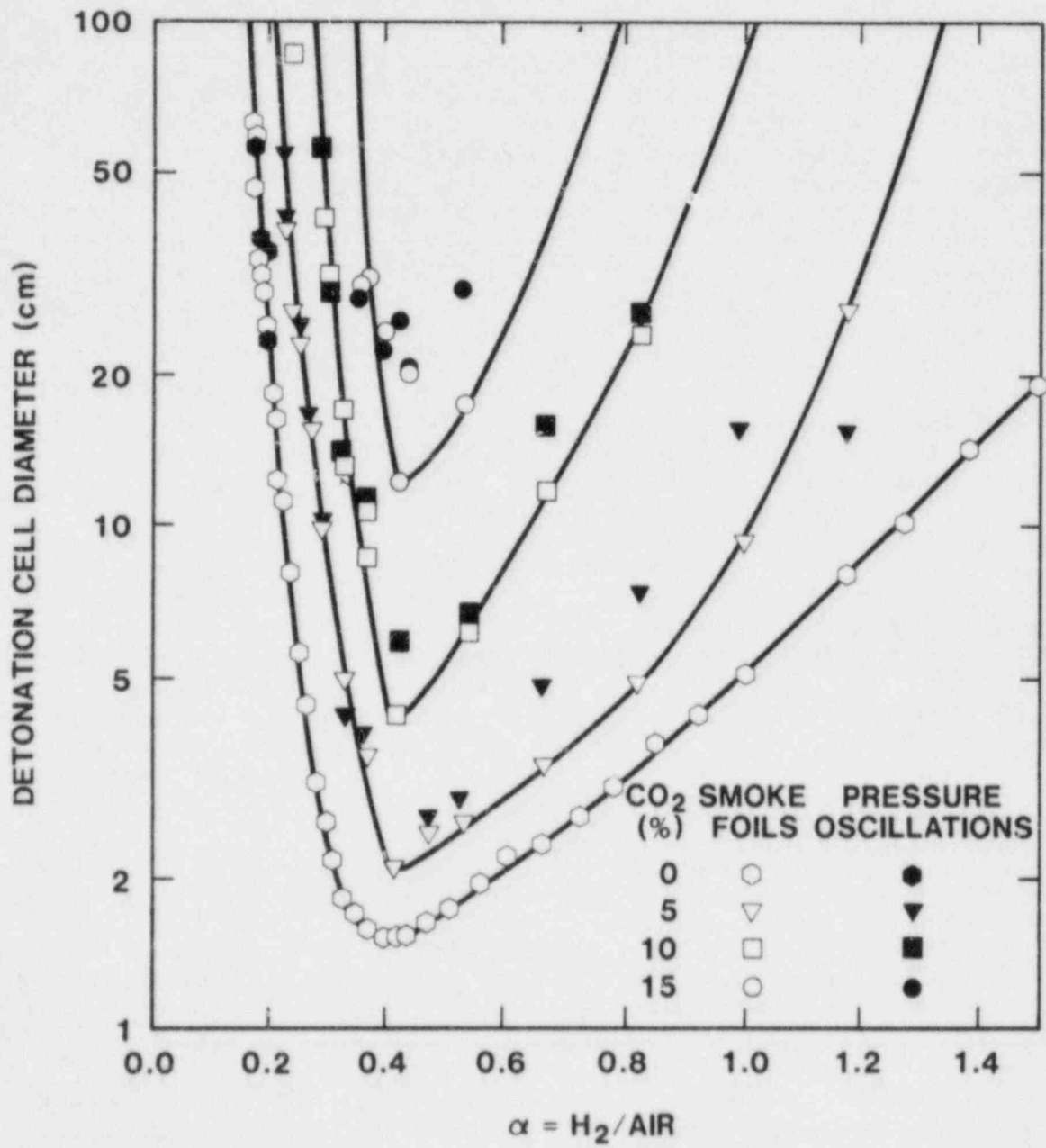
Figure 3.54. Detonation Cell Diameter vs Fuel Concentration

comparison of cell size data of undiluted and diluted mixtures, the data in Figure 3.54 have been plotted with respect to a concentration parameter α, which is independent of dilution. The concentration parameter α is defined as the ratio of the fuel concentration to the air concentration, $\alpha = y/(1- y)$ where y is the fuel mole fraction in the undiluted hydrogen:air mixture, whereas the composition of the diluted mixture is given by the relation

$$x \; CO_2 + (1 - x)(y \; H_2 + (1 - y) \; air)$$
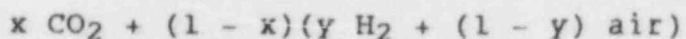
where x is the mole fraction of CO_2 diluent in the diluted mixture. The dilution ranges from $x = 0.0$ to $x = 0.15$ in increments of 0.5.

The cell data plots exhibit a typical U shape. The curves narrow and shift upwards with increasing CO_2 dilution. The cell data reach a minimum for $\alpha \simeq 0.4$ for both undiluted and diluted mixtures (i.e., for $y \simeq 29.6\%$, the stoichiometric composition of the undiluted mixture). These minima increase $\lambda = 1.51$ cm for 0% CO_2 dilution to $\lambda = 12.1$ cm for 15% CO_2 dilution (an order of magnitude increase in cell size) with $\lambda = 2.05$ cm and 4.2 cm for the 5% and 10% CO_2 dilution cases, respectively. For the largest dilution used in the present experiments, namely 15% CO_2, the detonation sensitivity (characterized by the detonation cell size) of hydrogen:air mixtures ranging from 17% to 35% hydrogen (i.e., $y = 0.17$ to 0.35, the limits of the present experiments) is reduced by an order of magnitude. A similar reduction is also observed with a smaller dilution (10% CO_2) for the leanest and the richest mixtures used in these experiments (namely, 25% and 45% hydrogen, i.e., $y = 0.25$ and 0.45). Therefore, CO_2 dilution appears quite effective in desensitizing hydrogen:air detonations in fuel-lean and fuel-rich mixtures.

3.2.12.2.2 Hydrogen:Air:Steam Detonations

To compare the efficiency of CO_2 and steam dilutions to desensitize hydrogen:air detonations at elevated temperatures, the properties of equilibrium Chapman-Jouguet (C-J) detonations in both mixtures have been computed using the classical, one-dimensional detonation model described in Reference 63. Three types of hydrogen:air mixtures have been investigated: (i) cold undiluted hydrogen:air mixtures at an initial temperature of 25°C, (ii) hot undiluted hydrogen:air mixtures at an initial temperature of 110°C, and (iii) hot hydrogen: air mixtures at an initial temperature of 110°C with various concentrations of water vapor or CO_2. For the diluted mixtures, the mixture composition is defined by the relation

$$x \; I + (1 - x)(y \; H_2 + (1 - y) \; air)$$

where I denotes the diluent H_2O or CO_2, x is the mole fraction
of diluent in the diluted mixture and y, the mole fraction of
fuel in the undiluted hydrogen:air mixture. The dilution range
extends from x = 0% H_2O (or CO_2) to x = 25% H_2O (and 15% CO_2)
in 5% increments. The fuel concentrations range from y = 10%
hydrogen to y = 60% hydrogen.

3.2.12.2.3 Results

The variations of the C-J detonation parameters (detonation
velocity and overpressure) with the concentration parameter
$\alpha = y/(1 - y)$ are compared in Figures 3.55 and 3.56 for
undiluted cold and hot hydrogen:air mixtures as well as
diluted hot hydrogen:air:steam mixtures. In the absences of
dilution, heating hydrogen:air mixtures from 25°C to 110°C
does not significantly affect the detonation velocity but
reduces the overpressure by approximately 25%.

In hot hydrogen:air mixtures, the largest H_2O dilution used in
the present study (namely, 25% H_2O reduces the maximum detona-
tion velocity and overpressure by approximately 17% and 40%
from their values for cold undiluted mixtures. This demon-
strates the efficiency of H_2O to reduce the detonation sensi-
tivity of hydrogen:air mixtures.

The effect of both CO_2 and H_2O dilutions on hydrogen:air deto-
nations at initial temperature of 110°C are compared in Fig-
ures 3.57 and 3.58 where the detonation velocity and overpres-
sure variations with the concentration parameter α have been
plotted for the same degree of dilution x = 15% CO_2 and 15%
H_2 along with both cold (25°C) and hot (110°C) undiluted mix-
tures. For all mixture compositions, the largest reduction in
detonation velocity occurs with CO_2 dilution. The maximum
detonation velocity of the cold, undiluted mixture (i.e., for
$\alpha = 1.5$, y = 60% hydrogen) is reduced by about 11% with H_2O
dilution and by approximately 23% with CO_2 dilution. For
fuel-rich mixtures, CO_2 dilution causes again the largest
reduction in overpressure whereas for fuel-lean mixtures, both
H_2O and CO_2 dilutions yield the same overpressure. Both dilu-
ents reduce the maximum overpressure of the cold undiluted
mixture (i.e., for $\alpha \simeq 0.42$, y $\simeq$ 29.6% hydrogen) by approxi-
mately 32% and 34%, respectively.

Based on a comparison of C-J detonation properties, the pre-
sent theoretical study demonstrates the slight superiority of
CO_2 dilution over H_2O dilution to decrease the detonation sen-
sitivity of hot, fuel-rich hydrogen:air mixtures. However,
for the most practical case of fuel-lean mixtures, the effects
of both diluents on the C-J detonation properties are almost
the same. Detailed measurements of C-J detonation parameters
as well as detonation cell sizes in hot CO_2 and H_2O diluted
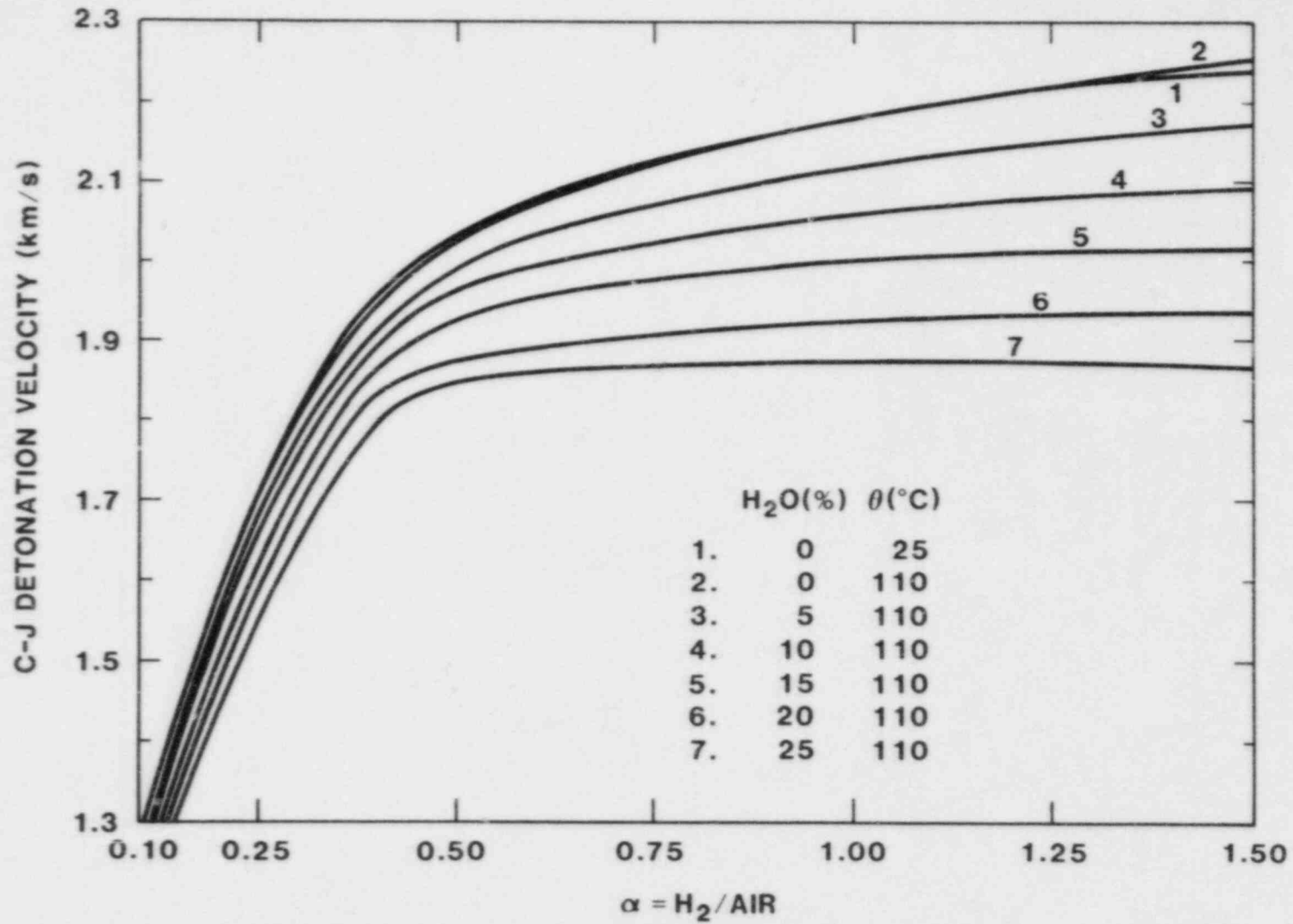
Figure 3.55.   Chapman-Jouguet Detonation Velocity vs Fuel Concentration
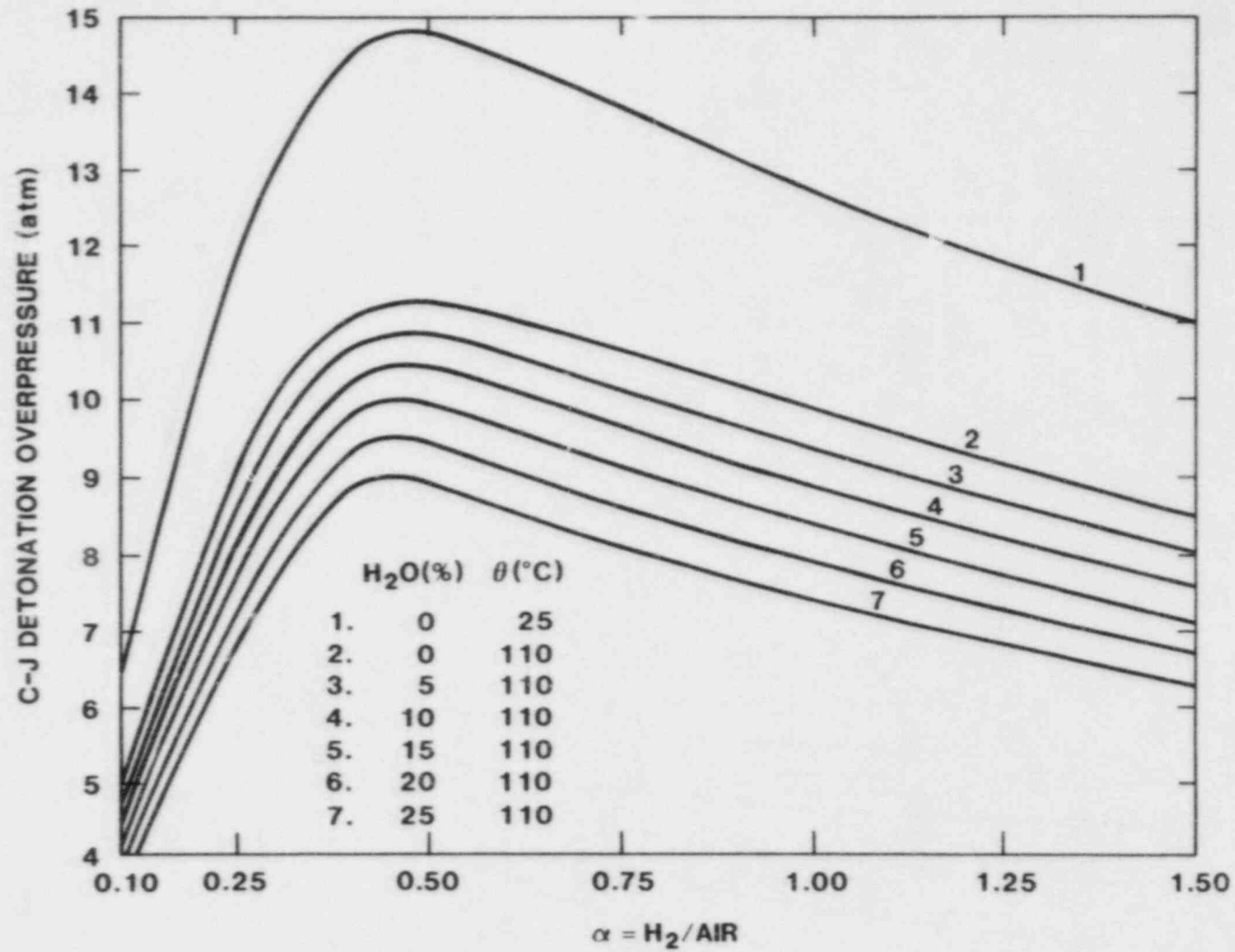
Figure 3.56. Chapman-Jouguet Detonation Overpressure vs Fuel Concentration
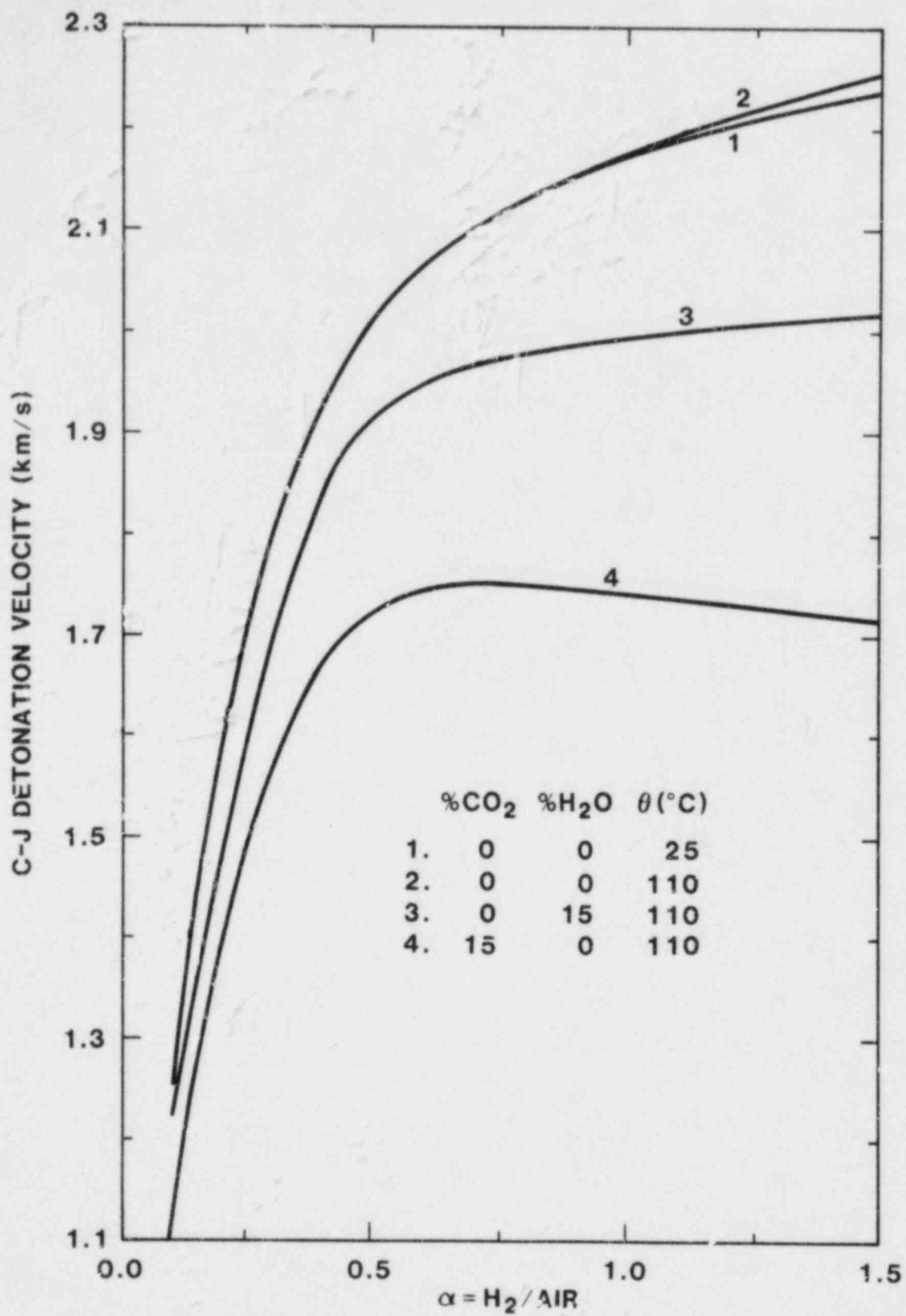
Figure 3.57.   Chapman-Jouguet Detonation Velocity vs Fuel
Concentration with CO_2 and H_2O Dilution
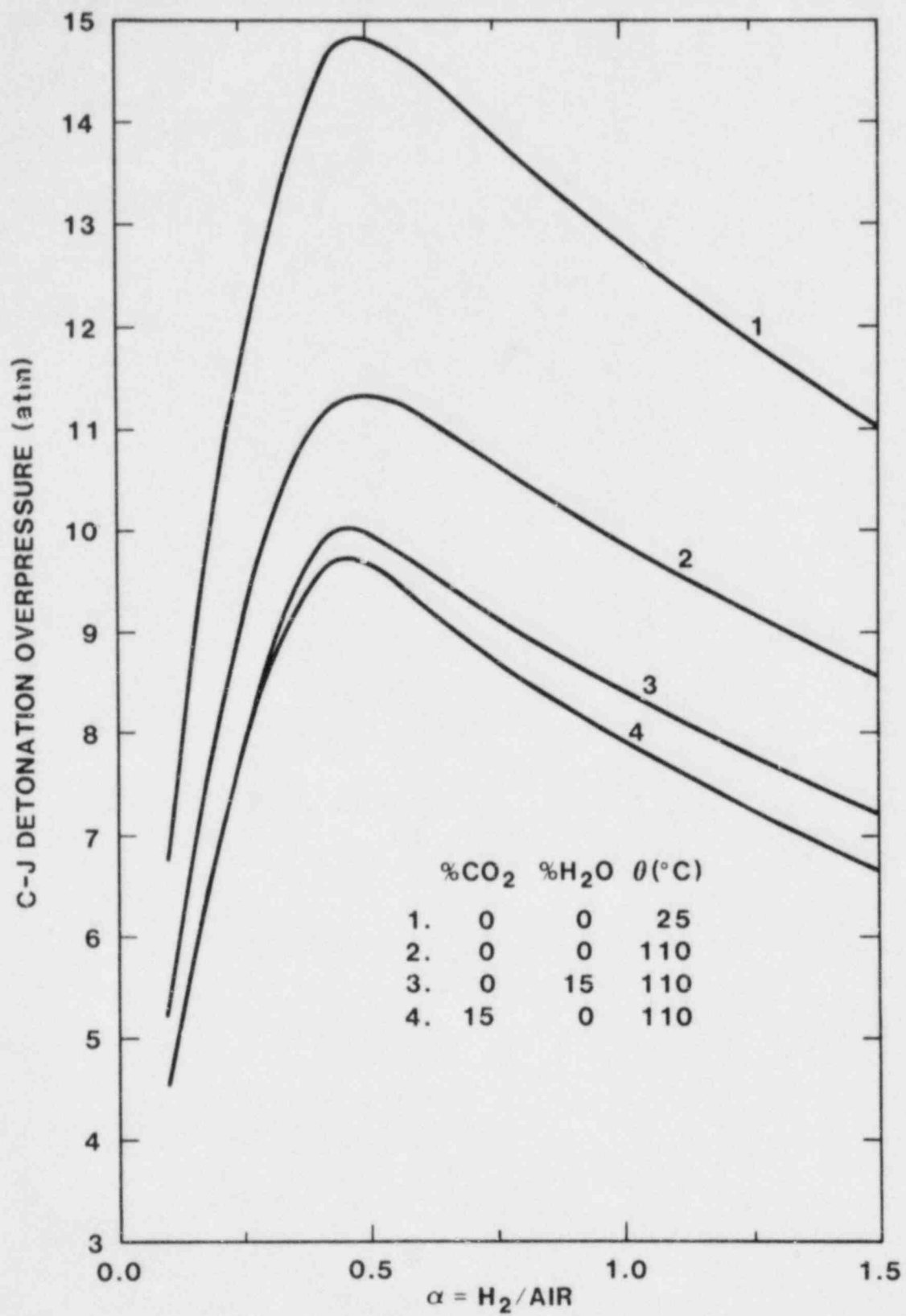
Figure 3.58. Chapman-Jouguet Detonation Overpressure vs Fuel Concentration with CO_2 and H_2O Dilution

hydrogen:air mixtures should provide a definite assessment of
the efficiency of both diluents to desensitize hydrogen:air
mixtures.

3.2.12.2.4 Effect of Geometry on the Transmission of Detonations through an Orifice

The first important detonation parameter to be linked to the
detonation cell size λ is the critical tube diameter d_c.
The critical tube diameter is the minimum diameter of a deto-
nation tube for the successful transmission of a planar deto-
nation wave propagating in this confining circular tube into
the unconfined environment and its transformation without
failure and subsequent propagation as a spherical detonation
wave. Extensive experiments have shown that there exists a
unique value of the critical tube diameter for each explosive
mixture.[64-67] On the basis of their experiments on the
diffraction of detonations, Mitrofanov and Soloukhin were
the first to point out that there exists a fundamental
empirical correlation between the critical tube diameter and
the detonation cell size λ, namely $d_c \simeq 13\lambda$.[65] Similar
experiments in detonation tubes of square cross sections indi-
cated that the critical tube width W_c for the successful
transmission and transformation of a confined planar detona-
tion into an unconfined cylindrical detonation requires about
10 detonation cell sizes, i.e., $W_c \simeq 10\lambda$.[68] In view of the
practical interest of the transmission of planar detonation
waves into a unconfined environment through orifices of dif-
ferent geometries and its implications for defining deton-
ability limits in partially confined clouds, an extensive
series of small-scale experiments conducted by the Shock Wave
Physics Laboratories at McGill and large-scale experiments
at SNLA have been carried out to address this problem.

Apparatus--The small-scale experimental apparatus con-
sisted of a linear detonation tube capable of producing
planar detonation waves up to 20 cm in diameter. The
tube was connected at one end to a large cylindrical
chamber (58 cm diameter x 75 cm long) in such a way that
20 cm diameter plates with different configuration ori-
fices milled into them could be inserted at the inter-
face between the end of the detonation tube and the
cylindrical chamber. The range of geometries for the
orifice covers circular, square, triangular, rectangular,
elliptical, and slotted shapes. Before each shot, the
detonation tube and chamber were first evacuated, then
both were filled with the explosive mixture via multiple
flushing in a flow displacement system. The mixture
composition was controlled by calibrated rotameter-type
flowmeters. The detonation in the tube was initiated by
exploding wires. The pressures in both detonation tube
and chamber were monitored by piezoelectric trans-
ducers (PCB 113A24).

In the large-scale experiments, two steel plates (6 ft wide x 8 ft long x 1 in. thick) were laid on a concrete block with the front end sticking out over the concrete block. The plates were spaced apart with tubular spacings near the four corners. A polyethylene bag (6 ft wide x 8 ft long x 3 ft high) was slipped over the protruding end of the plates sticking out over the concrete block. The bag was then sucked back between the two plates by means of a slight vacuum produced by a vacuum-type cleaner. Premixed explosive mixtures were drawn from a large reservoir to fill the space between the plates and inflate the plastic bag. Direct initiation was achieved via an explosive charge held down on a wooden board placed at the back end of the plates. Typically, a #8 detonator set off a detonation of 8 g of C4 explosive over which was laid a small strip (1 in. x 3 in.) of detasheet covered by a (55 in. long x 1/2 in. wide x 0.04 in. thick) strip of detasheet (Dupont EL506C-1). A high-speed camera (NOVA, 7500 frames/s) was used to observe the propagation of the combustion wave in the bag. Detonation cell diameters were also measured from smoked foil records.

Results--Stoichiometric fuel (H_2, C_2H_2, and C_2H_4)-oxygen mixtures diluted with various amounts of nitrogen at atmospheric pressure, initially were investigated in the small-scale experiments. The data indicate that for circular orifices the detonation transmission capabilities are identical to the critical tube diameter situation. For noncircular shapes (square, triangular, elliptical, and rectangular), the transmission of detonation through an orifice is more efficient than for the circular shape when based on the hydraulic diameter. However, the detonation transmission results for noncircular orifices correlate well when normalized to some effective diameter d_{eff} defined as the average between the radii of the inscribed and circumscribed circles. In this case $d_{eff} \simeq 13\lambda$ as for the case of the critical diameter.

When the orifice opening is in the form of a narrow slot with large length to width ratio, two-dimensional effects become dominant as shown in Figure 3.59 where the variations of the number of cell diameters across the width W of the orifice have been plotted with respect to the length to width ratio L/W. For square orifices, L/W = 1 and $W/\lambda \simeq 13$. As L/W increases, W/λ decreases and approached asymptotically a value of 3 when L/W exceeds approximately 8 as shown by the large-scale data in lean hydrogen:air mixtures. In other words, the transmission criterion for narrow slots becomes $W/\lambda \simeq 3$.
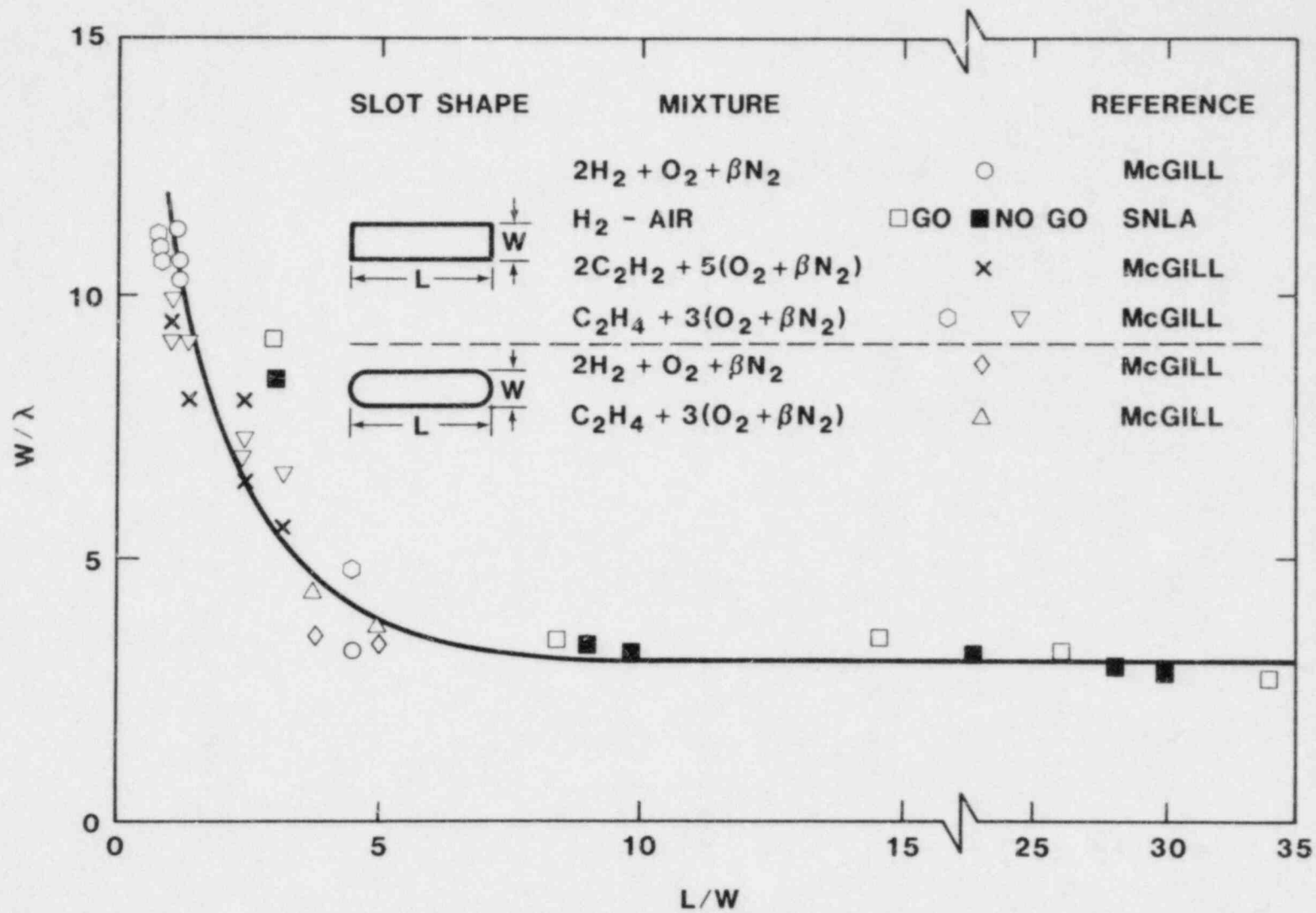
Figure 3.59. Ratio of Slot Width to Cell Diameter vs Ratio of Slot Length to Slot Width

3.3 Review of the Grand Gulf Hydrogen Igniter System II

(J. C. Cummings, A. L. Camp, J. E. Shepherd, M. P. Sherman, R. G. Spulack, R. K. Byers, S. E. Dingman, and R. Watson)

As a result of the experience derived from the TMI-2 accident, the NRC required that Mark III containments be equipped with additional systems to control excessive amounts of hydrogen generation. In this regard, the Mississippi Power and Light Company (MP&L) proposed installation of an igniter system in the Grand Gulf plant to burn the hydrogen generated during accidents more severe than the design-basis accidents. In conjunction with the licensing activities for the Grand Gulf Nuclear Station, there exists a need for an assessment of the effectiveness and reliability of the Hydrogen Igniter System (HIS) proposed by MP&L.

As part of the interim evaluation of the Grand Gulf HIS in 1982, the NRC contracted with Sandia National Laboratories to obtain an independent assessment of specific review items. The technical assistance effort of 1982 resulted in the identification of areas where further research would improve the current understanding of controlled ignition in Mark III containments.[69] The purpose of this follow-on program is to reduce the level of uncertainty by extending the previous investigation.

3.3.1 Work to be Performed

3.3.1.1 Task 1

Perform an evaluation of the research program proposed by the applicant (MP&L) to determine its adequacy in addressing the efficacy of controlled ignition in the Grand Gulf plant. In particular, Sandia shall review those portions of the testing concerned with the investigation of combustion in the wetwell region of the containment and testing related to the demonstration of mixing within containment.

3.3.1.2 Task 2

Sandia shall provide analyses of the containment atmosphere pressure and temperature response following postulated degraded-core accident scenarios. The analyses will consider the sensitivity to various items including containment modelling, combustion parameters, flow and mixing models, containment systems performance, and hydrogen:steam releases. The analyses will be performed with the revised HECTR code (code modifications will allow for modelling of drywell, suppression pool, and convective mixing). Sandia shall also evaluate, as necessary, any additional analyses performed by MP&L.

3.3.1.3 Task 3

Sandia shall evaluate, on a generic basis, the likelihood and consequences of local detonations within containments. As required, the NRC will furnish applicant submittals and available pertinent plant information. Sandia will provide criteria for establishing the credible volume of gas which may detonate for various containment designs and the results of analyses to determine the transient pressure histories of local detonations.

3.3.2 Results to Date

The status of Tasks 2 and 3 were discussed in Sections 3.1.1.5 and 3.1.5, respectively. Our progress on Task 1 is described in this section. Part of our approach to meet the Task 1 requirements involved our attendance at the meeting between Hydrogen Control Owner's Group (HCOG); (MP&L is a member of this organization of electric utilities) and the NRC. This meeting was held on September 10, 1982, at an NRC office in Bethesda, MD. We actively participated in the meeting and resolved a number of questions during the day.

After returning to Sandia, we began to examine in detail Froude modelling. This is the scaling concept that HCOG (Francisco Tamanini of Factory Mutual Research, under contract to HCOG) proposes to use in interpreting and extrapolating results from small-scale tests. We have obtained numerous literature references on this subject and made direct contact with Tamanini concerning our questions. Brief discussions were also held with Sam Hobbs (MP&L) and John Hosler (EPRI) during the Second International Workshop on the Impact of Hydrogen on Water Reactor Safety (Albuquerque, NM; October 3-7, 1982). Preliminary design of the vents for the 1/20-scale apparatus was the subject of those discussions.

A draft version of our Task 1 report was published on October 27, 1982 and a final version on November 30, 1982.[70] A summary of the HCOG research program and our Task 1 report follow.

3.3.2.1 Hydrogen Upper Flammability Limit Testing

The objective of these tests is to define flammability limits for hydrogen-rich mixtures of hydrogen:air:steam using a 12-V glow plug (GM AC-G7) as an ignition source. The testing contractor is Atomic Energy of Canada Limited. Approximately 50 tests are to be conducted in a 17-ℓ vessel with hydrogen:air:steam mixtures varying from 75:25:0 to 30:25:45. Basically, these tests will determine whether or not combustion has occurred (ionization gauge) and measure the associated pressure rise if it has. Apparently, a combustion completeness measurement will be attempted using a mass spectrometer

to determine the postcombustion mixture composition (H_2, O_2, and N_2 concentrations).

We consider these tests to be valuable. The data from them will be useful for estimating flammability limits in computer codes (e.g., CLASIX-3 and HECTR). However, direct extrapolation of results from the 17-ℓ vessel to a full-scale drywell or containment will not be warranted.

It appears that the only type of combustion being considered inside the drywell is volume or deflagrative combustion. An alternative which was briefly discussed at the September 10 meeting is an inverted diffusion flame located at the source of air (from the vacuum breakers or purge compressors, at the top of the drywell). The overpressure hazard would be greatly reduced in this case; however, heat loads imposed on nearby equipment could be quite large. Some experimental work may be necessary to define this problem. We suggest that the 8-ft-diameter sphere at Whiteshell would be much more appropriate for this study than the 17-ℓ vessel.

3.3.2.2 1/20-Scale Combustion Tests

The objective of these tests will be to provide a visual record of hydrogen combustion phenomena in a full, 360° model of a BWR Mark III containment. Seeding of the hydrogen with C_2H_2 will provide visible luminescence from the combustion zone(s). Video cameras will be the primary instrumentation tion used to record data from these tests. Acurex Corporation is the contractor for the apparatus and the tests. Approximately 40 tests will be conducted in order to qualitatively assess the effects on combustion phenomena of variations in: (1) hydrogen release rate, (2) blockages and heat sinks in the wetwell region, (3) release location (spargers vs suppression-pool vents), (4) number/location of active spargers, and (5) igniter location (above the suppression pool).

A number of technical issues need to be addressed and resolved before testing actually begins. These issues range from simple questions about experimental techniques and instrumentation to fundamental concerns about the proper treatment of fluid mechanical and combustion details:

- The combustion visualization technique is an established one, but care must be taken to insure that the amount of C_2H_2 "seed" added to the hydrogen does not significantly influence the ignition and combustion processes.

- Sprays may be important in determining the overall mixing and combustion behavior. If they could be added

for some tests, it would make the program results more comprehensive and provide guidance for the 1/4-scale tests.

• The "hydrogen release rate" is, in our opinion, an extremely important parameter in determining combustion phenomena in the wetwell region. Consequently, we recommend that a wide range of hydrogen release rates be used and that a significant portion of the total number of tests be used to examine the effects of variations in this parameter.

• We believe that full-scale glow plugs should not be used in the 1/20-scale apparatus. The wetwell region is only ~1 ft wide at this scale, and full-scale igniters would create convective flows that dominate the fluid mechanics of the region. Scaled igniters that have the proper power per unit surface area or per unit volume (of the full-scale igniters) would be our recommendation.

• The existence of steady-state diffusion flames in the wetwell will depend crucially on both the extent of blockage above the wetwell and the symmetry of the release rate. We are cognizant of the HCOG position on the symmetry of sparger operation, but we believe that some tests with asymmetric releases of hydrogen should be carried out in order to obtain a comprehensive understanding of _possible_ combustion phenomena in the wetwell.

• Finally, one of the key technical problems with the 1/20-scale apparatus is the need to vent the wetwell/containment volume in order to avoid high pressures. The "proper" way to carry out this venting is not clear. The vent inlets act as mass sinks, and their effect as fluid-mechanical disturbances may be important under some conditions.

3.3.2.3 1/4-Scale Combustion Tests

The objective of these tests will be to provide generic (to HCOG plants), directly scalable heat flux, gas flow, temperature, and concentration histories throughout the wetwell and containment regions. The device will be built at 1/4 linear scale using the full 360° design. Roughly 35 tests will be performed to determine the effects of: (1) variations in level and nature of blockages and heat sinks (in the wetwell region), (2) sparger and/or vent release, (3) suppression pool heating, (4) containment sprays, (5) igniter banks (1 or 2 activated), and (6) hydrogen release rate. Thirteen runs will be devoted to noncombustion (mixing) tests, and most will use helium in place of hydrogen.

Some of the technical issues raised in the discussion of the 1/20-scale tests may also be raised for the 1/4-scale tests. In particular, the igniter scale and design of the containment venting system may be important factors even at larger scale. Since the proposed HCOG schedule calls for construction of the facility to begin after the 1/20-scale combustion tests are completed, we believe that final decisions on these issues can be made after the initial tests in the 1/20-scale device have been conducted.

As far as the tentative test matrix is concerned, we would suggest a minor change in emphasis from hydrogen vent release to sparger release. This suggestion is made based upon our understanding (from General Electric) of the probability of various accident scenarios. The selection of hydrogen release rates may be best guided by observations made in the 1/20-scale tests. Finally, asymmetric hydrogen release from the spargers should be included if there is any significant probability of occurrence in a real accident.

3.3.2.4 Froude Modelling

Froude modelling assumes that the combustion is in the form of buoyancy-controlled, turbulent diffusion flames. In the event that hydrogen does not burn as it is released but accumulates and leads to a premixed flame, the Froude modelling will not properly scale the flame speed, combustion completeness, or heat flux to walls and equipment. Since additional restrictive assumptions are required in modelling the heat flux, the Froude modelling experiments may give satisfactory data on the nature of the combustion but not on the heat flux to walls and equipment.

In Froude modelling, the velocities scale as the square root of the length, and therefore, the corresponding Reynolds numbers in the experiments will be less than in containment by a factor of the length scale to the 3/2 power. For a 1/20-scale test, the Reynolds number is reduced by a factor of 89. We are concerned that there will be considerably more laminar flow in the small-scale tests than in the full-scale containment, possibly affecting some of the test results. Consider the hydrogen plume leaving the suppression pool. If the hydrogen generation rate is 1 lbm/s and the hydrogen leaves through eight spargers, the hydrogen plumes leaving the suppression pool will have a Reynolds number of about 4000 based on the plume diameter and the mean upward velocity. For hydrogen jets in air, the laminar to turbulent transition Reynolds number is about 2000. This means that in containment, for the high end of the range of hydrogen generation rates expected in accidents, the hydrogen plumes may be largely turbulent, but for the lower end, they will be near or below the transition point for laminar flow. In the tests, with their lower Reynolds numbers, considerably more laminar flow is expected. It therefore appears to us

that this issue (laminar flow in the tests contrasted with turbulent flow in containment) should be addressed in more detail.

The two important mechanisms of heat transfer from the hot gases to the walls and equipment will be convection and radiation. For equipment or walls outside the diffusion flame and its plume, with relatively cool intervening gas, radiative heat transfer should dominate. For surfaces inside the flame and its plume, convection is expected to dominate. Convective and radiative heat transfer scale differently in Froude modelling. Consequently, for surfaces in which both mechanisms are important, the test results for heat transfer will not be valid. In order to interpret the results for other surfaces, assumptions will have to be made as to the dominant heat-transfer mechanism.

3.4 References for Section 3

1. M. Berman, "Light Water Reactor Safety Research Program Semiannual Report, Sandia National Laboratories, Albuquerque, NM, April-September 1982", NUREG/CR-3407, (SAND83-1576).

2. Report on the Grand Gulf Nuclear Station Hydrogen Ignition System, Mississippi Power & Light Co., August 31, 1981.

3. R. O. Wooton and H. I. Avci, MARCH (Meltdown Accident Response Characteristics) Code Description and User's Manual, Battelle Columbus Laboratories, NUREG/CR-1711, October 1980.

4. "Containment Response to Degraded Core Events for the Sequoyah Nuclear Plant," Amendment 3 of letter from L. M. Mills, Tennessee Valley Authority, to Director of Nuclear Reactor Regulation, U.S. Nuclear Regulatory Commission, attention of Ms. Adensam, Docket Nos. 50-327 and 50-328, December 1, 19'1.

5. R. G. Gido and A. Koestel, "Hydrogen Burn Analyses of Ice-Condenser Containments", Los Alamos National Laboratory, NUREG/CR-3278, to be published.

6. J. C. Cummings et al., "Review of the Grand Gulf Hydrogen Igniter System", Sandia National Laboratories, NUREG/CR-2530; SAND82-0218, Sandia National Laboratories, March 1983.

7. G. Langer, R. Jenior, and H. G. Wentlandt, Experimental Investigation of the Hydrogen Distribution in the Containment of a Light Water Reactor Following a Coolant Loss Accident, NRC Translation 801, BF-F-63.363-3, Battelle Institute V. Frankfurt, Federal Republic of Germany, October 1980.

8. W. T. Ashurst, "Numerical Simulation of Turbulent Mixing Layers via Vortex Dynamics," in Turbulent Shear Flows I, edited by F. Durst et al. (Springer-Verlag, Berlin), pp. 402-413 (1979).

9. W. T. Ashurst, "Vortex Simulation of a Model Turbulent Combustor," in Combustion in Reactive Systems, edited by J.R. Bowen et al. Vol. 76 of Progress in Astronautics and Aeronautics, pp. 259-273 (1981).

10. W. T. Ashurst and P. K. Barr, "Stochastic Calculation of Laminar Wrinkled Flame Propagation via Vortex Dynamics," SAND82-8643, April 1983 and as Western States Paper WSS/CI 83-29 and an invited paper in Combustion Science and Technology (to appear).

11. P. K. Barr and W. T. Ashurst, "An Interface Scheme for Turbulent Flame Propagation," Sandia National Laboratories Report, SAND82-8773 (1982).

12. B. R. Sanders et al., "Flame Acceleration Modelling," in _Light Water Reactor Safety Research Program Semiannual Report, October 1981-March 1982_, edited by M. Berman, Sandia National Laboratories Report, 82-1572, also NUREG/CR-2841.

13. W. T. Ashurst and P. K. Barr, "Discrete Vortex Simulation of Flame Acceleration Due to Obstacle-Generated Flow," presented at the 1982 Fall Meeting of the Western States Section of the Combustion Institute, Paper WSS/CI 82-84; see also SAND82-8724, Sandia National Laboratories, Livermore, California.

14. J. H. Lee, R. Knystautas, and C. Guirao, "Hydrogen-Air Deflagrations: Recent Results," in _Proceedings of the Second International Workshop on the Impact of Hydrogen on Water Reactor Safety_, cosponsored by NRC/EPRI, October 3-7, 1982.

15. A. L. Camp, M. J. Wester, S. E. Dingman, and M. P. Sherman, "HECTR: A Computer Program for Modelling the Response to Hydrogen Burns in Containment," in _Proceedings of the Second International Workshop on the Impact of Hydrogen on Water Reactor Safety_, cosponsored by NRC/EPRI, October 3-7, 1982.

16. L. D. Cloutman, J. K. Dukowicz, J. D. Ramshaw, and A. A. Amsden, "CONCHAS-SPRAY: A Computer Code for Reactive Flows with Fuel Sprays," Los Alamos National Laboratory Report, LA-9294-MS, May 1982.

17. P. J. O'Rourke and F. V. Bracco, "Two Scaling Transformations for the Numerical Computation of Multidimensional Unsteady Laminar Flames", _J. Comp. Phys._ **33**, p. 185 (1979).

18. See, e.g., the bimonthly status reports for the Sandia Hydrogen Programs for October-November 1981, and December 1981-January 1982.

19. R. J. Kee, J. A. Miller, and T. H. Jefferson, "CHEMKIN: A General-Purpose, Problem-Independent, Transportable, Fortran Chemical Kinetics Package", Sandia National Laboratories Report, SAND80-8003, March 1980.

20. R. J. Kee, J. Warnatz, and J. A. Miller, "A FORTRAN Computer Code Package for the Evaluation of Gas-Phase Viscosities, Conductivities, and Diffusion Coefficients", Sandia Laboratories Report, SAND83-8209, March 1983.

21. C. S. McCamy, H. Shoub, and T. G. Lee, "Fire Extinguishment by Means of Dry Powder", 6th Symp. (Int'l) on Combustion, (Reinhold, NY, 1957), pp. 795-801.

22. I. Liebman, J. Corry, R. Pro, and J. K. Richmond, "Extinguishing Agents for Mine Face Gas Explosions", U. S. Bureau of Mines Bulletin RI 8294 (1978).

23. M. Berman, "Light Water Reactor Safety Research Program Quarterly Report," July-September 1979, Vol. 13, NUREG/CR-1177; and SAND79-2290 (1980).

24. See various references cited by T. S. Kress and M. L. Tobias, LMFBR Aerosol Release and Transport Program Quarterly Progress Report for January-March 1981, NUREG/CR-2299, Vol. 1, ORNL/TM-7946.

25. Memo, J. E. Brockmann to D. A. Powers, dated July 23, 1982, Subject: Burn Bar Tests.

26. P. Lafitte and R. Bouchet, "Suppression of Explosion Waves in Gaseous Mixtures by Means of Fine Powders", 7th Symp. (Int'l) on Combustion, (Butterworths, London, 1959), pp. 504-508.

27. W. Baukal, Battelle Institute, Frankfurt am Main, FRG, personal communication (1982).

28. K. Enomoto, S. Furuhama, and Y. Kobayashi, "Ignitability of Hydrogen-Air Mixture by Hot Surfaces and Hot Gases," Adv. Hydrogen Energy, (Hydrogen Energy Prog., Vol. 2), pp. 1149-63 (1981).

29. L. C. Beavis, "Interaction of Hydrogen with the Surface of Type 304 Stainless Steel," J. Vac. Sci. Technol. ID, pp. 386-390 (1973).

30. S. J. Collocott, V. T. Morgan, and R. Morrow, "Electrostatic Hazard Involved in Discharging CO_2 Fire Extinguisher," IEE Proc. 127, No. 2, Pt. A, pp. 119-120 (1980).

31. M. Berman et al., Analysis of Hydrogen Mitigation for Degraded Core Accidents in the Sequoyah Nuclear Power Plant, NUREG/CR-1726; SAND80-2714, Sandia National Laboratories, Albuquerque, NM, 1981.

32. T. Tanaka, "The Method for Measuring Water Droplets by Means of Polyvinyl Alcohol (Poval) Film," Pap. Meteorol. Geophys. 23, pp. 287-306 (1972).

33. A. L. Camp, X-Ray Measurements of Water Fog Density, Sandia National Laboratories, Albuquerque, NM, NUREG/CR-2767; SAND82-1292, 1982.

34. Memorandum, M. Berman and L. S. Nelson, Sandia National Laboratories, to P. Worthington, U. S. Nuclear Regulatory Commission, dated March 18, 1983.

35. L. M. Mills, TVA, to E. Adensam, USNRC, "Proposed Test Program to Demonstrate Igniter Operability in a Spray Environment", Enclosure, Letter, dated January 31, 1983, Tennessee Valley Authority, January 1983.

36. L. M. Mills, TVA, to E. Adensam, USNRC, "Additional Testing Performed on Tayco Igniters, Sequoyah Nuclear Plant", Enclosure No. 1, Letter, dated January 31, 1983, Tennessee Valley Authority, January 1983.

37. L. M. Mills, TVA, to E. Adensam, USNRC, "Additional Information on Adequacy of PHMS, Sequoyah Nuclear Plant", Enclosure No. 2, Letter, dated January 31, 1983, Tennessee Valley Authority, January 1983.

38. W. H. Walton and W. C. Prewett, "The Production of Sprays and Mists of Uniform Drop Size by Means of Spinning Disc Type Sprayers," Proc. Phys. Soc. Vol. 62, Part 6, p. 341, (June 1949).

39. B. E. Dixon, A. A. W. Russell, and J. E. L. Swallow, "Liquid films formed by means of rotating disks," British Journal of Applied Physics Vol. 3, p. 115, (April 1952).

40. D. J. Ryley, "Analysis of a polydisperse aqueous spray from a high-speed spinning disk atomizer," British Journal of Applied Physics Vol. 10, p. 180, (April 1959).

41. K. R. May, "An Improved Spinning Top Homogeneous Spray Apparatus," J. App. Phys. Vol. 20, p. 932, (October 1949).

42. D. J. Ryley, "Experimental determination of the atomizing efficiency of a high-speed spinning disk atomizer," British J. App. Phys. Vol. 10, p. 93, (February 1959).

43. Unpublished experimental results obtained by the author and Dr. Marx Brooks.

44. U. S. Patent No. 2,583,899 to L. H. Smith (1952).

45. U. S. Patent No. 4,215,818 to P. R. Hopkinson (1980).

46. U. S. Patent No. 1,832,096 to E. L. Chaffee (1931).

47. U. S. Patent No. 2,539,344 to T. W. Carraway (1951).

48. S. N. Grover and H. R. Pruppacher, "A Numerical Deter-
     mination of the Efficiency with Which Spherical Aerosol
     Particles Collide with Spherical Water Drops Due to
     Inertial Impaction and Phoretic and Electrical Forces,"
     J. Atmos. Sci., p. 1655 (October 1977).

49. J. R. Adam and R. G. Semonin, "Collection Efficiencies
     of Raindrops for Submicron Particulates," Precipitation
     Scavenging, AEC Symp. Ser. No. 22, pp. 151-160 (1970).

50. M. P. Sherman et al., The Behavior of Hydrogen During
     Accidents in Light Water Reactors, NUREG/CR-1561;
     SAND80-1495, (August 1980).

51. D. G. Johnston et al., "Development of Ventless Appli-
     ances and a Catalytic Ignition System," New Fuels and
     Advances in Combustion Technologies, Institute of Gas
     Technology, p. 461 (1979).

52. R. W. Schefer, F. Robben, and R. K. Cheng, "Catalyzed
     Combustion H_2/Air Mixtures in a Flat Plate Boundary
     Layer: I. Experimental Results," Comb. and Flame 38,
     51 (1980).

53. R. W. Schefer, "Catalyzed Combustion of H_2/Air Mix-
     tures in a Flat Plate Boundary Layer: II. Numerical
     Model," Comb. and Flame 45, 171 (1982).

54. R. W. Schefer, F. Robben, and N. J. Brown, "High Temper-
     ature Oxidation of H_2 on a Platinum Catalyst," Comb.
     and Flame, (in press).

55. R. J. Cattolica and R. W. Schefer, "Laser Fluorescence
     Measurements of the OH Concentration in a Combustion
     Boundary Layer," Comb. Sci. and Tech. 30, 205 (1983).

56. R. J. Cattolica and R. W. Schefer, "The Effect of Sur-
     face Chemistry on the Development of the OH in a Combus-
     tion Boundary Layer," Nineteenth Symposium (Interna-
     tional) on Combustion, The Combustion Institute,
     Pittsburgh, PA, p. 311 (1983).

57. H. Z. You and G. M. Faeth, "Ceiling Heat Transfer during
     Fire Plume and Fire Impingement", Fire and Materials 3,
     p. 140 (1979).

58. R. Connoly and R. M. Davies, "A Study of Convective
     Heat Transfer From Flames," Int. J. Heat Mass Transfer
     15, 2155 (1972).

59. J. K. Kilham and M. R. I. Purvis, "Heat Transfer from
     Normally Impinging Flames," Comb. Sci. and Tech. 18, 81
     (1978).

60. C. D. Donaldson, R. S. Snedeker, and D. P. Margolis, "A Study of Free Jet Impingement. Part 2. Free jet turbulent structure and impingement heat transfer," J. Fluid Mech. 45, 477. (1971).

61. C. Chan, I. O., Moen, and J. H. S. Lee, "Influence of Confinement on Flame Acceleration due to Repeated Obstacles", Combustion and Flame 49, pp. 27-39 (1983).

62. C. M. Guirao, R. Knystautas, J. H. Lee, W. Benedick, and M. Berman, "Hydrogen-Air Detonations", 19th Symposium (International) on Combustion, Haifa, Israel, (August 1982).

63. C. M. Guirao, R. Knystautas, and J. H. Lee, "C-J Detonation Studies in H_2-Cl_2, CS_2-O_2, and $CO-H_2-O_2-N_2$ Mixtures", AFOSR Interim Scientific Report, MERL 72-6, (July 1972).

64. Ia. B., Zeldovich, S. M. Kogarko, and M. N. Simonov, Soviet Physics Technical Physics Vol. 1, p. 1689 (1965).

65. V. V. Mitrofanov and R. I. Soloukhin, Soviet Physics-Doklady Vol. 9, No. 12, p. 1055 (1965).

66. H. Matsui and J. H. Lee, 17th Symposium (International) on Combustion, The Combustion Institute, Pittsburgh, PA, p. 1269 (1969).

67. R. Knystautas, J. H. Lee, and C. M. Guirao, Combustion and Flame 48, pp. 63-83 (1982).

68. D. H. Edwards, G. O. Thomas, and A. A. Nettleton, J. Fluid Mechanics 95, Part 1 (1979).

69. J. C. Cummings, A. L. Camp, M. P. Sherman, M. J. Wester, D. Tomasko, R. K. Byers, and B. W. Burnham, Review of the Grand Gulf Hydrogen Igniter System, NUREG/CR-2530; SAND82-0218, (March 1983).

70. J. C. Cummings, J. E. Shepherd, and M. P. Sherman, Review of the Grand Gulf Hydrogen Igniter System II (Task 1 Report), (November 30, 1982).

U. S. NRC Distribution Contractor (CDSI)
7300 Pearl Street
Bethesda, MD 20014
275 copies for R3

U. S. Bureau of Mines
Pittsburgh Research Center
P. O. Box 18070
Pittsburgh, PA 15236
Attn: M. Hertzberg

U. S. Nuclear Regulatory Commission   (6)
Office of Nuclear Regulatory Research
Washington, DC 20555
Attn: G. A. Arlotto
       R. T. Curtis
       J. T. Larkins
       L. C. Shao
       K. G. Steyer
       P. Worthington

U. S. Nuclear Regulatory Commission   (5)
Office of Nuclear Regulatory Research
Washington, DC 20555
Attn: B. S. Burson
       M. Silberberg
       J. L. Telford
       T. J. Walker
       R. W. Wright

U. S. Nuclear Regulatory Commission   (6)
Office of Nuclear Reactor Regulation
Washington, DC 20555
Attn: J. K. Long
       J. F. Meyer
       R. Palla
       K. I. Parczewski
       G. Quittschreiber
       D. D. Yue

U. S. Nuclear Regulatory Commission   (6)
Office of Nuclear Reactor Regulation
Washington, DC 20555
Attn: V. Benaroya
       W. R. Butler
      .G. W. Knighton
       T. M. Su
       Z. Rosztoczy
       C. G. Tinkler

U. S. Department of Energy
Operational Safety Division
Albuquerque Operations Office
P.O. Box 5400
Albuquerque, NM 87185
Attn: J. R. Roeder, Director

Swedish State Power Board
El-Och Vaermeteknik
Sweden
Attn: Eric Ahlstroem

Berkeley Nuclear Laboratory
Berkeley GL 139PB
Gloucestershire
United Kingdom
Attn: J. E. Antill

Gesellschaft fur Reakforsicherheit (GRS)
Postfach 101650
Glockengasse 2
5000 Koeln 1
Federal Republic of Germany
Attn: Dr. M. V. Banaschik

Battelle Institut E. V.
Am Roemerhof 35
6000 Frankfurt am Main 90
Federal Republic of Germany
Attn: Dr. Werner Baukal

UKAEA Safety & Reliability Directorate
Wigshaw Lane, Culcheth
Warrington WA34NE
Cheshire
United Kingdom
Attn: J. G. Collier   (3)
       S. F. Hall
       A. J. Wickett

British Nuclear Fuels, Ltd.
Building 396
Springfield Works
Salwick, Preston
Lancs
United Kingdom
Attn: W. G. Cunliffe

AERE Harwell
Didcot
Oxfordshire OX11 ORA
United Kingdom
Attn: J. Gittus, AETB   (2)
        J. R. Matthews, TPD

Kernforschungszentrum Karlsruhe
Postfach 3640
75 Karlsruhe
Federal Republic of Germany
Attn: Dr. S. Hagen   (3)
        Dr. J. P. Hosemann
        Dr. M. Reimann

Simon Engineering Laboratory
University of Manchester
M139PL,
United Kingdom
Attn: Prof. W. B. Hall

Kraftwerk Union
Hammerbacher strasse 12 & 14
Postfach 3220
D-8520 Erlangen 2
Federal Republic of Germany
Attn: Dr. K. Hassman   (2)
        Dr. M. Peehs

Gesellschaft fur Reaktorsickerheit (GRS mbH)
8046 Garching
Federal Republic of Germany
Attn: E. F. Hicken   (2)
        H. L. Jahn

Technische Universitaet Muenchen
D-8046 Garching
Federal Republic of Germany
Attn: Dr. H. Karwat

McGill University
315 Querbes
Outremont, Quebec
Canada H2V 3W1
Attn: John H. S. Lee   (3)

AEC, Ltd.
Whiteshell Nuclear Research Establishment
Pinawa, Manitoba, Canada
Attn: D. Liu   (2)
        H. Tamm

National Nuclear Corp. Ltd.
Cambridge Road
Whetestone, Leicester, LE83LH
United Kingdom
Attn: R. May

CNEN NUCLIT
Rome, Italy
Attn: A. Morici

Director of Research, Science & Education
CEC
Rue De La Loi 200
1049 Brussels
Belgium
Attn: B. Tolley

Bechtel Power Corporation
15740 Shady Grove Road
Gaithersburg, MD 20877
Attn: D. Ashton

Northwestern University
Chemical Engineering Department
Evanston, IL 60201
Attn: S. G. Bankoff

Brookhaven National Laboratory
Upton, NY 11973
Attn: R. A. Bari   (2)
      T. Pratt

Westinghouse Hanford Company
P. O. Box 1970
Richland, WA 99352
Attn: G. R. Bloom   (3)
      L. Muhlstein
      R. D. Peak

UCLA
Nuclear Energy Laboratory
405 Hilgard Avenue
Los Angeles, CA 90024
Attn: I. Catton

Argonne National Laboratory
9700 South Cass Avenue
Argonne, IL 60439
Attn: H. M. Chung

Sandia National Laboratories
Directorate 6400
P. O. Box 5800
Albuquerque, NM 87185
Attn: R. Cochrell   (20)

Sandia National Laboratories
Organization 6427
P. O. Box 5800
Albuquerque, NM 87185
Attn: G. Shaw   (20)

University of Wisconsin
Nuclear Engineering Department
1500 Johnson Drive
Madison, WI 53706
Attn: M. L. Corradini

Los Alamos National Laboratory
P. O. Box 1663
Los Alamos, NM 87545
Attn: H. S. Cullingford   (4)
       R. Gido
       G. Schott
       J. Travis

Battelle Columbus Laboratory
505 King Avenue
Columbus, OH 43201
Attn: P. Cybulskis   (2)
       R. Denning

Power Authority State of NY
10 Columbus Circle
New York, NY 10019
Attn: R. E. Deem   (2)
       S. S. Iyer

Offshore Power System   (2)
8000 Arlington Expressway
Box 8000
Jacksonville, FL 32211
Attn: G. M. Fuls
       D. H. Walker

Electric Power Research Institute
3412 Hillview Avenue
Palo Alto, CA 94303
Attn: J. J. Haugh   (3)
       K. A. Nilsson
       G. Thomas

Fauske & Associates
627 Executive Drive
Willowbrook, IL 60521
Attn: R. Henry

Mississippi Power & Light
P. O. Box 1640
Jackson, MS 39205
Attn: S. H. Hobbs

General Electric Co.
175 Curtner Avenue
Mail Code N 1C157
San Jose, CA 95125
Attn: K. W. Holtzclaw

NUS Corporation
4 Research Place
Rockville, MD 20850
Attn: R. Sherry

Duke Power Co.
P. O. Box 33189
Charlotte, NC 28242
Attn: F. G. Hudson   (2)
       A. L. Sudduth

Westinghouse Corporation
P. O. Box 355
Pittsburgh, PA 15230
Attn: N. Liparulo   (3)
       J. Olhoeft
       V. Srinivas

General Physics Corporation
1000 Century Plaza
Columbia, MD 21044
Attn: Chester Kupiec

TVA
400 Commerce
W9C157-CD
Knoxville, TN 37902
Attn: Wang Lau

EG&G Idaho
Willow Creek Building, W-3
P. O. Box 1625
Idaho Falls, ID 83415
Attn: Server Sadik

Department of Aerospace Engineering
University of Michigan
Ann Arbor, MI   47109
Attn: Martin Sichel

Dr.Roger Strehlow
505 South Pine Street
Champaign, IL   61820

Applied Sciences Association, Inc.
P. O. Box 2687
Palos Verdes Pen., CA   90274
Attn: D. Swanson

Purdue University
School of Nuclear Engineering
West Lafayette, IN   47907
Attn: T. G. Theofanous

Acurex Corporation
485 Clyde Avenue
Mountain View, CA   94042

Astron
2028 Old Middlefield Way
Mountainview, CA   94043
Attn: Ray Torok

Bechtel Power Corporation
P. O. Box 3965
San Francisco, CA   94119
Attn: R. Tosetti

Thompson Associates
639 Massachusetts Avenue
Third Floor
Cambridge, MA   02139
Attn: Timothy Woolf

Factory Mutual Research Corporation
P. O. Box 688
Norwood, MA   02062
Attn: R. Zalosh

Sandia Distribution:
1131   W. B. Benedick
1131   J. Fisk
1512   J. C. Cummings
1513   S. N. Kempka
1513   A. C. Ratzel
2512   V. M. Loyola
2513   J. E. Shepherd
6400   A. W. Snyder
6410   J. W. Hickman
6411   V. L. Behr
6411   A. L. Camp
6411   S. E. Dingman
6411   F. E. Haskin
6420   J. V. Walker
6421   J. B. Rivard
6422   D. A. Powers
6422   A. R. Taig
6425   W. J. Camp
6425   W. Frid
6427   M. Berman (20)
6427   K. P. Guay
6427   J. Kotas
6427   M. S. Krein
6427   B. W. Marshall, Jr.
6427   L. S. Nelson
6427   O. Seebold
6427   M. P. Sherman
6427   S. R. Tieszen
6427   G. Valdez
6427   M. J. Wester
6427   C. C. Wong
6440   D. A. Dahlgren
6442   W. A. von Riesemann
6444   R. K. Cole, Jr.
6444   S. L. Thompson
6445   E. H. Richards
6449   K. D. Bergeron
8424   M. A. Pound
8513   W. J. McClean
8523   W. T. Ashurst
8523   K. D. Marx
8523   B. R. Sanders
3141   C. M. Ostrander (5)
3151   W. L. Garner

2. Leave blank

3. TITLE AND SUBTITLE

Light Water Reactor Safety Research Program
Semiannual Report, October 1982 - March 1983

4. RECIPIENT'S ACCESSION NUMBER

5. DATE REPORT COMPLETED

MONTH	YEAR

6. AUTHOR(S)

Marshall Berman

7. DATE REPORT ISSUED

MONTH	YEAR

8. PERFORMING ORGANIZATION NAME AND MAILING ADDRESS (Include Zip Code)

Sandia National Laboratories
Albuquerque, NM 87185

9. PROJECT/TASK/WORK UNIT NUMBER

10. FIN NUMBER

A1019, A1030, A1237,
A1246

11. SPONSORING ORGANIZATION NAME AND MAILING ADDRESS (Include Zip Code)

Office of Nuclear Regulatory Research
U.S. Nuclear Regulatory Commission
Washington, DC 20555

12a. TYPE OF REPORT

Semiannual

12b. PERIOD COVERED (Inclusive dates)

Oct. 1982 - March 1983

13. SUPPLEMENTARY NOTES

14. ABSTRACT (200 words or less)

This report describes the investigations and analyses conducted at Sandia
National Laboratories, Albuquerque, in support of the Light Water Reactor
Safety Research Program from October 1982 through March 1983. The Molten
Fuel/Concrete Interactions (MFCI) Study investigates the mechanism of
concrete erosion by molten core materials, the nature and rate of genera-
tion of evolved gases, and the effects of fission-product release. The
Core Melt/Coolant Interactions (CMCI) Study investigates the characteristics
of explosive and nonexplosive interactions between molten core materials
and concrete, and the probabilities and consequences of such interactions.
In the Hydrogen Program, the HECTR code for modelling hydrogen deflagration
is being developed, experiments (including those in the FITS facility)
are being conducted, and the Grand Gulf Hydrogen Igniter System II is
being reviewed. All activities are continuing.

15a. KEY WORDS AND DOCUMENT ANALYSIS

15b. DESCRIPTORS

16. AVAILABILITY STATEMENT	17. SECURITY CLASSIFICATION (This report)	18. NUMBER OF PAGES
NTIS and GPO Sales	Unclassified	
	19. SECURITY CLASSIFICATION (This page)	20. PRICE
	Unclassified	S

Org.	Bldg.	Name	Rec'd by	Org.	Bldg.	Name	Rec'd by

Sandia National Laboratories